

IDŐJÁRÁS

QUARTERLY JOURNAL
OF THE HUNGARIAN METEOROLOGICAL SERVICE

CONTENTS

<i>Judit Bartholy and Rita Pongrácz: Tendencies of extreme climate indices based on daily precipitation in the Carpathian Basin for the 20th century</i>	1
<i>Angéla Anda and Zsuzsanna Lőke: Microclimate simulation in maize with two watering levels</i>	21
<i>Márta Hunkár: On the use of standard meteorological data for microclimate simulation.....</i>	39
<i>Tania Marinova, Lilia Bocheva and Vladimir Sharov: On some climatic changes in the circulation over the Mediterranean area</i>	55
<i>Book review</i>	69

http://omsz.met.hu/english/ref/jurido/jurido_en.html

IDŐJÁRÁS

Quarterly Journal of the Hungarian Meteorological Service

Editor-in-Chief
LÁSZLÓ BOZÓ

Executive Editor
MARGIT ANTAL

EDITORIAL BOARD

AMBRÓZY, P. (Budapest, Hungary)	MIKA, J. (Budapest, Hungary)
ANTAL, E. (Budapest, Hungary)	MERSICH, I. (Budapest, Hungary)
BARTHOLY, J. (Budapest, Hungary)	MÖLLER, D. (Berlin, Germany)
BATCHVAROVA, E. (Sofia, Bulgaria)	NEUWIRTH, F. (Vienna, Austria)
BRIMBLECOMBE, P. (Norwich, U.K.)	PAP, J. (Washington, U.S.A.)
CZELNAI, R. (Dölgicse, Hungary)	PINTO, J. (R. Triangle Park, NC, U.S.A.)
DÉVÉNYI, D. (Boulder, U.S.A.)	PRÁGER, T. (Budapest, Hungary)
DUNKEL, Z. (Budapest, Hungary)	PROBÁLD, F. (Budapest, Hungary)
FISHER, B. (Reading, U.K.)	RADNÓTI, G. (Budapest, Hungary)
GELEYN, J.-Fr. (Toulouse, France)	ROCHARD, G. (Lannion, France)
GERESDI, I. (Pécs, Hungary)	S. BURÁNSZKY, M. (Budapest, Hungary)
GÖTZ, G. (Budapest, Hungary)	SZALAI, S. (Budapest, Hungary)
HANTEL, M. (Vienna, Austria)	TAR, K. (Debrecen, Hungary)
HASZPRA, L. (Budapest, Hungary)	TÁNCZER, T. (Budapest, Hungary)
HORÁNYI, A. (Budapest, Hungary)	TOTH, Z. (Camp Springs, U.S.A.)
HORVÁTH, Á. (Siófok, Hungary)	VALI, G. (Laramie, WY, U.S.A.)
KONDRATYEV, K. Ya. (St. Petersburg, Russia)	VARGA-HASZONITS, Z. (Moson- magyaróvár, Hungary)
MAJOR, G. (Budapest, Hungary)	WEIDINGER, T. (Budapest, Hungary)
MÉSZÁROS, E. (Veszprém, Hungary)	

*Editorial Office: P.O. Box 39, H-1675 Budapest, Hungary or
Gilice tér 39, H-1181 Budapest, Hungary
E-mail: bozo.l@met.hu or antal.e@met.hu
Fax: (36-1) 346-4809*

Subscription by

*mail: IDŐJÁRÁS, P.O. Box 39, H-1675 Budapest, Hungary;
E-mail: bozo.l@met.hu or antal.e@met.hu; Fax: (36-1) 346-4809*

IDŐJÁRÁS

Quarterly Journal of the Hungarian Meteorological Service
Vol. 109, No. 1, January–March 2005, pp. 1–20

Tendencies of extreme climate indices based on daily precipitation in the Carpathian Basin for the 20th century

Judit Bartholy and Rita Pongrácz

*Department of Meteorology, Eötvös Loránd University,
P.O. Box 32, H-1518 Budapest, Hungary
E-mails: bari@ludens.elte.hu; prita@elte.hu*

(Manuscript received in final form November 10, 2004)

Abstract—Precipitation is one of the most important elements of the hydrological cycle, and extreme events associated with precipitation are considered a key factor in several types of human activities, including agriculture, for instance. Therefore, the main objective of this paper is to evaluate extreme precipitation indices. Several climate extreme indices have been analyzed and compared for the entire world, the European continent, and the Carpathian Basin for the second half of the twentieth century according to the guidelines suggested by the joint WMO-CCl/CLIVAR Working Group (formed at the end of the 1990s) on climate change detection. These extreme precipitation indices include the number of wet days using several threshold values, e.g., 20 mm (RR20), 10 mm (RR10), 5 mm (RR5), 1 mm (RR1), 0.1 mm (RR0.1), the upper quartile and the 95th percentile of daily precipitation in the baseperiod 1961–1990 (R75 and R95); the maximum number of consecutive dry days (CDD); the highest 1-day precipitation amount (Rx1); the greatest 5-day rainfall total (Rx5); the annual fraction due to extreme precipitation events (R95T); simple daily intensity index (SDII); etc. Our results suggest that regional intensity and frequency of extreme precipitation increased in the Carpathian Basin during the second half of the twentieth century, while the total precipitation decreased, and the mean climate became slightly drier.

Key-words: extremes, climate index, daily precipitation, Carpathian Basin, Europe, tendency analysis

1. Introduction

National meteorological services usually monitor climate means, tendencies, and extremes only for their own region. First, IPCC (1995) declared the global warming trend of the last 150 years due to anthropogenic activity, which increased the annual global mean temperature by 0.7 °C. This IPCC report also

concluded that changes in both the mean and extreme climate parameters may strongly affect human and natural systems. In the mean time, several research projects published results on the analysis of climate extremes on global or continental scales (e.g., *Nicholls et al.*, 1996; *Folland et al.*, 2000; *Easterling et al.*, 2000; *Peterson et al.*, 2002). Furthermore, the Workshop on Indices and Indicators for Climate Extremes was held in Asheville, North Carolina, on June 3–6, 1997. The main objectives of this meeting were to determine the required data sets for climate extreme analysis on larger scales, and to compile the list of climate extreme indices suggested for the global analysis (*Karl et al.*, 1999). Then, in 1998, a joint WMO-CCI/CLIVAR Working Group formed on climate change detection; one of its task groups aimed to identify the climate extreme indices and completed a climate extreme analysis on all part of the world where appropriate data was available (*Frich et al.*, 2002). Some results of this working group also appeared in *IPCC* (2001).

The next section of this paper summarizes and compares the results of the global (*Frich et al.*, 2002) and European (*Klein Tank and Können*, 2003) extreme precipitation analysis. Similar methodology has been applied to precipitation extremes of the Carpathian Basin. Section 3 discusses the differences between continental (for Europe) and regional (for the Carpathian Basin) extreme tendencies. Section 4 presents detailed analysis of regional extreme precipitation indices for Hungary. Finally, Section 5 concludes the main findings of this paper.

2. Definition of extreme indices based on daily precipitation, comparison of the global and European analyses

In order to compile a global climate database suitable for extreme analysis, the CCI/CLIVAR task group on extreme indices contacted the national meteorological services and collected daily precipitation, maximum, minimum, and mean temperature time series for the period 1946–1999. Beside data from the national meteorological services, sources include the NOAA NCDC datasets (*Peterson and Vose*, 1997), the European Climate Assessment Dataset (*Klein Tank et al.*, 2002b), and daily meteorological time series for Australia (*Trewin*, 1999). All these datasets have been quality controlled and adjusted for inhomogeneities. Then, in order to include a given observation station, the following general criteria have been used: (i) from the entire 1946–1999 period data must be available for at least 40 years; (ii) missing data cannot be more than 10%; (iii) missing data from each year cannot exceed 20%; (iv) more than 3 months consecutive missing values are not allowed each year. In spite

of all these selection criteria, results of any analysis are strongly dependent on the precipitation series themselves, including the instrumental issues.

The CCI/CLIVAR task group decided to map station data instead of gridded database, since extreme events (e.g., local floods and droughts, heat waves, local cold spells) often occur on local scale, but on the other hand, they are all important parts of global climate patterns which could disappear in case of a spatial data interpolation. Therefore, maps presented in this paper use similar technique applying station-based analysis.

Results of the global and European extreme climate analysis have been published in 2002–2003 (e.g., *Frich et al.*, 2002; *Klein Tank and Können*, 2003). In this section these results are summarized and compared for the global and continental scales. *Table 1* presents the main extreme precipitation indices that the CCI/CLIVAR task group identified and suggested for global climate extreme analysis. Beside the definition of each extreme precipitation index, *Table 1* indicates the scale (i.e., global, continental, regional) of application, as well. From the total 12 extreme climate indicators, 5, 9, and 12 were used in the analysis for the world (*Frich et al.*, 2002), Europe (*Klein Tank and Können*, 2003), and the Carpathian Basin (*Bartholy and Pongrácz*, 2004), respectively. For instance, *Figs. 1–3* present one of the extreme precipitation indices, namely, the change of the fraction of annual total rainfall due to events above the 95th percentile of daily precipitation in the baseperiod 1961–1990. Spatial distribution of global tendencies can be seen in *Fig. 1*, while the graph shown in *Fig. 2* provides the temporal details of the global mean change of the annual fraction of extreme precipitation during the second half of the 20th century. Results of the similar analysis for Europe is presented in *Fig. 3*.

Changes between the two subperiods of the second half of the century (1946–1975 and 1976–1999) have been determined during the analysis presented in *Frich et al.* (2002). The world map of *Fig. 1* indicates both the sign of change (black and grey circles for increasing and decreasing tendencies, respectively) and the magnitude of change (applying 4 different circle sizes for the percentage intervals) at each station involved in the analysis. Stations with significant changes (at 95% level of confidence) in the fraction of annual total rainfall due to events above the 95th percentile of daily precipitation in the baseperiod 1961–1990 are mapped with filled circles, while open circles indicate not significant changes. The large number of black filled circles and few grey circles on the map suggest that the annual fraction of very wet events increased between 1946 and 1999.

Based on the available time series, annual global weighted anomalies have been calculated using the baseperiod of 1961–1990. *Fig. 2* presents the annual value (in percentage) of the anomaly for the entire 1950–1999 period, as well as the fitted linear trend emphasizing the significant increasing tendency.

Table 1. Definition and indicator of extreme climate parameters

Nr.	Indicator (ECAD)	World (Frich et al., 2002)	Europe (Klein Tank and Können, 2003)	Carpathian Basin (Bartholy and Pongrácz, 2004)	Definition of the extreme precipitation index	Unit
1	CDD	x		x	Maximum number of consecutive dry days (when $R_{day} < 1$ mm)	day
2	Rx1		x	x	Highest 1-day precipitation amount	mm
3	Rx5	x	x	x	The greatest 5-day rainfall total	mm
4	SDII	x		x	Simple daily intensity index (total precipitation sum / total number of days when $R_{day} \geq 1$ mm)	mm/day
5	R95T	x	x	x	Fraction of annual total rainfall due to events above the 95th percentile of the daily precipitation in the baseperiod 1961–1990 ($\Sigma R_{day} / R_{total}$, where ΣR_{day} indicates the sum of daily precipitation exceeding $R_{95\%}$)	%
6	RR10	x	x	x	Number of heavy precipitation days ($R_{day} \geq 10$ mm)	day
7	RR20		x	x	Number of very heavy precipitation days (when $R_{day} \geq 20$ mm)	day
8	R75		x	x	Number of moderate wet days ($R_{day} > R_{75\%}$, where $R_{75\%}$ indicates the upper quartile of the daily precipitation in the baseperiod 1961–1990)	day
9	R95		x	x	Number of very wet days ($R_{day} > R_{95\%}$, where $R_{95\%}$ indicates the 95th percentile of the daily precipitation in the baseperiod 1961–1990)	day
10	RR5			x	Number of precipitation days exceeding a given threshold ($R_{day} \geq 5$ mm)	day
11	RR1			x	Number of precipitation days exceeding a given threshold ($R_{day} \geq 1$ mm)	day
12	RR0.1			x	Number of precipitation days exceeding a given threshold ($R_{day} \geq 0.1$ mm)	day

The figure includes a small graph (in its upper left part) indicating the total number of stations used for the analysis each year. Except the beginning and the end of the period, about 300 stations provided valuable precipitation data to determine the annual fraction of extreme precipitation.

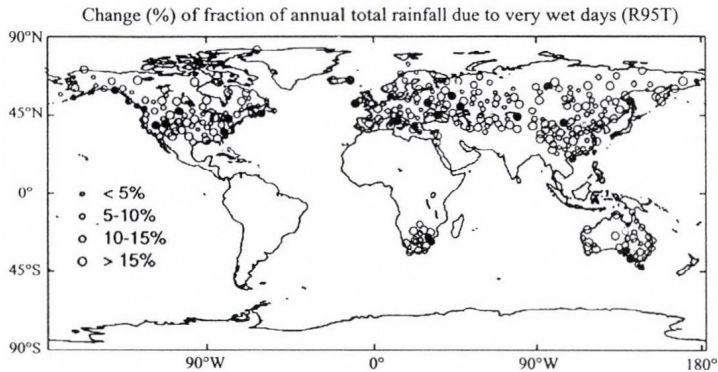


Fig. 1. Changes (%) in fraction of annual total rainfall due to events above the 95th percentile of daily precipitation in the baseperiod 1961–1990, in the second half of the 20th century. Filled circles are significant at 95% level of confidence. Grey and black indicate negative and positive changes, respectively. Circle sizes represent the magnitude of change.

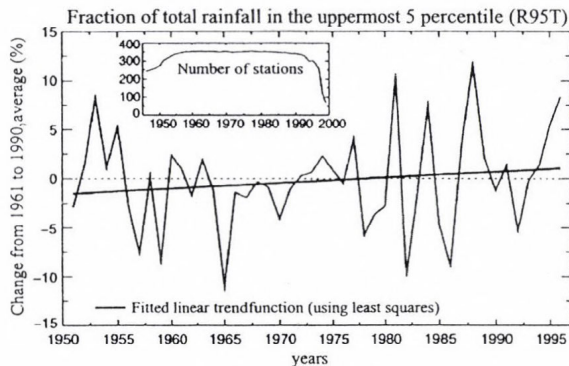


Fig. 2. Mean annual values of the fraction of annual total rainfall due to events above the 95th percentile of daily precipitation in percentage differences from the 1961–1990 weighted average values for the second half of the 20th century. The inserted graph represents the weighting factors (number of stations with valuable data) used in the linear regression analysis. The fitted linear trend is statistically significant at 95% level of confidence.

The European tendency analysis of the annual precipitation fraction due to very wet days is shown in Fig. 3, where the mean decadal changes of this extreme index is mapped for the stations with sufficient data for the 1946–1999

period. Open circles indicate not significant changes, while dark and grey filled circles indicate positive and negative trends, respectively. Similarly to the global analysis, significant positive tendency can be seen. According to the above results of the two large scale analyses, fraction of annual total rainfall due to events above the 95th percentile of the daily precipitation considerably increased by the end of the 20th century. Regional details of the Carpathian Basin will be presented in Section 4.

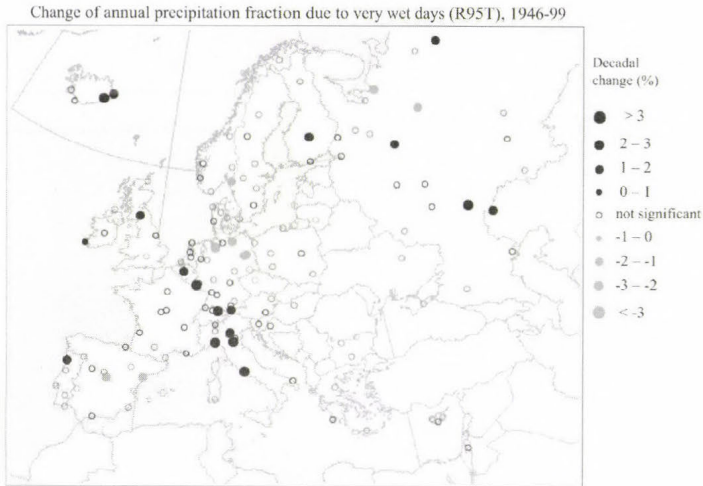


Fig. 3. Decadal trend in the fraction of annual total rainfall due to events above the 95th percentile of daily precipitation in the baseperiod 1961–1990 in Europe, for the period 1946–1999. Circles are scaled according to the magnitude of the trend. Open circles indicate not significant changes, while dark and grey filled circles indicate positive and negative trends, respectively.

Table 2 summarizes the tendencies of all extreme precipitation indices for the global and continental scale climate analyses based on the papers of Frich *et al.* (2002) and Klein Tank and Können (2003), respectively. The comparison of these results is accomplished for the second half of the last century (1946–1999). Increasing, decreasing, and not significant trends are indicated with symbols „+“, „-“, and „0“, respectively. Considerable spatial differences are emphasized using more than one type of symbol (e.g., -/+ , ++/- , +/-0, etc.). After identifying the main dominant trends, exceptions are listed in case of each extreme climate index. In general, global and European tendencies are similar, and only a few small areas differ from the worldwide and continental dominant trends. Sometimes the Carpathian Basin belongs to these exceptions. For instance, both the SDII (simple daily intensity index) and the R95T

(fraction of annual total rainfall due to events above the 95th percentile of the baseperiod) are dominantly increasing for the world, as well as for Europe. However, for the Carpathian Basin neither the global, nor the continental scale analysis include significant trends. One of the aims of our research presented in this paper is to specify these cases on a finer spatial scale and provide more details for Hungary and the surrounding region. The next sections contain our results.

Table 2. Comparison of the tendencies of extreme climate indices based on global (Frich et al., 2002) and European (European Climate Assessment & Dataset (ECAD) project; Klein Tank and Können, 2003) extreme analysis for the period 1946–1999

Nr.	Extreme index	World (Frich et al., 2002)	Europe (Klein Tank and Können, 2003)
1	CDD Consecutive dry days	– / + Negative tendency dominates except the eastern part of Asia	0 No significant trend
2	Rx1 Highest 1-day precipitation amount	No analysis provided	+ / – Positive tendency dominates in Western and Northern Europe, while negative tendency dominates in Eastern and Southern Europe
3	Rx5 Greatest 5-day rainfall total	+ / – Positive tendency dominates except the eastern part of Asia	+ / – Positive tendency dominates except Central and Southern Europe
4	SDII Simple daily intensity index	+ / – Positive tendency dominates except Asia	+ / 0 Positive tendency dominates in Western and Northern Europe, while no significant trend can be observed at other places
5	R95T Fraction of annual total rainfall due to events above the 95th percentile	+ / – Positive tendency dominates except Asia	+ / 0 Positive tendency dominates in Northern Europe and the Alps, while no significant trend can be observed at other places
6	RR10 Heavy precipitation days	+ + / – Positive tendency dominates except the eastern part of Asia	+ / – Positive tendency dominates except Central and Southeastern Europe
7	RR20 Very heavy precipitation days	No analysis provided	+
8	R75 Moderate wet days	No analysis provided	+ + / – Positive tendency dominates except Central and Southern Europe
9	R95 Very wet days	No analysis provided	+

3. Comparison of tendencies of extreme precipitation indices for the Carpathian Basin and Europe

In order to evaluate the past and future climate tendencies of the Carpathian Basin, it is essential to compare regional tendencies of the different climate parameters to larger (i.e., continental) scale.

Giorgi and Francisco (2000) analyzed the future continental temperature and precipitation changes expected for the 21st century based on model outputs of five main AOGCMs (Atmosphere-Ocean General Circulation Model). Global continental areas were divided into 23 regions, from which 2 cover the European continent, namely, (i) Northern Europe (NEU), and (ii) the Mediterranean region (MED).

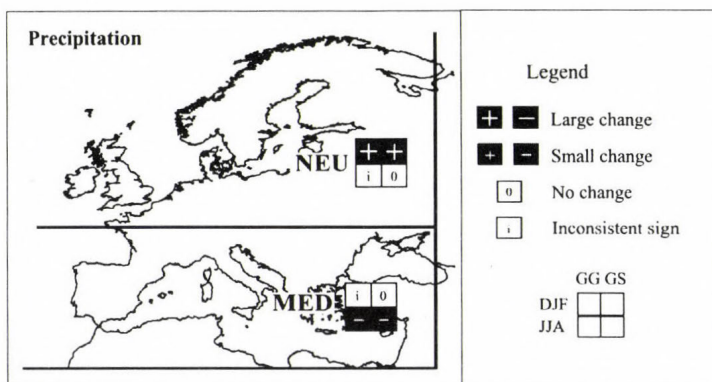


Fig. 4. Summary of precipitation tendency analysis for Northern Europe (NEU) and the Mediterranean region (MED) for two seasons (winter and summer) and two climate scenarios (GG, GS) based on inter-model consistency analysis of *Giorgi and Francisco (2000)*.

Fig. 4 summarizes intensity, sign, and consistency of the GCM-based precipitation changes for these two European regions. Expected changes in precipitation conditions are presented in four small boxes for NEU and MED for 2071–2100. The upper and the lower two boxes represent expected changes in winter (December–January–February), and in summer (June–July–August), respectively. Furthermore, results for the GG (greenhouse gas only case) and GS (greenhouse gas with increasing sulphate aerosol case) scenario are shown in the left two boxes, and in the right two boxes, respectively. “+” and “-” signs appearing in the small boxes indicate the intensity of precipitation change compared to the baseperiod 1961–1990. Similarly, black and grey colors imply large (greater than 20%) and small (between 5% and 20%) average change, respectively. “0” indicates no change (between –5% and +5%), while in case

of model disagreement, sign of inconsistency (“i”) appears in the small box. Results of *Giorgi and Francisco (2000)* suggest that winters in Northern Europe are tend to become considerably wetter, and Mediterranean summers are likely to become drier than today for both GG and GS scenarios. Estimations of the five main AOGCMs are inconsistent for NEU summers and MED winters for the GG scenario, while they do not indicate significant changes for the GS scenario.

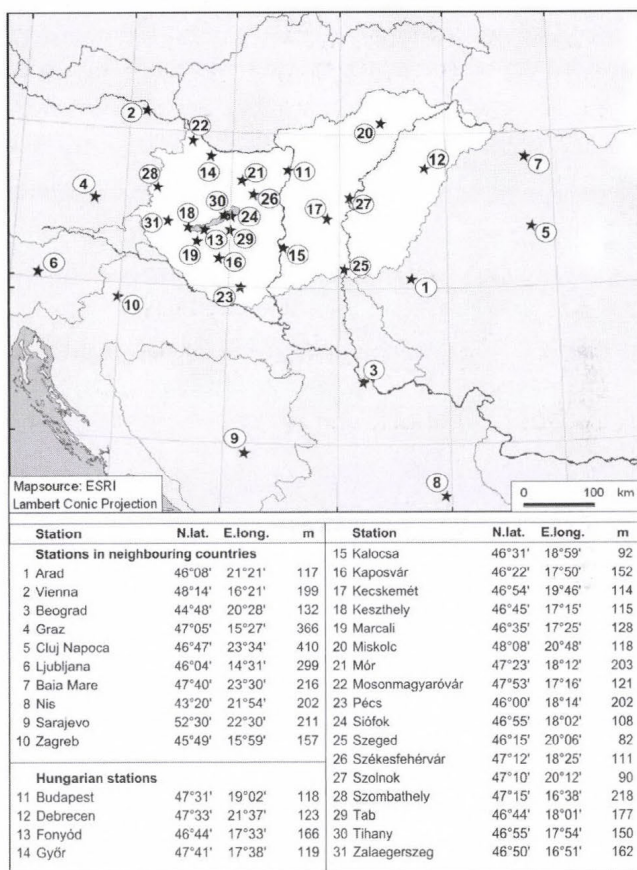


Fig. 5. Geographical locations of meteorological stations in the Carpathian Basin.

Tendency analysis of precipitation extreme indices for the last century is presented in this section for the Carpathian Basin, and compared to the results of the European analysis based on *Klein Tank and Können (2003)*. For the evaluation of recent tendency of precipitation extremes in the Carpathian Basin, 31 meteorological stations have been used (*Fig. 5*). Datasets for the 21

Hungarian stations were bought from the Hungarian Meteorological Service, while datasets for the 10 stations in the neighbouring countries are freely available via Internet from ECAD (*Klein Tank, 2003*). Stations have been selected considering two main criteria, namely, (i) homogeneous spatial coverage, and (ii) minimal number of missing data. However, none of these criteria could be fulfilled absolutely. *Fig. 6* presents the relative number of missing data for each station using two concentric circles. In front of the grey circles indicating missing data for the entire 20th century, black circles represent missing data ratio for the second half of the century. Annual total numbers of meteorological stations with valuable precipitation data are shown for Hungary, for the neighbouring countries, and for the entire Carpathian Basin in *Fig. 7*. Obviously, in the first half of the century the database contains much less information available than in the second half.

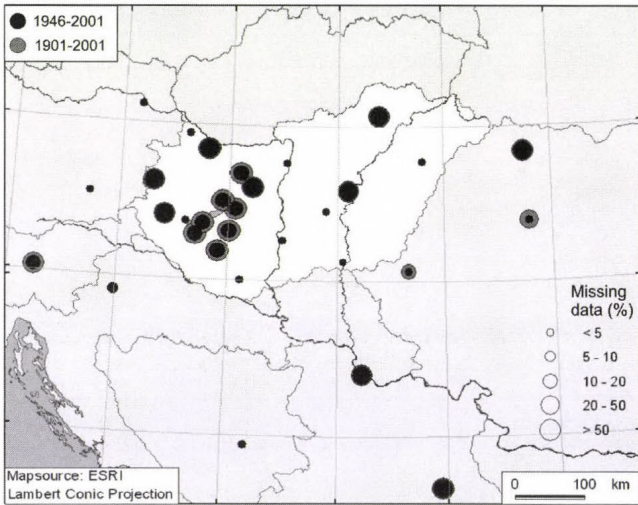


Fig. 6. Fraction of missing data during 1901–2001 (grey circles) and 1946–2001 (black circles).

Our datasets are compiled for 1901–2001. However, based on previous analyses (*IPCC, 2001*) suggesting that precipitation and temperature tendencies of the last quarter of the 20th century and the second half of the century are significantly different, and due to the limited extent of the European time series (*Klein Tank et al., 2002a; Klein Tank and Können, 2003*), the European-Carpathian comparison has been accomplished for 1946–2001 and 1976–2001. *Table 3* summarizes the spatial structures of decadal tendency maps for the 12 extreme precipitation indices for both periods. When similar changes are detected for all stations appearing on the map, only one “+” or “–” sign

indicates the tendency. While in case of more complex spatial structures, two or four signs have been used to illustrate the regional tendencies. The intensity of the changes is represented by three categories (i.e., weak, medium, strong). Based on the analysis of tendency maps, only very few extreme indices can be characterized by homogeneous positive or negative trends in both periods and for both regions. However, in general, the precipitation extremes decreased slightly in the Carpathian Basin during the last 56 years, while they increased more intensely during the last 26 years. Opposite tendencies can be observed in the entire European continent, namely, increased and decreased extreme precipitation trends in the second half and in the last quarter of the century, respectively.

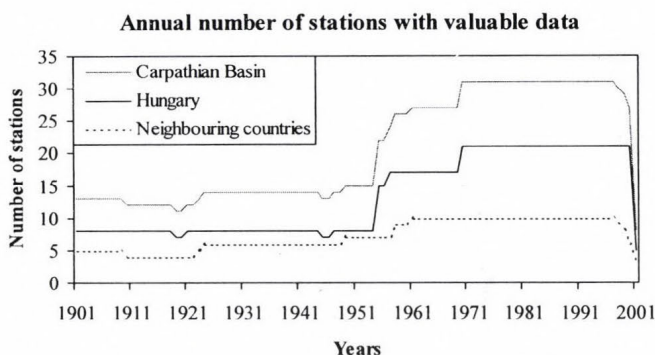
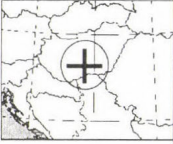
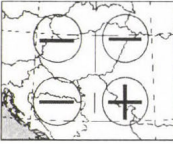
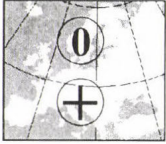
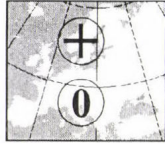
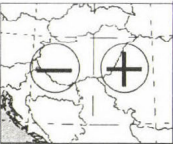

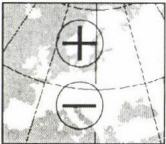
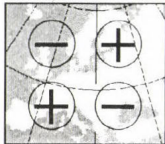
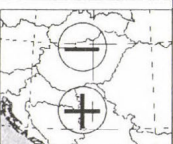
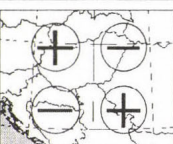
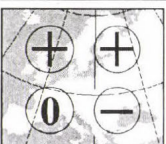
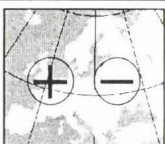
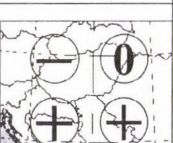
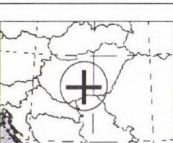
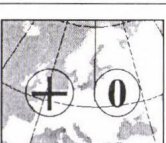
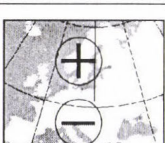
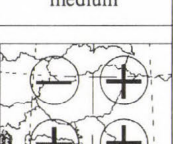

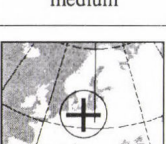
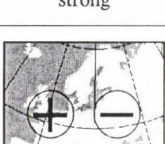
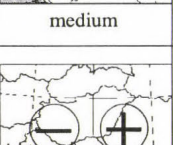
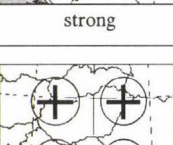
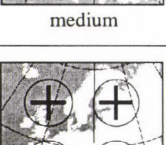
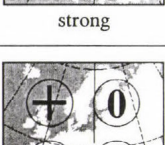


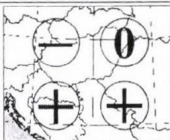
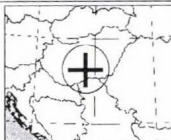
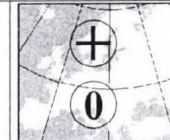
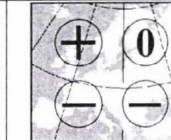
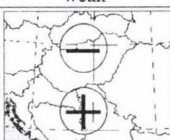
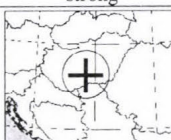
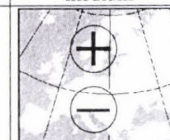
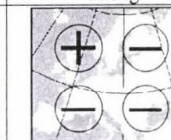
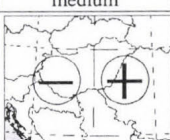
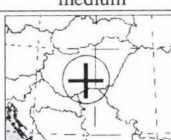
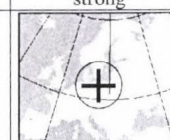
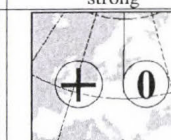
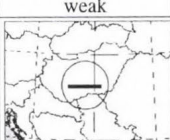
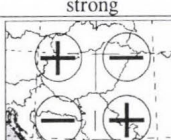
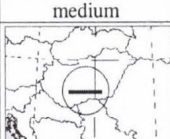
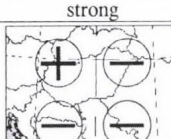
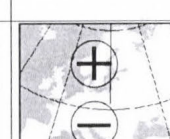
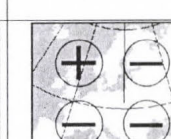

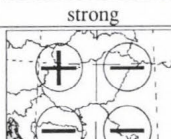
Fig. 7. Annual total number of meteorological stations of the Carpathian Basin with valuable precipitation data (1901–2001).

In this paper two parameters of *Table 3* are presented in details. European and Carpathian tendencies of annual number RR10 of heavy precipitation days (when daily precipitation is greater than 10 mm) are compared for the last quarter of the 20th century in *Fig. 8*. Circles represent decadal trend coefficients of the meteorological stations (using the baseperiod 1961–1990). Black and grey circles indicate increasing and decreasing tendencies, respectively, while circle size depends on the intensity of these positive or negative trends. Based on the tendency analysis of the entire European continent (upper panel of *Fig. 8*), heavy precipitation days occurred more often in the last 2–3 decades in northern stations, while they became less frequent in the Mediterranean region. The Carpathian Basin is located in-between, however, our detailed regional analysis (lower panel of *Fig. 8*) suggests that except a few southern stations, the annual number of heavy precipitation days (RR10) increased during the last 26 years.

Table 3. Summary of tendency analyses of extreme precipitation indices for the Carpathian Basin (Bartholy and Pongrácz, 2004) and Europe (based on ECAD, Klein Tank, 2003; Klein Tank and Können, 2003) for the 1946–2001 and for the 1976–2001 periods

Nr.	Extreme index	Carpathian Basin		Europe	
		1946-2001	1976-2001	1946-1999	1976-1999
1	CDD Consecutive dry days	 medium	 strong	 weak	 weak
2	Rx1 Highest 1-day precipitation amount	 medium	 strong	 strong	 strong
3	Rx5 Greatest 5-day rainfall total	 strong	 strong	 medium	 strong
4	SDII Simple daily intensity index	 medium	 strong	 medium	 strong
5	R95T Fraction of annual total rainfall due to events above the 95th percentile	 medium	 strong	 medium	 strong
6	RR10 Heavy precipitation days	 medium	 strong	 strong	 strong

→

7	RR20 Very heavy precipitation days	 weak	 strong	 medium	 strong
8	R75 Moderate wet days	 medium	 medium	 strong	 strong
9	R95 Very wet days	 weak	 strong	 medium	 strong
10	RR5 Precipitation days exceeding 5 mm	 medium	 strong	No analysis available	No analysis available
11	RR1 Precipitation days exceeding 1 mm	 strong	 strong	 strong	 strong
12	RR0.1 Precipitation days exceeding 0.1 mm	 medium	 strong	No analysis available	No analysis available

Indices listed in *Table 1* include a few precipitation-related parameters which do not indicate extreme conditions. They belong to the index type *annual number of precipitation days exceeding a given threshold*, for instance, RR1 is one of them. Decadal tendency of the annual number of wet days with daily precipitation exceeding 1 mm (RR1) is analyzed for the second half of the 20th century (*Fig. 9*). Similarly to *Fig. 8*, the upper two maps compare spatial distribution of decadal trends for the European continent and the Carpathian Basin, while the lower graph shows the regional mean time series of the RR1 anomalies (using the baseperiod 1961–1990) for the Carpathian

Basin only. The small graph in the upper right part illustrates the number of stations used for calculating the spatial average. For Europe, similarly to RR10, considerable zonal pattern can be recognized, namely, positive trends in the northern regions, while negative trends in the southern part. For the Carpathian Basin decadal tendency of RR1 is strongly negative in the last 56 years in most of the stations, as well as in case of the regional mean anomaly.

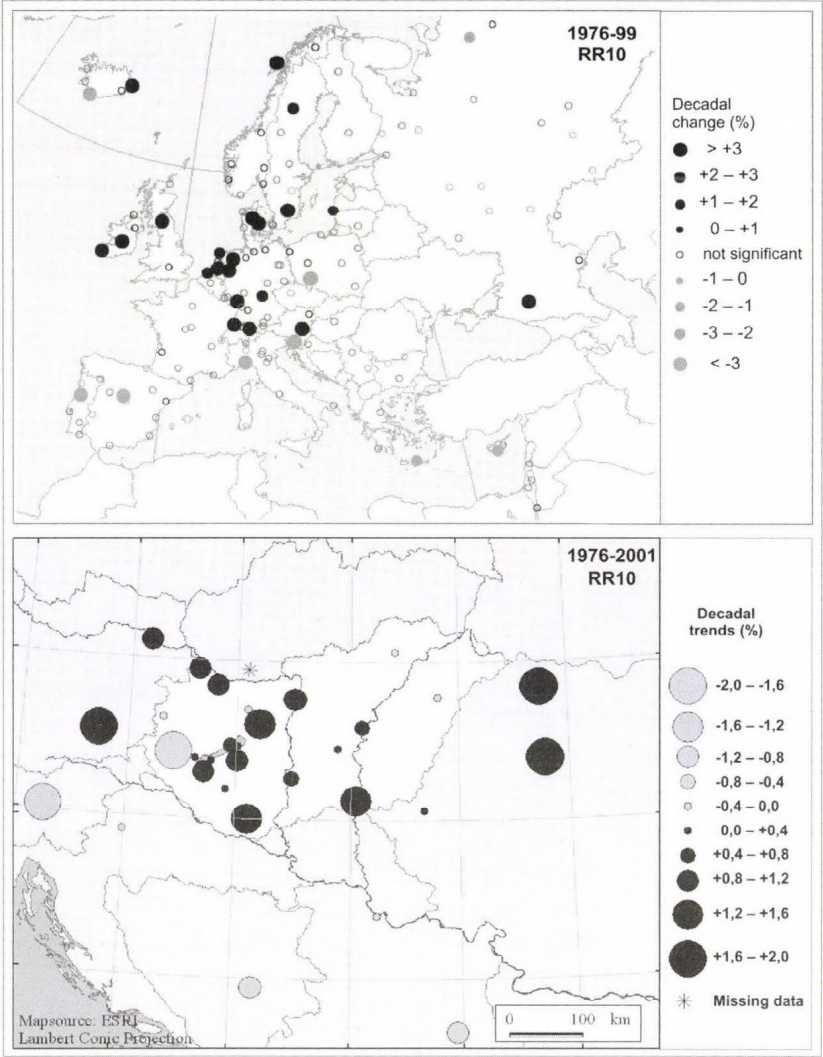


Fig. 8. Tendency of annual number of heavy precipitation days exceeding 10 mm (RR10) in Europe and the Carpathian Basin during the last quarter of the 20th century. Trend coefficients of the Carpathian Basin greater than 0.4 in absolute value are significant at 95 % level of confidence.

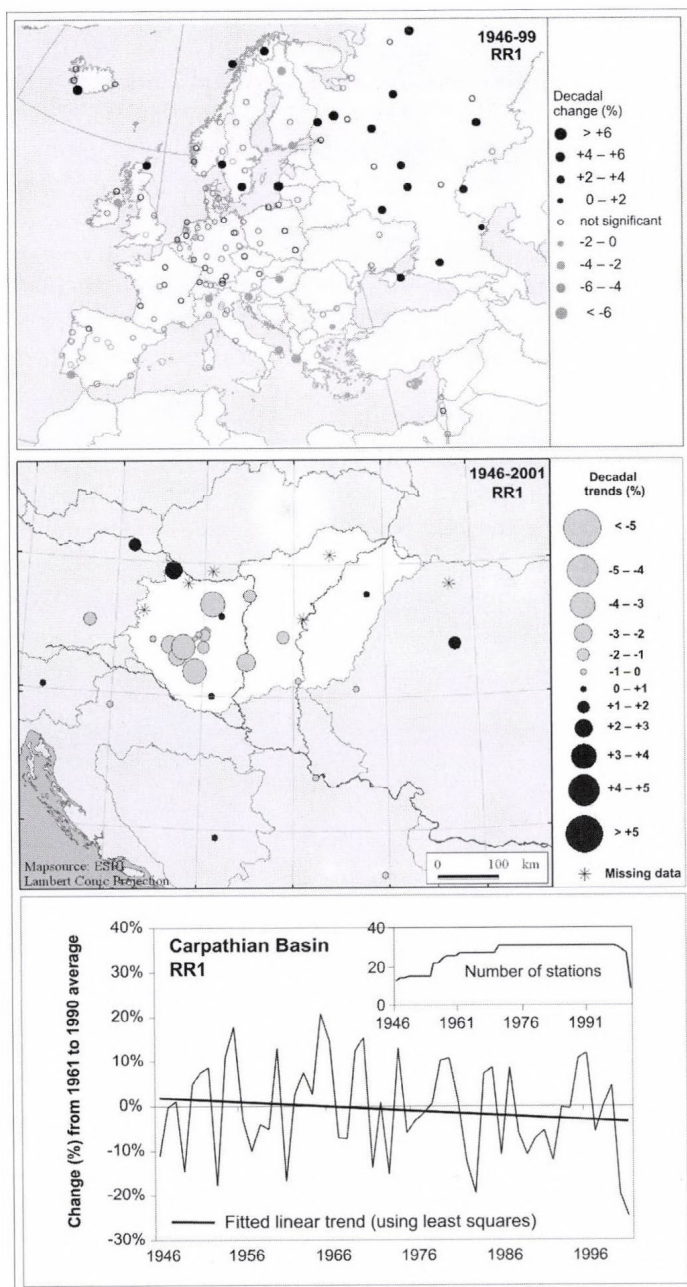


Fig. 9. Tendency of annual number of precipitation days exceeding 1 mm (RR1) in Europe and the Carpathian Basin during the second half of the 20th century. Trend coefficients of the Carpathian Basin greater than 0.3 in absolute value are significant at 95% level of confidence.

4. Analysis of extreme precipitation indices for the Carpathian Basin

According to the *IPCC TAR* (2001), climate and agriculture of several regions of the world can be strongly affected by increasing occurrence of precipitation extremes in the 21st century. Based on the information of the 44 small maps presented in *Table 3*, most of the extreme precipitation indices increased considerably in the Carpathian Basin by the end of the 20th century. Positive trends were detected mostly in the last 26 years. The strongest increasing tendencies appear in case of extreme indices indicating very intense or large precipitation (i.e., SDII, R95T, RR20, RR75, R95). Similar results were concluded in *Bartholy and Pongrácz* (1998), *Pongrácz and Bartholy* (2000), and *Bartholy et al.* (2003).

In this section, spatial distribution maps of tendency of extreme precipitation indices changed the most are presented in *Figs. 10–12*. Decadal changes of annual number of very heavy precipitation days (RR20) are illustrated in *Fig. 10* for the last 26 years (1976–2001). The entire Carpathian Basin can be characterized by a strong positive trend. Considering only the Hungarian stations, the annual number of wet days exceeding 20 mm increased more in Transdanubia than in the Great Plains.

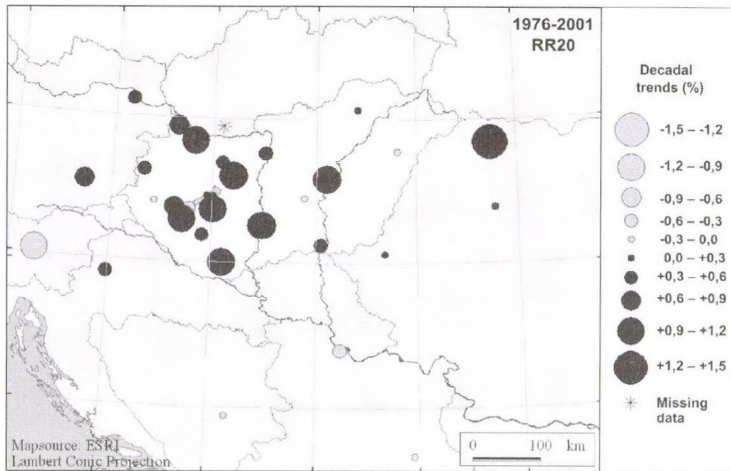


Fig. 10. Tendency of annual number of very heavy precipitation days exceeding 20 mm (RR20) in the Carpathian Basin during the last quarter of the 20th century. Trend coefficients greater than 0.3 in absolute value are significant at 95% level of confidence.

Fig. 11 compares the tendency of annual rainfall fraction due to very wet days (R95T) during the second half and the last quarter of the 20th century. Slight decreasing tendencies can be detected in the Transdanubian stations

during 1946–2001, while intermediate positive trends appear in other stations of the region on the left map of the figure. Furthermore, very strong positive trends were found during the last 26 years (shown on the right map) indicating that the annual fraction of total rainfall (R_{total}) due to events above the 95th percentile ($R_{95\%}$) of daily precipitation in the baseperiod 1961–1990 ($\Sigma R_{day}/R_{total}$, where ΣR_{day} indicates the sum of daily precipitation exceeding $R_{95\%}$) increased significantly between 1976 and 2001.

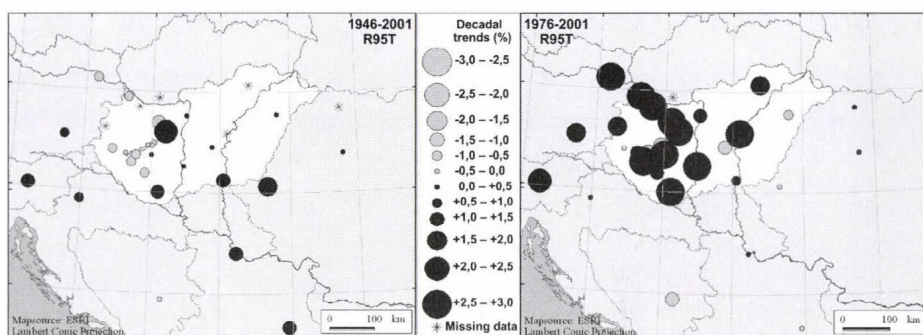


Fig. 11. Tendency of fraction of total annual rainfall due to very wet days (R95T) in the Carpathian Basin. Trend coefficients greater than 0.3 and 0.4 in absolute value are significant at 95% level of confidence on the left and right map, respectively.

Finally, tendency analysis of RR0.1 (annual number of precipitation days exceeding 0.1 mm) for the second half of the 20th century for the Carpathian Basin is presented in Fig. 12. Although, according to the definition, this parameter does not refer to extreme precipitation events, in order to accomplish a complex analysis of precipitation conditions in the Carpathian Basin, several indices defined as numbers of precipitation days exceeding a given threshold (i.e., 20 mm, 10 mm, 5 mm, 1 mm, 0.1 mm) were included.

The upper two maps compare annual tendency of RR0.1 for the last 56 years (on the left) and the last 26 years (on the right). Seasonal tendencies of RR0.1 are compared for the last quarter of the 20th century on the lower two maps (winter and summer trends are presented on the left and right map, respectively). All these maps indicate intermediate or strong negative trends, the strongest trends occur in case of annual RR0.1 values between 1976 and 2001, when both increasing and decreasing tendency appeared in the Transdanubian region. Furthermore, negative trends in winter (on the lower left map) exceed summer trends (on the lower right map).

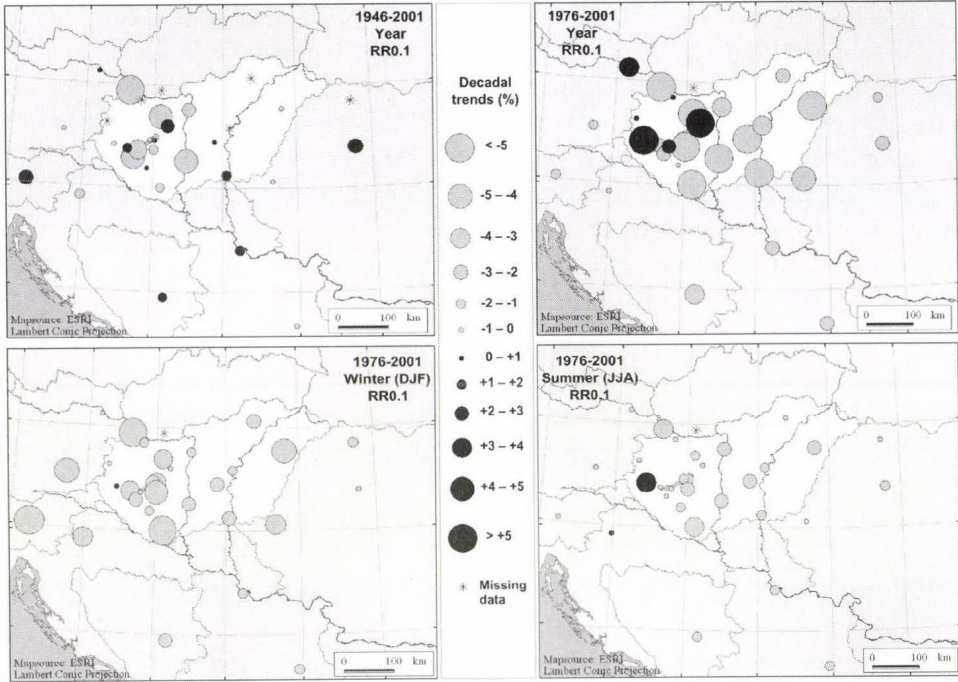


Fig. 12. Tendency of annual number of precipitation days exceeding 0.1 mm (RR0.1) in the Carpathian Basin. Trend coefficients greater than 0.3 (on the upper left map) and 0.4 (on the other three maps) in absolute value are significant at 95% level of confidence.

Summarizing the results presented in *Figs. 11* and *12*, these analyses can be concluded that although, in general, precipitation occurred more rarely in the Carpathian Basin, the ratio of heavy or extreme precipitation days increased considerably by the end of the 20th century.

5. Conclusions

Based on the analysis of extreme precipitation indices for the second half of the 20th century presented in this paper, the following conclusions can be drawn.

1. Comparison of the global and European tendency resulted in:
 - (i) Positive trends dominate in both analyses in case of Rx5, SDII, R95T, and RR10. Opposite (i.e., negative) trends occurred in Asia and Central/Southeastern Europe.

- (ii) Most of the European continent can be characterized by increasing tendency of indices Rx1 and R75, while decreasing tendency was found only in Central and Southeastern Europe. Global analysis is not available for these indices.
 - (iii) In case of RR20 and R75, significant positive trend appeared in Europe (global analysis is not available for these indices).
 - (iv) Global decreasing (except Eastern Asia) tendency of CDD implies similar climate conditions to the consequent trends of extreme precipitation indices listed above. However, trends are not significant for the European continent.
2. Comparison of the analysis for Europe and the Carpathian Basin:
- (i) Decadal trends were evaluated separately for two periods (1946–2001 and 1976–2001). Tendencies in both the European and Carpathian regions were more intense and spatially more homogeneous during the last 26 years than the last 56 years.
 - (ii) Spatial structure of the decadal tendency maps is classified into several main patterns using one, two (meridionally or horizontally), or four “+” or “–” signs. Considerable zonal patterns were often recognized in Europe, when different tendency occurred in Northern Europe and the Mediterranean region.
3. Analysis of the extreme precipitation indices for the Carpathian Basin (according to the suggestions of the CCI/CLIVAR Working Group):
- (i) Strong positive trends were detected in most of the extreme precipitation indices (e.g., SDII, R95T, RR20, R75, R95) for the last quarter of the 20th century indicating increasing precipitation extremity in the Carpathian Basin.
 - (ii) Significant negative trends dominate the region in case of the non-extreme parameters (i.e., RR5, RR1, and RR0.1) during the second half of the 20th century.
 - (iii) In general, precipitation occurred less frequently in the Carpathian Basin, however, the ratio of heavy or extreme precipitation days increased considerably by the end of the 20th century.

Acknowledgements—Research leading to this paper has been supported by the Hungarian National Science Research Foundation (OTKA) under grants T-026629, T-034867, and T-038423, also by the AEROCARB and CHIOTTO projects of the European Union Nr. 5 program under grants EVK2-CT-1999/0013, EVK2-CT-2002/0163, the Hungarian National Research Development Program under grant NKFP-3A/0006/ 2002, and VAHAVA project of the Hungarian Academy of Sciences and the Ministry of Environment and Water. ESRI software has been used to create maps. Furthermore, supports of the Bolyai János Research Fellowship of the Hungarian Academy of Sciences is appreciated.

References

- Bartholy, J. and Pongrácz, R., 1998: The differing trends of the Hungarian precipitation time series, areal and decadal changes of extreme precipitation (in Hungarian). In *Second Conference on Forest and Climate* (eds.: K. Tar and K. Szilágyi). Kossuth Egyetemi Nyomda, Debrecen, 62-66.
- Bartholy, J. and Pongrácz, R., 2004: *Global and regional tendencies of extreme indices based on daily precipitation for the 20th century* (in Hungarian). Research Paper. Eötvös Loránd Tudományegyetem, Budapest. 20p.
- Bartholy, J., Pongrácz, R., Matyasovszky, I., and Schlanger, V., 2003: Expected regional variations and changes of mean and extreme climatology of Eastern/Central Europe. In *Combined Preprints CD-ROM of the 83rd AMS Annual Meeting*. American Meteorological Society, Boston. Paper 4.7, 10p.
- Easterling, D.R., Meehl, G.A., Parmesan, C., Chagnon, S.A., Karl, T., and Mearns, L.O., 2000: Climate extremes: Observation, modelling and impacts. *Science* 289, 2068-2074.
- Folland, C.K., Frich, P., Rayner, N., Basnett, T., Parker, D.E., and Horton, B., 2000: Uncertainties in climate datasets: A challenge for WMO. *WMO Bulletin* 49, 59-68.
- Frich, P., Alexander, L.V., Della-Marta, P., Gleason, B., Haylock, M., Klein Tank, A.M.G., and Peterson, T., 2002: Observed coherent changes in climatic extremes during the second half of the twentieth century. *Climate Res.* 19, 193-212.
- Giorgi, F. and Francisco, R., 2000: Evaluating uncertainties in the prediction of regional climate change. *Geophys. Res. Lett.* 27, 1295-1298.
- IPCC, 2001: *Climate Change 2001: Third Assessment Report. The Scientific Basis*. Cambridge University Press, Cambridge, UK.
- IPCC, 1995: *Climate Change 1995: The Science of Climate Change. Contribution of Working Group I to the Second Assessment of the Intergovernmental Panel on Climate Change*. Cambridge University Press, Cambridge, UK.
- Karl, T.R., Nicholls, N., and Ghazi, A., 1999: Clivar/GCOS/WMO Workshop on Indices and Indicators for Climate Extremes Workshop Summary. *Climatic Change* 42, 3-7.
- Klein Tank, A.M.G., 2003: *The European Climate Assessment and Dataset Project*. <http://www.knmi.nl/samenw/eca/index.html>.
- Klein Tank, A.M.G., and Können, G.P., 2003: Trends in indices of daily temperature and precipitation extremes in Europe, 1946-99. *J. Climate* 16, 3665-3608.
- Klein Tank, A.M.G., and Coauthors, 2002a: Daily dataset of 20th-century surface air temperature and precipitation series for the European Climate Assessment. *Int. J. Climatol.* 22, 1441-1453.
- Klein Tank, A.M.G., Wijngaard, J.B., and van Engelen, A., 2002b: *Climate of Europe; Assessment of observed daily temperature and precipitation extremes*. KNMI, De Bilt, The Netherlands, 36p.
- Nicholls, M., Gruza, G.W., Jouzel, J., Karl, T.R., Ogallo, L.A., and Parker, D.E., 1996: Chapter 3, Observed climate variability and change. In *Climate Change 1995: The Science of Climate Change. Contribution to Working Group I to IPCC SAR*. (eds.: J.T. Houghton et al.) Cambridge Univ. Press, 137-192.
- Peterson, T.C. and Vose, R.S., 1997: An overview of the global historical climatology network database. *B. Am. Meteorol. Soc.* 78, 2837-2849.
- Peterson, T., Folland, C.K., Gruza, G., Hogg, W., Mokssit, A., and Plummer, N., 2002: Report on the Activities of the Working Group on Climate Change Detection and Related Rapporteurs, 1998-2001. *World Meteorological Organization Rep. WCDMP-47. WMO-TD 1071*. Geneva, Switzerland. 143p.
- Pongrácz, R. and Bartholy, J., 2000: Changing trends in climatic extremes in Hungary. In *Third Conference on Forest and Climate* (ed.: A. Kircsi). Kossuth University Press, Debrecen, 38-44.
- Trewin, B.C., 1999: The development of a high-quality daily temperature datasets for Australia and implications for the observed frequency of extreme temperatures. In *Meteorology and Oceanography at the Millenium: AMOS'99 Proc. of the 6th National Australian Meteorological and Oceanographic Society Congress*, Canberra, 1999, pp. 87.

IDŐJÁRÁS

Quarterly Journal of the Hungarian Meteorological Service
Vol. 109, No. 1, January–March 2005, pp. 21–37

Microclimate simulation in maize with two watering levels

Angéla Anda* and Zsuzsanna Lőke

University of Veszprém, Georgikon Faculty of Agronomy,
P.O. Box 71, H-8361 Keszthely, Hungary; E-mail: anda-a@georgikon.hu

(Manuscript received in final form January 6, 2005)

Abstract—Various components in the microclimate of irrigated and rainfed maize stands were examined in Keszthely, Hungary, from the end of June 2001 until the first ten days of August. To simulate the elements of microclimate, Crop Microclimate Simulation Model of *Goudriaan* (1977) was applied. The air temperature and humidity were registered using a Temperature/Relative Humidity Sensor, attached to a data recorder placed in a Stevenson screen, close to the tassel level of the adult plants (1.40 m above the soil surface). Measured and simulated values were compared with respect to hourly means of samples taken every 4 seconds, and diurnal means calculated for the daylight hours. The weather on certain sampling days (rain and strong winds) resulted in a microclimate simulation so far from reality, that these days were omitted from the evaluation. The difference between the diurnal means of simulated sampling days and the measured values was small, less than 1 °C for the air temperature, and below 10% for the relative humidity. The simulation of air temperature was closer to the field parameters in the non-irrigated treatment. The difference between the observed and simulated air moisture values was much the same in the two water supply treatments. The microclimate simulated was such a good approximation to reality that the simulation was able to reflect events causing very slight differences, such as the effect of irrigation. This indicates that a knowledge of the changes in the microclimate, expected as the result of various agronomic measures, could form the basis for better decisions by farmers.

Key-words: Goudriaan microclimate-simulation, maize, irrigation, CWSI

1. Introduction

The most widely-used model for the simulation of maize production is the CERES-Maize model (*Jones and Kiniry, 1986*), which has been modified and improved by many authors, including *Stockle and Kiniry (1990)*, *Kiniry* and

* Corresponding author

Knierel (1995), *Kiniry et al.* (1997), *Kiniry and Bockholt* (1998), and *Xie et al.* (2001). The model has been applied under a wide variety of climatic conditions (*Carberry et al.*, 1989; *Liu et al.*, 1989; *Plantureaux et al.*, 1991; *Nouna et al.*, 2001). *Mantovani et al.* (1995) and *Cavero et al.* (2001) combined the CERES model with the CROPWAT irrigation model in order to give a more precise description of yield variability. The spatial variability in yield caused by yield losses in crop patches exposed to various stress factors was numerically determined by *Paz et al.* (1998). During the past decade, the CERES model was applied by *Huzsvay and Nagy* (1994), and by *Fodor et al.* (2003) for yield simulation purposes. The soil-vegetation-atmosphere transfer schemes, as for example SVAT, produce another important and popular model category (*Franks et al.*, 1997; *Calveta et al.*, 1998; *Calveta*, 2000; *Gottschalk et al.*, 2001).

Probably due to the limited number of users, none of the microclimate models is applied on such a wide global scale as the above-mentioned models. In Europe, *Goudriaan* (1977) compiled a model for the simulation of the maize microclimate, which was simplified by *Chen* (1984) and adapted for PC application, thus broadening the range of possible users. The model was based on the synthesizing work of many other authors (*Sellers*, 1965; *Evans*, 1972; *Nobel*, 1974; *Rosenberg*, 1974; *de Wit and Goudriaan* 1978; etc.). Research continued after the publication of the model, and *Jones* (1983) published a comprehensive work on plant microclimates, which could be regarded as a theoretical manual. The latest results about the Goudriaan's model "team-work" appeared in 1994 (*Goudriaan and van Laar*, 1994).

Before applying the Goudriaan model in the present work, further slight modifications were made, which facilitated its application without affecting the basic structure of the model (*Anda et al.*, 2001).

Research on the use of plant temperatures to determine irrigation dates began in the early '80s, in two separate directions. One is linked with the work of *Jackson et al.* (1981), and involves the determination of a water stress index with a strong theoretical basis, while the other involves the formation of a water stress index on a largely empirical basis, the first work on which was published by *Idso et al.* (1981). The advantages of estimating the water status of maize on the basis of plant temperature were discussed among others by *Gardner et al.* (1981), *Hatfield* (1990), and *Irmak et al.* (2000).

The aim of the present paper was to control the Goudriaan simulation model (CMSM, Crop Microclimate Simulation Model) for the microclimate of maize grown under rainfed conditions, or with irrigation based on the real water requirements of the plant. Although the effect of irrigation on the plant microclimate has long been known, the more exact measurements of air temperature and humidity, made possible by developments in instrumental

techniques, justify a new look at the microclimate modifications occurring as the result of supplementary water supplies. The exact value of air temperature is important in plant studies, because it governs physiological processes. The humidity of the air determines the appearance of some plant diseases. Modeling could provide a basis for a better understanding of the microclimatic differences arising as the result of various human interventions such as irrigation. A more detailed knowledge of the microclimate of irrigated plants could also be of importance in farm practice (e.g., through the consideration of environmental conditions in controlling the spread of plant diseases). The sophisticated consideration of the elements of microclimate could provide better understanding of the processes near the plants. The investigations did not aim to compare the well known microclimates of irrigated and non-irrigated plant stands; these treatments were used only to achieve two different levels of water supplies.

2. Materials and methods

The experiment was set up at the Agrometeorological Research Station in Keszthely, during the 2001 growing season, using a widely cultivated, Hungarian-bred maize hybrid with a short vegetation period (Gazda, FAO 400, dent variety, prolific and tolerant of water stress). The typical soil type on this area was Ramann's brown forest soil (Anda and Stephens, 1996).

Plants sown in late April emerged during the first ten days of May, after which the plant density was adjusted to 7 plants/m². The usual agronomic measures (plant protection, weed control), recommended for the location by the staff of Keszthely University of Agricultural Sciences, were applied. Nutrients (100 kg ha⁻¹ N, 80 kg ha⁻¹ P and 120 kg ha⁻¹ K) were applied in spring immediately prior to sowing. Harvesting was carried out in late September.

The plots measured 0.25 ha, and were arranged in blocks to facilitate the placement of the trickle irrigation pipes. The irrigation dates were determined on the basis of the crop water stress index (CWSI) calculated from differences in the plant and air temperatures and humidity. This index is based on the heat balance, transformed to a certain extent using diffusion resistance values (r_c : crop resistance (s m⁻¹), r_a : aerodynamic resistance (s m⁻¹), subscript p designates unlimited water supplies), giving:

$$CWSI = \frac{\gamma (1 + r_c / r_a) - \gamma}{\Delta + \gamma (1 + r_{c\ p} / r_a)}, \quad (1)$$

where γ is psychrometric constant (Pa K⁻¹),

Δ is slope of saturated vapor pressure-temperature relation (Pa K⁻¹).

In the calculation of the index, a central parameter formed from the difference between the plant canopy and air temperatures ($T_c - T_a$) is an important factor when expressing the resistances:

$$r_c / r_a = \frac{\gamma r_a R_n / (\rho c_p) - (T_c - T_a)(\Delta + \gamma) - [e_s(T_c) - e]}{\gamma [(T_c - T_a) - r_a R_n / (\rho c_p)]}, \quad (2)$$

where R_n : net radiation (W m^{-2}),

$e(T_c) - e$: difference between saturation and actual vapor concentrations of the air (Pa),

ρ : air density (kg m^{-3}),

c_p : specific heat capacity of the air at constant pressure ($\text{J kg}^{-1} \text{K}^{-1}$).

For details of the CWSI determination, see *Jackson (1982)*.

The most important plant parameter in this index is the diurnal plant surface (canopy) temperature (T_c), which could be measured after canopy closure only, under unclouded conditions when the sun was high in the sky. The RAYNGER II.RTL infra-thermometer was held approximately 1 m above the plant stand at an angle of 30° to the horizontal, assuming an emission factor of 0.96.

Irrigation was applied at higher rates (55–60 mm) at the beginning and end of the vegetation period to counteract the substantial water deficiency, while lower rates (20–30 mm) were applied in the intervening periods. Irrigation was carried out when the CWSI value exceeded 0.25. This limit value was determined on the basis of 12 years of maize irrigation experiments carried out locally (*Anda, 1993; Anda et al., 2001*).

The LAI was measured on the same 10 sample plants for each treatment weekly, using the LI-3000A type leaf-area-meter. The model divides the whole canopy into homogeneous layers. The number of layers depends on the actual structure of the plant stand.

Among the components of the microclimate, the air temperature and air humidity were recorded between June 29 and August 6 with a Temperature/Relative Humidity Sensor connected to an LI-1000 DataLogger housed in a Stevenson screen. The instrument shelter was placed at 1.40 m above the soil surface. In the first half of the experiment the sensor was placed in the non-irrigated control stand, but later it was transferred to the irrigated stand. The limited equipment availability did not make it possible to quantify the effect of irrigation by carrying out parallel observations. The time of investigation was chosen after canopy closure, when the environmental conditions are the most suitable for microclimate measurements. The duration of the study was in accordance with the time periods of model constructors applied during the controlling process of the model (*Goudriaan, 1977*).

The theory of the CMSM is the calculation of the radiation distribution among different environmental processes. The sensible heat flux (H_i) in the i th layer is:

$$H_i = \rho c_p \frac{T_{ci} - T_{ai}}{r_{ahi}}, \quad (3)$$

where T_{ai} : air temperature in the i th layer (K),

T_{ci} : air temperature in the i th layer (K),

r_{ahi} : aerodynamic resistance for sensible heat transfer in the i th layer ($s\ m^{-1}$).

The latent heat flux (λE_i) in the i th layer can be calculated as follows:

$$\lambda E_i = \rho c_p \{e_s(T_{ci}) - e_i\} / [\gamma(r_{awi} + r_{ci})], \quad (4)$$

where $e_s(T_{ci}) - e_i$: difference between saturation vapor concentration at plant temperature and actual vapor concentration ($m^3\ m^{-3}$),

r_{awi} : aerodynamic resistance for water vapor transfer in the i th layer ($s\ m^{-1}$),

r_{ci} : crop resistance in the i th layer ($s\ m^{-1}$).

After calculation of the sensible and latent heat, the estimation of the air temperature (T_{ai}) and vapor pressure (e_i) in the i th layer were as follows (Goudriaan, 1977):

$$T_{a,i} = T_{a,i-1} + H_i R_i / \rho c_p, \quad (5)$$

$$e_i = e_{i-1} + \lambda E_i R_i (\rho c_p / \gamma), \quad (6)$$

where R_i is a value characteristic to resistance in the i th layer ($s\ m^{-1}$). When $i=1$, $T_{a,i-1}$ and e_{i-1} are the temperature and water vapor pressure from the separated standard meteorological measurement, respectively.

The inputs of the model are site and plant specific parameters (plant height, leaf density in three layers), different soil characteristics (soil moisture content and physical properties) and hourly meteorological data are from standard measurements (Goudriaan, 1977). From the outputs the air temperature and humidity in the upper third of plant height are included in the study.

The meteorological data were provided by the local standard QLC automatic weather station.

The reconstruction of the Goudriaan model was designed to make the input of measured data easier and to display the results in a user-friendly manner. A further aim was to increase the maximum number of input data,

which was previously limited to 20. Nevertheless, the program still uses the basic equations elaborated by *Goudriaan* (1977).

To validate the model, the root mean square deviation (*RMSD*) of a number (*n*) of pairs of simulated (*S*) and measured (*M*) microclimate elements was applied:

$$RMSD = \left\{ \left[\sum (M - S)^2 \right] / n \right\}^{0.5} \quad (7)$$

The *RMSD* is one of the best overall measures of model performance (*Willmott*, 1982; *Castrignano et al.*, 1997).

The ear dry matter as a season long integrator of actual weather was measured at the end of the vegetation period by drying the samples to constant weight at 60 °C.

3. Results

3.1 Climatic conditions

The vegetation period in 2001 was substantially drier than the average, having 28.2% less rainfall than the many years' mean. If the monthly means are considered, the deviation from the 30-year mean was positive only in September, but in this case the difference was very great, since there was about 80 mm more rainfall than usual (*Fig. 1*).

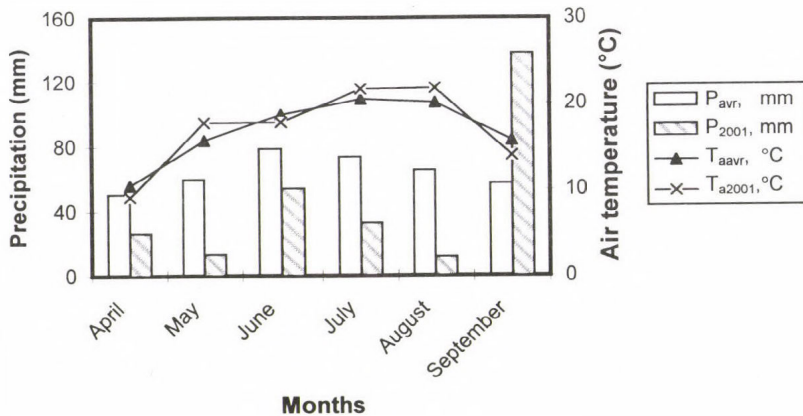


Fig. 1. Monthly precipitation sums and average air temperatures for 1970–1999 (P_{avr} , T_{aavr}) and in the season of 2001 (P_{2001} , T_{a2001}).

The water deficiency level for the vegetation period should thus be calculated without the September figures, in which case a value of 42.1% is

obtained. The distribution of the rainfall within the vegetation period may have caused a further deterioration in the growing conditions of maize, since the greatest deficiencies were observed in August, May, and July.

The rainfall deficiency during the periods when the water supply is critical for maize development was accompanied by warmer weather than usual. The mean monthly temperature was more than 2 °C higher in May and 1.2–1.7 °C higher in July and August than the normal values.

3.2 Size and distribution of the assimilatory surface

Irrigation increased the annual mean value of the green leaf area by 38.8%, mainly due to the delay in leaf withering in the irrigated stand (*Fig. 2*). The supplementary water supplies did not modify the date by which the greatest leaf area developed, but in the control treatment the extreme drought caused the lower leaf levels to wither by mid-August, so that practically the whole stand had become defoliated by the end of August. In the irrigated stand this did not occur until much later, in mid-September.

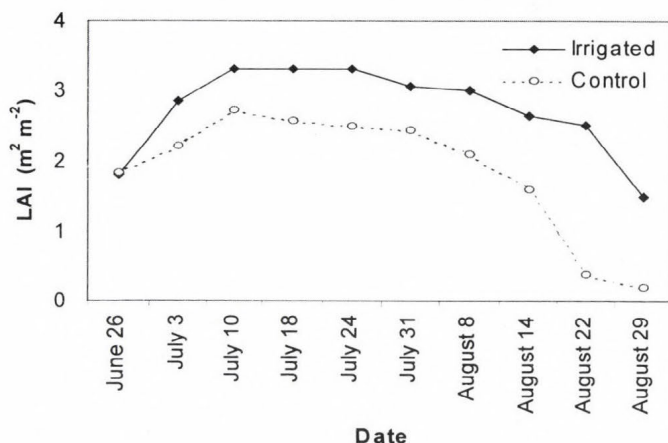


Fig. 2. Yearly trend in the leaf area index (LAI) of maize at two watering levels.

During the simulation, irrigation had a different effect on the leaf area distribution of the three plant height levels used as input parameters for the model. The three levels were obtained by simply dividing the total plant height by three ($i=1,2,3$). In the upper ($i=1$) and middle thirds ($i=2$) irrigation caused a constant increase in the leaf area (around 20% and 10% for the upper and middle thirds, respectively), while in the lower third, closest to the ground, due to the different extents of leaf withering, 14.2% deviation in leaf

area was recorded on July 10 as the result of irrigation, which was increased to 567.9% by the end of the month. The distribution of the total leaf area between the three levels during the simulation is presented in *Table 1* as a ratio of the leaf area of the upper third (the input parameter required by the model). Results in leaf area distribution of irrigated stand showed the success of irrigation during the 2001 season.

Table 1. Distribution of the leaf area over the different plant height levels as the ratio of the leaf area of the upper third (the input of the model)

	July 10	July 17	July 24	July 31	August 8
Irrigated plants					
Upper third	1	1	1	1	1
Middle third	1.56	1.56	1.56	1.56	1.56
Lower third	0.81	0.76	0.74	0.61	0.50
Control treatment					
Upper third	1	1	1	1	1
Middle third	1.73	1.73	1.73	1.73	1.73
Lower third	0.84	0.69	0.51	0.12	0.05

3.3 Irrigation and changes in CWSI

The water stress index is a complex index which provides a numerical indication of plant water deficiency, based on trends in plant properties and meteorological elements, before visible symptoms appear. During the 2001 vegetation period, the plants exhibited signs of water deficiency on four occasions due to the extreme drought (*Fig. 3*). The total water quantity in 2001, together with irrigation water, was 20 mm less than the long-term rainfall average for the vegetation period in the Keszthely region, suggesting that the irrigation was carried out very circumspectly (*Table 2*).

When the measurements began, double of the normal irrigation water amount was applied, since the mean water deficiency had already exceeded 70–80 mm. The CWSI is not suitable for the determination of earlier irrigation dates due to the nature of the plant temperature measurements which form the basis of the index. Plant temperatures characteristic of the stand can only be measured after canopy closure ($LAI \approx 2.0\text{--}2.5 \text{ m}^2 \text{ m}^{-2}$). This stage was reached at the end of June in 2001. (A greater quantity of water was also applied at the

last irrigation on August 8, since no further *CWSI* measurements or irrigation were planned.)

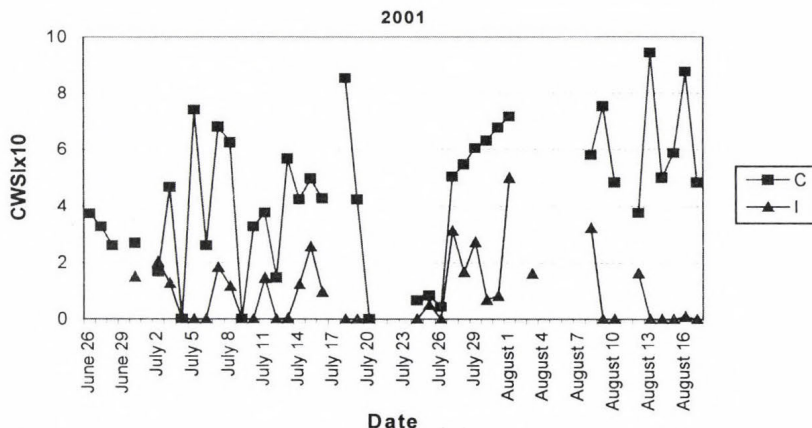


Fig. 3. Seasonal variation in crop water stress index of non-irrigated (C) and irrigated (I) plants. On cloudy days there were no samples taken, causing discontinuity in the figure.

Table 2. Quantity of irrigation water applied on each occasion in 2001

Irrigation date	Water rate (mm)	Intensity (mm/h)
June 28	60	6–8
July 15	35	6–8
August 1	18	6
August 8	56	6–8
Total	169	

Many papers have dealt with the difficulties of detecting plant temperatures, especially in semi-dry areas (Keener and Kirchner, 1983; Jensen *et al.* 1990; Wanjura and Upchurch, 1997). The greatest problem is caused by the disturbing effect of clouds on the intensity of the radiation and on the stand temperature; in some cases this may make the measurements impossible. This explains the lack of data in several places in Fig. 3, which depicts changes in *CWSI*. This often, but not always, coincided with the appearance of rainfall.

In 2001, a total of 170 mm of irrigation water was required to keep the *CWSI* value below the critical level and avoid damage to the life processes of the crop. Averaged over the whole measurement period, this water rate was sufficient to reduce the stress index by 131.6%. During the modeling period,

this change was somewhat more moderate, being only 116.9%. Irrigation led to a significant 22.4% rise in the grain yield (*Table 3*).

Table 3. Effect of irrigation on grain yields

	Irrigated treatment	Control plants
Yield (kg m ⁻²)	0.80	0.68
Deviation	0.09	0.052
f test		0.598
t test		0.023
LSD _{5%}		0.10

3.4 Microclimate simulation

3.4.1 Modification of the CMSM model (Goudriaan, 1977; Goudriaan and van Laar, 1994)

The program written by *Chen* in 1984 in BASIC programming language was unsuitable for automatic data input. Converting the input data before the program run was very time-consuming. The version elaborated by the authors is able to treat all the input data as parameters, thus reducing the running time considerably. In the original program the number of input data was limited to 20, but this has been expanded, since hourly measurements will mean at least twenty-four data a day. The new version of the program is also capable of displaying graphs, in addition to an hourly presentation of the data and the profiles of the elements (*Anda and Lőke, 2002*).

3.4.2 Results of the simulation

A microclimate simulation was carried out on the fully developed stand between the end of June and the beginning of August, 2001. The simulation was not a complete success on all the 38 days included in the study. On some of the sampling days, for reasons of extreme weather, the model either failed to run or the simulated values were substantially different from the measured values. On wet and windy days the deviation, especially for air humidity content, was more than 15–20% in all cases, the most extreme difference was 35%. For this reason, seven extremely stormy days – where the wind speed at 2 m above the canopy exceeded the 4–5 m s⁻¹ and the amount of precipitation was above 5 mm – were excluded from the evaluation. The number of stormy day in 2001 was less than in most of the years.

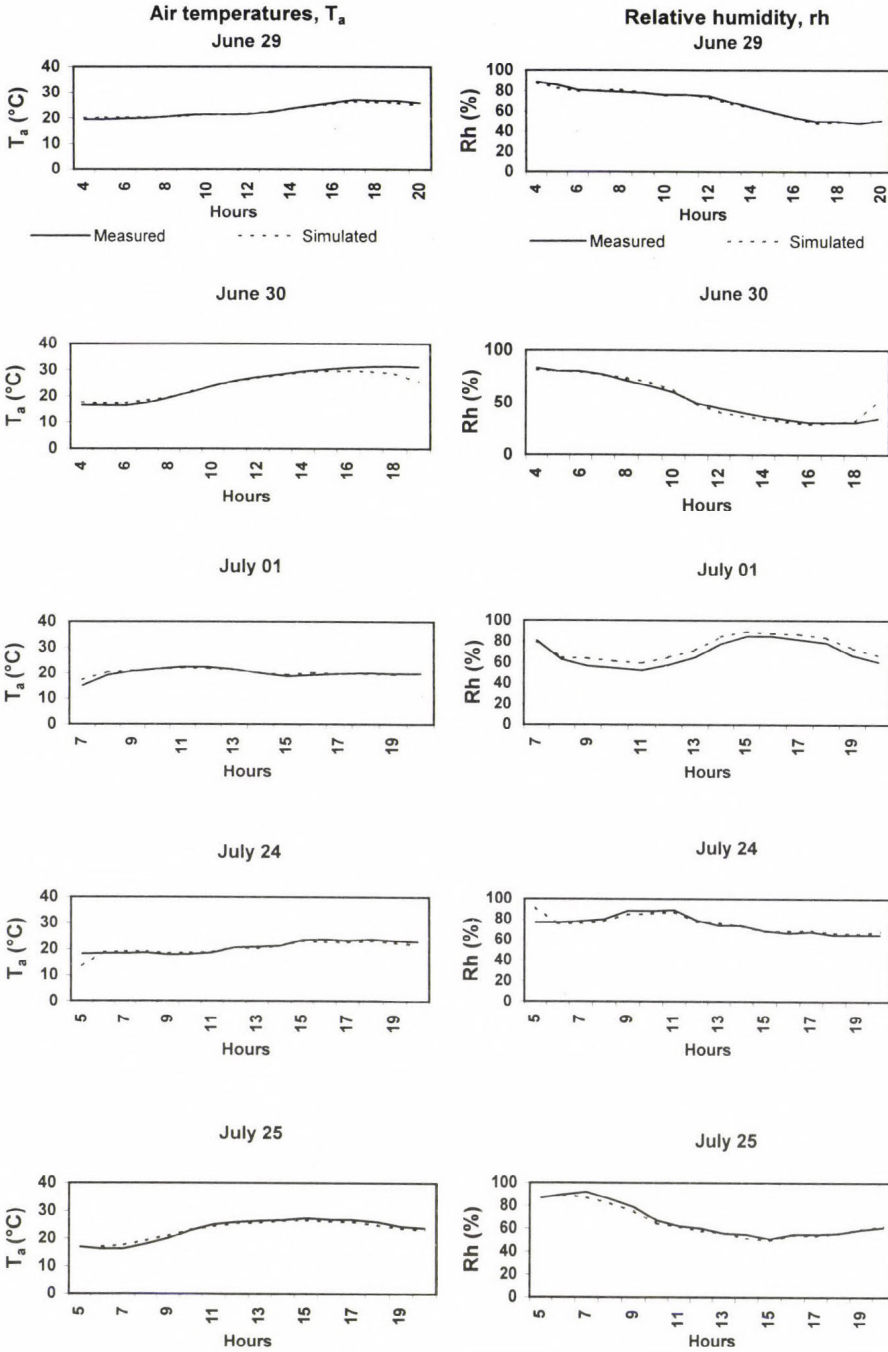
In contrast to expectations, the presence of these meteorological elements, especially of wind, was less of a problem for the simulation of air temperature. The model could be run most successfully on bright, clear days. On some sample days, the simulation deteriorated substantially for some hours during the night, compared with the period from sunrise to sunset. The probably reason might have been the extreme weather of these days. In some cases, these data caused a substantial deterioration in the mean for the whole day. In order to avoid excluding further days from the evaluation, the success of the simulation was only calculated for the sunshine hours. This improved the estimation of the air temperature by a few tenths of a degree Celsius and that of relative humidity by around 5%. The results for sunshine hours were applied in further plant investigations such as stomatal resistance and photosynthesis (not published).

The justification for this procedure was that the change in the microclimate induced by the irrigation was relatively small in absolute terms, so even a deterioration of a few percent in the accuracy of the estimation may make the applicability of the method questionable. The sign of the deviation between the microclimate elements measured and calculated for the night hours was not the same on all of the days, though the values of relative humidity tended to be overestimated (*Fig. 4a, b*), and those of air temperature tended to be underestimated.

Irrespective of the water supplies, the most accurate microclimate simulation was obtained on clear days during the period from sunrise to sunset. The results are illustrated on the simulated and measured microclimate data of 5 irrigated and 5 control sample days. Averaged over the whole measuring period, the simulated air temperature mean for the sunshine hours was 0.27 °C higher than the true value in the control and 1.03 °C higher in the irrigated stand. (During the observation period, the greatest deviation found for the daylight hours was 1.07 °C in the control and 3.85 °C in the irrigated treatment.) The difference in the measured and simulated data for the mean air humidity during the daylight hours was 6.31% in the non-irrigated and 5.88% in the irrigated treatment. (The greatest deviation observed in the mean for the daylight hours was 13.94% without irrigation and 11.93% in the irrigated variant.) We compared measured and simulated data for the upper third of plant height.

On the basis of publication of *Pearcy et al.* (1991) on accuracy of estimation of the air temperature and humidity, the alteration between the measured and simulated microclimate elements is acceptable. The desirable accuracy of temperature measurements in plant studies is ± 1 °C. The wanted accuracy of relative humidity determination is about 20%.

(a) Non-irrigated control



→

(b) Irrigated treatment

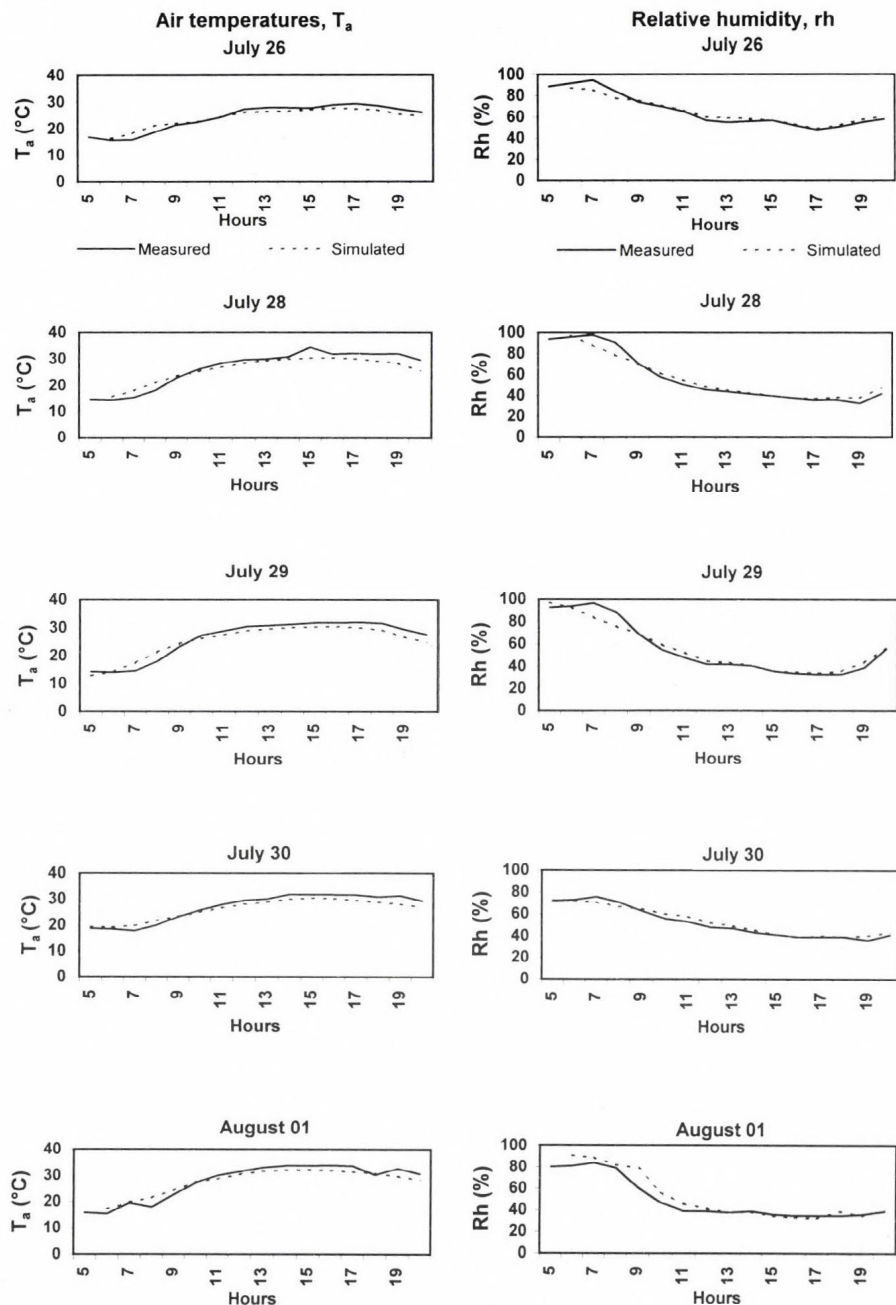


Fig. 4. Measured and simulated air temperatures and humidity in the upper third of plant stand on five sample days during 2001 in control (a) and irrigated (b) treatments, respectively.

3.5 Validation of the model

In the linear regression between simulated (P) and observed (O) values, $P = a + bO$, the intercept a was not significantly different from zero at $p = 0.05\%$, so a regression through the origin was applied. The slopes were close and not significantly different from 1. (Each 95% confidence interval includes 1, as Table 4 shows.) We can conclude that the model well estimated both the air temperatures and relative humidity.

Table 4. Table of results in statistical analysis of measured and simulated data in the upper third of plant height

	Non irrigated control		Irrigated treatment	
	T_a	Rh	T_a	Rh
RMSD	0.474	3.055	0.931	2.780
Slope	0.997	1.003	1.013	0.961
95% confidence interval	[0.968;1.026]	[0.939;1.066]	[0.967;1.059]	[0.919;1.003]
R^2	0.999	0.998	0.999	0.999
Slope standard error	0.010	0.023	0.016	0.015
Regression root mean square error	0.525	3.408	0.966	1.913

4. Conclusions

Hourly values of the air temperature and humidity in the upper third of plant stand were simulated using the CMSM (Goudriaan, 1977; Goudriaan and van Laar, 1994) in irrigated and non-irrigated maize stands. Results in simulation were controlled by direct measurements after canopy closure during the 2001 growing season. The term of canopy temperature used in irrigation timing (CWSI) limited the beginning of the study (June 29–August 6). The aim of the investigation was to control the more precise and quick results on plant microclimate than that of we had earlier. The simulated elements of microclimate could serve a good basis in plant studies, because almost all physiological processes deeply depend on those parameters surround the plants.

- Among the microclimate elements, the accuracy of the estimation of air temperature in the upper third of non-irrigated stands was better than that found for irrigated stands. In the case of humidity, the deviations between the simulated and measured elements were similar for the two water supply treatments. In order to reduce the difference, the estimations for the night hours were ignored, since the error of these values was greater than that of the simulation for the daylight hours. Using this technique, the accuracy of estimation for the investigated parameters improved, since the differences in air temperature values dropped to 0.5–1.0 °C and those of air humidity dropped below 10%. These deviations were small enough to enable the slight changes caused by irrigation to be detected. The limited use for sunshine hours is acceptable when plant physiological processes are studied, but further investigations are needed.
- Provided, that the distribution of the leaf area between the various levels of the plant stand is known, the *Goudriaan* (1977) model appears to be suitable for the demonstration of changes in the microclimate as the result of irrigation, even if these are very slight. This could be of importance in predicting the probable effect of human interventions. In particular, a new light could be shed on the relationship between the changes in air humidity and the multiplication of certain plant diseases, which could lead to more efficient planning of disease control measures.
- At present the model is the most satisfactory for the simulation of the daylight hours of clear days. When the wind speed exceeded 4–5 m s⁻¹ above the stand and the amount of precipitation was above 5 mm, the accuracy of simulation deteriorated (seven days from 38). Further research will be required to make it adaptable for rainy, windy days.

Acknowledgement—The study was sponsored by the Hungarian Academy of Sciences under the work of T 043147.

References

- Anda, A.*, 1993: The use of infrared thermometry in irrigation timing (in Hungarian). *PhD Thesis*. MTA, Budapest.
- Anda, A. and Stephens, W.*, 1996: Sugar beet production as influenced by row orientation. *Agron. J.* 88, 991-996.
- Anda, A. and Lőke, Zs.*, 2002. Modelling the factors determining maize evapotranspiration: The stomatal resistance, surface temperature and photosynthesis (in Hungarian). *Növénytermelés* 52, 351-363.
- Anda, A., Lőke, Zs., and Burucs, Z.*, 2001: Microclimate of irrigated and non-irrigated maize (in Hungarian). *Növénytermelés* 50, 249-260.

- Calveta, J.C., 2000: Investigating soil and atmospheric plant water stress using physiological and micrometeorological data. *Agr. Forest Meteorol.* 103, 229-247.
- Calveta, J.C., Noilhana, J., Roujeana, J.L., Bessemoulina, P., Cabelguenneb, M., Oliosoc, A., and Wigneroc, J.P., 1998: An interactive vegetation SVAT model tested against data from six contrasting sites. *Agr. Forest Meteorol.* 92, 73-95.
- Carberry, P.S., Muchow, R.C., and McCown, R.L., 1989: Testing the CERES-Maize simulation model in a semi-arid tropical environment. *Field Crop. Res.* 20, 297-315.
- Castrignano, A., Di Bari, V., and Stelluti, M., 1997: Evapotranspiration predictions of CERES-Sorghum model in Southern Italy. *Eur. J. Agron.* 6, 265-274.
- Cavero, J., Playán, E., Zapata, E., and Faci, M.J., 2001: Simulation of maize grain yield variability within a surface-irrigated field. *Agron. J.* 93, 773-782.
- Chen, J., 1984: Mathematical analysis and simulation of crop micrometeorology. *Ph.D. Thesis*. The Netherlands.
- Evans, G.C., 1972: *The Quantitative Analysis of Plant Growth*. Blackwells, Oxford.
- Fodor, N., Mathene-Gaspar, G., Pokovai, K., and Kovacs, G.J., 2003: 4M-software package for modelling cropping systems. *Eur. J. Agron.* 18, 389-393.
- Franks, S.W., Beven, K.J., Quinn, P.F., and Wright, I.R., 1997: On the sensitivity of soil-vegetation-atmosphere-transfer (SVAT) schemes: Equifinality and the problem of robust calibration. *Agr. Forest Meteorol.* 86, 63-75.
- Gardner, B.R., Blad, B.L., and Watts, D.G., 1981: Plant and air temperatures in differentially irrigated corn. *Agr. Meteorol.* 25, 207-217.
- Gottschalk, J.C., Gillies, R.R., and Carlson, T.N., 2001: The simulation of canopy transpiration under doubled CO₂: The evidence and impact of feed-backs on transpiration in two 1-D soil-vegetation-atmosphere-transfer models. *Agr. Forest Meteorol.* 106, 1-21.
- Goudriaan, J., 1977: *Crop Micrometeorology: A Simulation Study*. Simulation monographs. Pudoc, Wageningen.
- Goudriaan, J. and van Laar, H.H., 1994. *Modelling Potential Crop Growth Processes*. Kluwer Academic Publishers, Dordrecht-Boston-London. 238p.
- Hatfield, J.L., 1990: Measuring plant stress with an infrared thermometer. *Hort. Science* 25, 1535-1538.
- Huzsvay, L. and Nagy, J., 1994: An analysis on correlation between plant number and yield in maize by models with different biological validity (in Hungarian). *Növénytermelés* 43, 533-544.
- Idso, S.B., Jackson, R.D., Pinter, P.J. Jr, Reginato, J.R., and Hatfield, J.L., 1981: Normalising the stress degree parameter for environmental variability. *Agr. Meteorol.* 24, 45-55.
- Irmak, S., Haman, D.Z., and Bastug, R., 2000: Determination of CWSI for irrigation timing and yield estimation of corn. *Agron. J.* 92, 1221-1227.
- Jackson, R.D., 1982: Canopy temperature and Crop Water Stress. *Adv. Irrig.* 1, 43-85.
- Jackson, R.D., Idso, S.B., Reginato, R.J., and Pinter, P.J. Jr., 1981: Canopy temperature as a crop water stress indicator. *Water Resour. Res.* 17, 1133-1138.
- Jensen, H.E., Svendsen, H., Jensen, S.E., and Mogensen, V.O., 1990: Canopy-air temperature of crops grown under different irrigation regimes in a temperate humid climate. *Irrigation Sci.* 11, 181-188.
- Jones, H.G., 1983: *Plants and Microclimate*. Cambridge Univ. Press, Cambridge. 323p.
- Jones, C.A. and Kiniry, J.Y., 1986: CERES-Maize: A simulation model of maize growth and development. Texas A&M Univ. Press, College Station.
- Keener, M.E. and Kirchner, P.L., 1983: The use of canopy temperature as an indicator of drought stress in humid regions. *Agr. Meteorol.* 28, 339-349.
- Kiniry, J.R. and Knievel, D.P., 1995: Response of maize seed number to solar radiation intercepted soon after anthesis. *Agron. J.* 87, 228-234.
- Kiniry, J.R., and Bockholt, A.J., 1998: Maize and sorghum simulation in diverse Texas environments. *Agron. J.* 90, 682-687.
- Kiniry, J.R., Williams, J.R., Richard, L., Vanderlip, J.D., Atwood, D., Reicosky, C., Mulliken, J., Cox, W.J., Mascagni, H.J., Hollinger, S.E., and Wiebold, W.J., 1997: Evaluation of two maize models for nine U.S. locations. *Agron. J.* 89, 421-426.

- Liu, W.T.H., Botner, D.M., and Sakamoto, C.M., 1989: Application of CERES-Maize to yield prediction of a Brazilian maize hybrid. *Agr. Forest Meteorol.* 45, 299-312.
- Mantovani, E.C., Villalobos, F.J., Orgaz, J., and Fereres, E., 1995: Modelling the effects of sprinkler irrigation uniformity on crop yield. *Agr. Water Manage.* 27, 243-257.
- Nobel, P.S., 1974: *Introduction to Biophysical Plant Physiology*. Freeman Press, San Francisco.
- Nouna, B.B., Katerji, N., and Mastrorilli, M., 2001: Using the CERES-Maize model in a semi-arid Mediterranean environment. Evaluation of model performance. *Eur. J. Agron.* 13, 309-322.
- Paz, J.O., Batchelor, T.S., Colvin, S.D., Logsdon, T.C., Kaspar, C., and Karlen, D.L., 1998: Analysis of water stress causing spatial yield variability in soybeans. *Trans. ASAE*, 41, 1527-1534.
- Pearcy, R.W., Ehleringer, J., Mooney, H.A., and Rundel, P.W., 1991: *Plant Physiological Ecology*. Chapman and Hall, London-New York-Tokyo, 457p.
- Plantureux, S., Girardin, P., Fouquet, D., and Chapot, J.Y., 1991: Evaluation et analyse de sensibilité du modèle CERES-Maize en conditions alsaciennes. *Agronomie* 11, 1-18.
- Rosenberg, N.J., 1974: *Microclimate: The Biological Environment*. Wiley, New York.
- Sellers, W.D., 1965: *Physical Climatology*. Chicago, Univ. of Chicago Press.
- Stockle, C.O. and Kiniry, J.R., 1990: Variability in crop radiation use efficiency associated with vapor pressure deficit. *Field Crop. Res.* 21, 171-181.
- Wanjura, F. and Upchurch, D.R., 1997: Accounting for humidity in canopy-temperature-controlled irrigation scheduling. *Agr. Water Manage.* 34, 217-231.
- Willmott, C.J., 1982: Some comments on the evaluation of model performance. *B. Am. Meteorol. Soc.*, 1309-1313.
- de Wit, C.T. and Goudriaan, J., 1978: *Simulation of Ecological Processes*. Wageningen, Pudoc.
- Xie, Y., Kiniry, J.R., Nedbalek, V., and Rosenthal, W.D., 2001: Maize and sorghum simulations with CERES-Maize, SORKAM, and ALMANAC under water limiting conditions. *Agron. J.* 93, 1148-1155.

IDŐJÁRÁS

Quarterly Journal of the Hungarian Meteorological Service
Vol. 109, No. 1, January–March 2005, pp. 39–53

On the use of standard meteorological data for microclimate simulation

Márta Hunkár

Department of Mathematics, Georgikon Faculty of Agriculture, University of Veszprém
P.O. Box 71, H-8360 Keszthely, Hungary; E-mail: hunkar@georgikon.hu

(Manuscript received in final form January 19, 2005)

Abstract—Multi-layer microclimate simulation models describe the profiles of meteorological variables inside the canopy. For a steady state model, the instantaneous values of air temperature, vapor pressure, wind speed, and global radiation are needed as input variables from a given height above the canopy. A standard automatic meteorological station provides all those data with high frequency in time, but from outside of the canopy. A simple calculation method is presented in this paper for evaluation „above canopy” data from standard data. Roughness parameters are considered in three different ways. Applying the methods for an experimental maize field, measured plant characteristics were used. At the beginning of the vegetation season and in the senescence period, the differences in roughness parameters due to different approaches were negligible, the largest difference in roughness parameters occurred at the fully developed plant stand. The differences occurred due to application of the calculated different roughness parameters in profiles of meteorological elements were small even at this time. We concluded that data transferring is needed because of keeping consistency among meteorological data, at least plant height must be taken into account in determination of surface roughness length and zero-plane displacement. Further plant characteristics as LAI, the width of the leaves, and the drag coefficient of the leaves can also be taken into account, for it makes the method more general, but in the case of maize stand, the effect on the profiles of meteorological elements is rather small.

Key-words: microclimate, surface roughness length, zero-plane displacement, simulation model

1. Introduction

The processes of energy exchange and flow of materials between the surface and the atmosphere provide all the conditions which are important for crop growth and also for parameterization of General Circulation Models. Taking a

vegetated surface, a soil vegetation atmosphere transfer scheme (SVAT) describes the fluxes of heat, water vapor, and CO₂ between a multi-component vegetated land surface and the atmosphere. The SVAT models are different in their complexity. The SVAT “big-leaf” models treat the canopy and underlying substrate as a single source (Ács, 1994). In a two-source model, the canopy component is treated either as a single big leaf, or as partitioned shaded-sunlit leaves (Sellers *et al.*, 1996; Tourula *et al.*, 1998; Boegh *et al.*, 1999). Transports of heat and soil moisture are often represented with three or more layers (Flerchinger *et al.*, 1998). The number of layers mostly depends on the purpose of the SVAT model. In land-surface hydrology, the soil is divided into several layers and vegetation is presented by one layer (Ács and Hantel, 1998, 1999; Ács and Kovács, 2001).

In production ecology, the basic question is how internal and external factors influence the growth and development of crops. Micrometeorological conditions within a crop canopy are important as direct environmental forces to photosynthesis, and also for the microorganisms living in the ecosystem. Therefore, a multi-layer approach for the vegetation is important to describe vertical profiles of air temperature, humidity, wind speed as micrometeorological conditions within the plant canopy. Those profiles depend on macrometeorological conditions prevailing above the canopy, and the structure and water status of the soil and the plant stand.

Information about meteorological conditions inside the canopy is often needed because of any kind of practical purpose, but direct measurement of the elements with a special mast equipped with sensors are not available inside and above the canopy. Meteorological stations are installed outside of the plant stand, concerning WMO standards: temperature and air humidity are measured at 2 m height in shelter, wind speed at 10 m height in open area, incoming global radiation at an open area. Nevertheless, the automation of the measurements provides meteorological data with high frequency in time, the problem is the place of the measurements. If we want to use micrometeorological model, we need data from a reference height above the canopy. For operational purpose, a rather crude solution might be that measured values of meteorological elements are taken directly as model inputs with fixed height of reference level. Statistical data analysis carried out by Anda *et al.* (2003) did not find significant differences between the data measured at the standard meteorological station and above the canopy, for the experimental site at Keszthely Agrometeorological Research Station. Nevertheless, in micrometeorology, “differences” are small and vary also in plus-minus direction in time for day-time and night-time, therefore, statistical relations are not applicable to get instantaneous values of the meteorological elements. A further viewpoint is keeping the physical consistency of data.

In this paper a simple solution is given to overbridge this problem for the situation of Keszthely Agrometeorological Station and experimental field. Nevertheless, the method is applicable for other places as well where the meteorological station is close enough to the field. It has to be emphasized, that our main purpose is to make an existing micrometeorological model to be operative by providing the required initial values.

2. Crop Micrometeorological Simulation Model

Crop Micrometeorological Simulation Model, CMSM, developed by *Chen* (1984a) gives detailed calculations of the profiles of meteorological elements within a plant stand. The basic equations of the model are summarized by *Goudriaan* (1977). The model consists of three main parts: radiation submodel which gives results both on macroscale (crop reflectance and transmittance) and microscale (distribution of absorbed radiation intensity over the leaves); the energy and mass balances of leaves and soil surface, which connects the radiation model to the phenomena of transpiration and photosynthesis; aerodynamical submodel for wind and turbulence, which are treated as related phenomena above as well as inside the canopy. CMSM is a multi-layer steady state model, according to the air conditions, assuming equilibrium at any time in the air, and dynamic for the soil heat transfer because of the significant value of soil heat capacity. Momentum-, sensible heat-, and latent heat transfer are calculated between the soil surface and the bottom layer, and between the individual layers of the canopy, as well as between the top of the canopy and the reference height. The fluxes are controlled by radiative forcing and aerodynamical resistances. A detailed description of fluxes and numerical solutions are given by *Chen* (1984b). Instability is considered by the Monin-Obukhov length, L , which has to be given as initial value for the time zero, but it is only a „first guess”, the model calculates its actual value for each time step. The time step of the model is optional, it is worth to choose few minutes. In our simulation experiments, 10 minutes were chosen for time step. Using that flux values, the actual air- and leaf temperature and vapor pressure are calculated “backward”. In real world, differences in temperatures and vapor pressure between the surface and the surrounding air, and between the individual layers generate fluxes of sensible and latent heat, and the values of meteorological elements above the canopy are controlled and determined by the energy exchange taking place at the leaves and soil, transferring by the fluxes on dynamic way. According to the CMSM concept, we know the results of these processes, namely the actual values of air temperature and vapor pressure at the reference height above the canopy at any time, therefore, the

fluxes resulting them can be calculated as well as the temperature and vapor pressure gradient.

It means that input meteorological data required by CMSM derive from measured data at a reference height above the canopy, those are: instantaneous values of global radiation, air temperature, vapor pressure, wind speed at any time characterizing daily course of the elements. Linear interpolation is used to get those values for the individual time steps. Soil heat transfer is calculated on dynamic way, therefore, the initial values of soil temperature profile must be given at time zero (usually at midnight).

The model was tested in Hungary as well, using measured meteorological, soil and plant data (Hunkár, 1990). Later on a user-friendly version was developed (Hunkár, 2002), which makes easier data handling and output interpretation on WINDOWS basis.

3. Description of the measurements and adjustments

At the site of the Agrometeorological Research Station at Keszthely (46°46'N; 17°20'E) an automatic meteorological station runs according to WMO standards. The place for meteorological measurements is located near the experimental field of maize, where micrometeorological characterization is required. Air temperature and humidity sensors are in a shelter located about 20 m from the edge of the maize field at 2 m height above the ground surface. Wind sensor is located at the top of a mast of 10 m height, and global radiation is also measured at the same mast at 5 m height. The mast is settled at the edge of the maize field. The ground surface below the station is covered with short grass. To have daily course of the elements, ten minutes average values between the 50th–60th minutes in each hour will be used from 00:00 until 24:00 CET.

There are different ways to get the required meteorological data above the canopy. One possibility is that the reference height is fixed at given height above the ground surface, and we have to modify the measured data, taking into account the theoretical shape of the vertical profiles of the elements, considering the surface roughness length, zero-plane displacement, and thermal stability. Another possibility is to choose a reference height where the data would be the same as the measured value. The values of surface roughness length and zero-plane displacement are also used for this approach. Both ways shall be used to get appropriate meteorological data (*Fig. 1*). In the case of air temperature and vapor pressure, we use the values measured at the meteorological station searching for the level above the canopy, where the same values could be occurred. Thermal stratification is assumed to be the

same both outside and above the canopy, therefore, the height of the reference level is different from the level of “outside” measurements just because of the roughness length and zero-plane displacement characteristic for the plant stand. In the case of wind, the measured data – which came from 10 m height – will be transformed to that reference level using logarithmic wind profile.

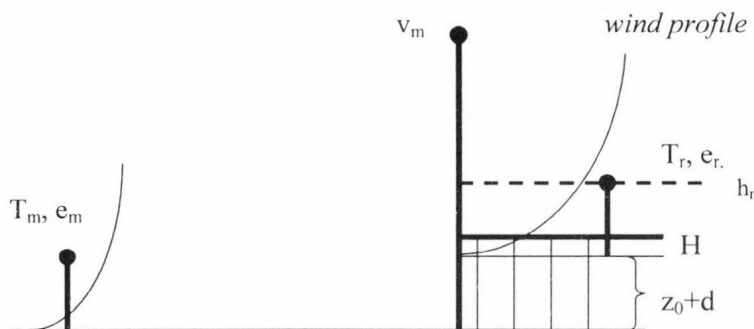


Fig. 1. The concept of data transformation. T_m, e_m are the measured values of air temperature and vapor pressure outside of the canopy at 2 m height, v_m is the measured wind speed at the edge of the canopy at 10 m height, T_r, e_r, v_r are those values transformed to the reference height, h_r is the reference height above the canopy, z_0 is the roughness length, d is the zero plane displacement, H is the height of the canopy (after Szász and Tőkei, 1997).

Horizontal advection is not taken into account, therefore, the method is applicable only when the place of meteorological measurement is close to the plant stand.

3.1 Surface roughness length and zero-plane displacement

The crucial point in our method is assessing a proper value of surface roughness length, z_0 , and zero-plane displacement, d . A sensitivity study carried out by Weidinger *et al.* (2000) shows the strong dependence of sensible heat flux on surface roughness length and zero-plane displacement height. Most of the studies concerning the exchange of mass and energy between the surface and the atmosphere are based on wind profile observations. A high tower equipped with sensitive anemometers is rather expensive, therefore, only small set of actually measured roughness parameters are available. Wieringa (1993) analyzed and summarized about fifty well documented experiments over various surfaces. When the surface is covered

by vegetation, the roughness parameters are determined by the structure of the plant stand, which is changing in time as plant grows. *Monteith* (1973) suggested an empirical linear relation for d using measured value of plant height, H :

$$d=0.63H. \quad (1)$$

The length of z_0 is often supposed to be about one tenth of the height of the vegetation:

$$z_0=0.1H. \quad (2)$$

Tanner and Pelton (1960) suggested an empirical formula for surface roughness length, z_0 :

$$\log_{10} z_0 = 0.997 \log_{10} H - 0.883. \quad (3)$$

Stanhill (1969) gives also an empirical formula for zero plane displacement, d :

$$\log_{10} d = 0.9793 \log_{10} H - 0.1536. \quad (4)$$

In Eqs. (1)–(4) the plant stand is characterized only with the height of the plants. Thinking on the roughness characteristics of a vegetated surface it is clear, that leaf area density and the drag coefficient of the leaves affect the strength of the sink for momentum, too. The greater the leaf area density belonging to the same plant height, the surface seems to be smoother with less z_0 but higher d , and, of course, a hairy type leaf makes stronger drag than a plain leaf.

A sophisticated and physically based calculation is used by *Goudriaan* (1977) which takes into account not only the height of the plant stand, H , but the leaf area index, LAI , the average width of the leaves, w , and the drag coefficient of the leaves, c . In our work the values of d and z_0 are considered after the theoretical description of *Goudriaan* (1977), which were applied in the model of *Chen* (1984a),

$$d = H - \sqrt{\frac{l_m \cdot a}{k}}, \quad (5)$$

where l_m is the mixing length, a is the extinction coefficient for wind inside the canopy, k is the Karman constant, 0.4. For the mean mixing length in the canopy the free space between the leaves or stems is used. The number of leaves per volume is given by $L_d w^{-2}$, where w is the width of the leaves and L_d is the leaf area density which comes from the measured values of leaf area index (LAI) and canopy height, H : $L_d = LAI/H$. When the leaves are long and

narrow, the mean mixing length is the diameter of a cylinder, containing on the average one leaf. Mixing length is calculated by

$$l_m = i_w \cdot \sqrt{\frac{4 \cdot w \cdot H}{\pi \cdot LAI}}, \quad (6)$$

where i_w is the relative turbulent intensity, a proportionality factor that expresses that eddy velocity or friction velocity is proportional to the local wind speed. After measurements of *Shaw et al.* (1974), the average value for maize is taken as 0.5 as first approach.

The extinction coefficient for wind inside the canopy is calculated using plant characteristics as well:

$$a = \sqrt{\frac{c \cdot LAI \cdot H}{2l_m}}, \quad (7)$$

where c is the drag coefficient of leaves, taken as 0.3.

Surface roughness length is determined by the formula:

$$z_0 = (H - d) \cdot \exp\left\{-\frac{H}{a \cdot (H - d)}\right\}. \quad (8)$$

Table 1. Roughness length and zero-plane displacement at different developmental stages of the maize stand* calculated after different authors (Keszthely, 1999 cv: Marietta)

Plant characteristics		Height of the plants (m)	Roughness length (m)			Zero-plane displacement (m)		
Leaf width (m)	LAI (m ² m ⁻²)		Monteith (1973)	Tanner and Pelton (1960)	Goudriaan (1977)	Monteith (1973)	Stanhill (1969)	Goudriaan (1977)
0.02	0.5	0.5	0.05	0.065	0.071	0.315	0.356	0.263
0.04	1.75	1.0	0.1	0.130	0.089	0.630	0.702	0.750
0.05	2.5	1.5	0.15	0.196	0.100	0.945	1.044	1.224
0.05	3.5	2.0	0.2	0.261	0.099	1.260	1.384	1.729
0.05	3.8	2.5	0.25	0.326	0.103	1.575	1.722	2.214

* leaf width and LAI have also changed in the approach of Goudriaan, while other authors take only plant height

A comparison of the results of calculated values of d and z_0 is presented in Table 1 for the maize stand. Plant characteristics as LAI and leaf width represent the average interpolated values belong to the given height. Surface

roughness length (z_0) increases with smaller rate with the plant height according to Goudriaan (1977) approaches, but zero-plane displacement (d) has a greater rate with plant height, therefore, the aerodynamic depth of the plant stand became higher when plant height exceeds 1 m. For a full developed maize stand the difference in z_0+d is about 0.5 m according to the different methods (Fig. 2).

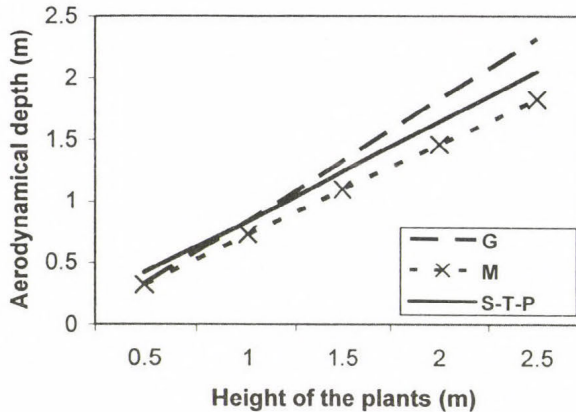


Fig. 2. Aerodynamical depth (z_0+d) of the plant canopy versus plant height according to the different approaches G: Goudriaan (1977), M: Monteith (1973), S-T-P: Stanhill (1969) and Tanner and Pelton (1960).

3.2 Vapor pressure and temperature

In the case of temperature and humidity, the measured data, T_m and e_m derive from 2 m height above the surface outside of the canopy. If we knew the depth of the aerodynamically active layer in the plant canopy, z_0+d , the data can be transferred adding that 2 m to the height of the active surface in the canopy (see Fig. 1). That height, the so called reference height, h_r , depends on the surface roughness length, z_0 , and the zero-plane displacement, d . It is a significant simplification that thermal stratification, hereby the profiles of temperature and vapor pressure are assumed to be the same at the meteorological station and above the maize canopy, only the zero level is different. Roughness length for a surface covered by short-cut grass is not exceeds 0.01 m, it is neglected in calculation of the height of the reference level. Since the radiation regime and soil properties, as well as soil moisture content for a short-cut grass and maize at the same site are similar, the differences in the vertical temperature and vapor pressure gradient are not

taken into account. The error caused by this simplification is acceptable. The reference height,

$$h_r = z_0 + d + 2 \text{ meters}, \quad (9)$$

and the measured values of air temperature, T_m , and vapor pressure, e_m , at the meteorological station can be used as the air temperature, T_r , and vapor pressure, e_r , at the reference height above the canopy:

$$T_r = T_m \quad (10)$$

$$e_r = e_m. \quad (11)$$

As the characteristics of the plants change during the vegetation period, the height of reference level will also change in time. Since the height of the reference level is optional as an input data in the simulation model, it can and must be changed according to the development of the plant stand.

3.3 Wind speed at the reference height

Wind speed was measured at the top of a mast with 10 m height at the edge of the plant stand. Since the location of the mast was under the influence of the aerodynamical effects of the plant stand, in our case wind data were considered as "above canopy" data where roughness characteristics were taken from the plant stand. CMSM is a one-dimensional model having only vertical fluxes, wind data means only wind speed, wind direction is not considered, therefore, fetch distance is not considered as well. In other cases, when the place of wind measurement is an open area outside of the plant stand, the different drag characteristics of the different surfaces as well as wind direction have to be taken into account for calculation of fetch. At the experimental site of Keszthely measured wind speed data have to be transferred to the reference height determined before. The profile of wind velocity above the canopy can be represented by a logarithmic relation:

$$U = \frac{u^*}{k} \ln \frac{z-d}{z_0}, \quad (12)$$

$$u^* = k \cdot \frac{U}{\ln \frac{(z-d)}{z_0}}, \quad (13)$$

where U is the wind velocity at 10 m height, u^* is friction velocity, $z=10$ m, k , d , and z_0 are as before. In this approach d and z_0 do not depend on the wind

speed, therefore, the relationship between u^* and U is linear, but some authors found nonlinear relationship explained by the assumption that z_0 and d are influenced by the wind speed (Long *et al.*, 1964; Tajchman, 1981). Others found this effect non significant (Munroe and Oke, 1973). Recently Hurtalova and Matejka (1999) analyzing profile measurements carried out within the framework of NOPEX CFE1 gave numerical relationship between the wind speed and roughness properties, z_0 and d . It seems to be logic, that a strong wind makes the surface smoother when it is covered by flexible stalks of grasses or cereals. Hurtalova *et al.* (2004) analyzed wind profiles above maize canopy, and found nonlinear dependence of friction velocity on the wind speed. Nevertheless, when wind speed is moderate or weak, the effect might be neglected. In our consideration this effect is not taken into account.

Having the value of u^* from Eq. (13), the wind velocity at the reference height, U_r is

$$U_r = \frac{u^*}{k} \ln \frac{h_r - d}{z_0}. \quad (14)$$

3.4 Global radiation

In the case of global radiation there is nothing to do, because the model uses the incoming radiation, and the distance of the measuring place from the plant canopy is so small, that there is no need to change the measured data of global radiation.

4. Model simulations

4.1 Data sets and parameters

During the vegetation season in 1999, the soil and plant characteristics were measured ten times from June 1 until September 1. Measured plant characteristics were determined using 10 sample plants each time. The height of the plants, the length of each leaves, and the maximum width of each leaves were measured with tape-measure. The average width of the leaves came from the maximum width multiplying by 0.75. The average values of soil water potential for upper one meter depth are shown in Table 2. Water potential of the soil was used in CMSM in determination of plant water status, which affects the stomatal resistances and, therefore, the latent heat flux. The values of soil water potential change between -0.1 bar at field capacity and -15 bar at wilting point for any type of soil. The changes in the height of reference level during the vegetation season in 1999 are presented in Fig. 3, as it was calculated by different approaches.

Table 2. Plant and soil characteristics used by the crop micrometeorological model.
(The line with grey background shows the experiment analyzed in details.)

Date	Height of the crop (m)	Leaf area index ($\text{m}^2 \text{m}^{-2}$)	Average width of the leaves (m)	Average soil water potential for 1 m depth (bar)
June 1	0.48	0.48	0.02	-0.96
June 11	0.58	0.75	0.03	-1.20
June 21	0.7	1.33	0.04	-0.88
July 1	1.5	2.49	0.05	-1.28
July 13	2.1	3.52	0.05	-0.80
July 20	2.2	3.56	0.05	-1.26
August 3	2.2	3.48	0.05	-2.20
August 12	2.2	3.24	0.05	-3.80
August 23	2.2	2.58	0.05	-3.35
September 1	2.2	1.95	0.05	-2.65

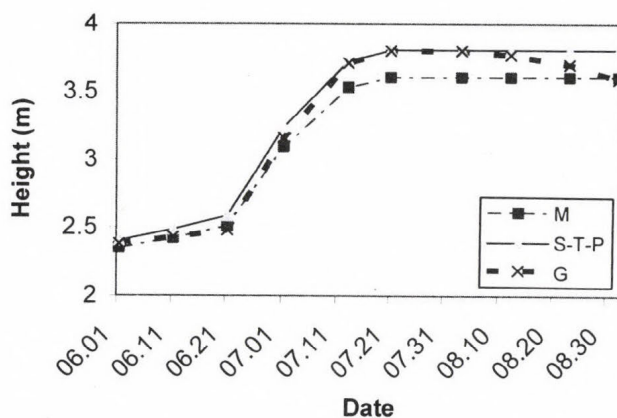


Fig. 3. Height of the reference level during the vegetation season, z_0+d is determined by different approaches G: Goudriaan (1977), M: Monteith (1973), S-T-P: Stanhill (1969) and Tanner and Pelton (1960).

The largest difference caused by the different methods occurs at the fully developed plant stand, it is about 0.2 m. This difference may cause some change in the calculated wind speed data, which is one of the required inputs

for the model. In Fig. 4 measured and calculated wind speed data are shown for July 20, according to determination of z_0 and d suggested by *Monteith* (1973) and *Goudriaan* (1977), respectively. Some difference occur only around noon and they do not exceed 0.02 m s^{-1} . Since in other time the differences in reference height is even less the model outputs are shown only for this time.

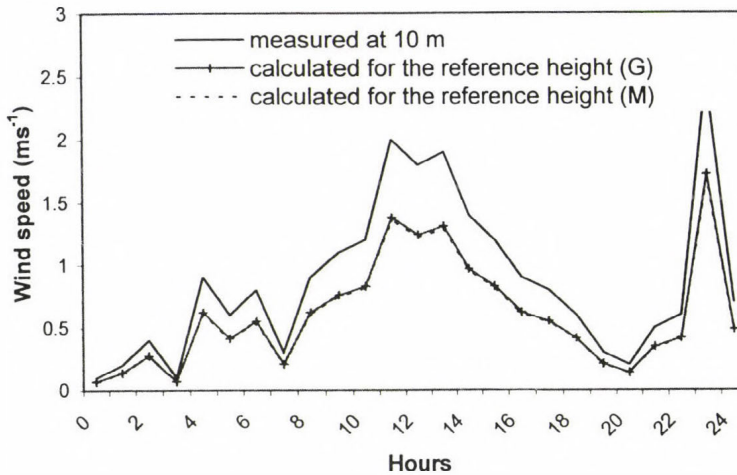


Fig. 4. Wind speed on July 20, 1999, measured at 10 m height, and calculated for different reference levels; M: $h_r=3.6 \text{ m}$, G: $h_r=3.8 \text{ m}$.

The CMSM is a multi-layer model. The canopy was divided into three layers, all of them have the same leaf area index, therefore, the depth of the layers are changing with the development of the plants. Vertical profiles of leaf area are given in the parameter sets that can be measured experimentally or calculated hypothetically. For a fully developed maize stand, parabolic LAI profile can be assumed, but at the beginning of the growing season and in the senescence period the leaf area has different shape. The depth of the layers for the simulation experiment on July 20, 1999 was determined experimentally that $LAI=3.56$ was divided by 3, so each layer has $LAI_i=1.19$ ($i=1,2,3$), and the depth of the layers are as follows: 0.85 m, 0.66 m, and 0.69 m from the bottom to the top of the canopy.

4.2 Scenarios for simulations

To compare the model outputs, the model was run with different reference heights calculated by different methods of calculation of roughness length and

zero-plane displacement. We show the differences in the profiles of meteorological elements inside and above the canopy calculated by the model only to that time, when the largest difference occurred in the reference height, i.e., on July 20, 1999, at 12:00 CET (Fig. 5). Scenario M means that z_0 and d were determined after *Monteith's* (1973) suggestion, scenario G means the method of *Goudriaan* (1977). Since the logarithmic formula suggested by *Stanhill* (1969) and *Tanner and Pelton* (1960) resulted in the same values of z_0 and d as *Goudriaan's* one for that time (see in Fig. 3), we did not make simulation with that. It is clear, that only very small differences occurred in the canopy layers. Values by M scenario are smaller than by G in each layer, both for temperature and vapor pressure. The largest differences were in the bottom layer for the temperature and vapor pressure, but they did not exceed 0.15 °C and 0.4 hPa, respectively. For wind speed, actually, there is no difference between the two scenarios.

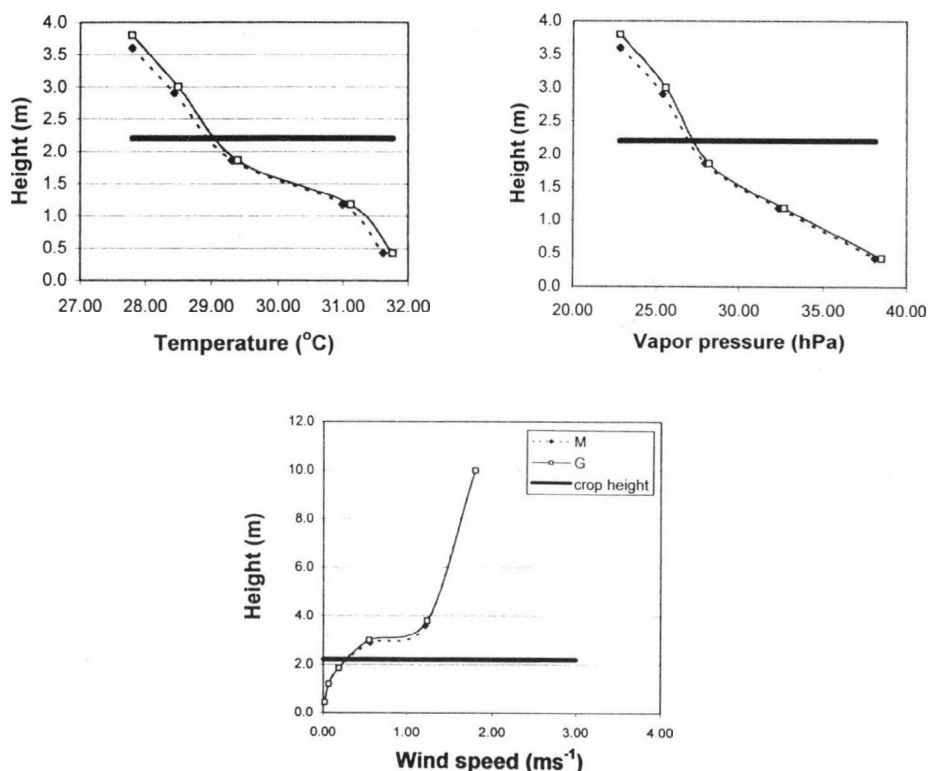


Fig. 5. Profiles of meteorological elements inside and above the canopy calculated by CMSM (on July 20, 1999, 12:00 CET) using different height for the reference level; M: $h_r=3.6$ m, G: $h_r=3.8$ m. Signs are positioned at the middle of the layers.

5. Conclusions

Micrometeorological simulation models are useful tools to get information about the environmental conditions for photosynthesis, transpiration, and evaluation of mass and energy exchange between the vegetated surface and the atmosphere. Application of this type of model is restricted because of their input data requirements, namely input meteorological data must be representative for a reference height above the canopy. Direct measurements of this kind of data are rare and expensive. At the same time, automation of standard meteorological measurements is quite common, and those equipments provide meteorological data with high frequency in time. Data assimilation can be solved by data transformation. In that process some plant characteristics have to be taken into account. This study showed that at least plant height must be determined to get the surface roughness parameters. Further plant characteristics make the transferring process more sophisticated, but the actual values of modeled profiles inside the canopy are not influenced too much in the case of a normal maize stand. Nevertheless, when the vegetation is characterized by the same plant height, but *LAI* and drag properties of the leaves are different in great extent, the method of Goudriaan is suggested to determine surface roughness length and zero-plane displacement.

Further possibilities in application of micrometeorological models arise, when data from the nowcasting will be available for this purpose. Parametrization of the surface is extremely important in the nowcasting methods.

Acknowledgement—The study was supported by the Hungarian Scientific Research Fund (OTKA), the project number is T43147.

References

- Ács, F., 1994: A coupled soil-vegetation scheme: description, parameters, validation, and sensitivity studies. *J. Appl. Meteorol.* 33, 268–284.
- Ács, F. and Hantel, M., 1998: Land-surface hydrology parametrization in PROGSURF: Formulation and test via Cabauw data. *Időjárás* 102, 109–127.
- Ács, F. and Hantel, M., 1999: The Penman-Monteith concept based land-surface model PMSURF. *Időjárás* 103, 19–36.
- Ács, F. and Kovács, M., 2001: The surface aerodynamic transfer parametrization method SAPA: description and performance analysis. *Időjárás* 105, 165–182.
- Anda, A., Lőke, Zs., and Varga, B., 2003: Possibility for using standard meteorological data as input for micrometeorological model (in Hungarian). *Légekör XLVIII* 2, 28–33.
- Boegh, E., Soegaard, H., Friberg, T., and Levy, P.E., 1999: Models of CO₂ and water vapor fluxes from a sparse millet crop in the Sahel. *Agr. Forest Meteorol.* 93, 7–26.
- Chen, J., 1984a: Mathematical analysis and simulation of crop micrometeorology. *PhD Thesis*. Pudoc, Wageningen.

- Chen, J., 1984b: Uncoupled multi-layer model for the transfer of sensible and latent heat flux densities from vegetation. *Bound.-Lay. Meteorol.* 28, 213-225.
- Flerchinger, G.N., Kustas, W.P., and Weltz, M.A., 1998: Simulating surface energy fluxes and radiometric surface temperatures for two arid vegetation communities using the SHAW model. *J. Appl. Meteorol.* 37, 449-460.
- Goudriaan, J., 1977: *Crop Micrometeorology: A Simulation Study*. Pudoc, Wageningen.
- Hunkár, M., 1990: Simulation of microclimate of maize (in Hungarian). *Időjárás* 94, 221-229.
- Hunkár, M., 2002: Moisture supply and microclimate- interactions with productivity potential. *Phys. and Chem of the Earth* 27, 1113-1117.
- Hurtalova, T. and Matejka, F., 1999: Surface characteristics and energy fluxes above different plant canopies. *Agric. Forest Meteorol.* 98-99, 491-500.
- Hurtalova, T., Matejka, F., Chalupnikova, B., and Rožnovský, J., 2004: Aerodynamic properties of air layer above maize canopy during windy conditions. *Időjárás* 108, 65-75.
- Long, I.F., Monteith, J.L., Penman, H.L., and Szeicz, G., 1964: The plant and its environment. *Meteorol. Rundsch.* 17, 97-101.
- Monteith, J.L., 1973: *Principles of Environmental Physics*. Edward Arnold, London.
- Munroe, D.S. and Oke, T.R., 1973: Estimating wind profile parameters for tall dense crops. *Agr. Meteorol.* 11, 223-228.
- Sellers, P.J., Randall, D.A., Collatz, G.J., Berry, T.A., and Field, C.B., 1996. A revised land surface parameterization (SIB2) for atmospheric GCMs. Part I: Model formulation. *J. Climate* 9, 676-705.
- Shaw, R.H., den Hartog, G., King, K.M., and Thurtell, G.W., 1974: Measurements of mean wind flow and three dimensional turbulence within mature corn canopy. *Agr. Meteorol.* 13, 419-425.
- Stanhill, G., 1969: A simple instrument for the field measurement of turbulent diffusion flux. *J. Appl. Meteorol.* 8, 509-513.
- Szász, G. and Tőkei, L. (eds.), 1997: *Meteorology for Agronomist, Gardeners and Foresters* (in Hungarian). Mezőgazda, Budapest.
- Tajchman, S.J., 1981: Comments on measuring turbulent exchange within and above forest canopy. *B. Am. Meteorol. Soc.* 62, 1550-1559.
- Tanner, C.B. and Pelton, W.L., 1960: Potential evapotranspiration estimates by approximate energy balance method of Penman. *J. Geophys. Res.* 65, 3391-3413.
- Tourula, T. and Heikiheimo, M., 1998: Modeling evapotranspiration from a barley field over the growing season. *Agr. Forest Meteorol.* 91, 237-250.
- Weidinger, T., Pinto, J., and Horváth, L., 2000: Effects of uncertainties in universal functions, roughness length, and displacement height on the calculation of surface layer fluxes. *Meteorol. Z.* 9, 139-154.
- Wieringa, J., 1993: Representative roughness parameters for homogeneous terrain. *Bound.-Lay. Meteorol.* 63, 323-363.

On some climatic changes in the circulation over the Mediterranean area

Tania Marinova, Lilia Bocheva and Vladimir Sharov

*National Institute of Meteorology and Hydrology,
66 Tsarigradsko Chaussee, Sofia 1784, Bulgaria
E-mails: Tania.Marinova@meteo.bg; Lilia.Bocheva@meteo.bg*

(Manuscript received in final form January 14, 2005)

Abstract—Global climate changes affect the atmospheric circulation over the European synoptic region and, in particular, over the Mediterranean. In recent years the activity of cyclogenesis has strongly diminished over the Western Mediterranean and is not typical for the eastern part of the region. The present work is a climatological investigation of synoptic scale Mediterranean cyclones in relation to the number of cyclones originating over the Mediterranean, their paths of movement, and the interannual activity of the Mediterranean center. A study was carried out using surface pressure charts from the Synoptic Archive of the National Institute of Meteorology and Hydrology of Bulgaria for the period 1980–2001. The comparison of the derived results with the results of other authors obtained for previous periods show a well pronounced decrease in the number of Mediterranean cyclones. At the same time, the activity of the Mediterranean center during the course of a year is about two months shorter. After 1990, considerable changes in the regular paths of Mediterranean cyclones were observed.

Key-words: Mediterranean cyclones, cyclonic activity and frequency, paths of movement

1. Introduction

The Mediterranean basin is well known as a favored region for cyclone formation, especially during the cold half of the year, when depressions are more pronounced and deeper, with magnitude of their central pressure often below 1005 hPa. The winter cyclonic activity over the area is related to the appropriate thermal conditions. These conditions are provided by the specific orography – a warm sea surface, surrounding by mountain massifs that stop

cold air advection from Western and Central Europe. At the same time, the tropical Atlantic and African air masses enter the Mediterranean unimpeded. Therefore, an active frontal zone, with large baric and temperature gradients, having seasonal quasi-stationary front characteristics, forms over the Mediterranean.

The Mediterranean cyclones and their formation, frequency, trajectories, and influence on weather and climate over the region, are presented by many authors such as *Martinov* (1967), *Blagoev* (1961), *Stanchev* (1954), *Pisarski* (1955a,b), *Radinovic* (1987), *Reiter* (1975). In their studies, the cyclones are identified and classified on the basis of synoptic charts for specific areas of the Mediterranean region.

Recently *Alpert et al.* (1990), *Trigo et al.* (1999), and *Maheras et al.* (2001) have presented cyclone climatologies based on objective methods for periods of 5, 18, and 40 years, respectively. These studies revealed three major centers of maximum cyclonic frequency: the Gulf of Genoa, Southern Italy, and Cyprus. The cyclones are identified with the aid of an objective method based on grid point values, available every 6 hours, and include all the initial cyclone detections, that is, cyclones developing within the Mediterranean basin plus cyclones entering the domain. *Alpert et al.* (1990) in his work focused on the month to month variations in cyclone tracks over the Mediterranean. *Trigo et al.* (1999) performed objective cyclone detection and tracking analysis in the Mediterranean region using a higher resolution dataset over a period of 18 years. A greater number of trajectories, including those for subsynoptic lows, were analyzed. The results were summarized by submitting the monthly trajectories (for January, April, and August only) to a k-means clustering procedure.

This paper presents a climatological investigation of subjectively selected synoptic scale Mediterranean cyclones using synoptic charts over a 22-year period from 1980 to 2001. A study was carried out comparing the derived results with the results of other authors obtained for previous periods of time. A series of differences were found in relation to the number of the cyclones originating in the Mediterranean, the interannual activity of the Mediterranean center, and the paths of movement of Mediterranean cyclones.

2. Cyclonic activity over the Mediterranean

The present study concerns the region between 30–45°N and 5°W–30°E. Only newly originating cyclones, which had at least one closed isobaric line on the synoptic surface chart (standard analysis with 5 hPa isobars) and a duration of more than 30 hours were considered. On the basis of surface pressure charts

from the Synoptic Archive of the National Institute of Meteorology and Hydrology of Bulgaria, the surface centers of the cyclones originating over the concerned area were plotted on special charts, from the time of the first closed isobar appearance. Furthermore, for every case, the location of the surface center over the area was plotted at 00 UTC. The time of the chart, where closed isobaric lines were observed for the last time, was accepted as the end of the process. All events were plotted on charts for the different years of the period. For the period 1990–1999, the locations of origination and trajectories of the cyclones were plotted for different months of the year, in order to study possible changes of cyclogenetic areas, as well as the paths of movement of the Mediterranean cyclones during the course of the year.

The summarized results for the monthly and annual distribution of cyclones originating over the Mediterranean area during the period 1980–2001 are presented in *Table 1*. It can be seen that cyclone frequency is the strongest in winter from December until March. On average, over the 22 years of consideration, there are cyclones every 16 to 17 days. The cyclonic activity decreases in April, when originated cyclones occur 3 times less frequently than in March. From May to September, cyclogenesis is a rare phenomenon in the region. The number of originated cyclones strongly increases in November – 4 times more than the previous month, while in October there are 30% more than in September. In November, the cyclogenesis over the region reaches its characteristic frequency for the cold part of the year, i.e., in autumn well pronounced transition to the Mediterranean center activation is not observed.

In comparison with similar climatic investigations by different authors for earlier periods – *Martinov* (1967), *Blagoev* (1961), *Stanchev* (1954), *Pisarski* (1955a,b), *Radinovic* (1987), *Reiter* (1975) – our results indicate that the duration of the Mediterranean winter cyclonic center activity within a year is shorter. All the above authors have given October as the beginning of the Mediterranean winter cyclone, while presented results indicate strong activation of cyclogenesis in November. Also, they have concluded that May is the transition month when the seasonal center is reduced, in contrast to our results which show April. During the period of study, there is a two-month decrease in the activity of the Mediterranean winter cyclones. In all studies, the seasonal character of the Mediterranean center activation is mentioned. Cyclogenesis during the cold half of the year (from October to March) occurs 3 times more often than during the warm half of the year (*Pisarski*, 1955b), while in our study it is more than 5 times larger for the entire investigated period.

Most of the authors dealing with climatic characteristics of the Mediterranean area, cyclogenesis conditions, frequency of originating and principal paths of depressions, as well as their influence on some climatic

Table 1. Annual and monthly distribution of the cyclones originating over the Mediterranean area for the period 1980–2001

Year→ Month	Number of cyclones																								
	'80	'81	'82	'83	'84	'85	'86	'87	'88	'89	'90	'91	'92	'93	'94	'95	'96	'97	'98	'99	'00	'01	Sum 1980- 1989	Sum 1990- 1999	Sum 1980- 2001
Jan	5	4	2		2	1	5	1	3	1					4	3	1	1	1	3	1	3	24	13	41
Feb	2	3	2	2	1	2	3	3	2		1	1	1	2	4		3	1	1	1	1	1	20	15	37
Mar	3	2	7	4	2	2	2	5	3	3			2	1		2			2		1		33	7	41
Apr	3					1		1			1		1	1	1		1	1			2	2	5	6	15
May	2	1	1	1								2											5	2	7
Jun		1	1									1											2	1	3
Jul		1		1																			2	0	2
Aug	1			1					1	1													4	0	4
Sep		1			1				1	1						1	1						4	2	6
Oct	1	2		2						1		1						2					6	3	9
Nov	1	2	2	1			1	3	3	2	3	1	1	1	2	3	1	2	2	1			15	17	32
Dec	4	5	1	3		1	2		2	2	3	2	1	1	1	3	2	2	1	2	1	1	20	18	41
General number	22	22	16	15	6	7	14	13	15	11	8	8	6	6	12	12	9	9	7	7	6	7	141	84	238

elements in the adjacent regions and in particular in Bulgaria, work with data for a 9–10 years period. For better comparison of our results with the results of other authors, two 10-year periods were determined: the first from 1980 to 1989, the second from 1990 to 1999. However, it is not possible to use the same investigation methods, as the different authors. Each method is based on a different approach for selecting a region, duration, and type of depressions to study. Most similar to this investigation are the studies of *Blagoev* (1961), *Radinovic* (1987), and to a certain degree *Martinov* (1967, 1983). The last one takes into consideration only well pronounced baric formations which originate or pass over the Balkan Peninsula; information about the duration of each of the processes is not given. In *Table 2* the number of Mediterranean cyclones is presented for the periods 1980–1989 and 1990–1999, in addition to other periods according to *Blagoev* (1961), *Radinovic* (1987), and *Martinov* (1967).

Table 2. Number of Mediterranean cyclones for different periods

Author	Period	Total number of cyclones	Average annual number of cyclones
<i>Blagoev</i> (1961)	1951–1960	295	29
<i>Radinovic</i> (1987)	1951–1960	283	28
<i>Martinov</i> (1967)	1958–1966	165	18
<i>Our team</i>	a. 1980–1989	148	15
	b. 1990–1999	84	8

If one examines the two 10-year periods (*Table 1*) separately, it can be seen that during the period 1980–1989, the cyclogenesis becomes weaker, although, it follows the interannual distribution described in earlier studies of other authors. In the period 1990–1999, a well pronounced decrease in the number of originated cyclones is observed in comparison with the results of the authors given in *Table 2*. In addition, the part of the year with the greatest activity of the Mediterranean center is shorter. For the first period the cyclogenesis over the Mediterranean in the cold half of the year is about 5 times greater than that during the rest of the year. For the second period it is about 7 times greater.

Further presented results concern only the period 1990–1999. During this period, the greatest activity of the Mediterranean center is observed in November, December, January, and February. In March the number of cyclones that originate over the Mediterranean is 2 times less than in February, and almost equals to that in April. In comparison, *Martinov* (1967) and *Pisarski* (1955b) conclude that in March cyclogenesis is more active than in

February. They also describe the almost equal number of originated cyclones in February and April, which only in May decreases approximately 2 times compared to April. During the period 1990–1999, only 7 cyclones originated in March and again, like typical winter months, their cyclogenetic area is in the region of the Gulf of Genoa, the Iberian Peninsula, and the Adriatic Sea. In April, there were 6 cases of cyclones originating mainly in the region of Ligurian and Tyrrhenian Sea around the Islands of Sardinia and Corsica.

It can be summarized that during the period 1990–1999, cyclogenesis over the Mediterranean was located mainly in its central parts, in the area of the Gulf of Genoa, the Ligurian and the Tyrrhenian Sea, the Iberian Peninsula, and in rarer cases, over the Adriatic and Ionian Sea. In view of the changed circulation conditions over the area in January and February, even in the case of the southernmost position of the seasonal quasi-stationary front and the line of negative heat balance, the meridional circulation is predominant. Consequently, the orographic cyclogenesis over the Alps continues to be the dominant cyclogenetic factor in the area. Nevertheless, there are some isolated cases of cyclones originating over the Gulf of Lion and to the east of the Balearic Islands. In January and February intensive cyclonic activity is observed over the southern parts of the Atlantic Ocean. As a result of the more northern position of the active frontal zone, the series of Atlantic cyclones pass to the east through the northern part of the Iberian Peninsula and France (i.e., they propagate and fill in Central Europe). The movement of the frontal zone from its usual position to the north by about 300 km (2–3°) in the spring months leads to a decreasing number of cyclones originating in March and April.

3. Paths of movement of Mediterranean cyclones in the period 1990–1999

The first studies on the trajectories of Mediterranean cyclones were carried out more than hundred years ago in order to explain the weather conditions in different regions of Europe. *Van Bebbber* (1891) presented a scheme in which the main path of the South European cyclones were indicated by the Roman letter V, and the variants of this path were indicated by the Arabic letters Vb, Vc, Vd, Vd₁, Vd₂.

Later, the principal paths of Mediterranean cyclones and their seasonal peculiarities were studied by many authors: *Pisarski* (1955a), *Blagoev* (1961), *Martinov* (1983), *Popova et al.* (1975). More recently, the tracks of surface depressions coming into and passing through the Mediterranean were described objectively by *Alpert et al.* (1990) and *Trigo et al.* (1999), but they only detected trajectories in the corresponding observed region. In almost all of the studies until now, 3 principal paths of movement are mentioned: I. To the

northeast through Croatia and Hungary; II. To the east through the Adriatic Sea and the Balkan Peninsula towards the Black Sea; III. To the east-southeast through the southernmost parts of the Balkan Peninsula towards Asia Minor. A generalized scheme of the principal cyclogenetic areas and of the paths of cyclone movement from west to east or from southwest to northeast is given in Fig. 1.

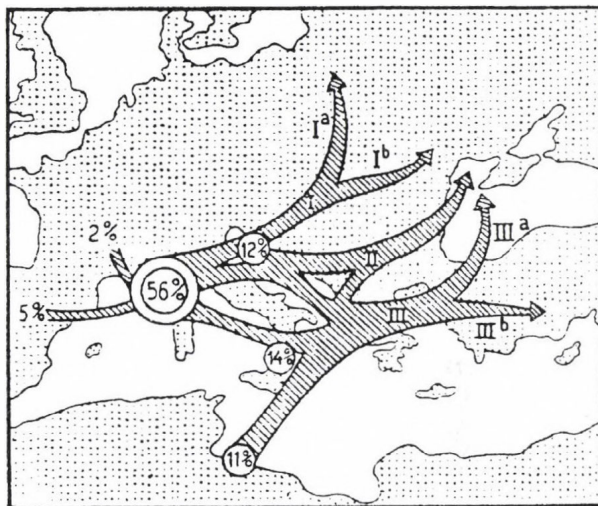


Fig. 1. Areas of generation and paths of movement of Mediterranean cyclones (after Pisarski, 1955a).

The derived results indicate considerable changes in the regular paths of cyclones after the year 1980, especially during the period 1990–1999.

The surface centers of cyclone origin were plotted on special charts for each month of the year, and in every case the cyclone paths were followed for the period 1990–1999.

The results of *Martinov* (1983) are used for comparison, as his work followed a similar approach to determine peculiarities in the paths of movement of Mediterranean cyclones in the different months. For each month, from November to April, the main paths of Mediterranean cyclones were plotted on the same chart after *Martinov* (1983) (solid curves) for the period 1958–1966, as well as our results for the period 1990–1999 (dashed curves).

According to *Martinov* (1983), in November (Fig. 2) activation of cyclogenesis is observed in the area of the Gulf of Genoa and Southern Italy, but only a small number of the cyclones move towards the Balkan Peninsula

and Bulgaria. The cyclones originating in the western parts of the Mediterranean basin are stationary or move eastward to Central Italy and the Adriatic Sea, where they fill. The rest of the cyclones move along the northwestern path to Hungary or eastward across the southernmost regions of the Balkan Peninsula, and from there northeastward to Crimea. In the period 1990–1999, a large part of the cyclones move across the Balkan Peninsula. From the Gulf of Genoa, part of the cyclones move through Northern Italy and the northern part of the Adriatic Sea, further northeastward to Romania and from there, southeastward to the Black Sea, where they fill.

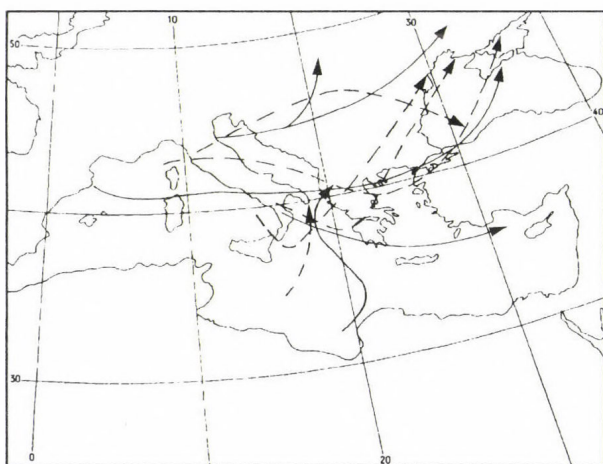


Fig. 2. Paths of movement of Mediterranean cyclones in November for the periods 1958–1966 (solid curves) and 1990–1999 (dashed curves).

Another part of the cyclones originating in the West Mediterranean follow a more southern path through the Apennines, the South Adriatic, and southern parts of the Balkan Peninsula towards Asia Minor and Crimea. A very small portion of the cyclones originating around the Islands of Sardinia, Corsica, and over the Central Mediterranean move through Southern Italy and the Ionian Sea, where they fill. In general, it can be said that about 2/3 of the studied cyclones in November continue their path over the Balkan Peninsula. However, a very small portion of them move across Bulgaria, as most of these cyclones pass south and southeast of the country.

The tendency of cyclones to move mainly along their southernmost paths and eastward across the Balkan Peninsula is retained in December (*Fig. 3*). The characteristic movement of cyclones originating in the West

Mediterranean along the northwestern path through Croatia and Hungary as described by *Martinov* (1983) is not observed. In the present study, a part of the cyclones originating around the Gulf of Genoa and the Island of Corsica move eastward across the North Adriatic and the Balkan Peninsula (and Bulgaria) towards the Black Sea. Another part from Northern Italy and the region of the Tyrrhenian Sea move southeastward over the Ionian Sea, Central Greece, then towards Asia Minor, and from there through the eastern parts of the Black Sea.

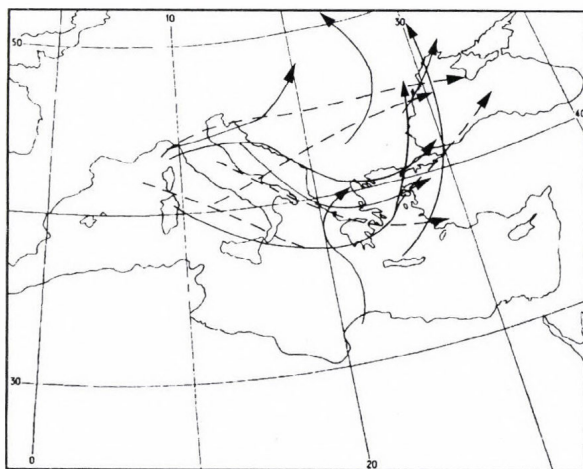


Fig. 3. Paths of movement of Mediterranean cyclones in December for the periods 1958-1966 (solid curves) and 1990-1999 (dashed curves).

Cyclones in January (*Fig. 4*) have the best outline paths resembling those described by *Martinov* (1983). A well defined zone of cyclone movement emerges clearly. The cyclones move from the Northwest Mediterranean and the central parts of the Apennines southeast across Italy, the Ionian Sea, the Island of Crete, and then northeast towards Asia Minor. This principal path of movement of Mediterranean cyclones is joined by additionally generated cyclones over the Ionian Sea.

In February (*Fig. 5*) some changes occur in the paths of Mediterranean cyclones. A significant part of cyclones originate over the central part of the Mediterranean Sea (along the northern coasts of Africa), but not over the Gulf of Genoa and Balearic Islands as in *Martinov* (1983). Initially they move northeastward to Southern Italy, where a small part of them fill. The largest

part, together with the cyclones originating over the Tyrrhenian Sea, move eastward across the Ionian Sea, Southern Greece, and the Island of Cyprus. From there they move eastward or northeastward across the Black Sea to Crimea. Very few cyclones move from the Gulf of Genoa and the Adriatic Sea straight eastward across the Balkan Peninsula and Bulgaria.

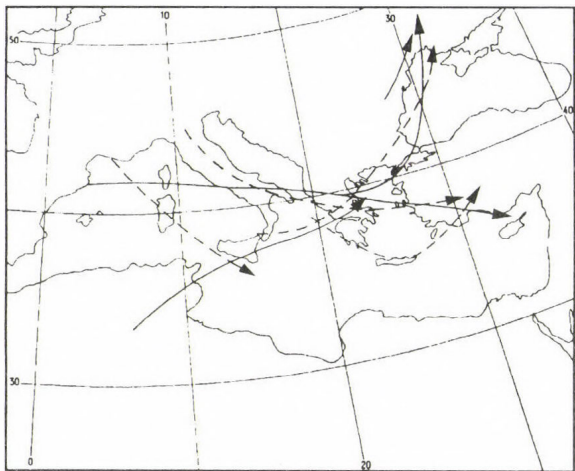


Fig. 4. Paths of movement of Mediterranean cyclones in January for the periods 1958–1966 (solid curves) and 1990–1999 (dashed curves).

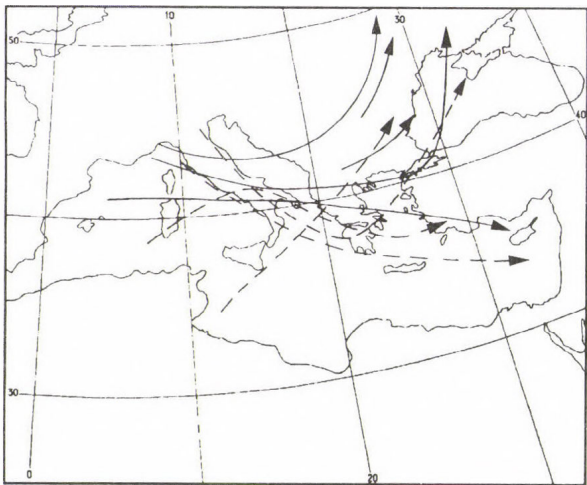


Fig. 5. Paths of movement of Mediterranean cyclones in February for the periods 1958–1966 (solid curves) and 1990–1999 (dashed curves).

In March (*Fig. 6*) there is a decrease in the number of cyclones generated over the Mediterranean and a shift of the cyclogenetic regions to the east over the Apennines, the Adriatic, and the Ionian Sea. All generated cyclones move to the east – northeast either across or south of the Balkans. There are no cyclones passing in a northwestern direction across Croatia and Hungary, and this cyclogenesis is not typical in the West Mediterranean. A portion of the cyclones passing across the southernmost regions of Greece move towards the Island of Cyprus, and others move eastward across Asia Minor. From there they move northeastward across the Black Sea towards Crimea. The trajectory of the cyclones originating along the northern coasts of Africa is orientated to the northeast across the Balkan Peninsula towards Ukraine.

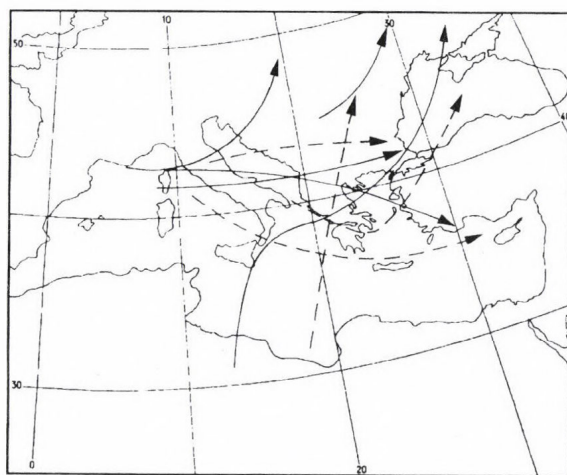


Fig. 6. Paths of movement of Mediterranean cyclones in March for the periods 1958–1966 (solid curves) and 1990–1999 (dashed curves).

Cyclogenesis in April (*Fig. 7*) is very weak and located over the West Mediterranean, in the region of the Balearic Islands, the Island of Sardinia, and the African coast. The trajectories of these cyclones cannot be arranged in groups. A portion of the cyclones moves southeastward and fill in the region of Southern Italy. Others move eastward across the southernmost areas of the Balkan Peninsula towards Asia Minor, where they join cyclones originating near North Africa. Again, there are no cyclones moving along the northwestern path across Croatia and Hungary.

Considering the paths of cyclones originated over the Mediterranean in the period 1990–1999, it can be concluded, that the greatest number of

depressions pass across the southernmost part of the Balkan Peninsula. Their influence on the weather in Turkey and Greece is the most significant. Bulgaria remains mostly in the northern periphery of the cyclonic vortex, and therefore, the meteorological phenomena connected with cyclones are decreased. More considerable changes in temperature, pressure, and especially in precipitation are observed, when the cyclonic vortex moves directly across the Balkans and northeastward across the Black Sea.

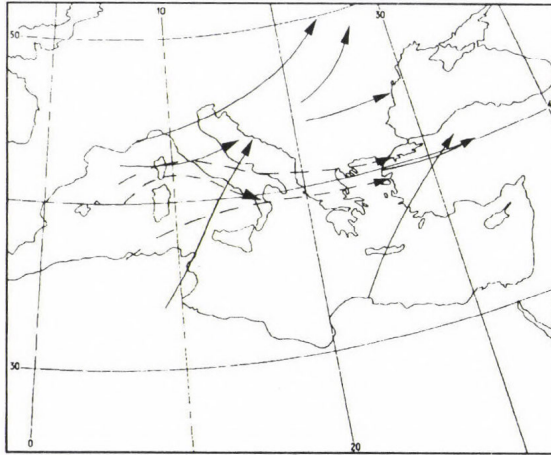


Fig. 7. Paths of movement of Mediterranean cyclones in April for the periods 1958–1966 (solid curves) and 1990–1999 (dashed curves).

4. Conclusions

The results obtained in the present work can be summarized as follows:

- A well pronounced decrease in the number of Mediterranean cyclones is observed during the period 1980–2001. At the same time, the activity of the Mediterranean winter cyclonic center within a year is about two months shorter.
- After 1990, cyclogenesis over the Mediterranean is located mainly in its central parts. Considerable changes of the regular paths of cyclones are observed. The greatest number of Mediterranean cyclones pass across the southernmost part of the Balkan Peninsula. The principal path of movement, to the northeast through Croatia and Hungary, is no longer typical for the Mediterranean cyclones nowadays.

References

- Alpert, P., Neeman, B.U., and Shay-El, Y., 1990: Intermonthly variability of cyclone tracks in Mediterranean. *J. Climate* 3, 1474-1478.
- Blagoev, Ch., 1961: Routes of the Mediterranean Sea cyclones (in Bulgarian). *Hydrol. Meteorol.* 1, 43-51.
- Maheras, P., Flocas, H.A., Patricas, I., and Anagnostopoulou, Chr., 2001: A 40-year objective climatology of surface cyclones in the Mediterranean region: Spatial and temporal distribution. *Int. J. Climatol.* 21, 109-130.
- Martinov, M., 1967: Some peculiarities of cyclogenesis in the region of the Mediterranean Sea and the Balkan Peninsula (in Bulgarian). *Hydrol. Meteorol.* 6, 7-21.
- Martinov, M., 1983: Synoptical and statistical processing of historical data for Mediterranean depressions. *PSMP Report Series*. Short- and medium-range weather prediction research publication series, No. 3, 121-144.
- Pisarski, A., 1955a: The Mediterranean cyclones and their influence on the weather in Bulgaria. Part I (in Bulgarian). *Hydrol. Meteorol.* 5, 33-50.
- Pisarski, A., 1955b: The Mediterranean cyclones and their influence on the weather in Bulgaria. Part II (in Bulgarian). *Hydrol. Meteorol.* 6, 3-15.
- Popova, T., Runcanu, T. Tanczer, T., and Sharov, V., 1975: *Mediterranean Cyclones in the Cloud Field* (in Russian). Gidrometeoizdat, Leningrad, 98p.
- Radinovic, D., 1987: Mediterranean cyclones and their influence on the weather and climate. *PSMP Report Series*, No. 24, 131.
- Reiter, E., 1975: Handbook for Forecasters in the Mediterranean, Environmental Prediction Research Facility. Naval Postgraduate School, Monterey, Californy. *Tech. Paper*, No. 5-75, 344.
- Stanchev, K., 1954: The South cyclones, their moving through the Balkan Peninsula and the weather in Bulgaria determined by them (in Bulgarian). *Hydrol. Meteorol.* 5, 19-39.
- Trigo, I.F., Davies, T.D., and Bigg, G.R., 1999: Objective climatology of cyclones in the Mediterranean region. *J. Climate* 12, 1685-1696.
- Van Bebber, W.J., 1891: Die Zugstrassen der barometrischen Minima nach den Bahnenkarten Deutschen Seewarte für den Zeitraum von 1875-1890. *Meteorol. Z.* 8, 361-366.

BOOK REVIEW

J. M. Pap and P. Fox (eds.): Solar Variability and Its Effects on Climate. Geophysical Monographs 141, American Geophysical Union, 2004, Washington D.C., 366 pages.

This book is a collection of papers dealing with our variable star (the Sun), and the terrestrial atmospheric and climate variations related to the solar changes. The editorial work had been helped by five contributing editors. The total number of papers is 24. The questions that are answered (on the basis of the most recent surface and satellite measurements) are the following:

- What physical processes occur in the various parts of the solar interior and atmosphere and how these processes relate to variations in solar energy flux at time scales ranging from solar evolution to decades and minutes?
- How do changes in the solar energy flux and energetic particle flux influence Earth's atmosphere and this way its climate?

The papers are divided into four sections. The first section (Fundamentals, 6 items) treats the up-to-date knowledge of solar physics and a short overview of the Earth's atmosphere and climate. The next section (Solar Energy Flux Variations, 8 items) describes the variations of total and spectral irradiation of the Sun as well the variations of solar output of energetic particles. Section 3 (Solar Variability and Climate, 9 items) shows the relations between the above mentioned variations and the changes of the climate of our planet. The last section (1 item) looks at the future, basically at the science requirements and the necessary measurements.

The well-written articles in the logically structured book are proposed to those scientists who are interested in understanding and predicting solar changes and their influences on our climate.

G. Major

GUIDE FOR AUTHORS OF *IDŐJÁRÁS*

The purpose of the journal is to publish papers in any field of meteorology and atmosphere related scientific areas. These may be

- research papers on new results of scientific investigations,
- critical review articles summarizing the current state of art of a certain topic,
- short contributions dealing with a particular question.

Some issues contain "News" and "Book review", therefore, such contributions are also welcome. The papers must be in American English and should be checked by a native speaker if necessary.

Authors are requested to send their manuscripts to

Editor-in Chief of IDŐJÁRÁS

P.O. Box 39, H-1675 Budapest, Hungary

in three identical printed copies including all illustrations. Papers will then be reviewed normally by two independent referees, who remain unidentified for the author(s). The Editor-in-Chief will inform the author(s) whether or not the paper is acceptable for publication, and what modifications, if any, are necessary.

Please, follow the order given below when typing manuscripts.

Title part: should consist of the title, the name(s) of the author(s), their affiliation(s) including full postal and E-mail address(es). In case of more than one author, the corresponding author must be identified.

Abstract: should contain the purpose, the applied data and methods as well as the basic conclusion(s) of the paper.

Key-words: must be included (from 5 to 10) to help to classify the topic.

Text: has to be typed in double spacing with wide margins on one side of an A4 size white paper. Use of S.I. units are expected, and the use of negative exponent is preferred to fractional sign. Mathematical formulae are expected to be as simple as possible and numbered in parentheses at the right margin.

All publications cited in the text should be presented in a *list of references*,

arranged in alphabetical order. For an article: name(s) of author(s) in *Italics*, year, title of article, name of journal, volume, number (the latter two in *Italics*) and pages. E.g., *Nathan, K.K.*, 1986: A note on the relationship between photo-synthetically active radiation and cloud amount. *IDőjárás* 90, 10-13. For a book: name(s) of author(s), year, title of the book (all in *Italics* except the year), publisher and place of publication. E.g., *Junge, C. E.*, 1963: *Air Chemistry and Radioactivity*. Academic Press, New York and London. Reference in the text should contain the name(s) of the author(s) in *Italics* and year of publication. E.g., in the case of one author: *Miller* (1989); in the case of two authors: *Gamov* and *Cleveland* (1973); and if there are more than two authors: *Smith et al.* (1990). If the name of the author cannot be fitted into the text: (*Miller*, 1989); etc. When referring papers published in the same year by the same author, letters a, b, c, etc. should follow the year of publication.

Tables should be marked by Arabic numbers and printed in separate sheets with their numbers and legends given below them. Avoid too lengthy or complicated tables, or tables duplicating results given in other form in the manuscript (e.g., graphs).

Figures should also be marked with Arabic numbers and printed in black and white in camera-ready form in separate sheets with their numbers and captions given below them. Good quality laser printings are preferred.

The text should be submitted both in manuscript and in electronic form, the latter on diskette or in E-mail. Use standard 3.5" MS-DOS formatted diskette or CD for this purpose. MS Word format is preferred.

Reprints: authors receive 30 reprints free of charge. Additional reprints may be ordered at the authors' expense when sending back the proofs to the Editorial Office.

More information for authors is available: antal.e@met.hu

Information on the last issues: http://omsz.met.hu/irodalom/firat_ido/ido_hu.html

Published by the Hungarian Meteorological Service

Budapest, Hungary

INDEX: 26 361

HU ISSN 0324-6329

IDŐJÁRÁS

QUARTERLY JOURNAL
OF THE HUNGARIAN METEOROLOGICAL SERVICE

CONTENTS

<i>Ferenc Ács, Gábor Szász and Miklós Drucza: Estimating soil moisture content of a grass-covered surface using an energy balance approach and agroclimatological observations</i>	71
<i>Ervin Zsótér: Downscaling EPS probabilities using SYNOP precipitation data</i>	89
<i>Ferenc Wantuch and Sándor Szonda: General characterization of the lightnings in the Carpatian Basin.....</i>	111
<i>S. M. Robaa: A study of ultraviolet solar radiation at Cairo urban area, Egypt.....</i>	123
<i>Book review</i>	139

http://omsz.met.hu/english/ref/jurido/jurido_en.html

IDŐJÁRÁS

Quarterly Journal of the Hungarian Meteorological Service

Editor-in-Chief
LÁSZLÓ BOZÓ

Executive Editor
MARGIT ANTAL

EDITORIAL BOARD

- | | |
|---|---|
| AMBRÓZY, P. (Budapest, Hungary) | MIKA, J. (Budapest, Hungary) |
| ANTAL, E. (Budapest, Hungary) | MERSICH, I. (Budapest, Hungary) |
| BARTHOLY, J. (Budapest, Hungary) | MÖLLER, D. (Berlin, Germany) |
| BATCHVAROVA, E. (Sofia, Bulgaria) | NEUWIRTH, F. (Vienna, Austria) |
| BRIMBLECOMBE, P. (Norwich, U.K.) | PAP, J.M. (Greenbelt, MD, U.S.A.) |
| CZELNAI, R. (Dörgicse, Hungary) | PINTO, J. (R. Triangle Park, NC, U.S.A.) |
| DÉVÉNYI, D. (Boulder, U.S.A.) | PRÁGER, T. (Budapest, Hungary) |
| DUNKEL, Z. (Budapest, Hungary) | PROBÁLD, F. (Budapest, Hungary) |
| FISHER, B. (Reading, U.K.) | RADNÓTI, G. (Budapest, Hungary) |
| GELEYN, J.-Fr. (Toulouse, France) | ROCHARD, G. (Lannion, France) |
| GERESDI, I. (Pécs, Hungary) | S. BURÁNSZKY, M. (Budapest, Hungary) |
| GÖTZ, G. (Budapest, Hungary) | SZALAI, S. (Budapest, Hungary) |
| HANTEL, M. (Vienna, Austria) | TAR, K. (Debrecen, Hungary) |
| HASZPRA, L. (Budapest, Hungary) | TÁNCZER, T. (Budapest, Hungary) |
| HORÁNYI, A. (Budapest, Hungary) | TOTH, Z. (Camp Springs, U.S.A.) |
| HORVÁTH, Á. (Siófok, Hungary) | VALI, G. (Laramie, WY, U.S.A.) |
| KONDRATYEV, K. Ya. (St. Petersburg, Russia) | VARGA-HASZONITS, Z. (Moson-
magyaróvár, Hungary) |
| MAJOR, G. (Budapest, Hungary) | WEIDINGER, T. (Budapest, Hungary) |
| MÉSZÁROS, E. (Veszprém, Hungary) | |

*Editorial Office: P.O. Box 39, H-1675 Budapest, Hungary or
Gillice tér 39, H-1181 Budapest, Hungary
E-mail: bozo.l@met.hu or antal.e@met.hu
Fax: (36-1) 346-4809*

Subscription by

*mail: IDŐJÁRÁS, P.O. Box 39, H-1675 Budapest, Hungary;
E-mail: bozo.l@met.hu or antal.e@met.hu; Fax: (36-1) 346-4809*

IDŐJÁRÁS

Quarterly Journal of the Hungarian Meteorological Service
Vol. 109, No. 2, April–June 2005, pp. 71–88

Estimating soil moisture content of a grass-covered surface using an energy balance approach and agroclimatological observations

Ferenc Ács^{1*}, Gábor Szász² and Miklós Drucza¹

¹*Eötvös Loránd University, Department of Meteorology,
P.O. Box 32, H-1518 Budapest, Hungary*

²*University of Debrecen, P.O. Box 36, H-4015 Debrecen, Hungary*

(Manuscript received in final form October 19, 2004)

Abstract—Diagnostic applications of the energy balance equation for vegetated surface (VSEBE) are briefly summarized. We tested whether VSEBE can be successfully applied for estimating surface soil moisture content (θ) in the growing season using agroclimatological observations. The analysis is performed using data set of the Agrometeorological Observatory of the University of Debrecen collected in the period 1974–1986.

In the study, the process-based VSEBE model is described in detail. It is shown that VSEBE is not suitable for estimating instantaneous values of θ , since the applicability of the model is fairly limited and the scattering of the estimates is relatively large. It is also shown that monthly mean values of θ can be estimated with acceptable accuracy applying VSEBE for a long time period. The results obtained can be useful for estimating climate characteristics of agrometeorological stations.

Key-words: agrometeorological station, grass-covered surface, energy balance equation, surface soil moisture content, instantaneous value of surface soil moisture content, monthly mean value of surface soil moisture content.

1. Introduction

The energy balance equation above vegetated surface is the basic equation for quantifying energy transfer processes at the land-surface/atmosphere interface. VSEBE can be applied either in prognostic or diagnostic mode. In both applications, the ground surface temperature T_g (for details see Section 3), and

* Corresponding author; E-mail: acs@caesar.elte.hu

the soil surface moisture content θ are intrinsically coupled. In this study, the attention is paid to diagnostic applications. The diagnostic application of VSEBE depends on the availability of T_g and θ (Table 1). When both T_g and θ are available, the Penman-Monteith's equation can be used to calculate the latent heat flux LE . Net radiation R_n can be simply estimated using radiation balance equation RBE; surface soil heat flux G can be parameterized either via R_n or using the force-restore method (Bhumralkar, 1975; Ács *et al.*, 2000), while sensible heat flux H is obtained as residual term of VSEBE (application 1) (Ács *et al.*, 2000). Note that deep soil temperature used in the force-restore method can be expressed via T_g (Ács *et al.*, 1991). If T_g is not directly available, R_n can be given (Holtslag and van Ulden, 1983). When θ is available but T_g is unknown, this is referred to as application 2. In this case, T_g can be simply calculated from VSEBE (van de Griend *et al.*, 1985).

Table 1. The energy balance equation applications

Surface state variables	Applications			
	Parameterization of the fluxes			
	R_n	G	H	LE
Application 1				
Known θ and known T_g	Radiation balance equation	Per cent of R_n	Residual term	Penman-Monteith equation
Application 2				
Known θ and unknown T_g	Radiation balance equation	Fourier equation, Force-restore method	Bulk formula	Bulk formula
Application 3				
Unknown θ and known T_g	Radiation balance equation	Fourier equation, Force-restore method	Bulk formula	Residual term
Application 4				
Unknown θ and known T_g	Radiation balance equation	Fourier equation, Force-restore method	Bulk formula	Bulk formula

Many times θ is unknown and T_g is known. Then H can be calculated on the basis of bulk formula (see Eq. (A.1)), R_n is estimated by RBE, G can be parameterized either by Fourier or force-restore method, and latent heat flux is obtained as a residual term of VSEBE (Szabó *et al.*, 1989; Dunkel *et al.*, 1989; Kustas *et al.*, 1989). In Table 1, this is referred to as application 3. In this case, two approaches can be used for estimating sensible heat flux (Friedl, 2002): the single-source or one-layer models (Inoue *et al.*, 1990) and the dual-source or two-layer models (Kustas *et al.*, 1996). In the first ones, there is no distinction between the surface temperature of vegetation canopy and soil surface. In two-layer models, radiation and energy balance of vegetation and soil surface is separately treated. These models are more detailed and physically based than the single-layer ones. In both models the bluff body

effect expressed in the form of excess resistance (often noted by kB^{-1} parameter) has to be implemented to parameterize the aerodynamic resistances for heat transfers. In the application 3, surface moisture status can be deduced either from soil water potential (Soer, 1980) or from canopy resistance (Inoue *et al.*, 1990). When θ is unknown and T_g is known, LE can also be estimated using bulk formulae. This is referred to as the application 4 in *Table 1*. The surface moisture status is mostly inferred from vegetation canopy resistance (Shuttleworth and Gurney, 1990). As in the former case, both single-source (Ács, 2003) and dual-source (Taconet *et al.*, 1986) models can be used.

All of these applications have been made by data obtained from carefully designed field experiments. In situ measurements are usually extended by means of remote sensing techniques. This combination of techniques is common in organizing large scale experiments in scope of World Climate Research Programme (WCRP) and Global Energy and Water Cycle Experiment (GEWEX). On the other hand, there are also measurements of standard climatological or agrometeorological stations. The question arises, whether characteristics of near-surface exchange processes can also be deduced with the aid of VSEBE using climatological or agrometeorological observations. Reasons for applying VSEBE using agrometeorological observations are as follows:

- Atmospheric forcing variables (ground temperature or near-surface air temperature, air temperature, air humidity, and wind speed at reference level) and soil/vegetation parameters are available at 00, 06, 12 and 18 UTC or even more frequently. Soil moisture content measurements in the growing season were also available at agrometeorological stations. These data can be used for both running and validating VSEBE.
- In principle, θ , H and LE can also be estimated by VSEBE which are not 'standard' climatological elements but their knowledge give a new insight into near-surface climate characteristics.

On the basis of all these, the aim of this study is to check whether VSEBE can be successfully applied for estimating surface soil moisture content θ in the growing season using agroclimatological observations. The analysis is performed using data of the Agrometeorological Observatory of the University of Debrecen (Hungary). The application 4 of VSEBE is used to compare estimated θ_{est} and measured θ_{mea} surface soil moisture content. The applicability of the method and the results are analyzed from both meteorological and climatological point of view. In the study, we assumed that there are no advective effects or mesoscale circulation patterns induced by surface discontinuities (Hupfer and Rabe, 1994). Then the atmosphere can be assumed to be horizontally homogeneous with constant meteorological boundary conditions above a certain height (Shuttleworth, 1988).

2. Measurement site and data

The dataset used was measured at the Agrometeorological Observatory of the University of Debrecen. The measurement site is located at the eastern part of Hungary at Hajdúhát (47°37'N; 21°36'E, 112 m asl). The climate is temperate rain climate with continental features. The annual mean temperature is 10.0 °C, while mean annual precipitation sum is 585 mm. The water table is at a depth of 10 m. The soil type is lime covered black loam (chernozem). Basic soil physical properties are presented in Table 2. The vegetation is short-cut natural grass.

Table 2. Soil physical properties of the 0–25 cm layer
at the Agrometeorological Observatory of the University of Debrecen

Properties	Values
Sand fraction	37 %
Silt fraction	39 %
Clay fraction	24 %
Bulk density	1400 kg m ⁻³
Specific heat capacity	840 J kg ⁻¹ K ⁻¹
Organic matter	2.8 %
Thermal diffusivity	2.09×10 ⁻⁷ m ² s ⁻¹
Soil moisture content at saturation (θ_s)	0.47 m ³ m ⁻³
Field capacity soil moisture content (θ_f)	0.36 m ³ m ⁻³
Wilting point soil moisture content (θ_w)	0.15 m ³ m ⁻³

The dataset used refers to the time period 1974–1986. Atmospheric forcing variables (air temperature, humidity, wind speed, wind direction, cloud fraction) and soil temperature were measured at 00, 06, 12, and 18 UTC. The reference level for air temperature and humidity is 2 m, while for wind speed it is 10 m. Soil temperature is measured at depths of 0.02 m, 0.05 m, 0.1 m, 0.2 m, 0.5 m, and 1.0 m. Both air and soil temperatures are observed by platinum resistance thermometers by accuracy of 0.2 °C. Air humidity is measured by psychrometer using platinum resistance thermometers. Precipitation is measured twice a day, at 06 and 18 UTC. Soil moisture content is measured roughly once a week using gravimetric method. The soil samples are taken from three locations being a few meters far from each other. Samples refer to layers of 10 cm thickness, except the first layer, up to a depth of 1 m. From the surface layer, the samples are taken from 0–5 cm and 5–10 cm layers.

3. Model

The VSEBE model represents a mix of vegetated and bare soil surfaces (Fig. 1). It is assumed that vegetation surface is always dry, that is, there is no intercepted water on the vegetation surface. Relative cover of vegetation is cov , while of bare soil is $1-cov$. In VSEBE, there is no difference between vegetation and bare soil surface temperature. Because of the simplicity, the bulk temperature of soil surface layer/vegetation system is modeled. This temperature is called *ground temperature* (T_g).

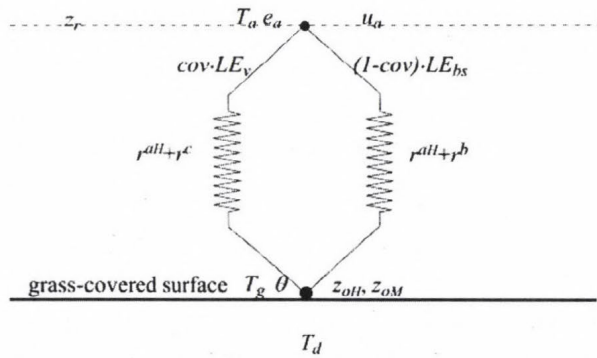


Fig. 1. Surface resistances in the VSEBE model. Symbols: z_r =reference height, T_a =air temperature at z_r , e_a =vapor pressure at z_r , u_a =wind speed at z_r , cov =fractional vegetation cover, LE_v =latent heat flux from vegetation, LE_b =latent heat flux from bare soil, r^aH =aerodynamic resistance for heat, r^c =vegetation canopy resistance, r^b =soil surface resistance, T_g =ground surface temperature, θ =surface soil moisture content, T_d =deep soil temperature, z_{0H} =roughness length for heat, and z_{0M} =roughness length for momentum.

We also assumed that the soil temperature at 10 cm depth and the soil surface moisture content of vegetated and bare soil surface fractions do not differ. Roughness length is treated as a single effective (Taylor, 1995) surface parameter valid for the soil-vegetation system, because the characteristic length scale of bare soil fractions is relatively small to vegetation height (Blümel, 1999). Surface temperature is also treated as a single effective quantity, since for sparse canopy both the vegetated and bare soil fractions are active at the surface/atmosphere interface. Based on these assumptions, the aerodynamic resistance is calculated for the soil-vegetation system. The surface resistances of vegetation and soil are calculated separately.

The core of the model is the surface energy balance equation:

$$R_n[T_g(\theta)] - G[T_g(\theta)] - L \cdot E[T_g(\theta)] - H[T_g(\theta)] = F[T_g(\theta)] = 0. \quad (1)$$

Note that all terms depend via T_g upon θ . This θ -dependence is important feature of VSEBE. It can be used for determining θ when T_g is mostly governed by evapotranspiration, for instance in strong unstable conditions. The model uses atmospheric boundary conditions, soil temperatures, and soil parameters (e.g., roughness length, soil texture or soil hydraulic parameters) as input. The outputs are the estimated turbulent fluxes and surface soil moisture content θ_{est} . Net shortwave radiation is estimated parameterizing global radiation and prescribing albedo of vegetated and bare soil surfaces. Global radiation is parameterized on the base of Kasten's formula after *Holtslag and van Ulden* (1983) as well as *Mészáros* (2002). Atmospheric emissivity is parameterized after *Brunt* (1932), while emissivity of the surface is taken to be 1 because of the simplicity. The turbulent heat fluxes are parameterized by bulk formulae. The surface and aerodynamic transfers are simulated by using resistance representation. The vegetation surface resistance is parameterized by *Jarvis* (1976) formula. The moisture availability function F_{ma} is expressed via soil moisture content θ using Theta-parameterization (*Ács*, 2003). The bare soil surface resistance is estimated after *Dolman's* (1993) empirical formula. The aerodynamic transport is simulated by Monin-Obukhov's similarity theory taking into account the atmospheric stability (*Ács and Kovács*, 2001). The thermal conductivity is simulated by using $\lambda(\theta)=k C(\theta)$ formula (k is the thermal diffusivity, C is the volumetric heat capacity). The thermal diffusivity is estimated on the base of measurement results of *Szász* (1964). Soil physical and hydraulic properties are presented in Table 2. The most important parameterizations are given in the Appendix.

As already mentioned, the model is applied only in unstable conditions. The calculation algorithm is schematically presented in Fig. 2. T_g is governed to a great extent by $LE(\theta)$ via $r^c(\theta)$, and/or $r^b(\theta)$, and $r^a(T_g-T_a)$. T_g is calculated for each $0 < \theta < \theta_s$ in steps of $\Delta\theta=0.01 \text{ m}^3 \text{ m}^{-3}$. For a given θ value, the computation always starts from neutral stratification with $T_g=T_a$. The new estimate of T_g is obtained calculating r^{aH} and solving the energy balance equation. This estimate of T_g is used again to improve the estimate of r^{aH} , and so on. In general no more than 5–10 iterations are needed to achieve the convergence in successive values of T_g . The surface soil moisture content θ_{est} is obtained simply by

$$\theta = \theta_{est} \quad \text{for} \quad T(\theta) = T_{mea}, \quad (2)$$

where T_{mea} represents a 'measured ground temperature' obtained by extrapolating measured soil temperatures at 2 and 5 cm depths. θ_{est} refers to the depth of root-zone of grass-covered surface, that is to about 0–20 cm soil surface layer.

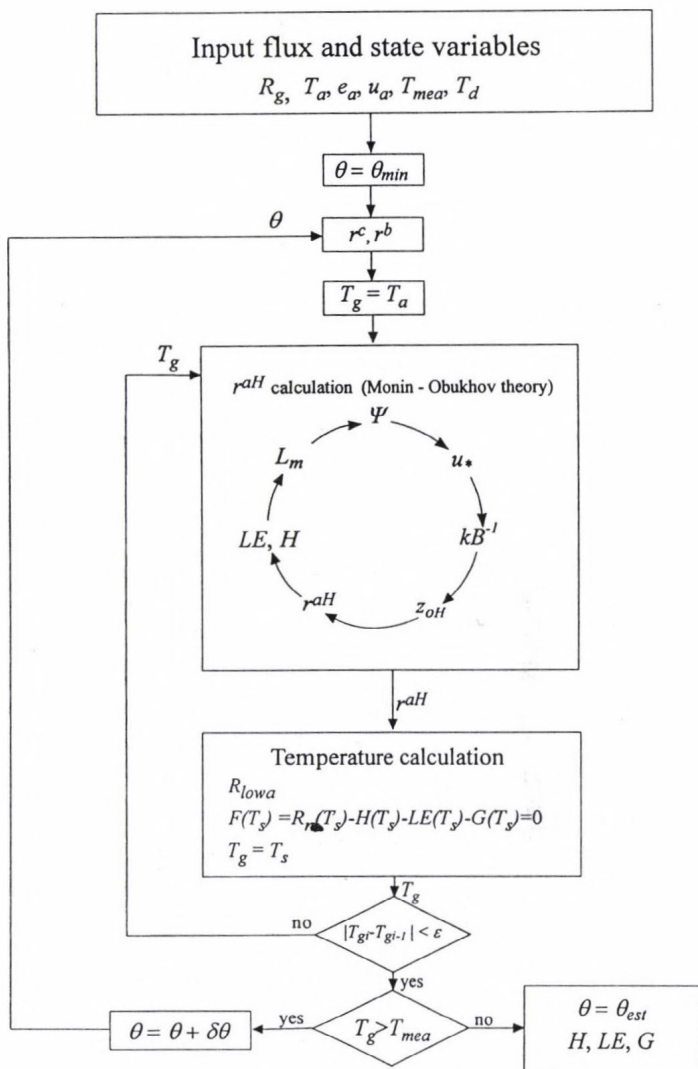


Fig. 2. Flow chart of calculation in the VSEBE model in one time step. Symbols: R_g =global radiation, T_a =air temperature, e_a =water vapor pressure, u_a =wind speed, T_{mea} =ground surface temperature extrapolated by measured soil temperatures at 2 and 5 cm depths, T_d =measured soil temperature at 10 cm depth, r^c =vegetation canopy resistance, r^b =bare soil surface resistance, r^{aH} =aerodynamic resistance for heat transport, ψ =stability function, u_* =friction velocity, $kB^{-1} = \ln(z_{0M}/z_{0H})$, z_{0M} =roughness length for momentum, z_{0H} =roughness length for heat, LE =latent heat flux, H =sensible heat flux, L_m =Monin-Obukhov length, R_{lowa} =long wave radiation from the atmosphere, T_s =surface temperature, ϵ =arbitrarily chosen small number, $\Delta\theta$ =increment of θ , θ_{est} = estimated θ , and G = soil heat flux at the surface.

4. Results

Results are discussed analyzing the applicability of the method, and the goodness of results comparing the estimates (θ_{est}) and measurements (θ_{mea}). The discussion of instantaneous and monthly mean values is separately performed.

4.1 Applicability of the method

Successful application of the method is limited by the meteorological conditions. As briefly discussed in a former study of Drucza and Ács (2004), the method is mainly applicable for clear-sky (0/8 or 1/8 cloud fraction) and strongly unstable conditions, when soil moisture content θ is less than field capacity θ_f and greater than wilting point θ_w . Consequently, in this study θ -estimates refer only to 12 UTC. The θ -estimates are analyzed with more attention inspecting the relationship between $\delta\theta = (\theta_{est} - \theta_{mea})/\theta_{mea}$, global radiation R_g , and the θ_{mea} . The scatter of these points is presented in Fig. 3.

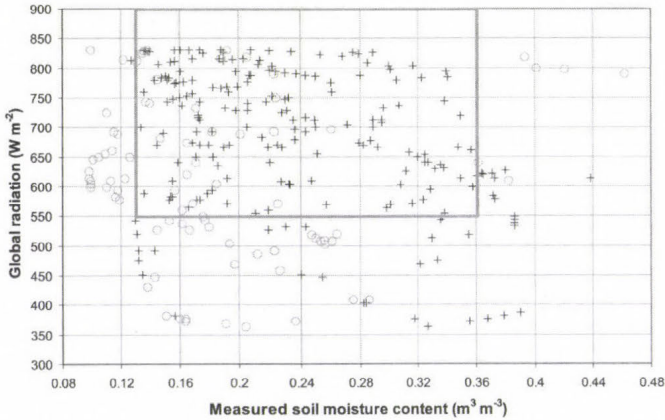


Fig. 3. Applicability of VSEBE for estimating θ as function of measured θ and global radiation. For applicable cases signed by +, $|\theta_{est} - \theta_{mea}| < 30\%$. O indicates not applicable cases. The limits of applicability ($R_g > 550 \text{ W m}^{-2}$ and $0.13 \text{ m}^3 \text{ m}^{-3} < \theta_{mea} < 0.36 \text{ m}^3 \text{ m}^{-3}$) are indicated by a grey rectangle.

A brief statistics referring to the scattering of these points is given in Table 3. Black + signs represent applicable, while grey o signs refer to not-applicable cases. In the analysis, those cases are treated as applicable when $\delta\theta < 30\%$. This criterion is subjectively chosen. Inspecting Fig. 3, it is obvious that applicable and not-applicable cases cannot be clearly separated. Nevertheless, most of the applicable cases lie in θ -region between θ_f ($0.36 \text{ m}^3 \text{ m}^{-3}$) and θ_w ($0.13 \text{ m}^3 \text{ m}^{-3}$) when R_g is strong (above 550 W m^{-2}). This region is indicated by a grey rectangle in Fig. 3. The method is not-applicable for extreme dry

and wet conditions, since then the sensitivity of transpiration to soil moisture content is too small. Note that parameterization of R_g refers to clear-sky conditions. R_g is greater than 550 W m^{-2} at 12 UTC from March 11 to September 24.

Table 3. Statistical survey of the applicability of VSEBE, at the Agrometeorological Observatory of the University of Debrecen, in the period 1974–1986

Conditions/cases	Applicable cases $\delta\theta < 30\%$	Not-applicable cases $\delta\theta > 30\%$	Total
$0.13 \text{ m}^3 \text{ m}^{-3} < \theta_{mea} < 0.36 \text{ m}^3 \text{ m}^{-3}$ and $R_g > 550 \text{ W m}^{-2}$	167	25	192
$0.13 \text{ m}^3 \text{ m}^{-3} > \theta_{mea}$ or $\theta_{mea} > 0.36 \text{ m}^3 \text{ m}^{-3}$ or $R_g < 550 \text{ W m}^{-2}$	40	57	97
Total	207	82	289

4.2 Instantaneous values

The relationship between the estimated θ_{est} and measured θ_{mea} surface soil moisture content is presented in Fig. 4. The scattering of points is obvious, but the correlation coefficient is still acceptable. There are many causes for scattering. They are caused by inadequacies in measurements and theory. Concerning the measurements, following facts have to be mentioned: (a) forcing variables are represented by instantaneous values, (b) θ_{est} refers to 12 UTC, while θ_{mea} is usually determined during the morning, (c) among θ_{mea} values there are also interpolated ones, because θ_{mea} is usually measured in 7–10 days intervals, and (d) the spatial variability of θ_{mea} can be significant. The methodological shortcoming can be deduced comparing Figs. 5, 6, and 7. Figs. 5 and 6 represent the sensible and latent heat fluxes, respectively, referring to θ_{est} and θ_{mea} . Note, that the agreement between H_{est} and H_{mea} is somewhat better ($R^2=0.71$) than that between LE_{est} and LE_{mea} ($R^2=0.56$). Fig. 7 represents surface temperatures referring to θ_{est} and θ_{mea} . It is to be noted, that the agreement between T_{est} and T_{mea} is very good ($R^2=0.90$). Inspecting either the LE and T (Figs. 6 and 7) or H and T (Figs. 5 and 7) plots, it is obvious that scattering of T is much smaller than scattering of LE or H ; that is for an acceptable T -agreement there is a weaker LE - or H -agreement. The scatter of LE and H is determined by scatter of θ . Scattering of θ is determined by slope $S = \delta T(\theta) / \delta \theta$ in the transition region between θ_f and θ_w . S is the measure of nonlinear relationship between T and θ . The smaller the slope of $T(\theta)$ curve is, the greater the scattering of θ will be. This physically determined feature of $T(\theta)$ curve basically limits the accuracy of simulations.

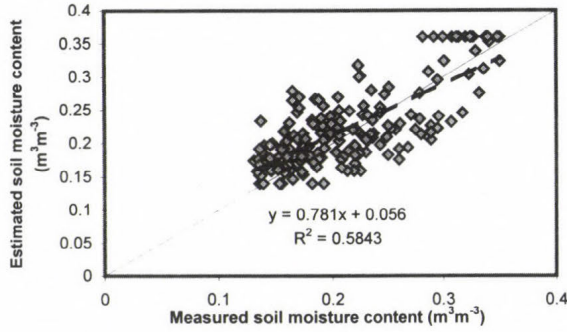


Fig. 4. Estimated versus measured soil moisture content in the surface 0-20 cm layer for the applicable cases (the estimates are obtained at 12 UTC for 0/8 and 1/8 cloud fraction, $R_g > 550 \text{ W m}^{-2}$, and $0.13 \text{ m}^3 \text{m}^{-3} < \theta_{mea} < 0.36 \text{ m}^3 \text{m}^{-3}$), in the 1974–1986 period. The regression line fitted is also indicated.

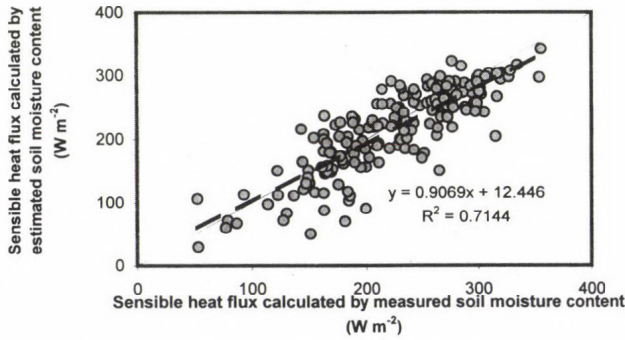


Fig. 5. Sensible heat flux calculated by θ_{est} versus sensible heat flux calculated by θ_{mea} in the 1974–1986 period.

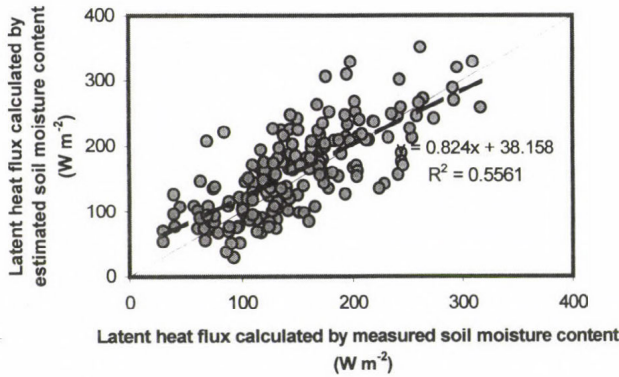


Fig. 6. Latent heat flux calculated by θ_{est} versus latent heat flux calculated by θ_{mea} in the 1974–1986 period.

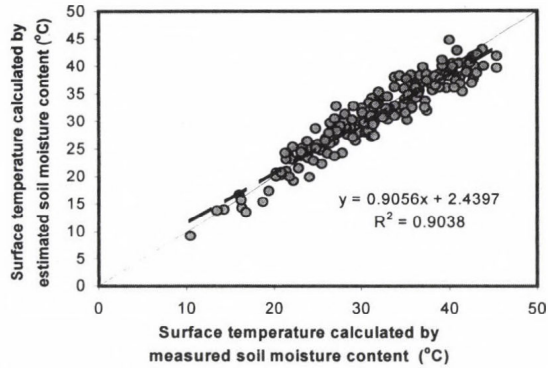


Fig. 7. Surface temperature calculated by θ_{est} versus surface temperature calculated by θ_{mea} in the 1974–1986 period.

Yearly course of θ_{est} and θ_{mea} values in 1976 is presented in Fig. 8. The main tendencies of θ_{mea} changes are captured, but there are also obvious discrepancies between θ_{est} and θ_{mea} . The tendency of θ_{mea} changes from March to May is unequivocally reproduced. The local maximum of θ_{mea} in June is also reproduced as well as its continuous decreasing up to August. The greatest discrepancies amount to in average $0.05 \text{ m}^3 \text{ m}^{-3}$ and usually appear in extreme moist (in vicinity of θ_f) and dry (in vicinity of θ_w) conditions, when the applicability and thus the accuracy of the method is limited.

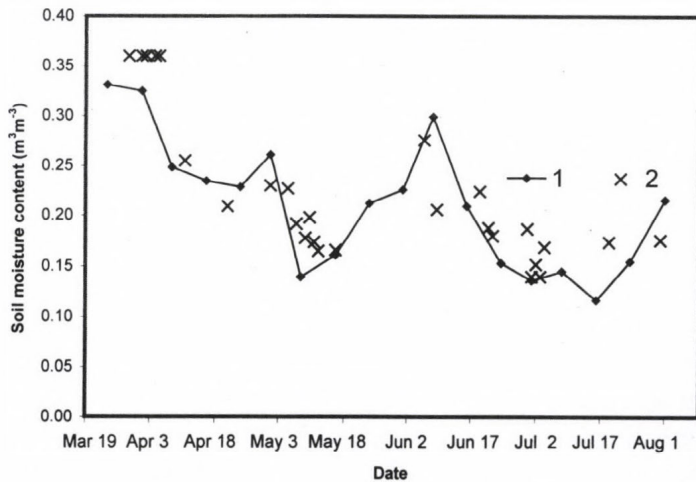


Fig. 8. Annual change of θ_{est} and θ_{mea} in the growing season of 1976. Symbols: (1) measured θ in 0–20 cm layer, (2) estimated θ .

4.3 Monthly mean values

From instantaneous θ_{est} and θ_{mea} values, their 12 years monthly mean values are calculated from March to September. 12 years monthly mean values of θ_{mea} are calculated in two ways: For the chosen month, θ_{mea}^{sel} monthly mean value is obtained from those θ_{mea} values, when the method was applicable. In spite of this, θ_{mea}^{all} monthly mean value is obtained using all θ_{mea} values, irrespective of that the method was applicable or not. The relationship between 12 years monthly means of θ_{est} and θ_{mea}^{sel} is presented in Fig. 9a. The agreement is excellent, namely the slope of the straight line obtained ($\theta_{est}=0.95 \theta_{mea}^{sel}+0.017$) is 0.95. In March, θ is about $0.30 \text{ m}^3 \text{ m}^{-3}$. In April, θ is somewhat smaller than in March, it amounts to about $0.25 \text{ m}^3 \text{ m}^{-3}$. In May, θ is about $0.20 \text{ m}^3 \text{ m}^{-3}$. Note, that θ values in June, July, August, and September are located close to each other and they are not significantly different from θ values obtained in May.

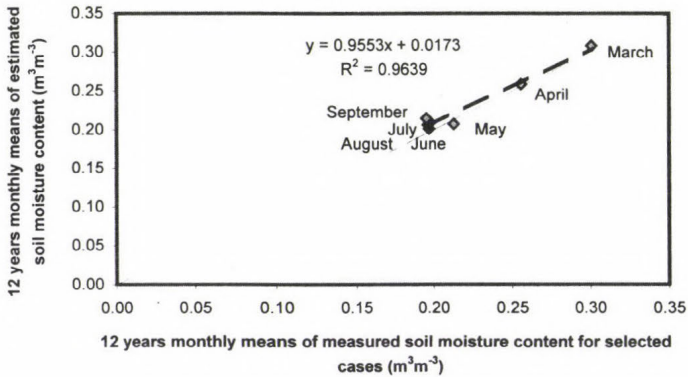


Fig. 9a. 12 years monthly means of θ_{est} versus 12 years monthly means of θ_{mea}^{sel} .
For the chosen month, θ_{mea}^{sel} represents the average of those θ_{mea} ,
when the method was applicable.

The relationship between 12 years monthly means of θ_{est} and θ_{mea}^{all} is presented in Fig. 9b. The agreement between θ_{est} and θ_{mea}^{all} is acceptable. The slope of straight line obtained ($\theta_{est}=0.71 \theta_{mea}^{all}+0.048$) is 0.71, that is θ_{est} values are somewhat underestimated with respect to θ_{mea}^{all} values. The points show greater scattering than in the former case, but the strength of the relationship is still acceptable ($R^2=0.73$). θ is the greatest (about $0.30\text{--}0.33 \text{ m}^3 \text{ m}^{-3}$) in March decreasing in spring (April: about $0.25\text{--}0.30 \text{ m}^3 \text{ m}^{-3}$, May: about $0.20\text{--}0.27 \text{ m}^3 \text{ m}^{-3}$, and June: about $0.19\text{--}0.25 \text{ m}^3 \text{ m}^{-3}$). In July, θ is about $0.20\text{--}0.23 \text{ m}^3 \text{ m}^{-3}$. The smallest values appear in August and September, they amount to about $0.20 \text{ m}^3 \text{ m}^{-3}$ in accordance with expectations.

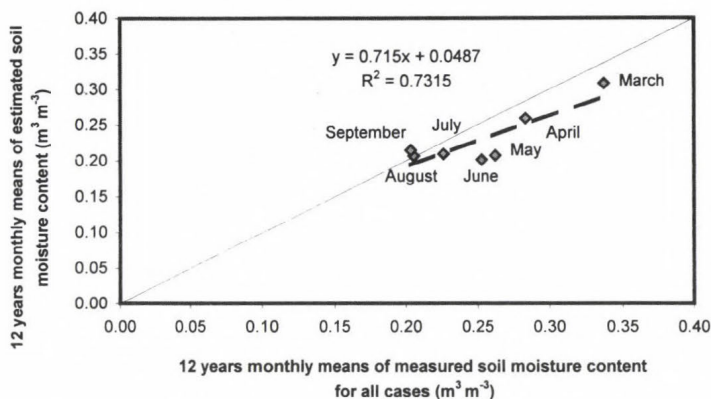


Fig. 9b. 12 years monthly means of θ_{est} versus 12 years monthly means of θ_{mea}^{all} . For the chosen month, θ_{mea}^{all} represents the average of all θ_{mea} , irrespective of that the method was applicable or not.

5. Conclusions

A diagnostic application of VSEBE for estimating surface soil moisture content θ is presented. We tested whether VSEBE can be successfully applied using agroclimatological observations. The analysis is performed using data of the Agrometeorological Observatory of the University of Debrecen collected in the period 1974–1986. The main findings are as follows:

- The applicability of VSEBE is determined by both the atmospheric stability and surface wetness state. The method is mainly applicable for clear-sky (0/8 or 1/8 cloud fraction) and strongly unstable conditions, when θ_{mea} is between θ_f and θ_w .
- The agreement between instantaneous values of θ_{est} and θ_{mea} is acceptable even if the scattering of points is relatively large. In spite of the scattering of instantaneous values, the 12 years monthly mean values of θ_{est} and θ_{mea} agree well. Note, that the agreement between θ_{est} and θ_{mea}^{sel} is excellent, while the agreement between θ_{est} and θ_{mea}^{all} is weaker. In this latter case, θ_{est} is somewhat underestimated with respect to θ_{mea}^{all} .

The results suggest that VSEBE cannot be successfully applied for estimating instantaneous θ values using agroclimatological observations. The successful applications are strongly limited and the scattering of the estimates is relatively large. Nevertheless, it is possible to estimate monthly mean values of θ with acceptable accuracy applying VSEBE in a long time period and grouping θ values according to months, as it is done in this study. That is, VSEBE can be

applied for climatological estimates using agroclimatological observations. The procedure is quite extensive, but in this way the non-linear effects are taken into account. In this case, it is strongly recommended to compare measurements and estimates, that is, to validate the model. Accordingly, VSEBE cannot be used for inferring monthly mean θ fields in Hungary, since there are only a few stations (for instance Keszthely, Kecskemét-Katonatelep, Karcag, and Debrecen-Pallag) possessing long time θ series (Erdős és Morvay, 1961). If we want to avoid the enormous data processing, that is the scaling up of outputs in time and space, the production of monthly mean θ fields has to be done on daily or monthly time scale using relevant variables. In most cases these are monthly values of precipitation and temperature, as it is done for instance by *Thornthwaite* (1948).

Aknowledgements—This study is financially supported by both the OTKA Foundation, project number T043695 and PhD School Foundation.

APPENDIX

Parameterizations used in VSEBE

Turbulent heat fluxes:

$$H = \rho \cdot c_p \cdot \frac{T_g - T_a}{r^{aH}}, \quad (\text{A.1})$$

$$LE = \frac{\rho \cdot c_p}{\gamma} \cdot \frac{e_s(T_g) - e_a}{r^{aH} + r^s}, \quad (\text{A.2})$$

ρ [kg m⁻³] is the air density, c_p [J kg⁻¹ K⁻¹] is the specific heat capacity of air at constant pressure, T_g [°C] is the ground surface temperature, T_a [°C] is the air temperature at 2 m height, r^{aH} [s m⁻¹] is the aerodynamic resistance for heat, γ [hPa K⁻¹] is the psychrometric constant, $e_s(T_g)$ [hPa] is the saturation vapor pressure at T_g , e_a [hPa] is the vapor pressure at 2 m height, r^s [s m⁻¹] indicates the surface resistance of bare soil (r^b) or vegetation canopy (r^c). The fluxes are positive upwards and negative downwards.

Ground heat flux:

Ground heat flux is approached by Fourier equation:

$$G = \lambda \frac{T_{s5} - T_{s10}}{z_5 - z_{10}}, \quad (\text{A.3})$$

where λ [$\text{W m}^{-1} \text{K}^{-1}$] is the thermal conductivity, $z_5=5$ cm, $z_{10}=10$ cm, T_{s5} [$^{\circ}\text{C}$] is the soil temperature at z_5 , and T_{s10} [$^{\circ}\text{C}$] is the soil temperature at z_{10} . The soil heat flux is positive downwards and negative upwards.

Roughness length for momentum and zero plane displacement height:

The roughness length for momentum transfer (z_{0M} [m]) and zero plane displacement height (d [m]) is expressed as the function of vegetation height (vegH [m]) after *Brutsaert* (1982):

$$z_{0M} = 0.136 \cdot \text{vegH}, \quad (\text{A.4})$$

$$d = 0.667 \cdot \text{vegH}. \quad (\text{A.5})$$

Roughness length for heat and/or vapor transfer:

Roughness length for heat and/or vapor transfer (z_{0H} [m]) is parameterized after *Kustas et al.* (1989):

$$kB^{-1} = \ln \frac{z_{0M}}{z_{0H}}, \quad (\text{A.6})$$

$$kB^{-1} = 0.17u_a(T_g - T_a), \quad (\text{A.7})$$

where u_a [m s^{-1}] is the wind speed and T_a [$^{\circ}\text{C}$] is the air temperature at reference height, T_g [$^{\circ}\text{C}$] is the ground surface temperature.

Surface resistances:

Vegetation canopy resistance is parameterized after *Jarvis'* (1976):

$$r^c = \frac{r_{stmin} \cdot F_{ad}}{LAI \cdot GLF \cdot F_{ma}}, \quad (\text{A.8})$$

where r_{stmin} [s m^{-1}] is the minimum stomatal resistance, LAI is the leaf area index, GLF is the green leaf fraction; it expresses the fraction of live leaves ranging between 0 and 1, F_{ad} and F_{ma} represent the atmospheric demand and soil moisture availability effect on stomatal functioning, respectively, ranging between 0 and 1.

F_{ma} is parameterized via volumetric soil moisture content (θ , [$\text{m}^3 \text{m}^{-3}$]), field capacity (θ_f [$\text{m}^3 \text{m}^{-3}$]), and wilting point θ_w [$\text{m}^3 \text{m}^{-3}$]:

$$F_{ma} = \min \left(\frac{\theta - \theta_w}{\theta_f - \theta_w}, 1 \right). \quad (\text{A.9})$$

The soil surface resistance [s m^{-1}] is parameterized after *Dolman* (1993):

$$r^b = 3.5 \cdot \theta^{-2.3}. \quad (\text{A.10})$$

List of Symbols

C	volumetric heat capacity of soil
cov	vegetated fraction of surface
c_p	specific heat capacity of air at constant pressure
d	zero plane displacement height
e_a	vapor pressure at reference height
$e_s(T_g)$	saturation vapor pressure at T_g ,
F_{ad}	atmospheric demand function
F_{ma}	moisture availability function
G	soil heat flux at the surface
GLF	green leaf fraction
H	sensible heat flux
H_{est}	estimated sensible heat flux
H_{mea}	measured sensible heat flux
k	soil thermal diffusivity
kB^{-1}	excess resistance term for heat transfer
LAI	leaf area index
LE	latent heat flux
LE_{est}	estimated latent heat flux
LE_{mea}	measured latent heat flux
r^a	aerodynamic resistance
r^{aH}	aerodynamic resistance for heat
r^b	surface resistance of bare soil
RBE	radiation balance equation
r^c	surface resistance of vegetation canopy
R_n	net radiation
r^s	surface resistance of bare soil (r^b) or vegetation canopy (r^c).
r_{smin}	minimum stomatal resistance
S	slope of the $T(\theta)$ curve
T_a	air temperature at reference level
T_g	ground surface temperature
T_{mea}	measured ground temperature obtained by extrapolating measured soil temperatures at 2 and 5 cm depths
u_a	wind speed at reference height
$vegH$	vegetation height ($vegH$ [m])
$VSEBE$	energy balance equation for vegetated surface
z_{0M}	roughness length for momentum transfer
γ	psychrometric constant
δ	difference between measured and estimated surface soil moisture content

θ_{est}	estimated soil moisture content
θ_f	soil moisture content at field capacity
θ_{mea}	measured soil moisture content at 0–20 cm layer
θ_{mea}^{all}	monthly mean value of all θ_{mea}
θ_{mea}^{sel}	monthly mean value of selected θ_{mea} (averaging θ_{mea} when θ_{est} is available)
θ_w	soil moisture content at wilting point
λ	soil thermal conductivity
ρ	air density

References

- Ács, F., Mihailovic, D.T., and Rajkovic, B. 1991: A Coupled Soil Moisture and Surface Temperature Prediction Model. *J. Appl. Meteorol.* 30, 812–822.
- Ács, F., Hantel, M., and Unegg, J.W., 2000: Climate Diagnostics with the Budapest-Vienna Land-Surface Model SURFMOD. *Austrian Contribution to the IGBP. Vol. 3, National Committee for the IGBP, Austrian Academy of Sciences*, 116 pp.
- Ács, F. and Kovács, M., 2001: The surface aerodynamic transfer parameterization method SAPA: description and performance analyses. *Időjárás* 105, 165–182.
- Ács, F., 2003: A comparative analysis of transpiration and bare soil evaporation. *Bound. - Lay. Meteorol.* 109, 139–162.
- Bhumralkar, C.M. 1975. Numerical experiments on the computation of ground surface temperature in an atmospheric general circulation model. *J. Appl. Meteorol.* 14, 1246–1258.
- Blümel K., 1999: A simple formula for estimation of the roughness length for heat transfer over partly vegetated surfaces. *J. Appl. Meteorol.* 38, 814–829.
- Brunt, D., 1932: Notes on radiation in the atmosphere. *Q. J. Roy. Meteor. Soc.* 58, 389–420.
- Brutsaert, W., 1982. *Evaporation into the Atmosphere*. D. Reidel, 299 pp.
- Dolman, A.J., 1993: A multiple-source land surface energy balance model for use in general circulation models. *Agr. Forest Meteorol.* 65, 21–45.
- Drucza, M. and Ács, F., 2004: On the use of energy-balance model for estimating soil moisture content (in Hungarian). In *Forests and Climate, IV tome* (ed.: Cs. Mátyás), Nyugat-Magyarországi Egyetem, Sopron, 123–132.
- Dunkel, Z., Bozó, P., Szabó, T., and Vadász, V., 1989: Application of thermal infrared remote sensing to the estimation of regional evapotranspiration. *Adv. Space Res.* 9, (7)255–(7)258.
- Erdős, L. and Morvay, A., 1961: Soil moisture course of some soil types (in Hungarian). *Időjárás* 65, 47–55.
- Friedl, M.A., 2002: Forward and inverse modelling of land surface energy balance using surface temperature measurements. *Remote Sens. Environ.* 79, 344–354.
- Holtislag, A.A.M. and Ulden, A.P.V., 1983: A simple scheme for daytime estimates of the surface fluxes from routine weather data. *J. Clim. Appl. Meteorol.* 27, 689–704.
- Hupfer, P. and Raabe, A., 1994: Meteorological transition between land and sea in the microscale. *Meteorol. Z.* 3, 100–103.
- Inoue Y., Kimball, B.A., Jackson, R.D., Pinter, P.J., and Reginato, R.J., 1990: Remote estimation of leaf transpiration rate and stomatal resistance based on infrared thermometry. *Agr. Forest Meteorol.* 51, 21–33.
- Jarvis, P.G., 1976: The interpretation of the variations in the leaf water potential and stomatal conductance found in canopies in the field. *Philos. Trans. Roy. Soc., Ser. B.* 273, 593–610.
- Kustas, W.P., Choudhury, B.J., Moran, M.S., Reginat, R.J., Jackson, R.D., Gay, L.W., and Weawer, H.L., 1989: Determination of sensible heat flux over sparse canopy using thermal infrared data. *Agr. Forest Meteorol.* 44, 197–216.

- Kustas, W. P., Humes, K. S., Norman, J. M., and Moran, M. S., 1996: Single- and Dual-Source Modelling of Surface Energy Fluxes with Radiometric Surface Temperature. *J. Appl. Meteorol.* 35, 110-121.
- Mészáros, R., 2002: Dry deposition of ozone over different surface types (in Hungarian). *PhD. Thesis*, pp.111.
- Shuttleworth, J.W., 1988: Macrohydrology-the new challenge for process hydrology. *J. Hydrol.* 100, 31-56.
- Shuttleworth, J.W. and Gurney, R., 1990: The theoretical relationship between foliage temperature and canopy resistance in sparse crops. *Q. J. Roy. Meteor. Soc.* 116, 497-519.
- Soer, G.J.R., 1980: Estimation of regional evapotranspiration and soil moisture conditions using remotely sensed crop surface temperatures. *Remote Sens. Environ.* 9, 27-45.
- Szabó, T., Tóth, R., Csapó, P., Tiringér, Cs., and Lambert, K., 1989: Estimation of evapotranspiration of wheat canopy under dry soil conditions using surface temperature data. *Időjárás* 93, 253-260.
- Szász, G., 1964: Measurement of diurnal change of the thermal conductivity (in Hungarian). *Agrokémia és Talajtan* 13, 137-148.
- Taconet, O., Bernard, R., and Vidal-Madjar, D., 1986: Evapotranspiration over an agricultural region using a surface flux/temperature model based on NOAA AVHRR data. *J. Clim. Appl. Meteorol.* 25, 284-307.
- Taylor C.H., 1995: Aggregation of wet and dry surfaces in interception schemes for General Circulation Models. *J. Climate* 8, 441-448.
- Thornthwaite, C.W., 1948: An approach toward a rational classification of climate. *Geogr. Rev.* 38, 55-89.
- van de Griend, A.A., Camillo, P.J., and Gurney, R.J., 1985: Discrimination of soil physical parameters, thermal inertia, and soil moisture from diurnal surface temperature fluctuations. *Water Resour. Res.* 21, 997-1009.

IDŐJÁRÁS

Quarterly Journal of the Hungarian Meteorological Service
Vol. 109, No. 2, April–June 2005, pp. 89–109

Downscaling EPS probabilities using SYNOP precipitation data

Ervin Zsótér

Hungarian Meteorological Service,*
P.O. Box 38, H-1525 Budapest, Hungary; E-mail: ervin.zsoter@ecmwf.int

(Manuscript received in final form November 18, 2004)

Abstract—The probability forecasts of precipitation (PoP) are of great interest in numerical weather forecasting. Besides the model errors and the ensemble spread insufficiencies, the quality of these PoP forecasts is strongly affected by the problem of representativity: while the original forecasts are valid on the scale of a gridbox, we want to verify them with observations of local stations. These inconsistencies can be treated by the so-called upscaling and downscaling methods. This paper presents a new approach for downscaling PoP forecasts with the combination of the ensemble prediction system (EPS) and the representativity conditions explored by conditional error statistics of the observations with respect to forecasts.

Regarding the probability density functions (PDF) of the observations respect to the different forecast values, we found that there is only a very small difference between two or three years seasonal PDF-s as long as the model environment was consistent, and the geographical variability of the PDF-s is also not significant between areas – like Central Europe and Northern Hemisphere.

The new downscaling method in general delivered better verification statistics than the operational one. The best results could have been obtained for winter, while the least improvement was attained for summer. While the old probabilities were underconfident for most of the cases, the new probabilities showed some overconfidency. In general, there is no significant improvement in the resolution, but as an important result there is no deterioration at all. The greatest improvement was gained for the Brier skill score, especially for the thresholds of 1 mm and 5 mm. Regarding ROC curves, higher hit rates were also present, mainly for bigger thresholds. In addition strong similarities were found between the results for JJA and MAM, and also in the case of DJF and SON, which can probably be explained by local scale convection.

Key-words: ensemble forecast, probability distribution function, representativity error, Brier score, relative operating characteristics

* Present address: European Centre for Medium-Range Weather Forecasts (ECMWF),
Shinfield Park, Reading, RG2 9AX, England

1. Introduction

Since the beginning of the 1990's, the probabilistic way of forecasting weather events has become more and more widespread (*Ehrendorfer, 1997*). Nevertheless, one of the most important tasks is the numerical forecasting of precipitation. To obtain comprehensive knowledge of the forthcoming weather scenarios regarding extreme events of rain and snow, probability forecasts are essential. The numerical forecast systems provide predictions – deterministic and probabilistic – directly for the scale of a grid-box. However, it is of great importance to know the accurate probability of the occurrence of weather events not only for a whole grid-box, but for any local point inside that grid-box. This paper presents a new approach for creating local probabilities with the combination of the EPS and representativity conditions explored by conditional error statistics of the observations with respect to forecasts.

When dealing with probabilistic forecasts in general, three types of errors have to be considered. At first, the atmospheric model is not perfect, so errors are likely to rise because of the physical or dynamic inconsistencies with the true atmosphere. Additionally, on many occasions the ensemble spread is not large enough, so the verifying observations are below or above all of the ensemble members, therefore, the perturbations of the initial state do not completely represent the real uncertainty of the atmosphere (*Hamill, 2000*). Finally, the problems associated with representativity have to be addressed. This arose from the fact that the forecast represents a grid-box value, while the verifying observations indicate local occurrences. The spatial scale of the grid-box is on the order of 1000 km^2 , while the representative scale of raingauges is only a fraction of 1 m^2 . Therefore, the quality of the forecast is highly dependent on the accidental choice of the particular local point (one or more) within the grid-box as a verifying station. The idea of this research concerns the representativity error. The reason why the operational PoP predictions strongly overforecast the precipitation at local observations might be the representativity error as well as, for example, model bias or lack of ensemble spread.

To deal with the representativity problem, two different methods can be identified. The first is called upscaling. In this method a representative observation value is created for every grid-box using as many local observations of the grid-box as possible (*Ghelli and Lalaurette, 2000*). In contrast, the downscaling method works in the opposite direction, we start from a grid-box forecast value and derive the probability forecast for the scale of local stations. Before describing our improved way for downscaling, we review two important ways of deriving PoP forecasts in general.

The first method is a simple conditional statistical analysis. The distributions of observations gathered over a long period are determined for every individual forecast or forecast interval. This could be interpreted by a set of cumulative probability distribution functions (PDF),

$$P(obs < x | f) = PDF_f(x), \quad (1)$$

where f is the forecast and x is the threshold. Here each PDF represents the probability distribution of observations below a certain threshold, knowing that the forecast was f .

A second method is to use an ensemble prediction system (EPS) (Palmer *et al.*, 1992). In the frame of the EPS we transform a prescribed distribution of initial errors into the future. This means that many possible weather outcomes can result from only a slight variation in the initial state of the atmosphere. At the time of this study, at the European Centre for Medium-Range Weather Forecasts (ECMWF) 50 perturbed forecasts were run operationally at T255 horizontal resolution with 40 vertical levels (L40). To obtain probability values from these 50 perturbed forecasts, a simple operational method was used. Assuming that the 50 members are independent, and each gives an equally probable state of the future weather (the ensemble spread is perfect), the probability of having the observation above a threshold within a certain time frame (usually 24 hours) is equal to the proportion of those ensemble members, which predict more than the threshold value. This method is called the democratic voting method, because every member is equal and they can be only pro or contra to the event. The overall probability can be derived simply by averaging the members' yes or no votes,

$$P(obs > x | f_1, f_2, \dots, f_{50}) = \frac{1}{50} \cdot \sum_{i=1}^{50} H(f_i - x), \quad (2)$$

where x is the threshold, f_i is the forecast of the i th member, and $H(v) > 1$, only if $v > 0$.

To emphasize the importance of the representativity problem, an example is presented. Let us have a set of 50 EPS member's quantitative precipitation forecasts, and let the threshold be 5 mm. Assume that every member predicts 10 mm for a grid-box, where we have 20 observations ranging from 1 to 28 mm, four of them being less than 5 mm. In the original procedure, the operational probability would be 100%, knowing that every member is above 5 mm. However, assuming that in the Global Telecommunication System (GTS) there is only one station for that grid-box (and this is the case for most of the grid-boxes), we would have an inbuilt error within our forecast. This would be a

consequence of the fact, that the official verifying observation could be one of the observations within that 20 locally available with less than 5 mm. This suggests that the operational probability of 100% is not correct at the scale of the local stations. The average of the observations within the grid-box could be 10 mm, notwithstanding that the expected local probability of more than 5 mm is less than 100%. In this example we might have forecasted less than 100% if we would have known the fact that statistically there is only approximately 80% of probability having more than 5 mm rain locally, assuming that the forecast for the grid-box was exactly 10 mm.

The underlying new concept is exactly the same what we had presented with the conditional statistical analysis of the observations explained above. Our approach is then to obtain more accurate probabilities using a combination of the ensemble prediction system and the conditional statistical analysis. It would be of great value if we could create a context, in which a problem of representativity could be statistically examined, excluding other errors. If this could be done successfully, we could superimpose the representativity correction onto the ensemble forecasts, producing accurate PoP forecasts on a local scale. The assumption that the EPS members are still independent, makes it possible to write the computation of the new probabilities as follows:

$$P(obs > x | f_1, \dots, f_{50}) = \frac{1}{50} \cdot \sum_{i=1}^{50} P(obs > x | f_i) = \frac{1}{50} \cdot \sum_{i=1}^{50} [1 - P(obs \leq x | f_i)], \quad (3)$$

where f_i is the i th member's forecast, x is the threshold, and $P(obs \leq x | f_i) = PDF_{f_i}$ is the cumulative probability distribution function of the observations knowing that the forecast is f_i .

In the following sections the PDF generation procedure and the behavior of these distributions will be described first. Then the property of the new probability fields will be discussed, and finally we present some verification results of the test periods together with a summary.

2. Generation of the probability distribution functions

For the generation of the probability distribution functions (PDFs) described in the introduction, a set of deterministic forecast and SYNOP observation pairs were needed. The ensemble prediction system (EPS) was running at T255L40. To attain the best results possible, the forecast for the statistical analysis had to be chosen consistently with the EPS version. Because of other experiments, the operational deterministic forecast data was available for many years,

interpolated onto the SYNOP station locations. Therefore, it was convenient and time efficient to use the operational forecast. The best fit could have been reached for the year of 2000, when the deterministic forecast was operational at T319L60 with very similar horizontal resolution as the EPS.

To perform the statistical calculations of PDFs, a vast amount of data was needed. It is not possible to apply the method on a relatively small area (e.g., Great Britain), because a very long time period (dozens of years) or data from a lot of stations (thousands) would have been required. The dynamic nature of model algorithm changes means that it is difficult to obtain consistent data over a long period of time. Another problem is the insufficient number of SYNOP stations for small regions.

We wanted to focus on seasonal changes, and an appropriate sample size had a great importance. Therefore the whole season periods (three months) and the extra tropical region of the Northern Hemisphere (between latitudes 30°N and 80°N) were considered. To obtain the deterministic forecast values for the station location, a bilinear interpolation was used. For the experiment only those SYNOP stations were selected, which reported at the frequency of the European stations. Altogether 2000 different stations were selected (*Fig. 1*). Those particular stations, where the 24 hours accumulation could not be obtained for a particular day, were excluded from the survey. For a three-month period we had about $91 \times 2,000 \sim 180,000$ forecast-observation pairs. Because of reporting problems, this number was reduced to about 130,000–40,000 cases for each season.

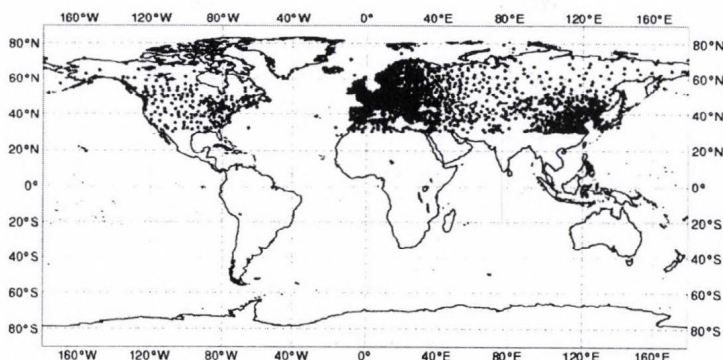


Fig. 1. The selected SYNOP stations over the extra tropical region of the Northern Hemisphere, between 30°N and 80°N.

To give an example data set, a scatter diagram is presented in *Fig. 2*. Ideally PDFs should be generated for every possible precipitation value, but according to the limited sample size, forecast intervals (bins, bounded by

vertical lines in *Fig. 2*) had to be defined instead of the single values. In addition, having too few intervals is also not desirable, because in this case quite large amount of information would be lost when interpolating between two PDF curves in order to get the probability value for an individual forecast. This interval selection scheme was tested on a number of occasions. To obtain a stable distribution (i.e., to give a representative sample of the reality), ideally we need at least 200–300 observations within one forecast interval. Because high amounts of rain are seldom forecasted, to have stable result, for higher forecast values wider and wider bins had to be defined. For all investigation performed the following stratification intervals were used: 0, 0.1, 0.2, 0.3, 0.4, 0.5–0.8, 0.8–1, 1–2, 2–3, 3–4, 4–5, 5–6, 6–7, 7–8, 8–10, 10–12, 12–15, 15–20, 20–30, 30–50, 50–100, >100 mm. Because of lack of data, at most of the cases we could not derive any valuable information for the interval of >100 mm, thus an extrapolation was used.

Traditionally, precipitation is accumulated over 24 hours from 06 to 06 UTC, which corresponds to the operational forecast range of 18–42 h. However, because of the need to keep the model error as small as possible in order to catch only the representativity properties, the forecast interval of 06–30 h had to be chosen. At first we undertook the statistical investigation for the whole area (Northern Extra tropics), and for all the seasons in 2000 (with DJF 1999–2000, MAM–2000, JJA–2000, SON–2000). PDF curves presented for the winter of 1999–2000 can be seen in *Fig. 3*. The distribution curve for the 0 mm forecast value is located at the upper left corner, while the rest of the curves follow after each other from the top left to the right, following the order of the stratifying forecast intervals described above (0, 0.1, 0.2, ..., 30–50, 50–100, >100 mm). The PDF curves are rather stepwise, because the observations are not continuous. Most of the cases in SYNOP stations, fractions of mm are not reported. On the diagram the curve of the last forecast interval (50–100 mm) is quite unstable, because we had less than 100 cases to create the distribution (above 100 mm we did not have forecast at all).

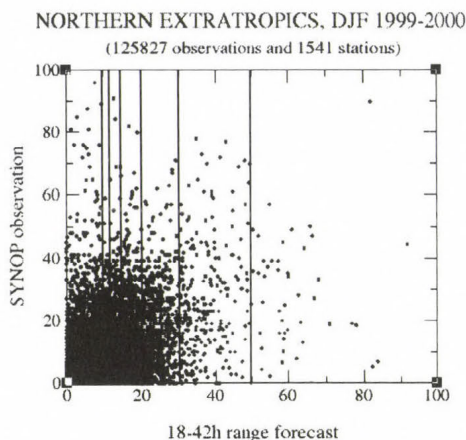


Fig. 2. Scatter diagram for winter 1999–2000. The vertical lines are the bounds of some stratifying forecast intervals.

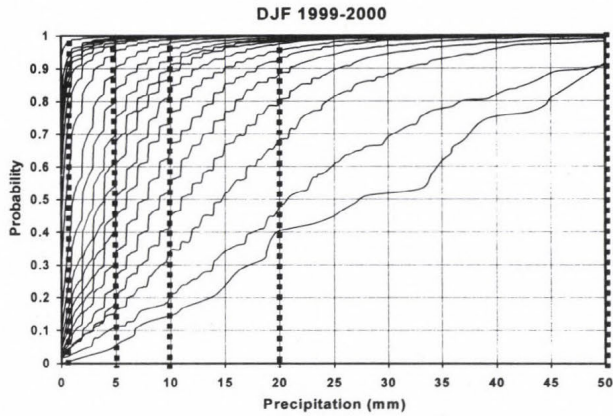


Fig. 3. Probability distribution functions for different forecast intervals, Northern Hemisphere, winter (DJF) of 1999-2000, forecast step 18-42 h.

In the following paragraphs we present some examinations of the behavior of the PDF curves. At first, the dependence of the PDFs on the chosen forecast ranges was tested. Besides the originally chosen 06-30 h interval, we set up two other periods with forecast ranges of 18-42 h and 90-114 h.

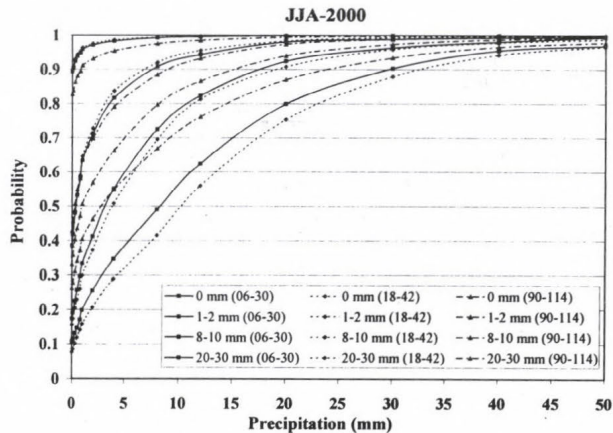


Fig. 4. Comparison of the PDFs for 06-30 h, 18-42 h and 90-114 h forecast ranges, Northern Hemisphere, JJA-2000, four different forecast intervals.

Fig. 4 shows a typical example for JJA-2000 (hereafter we chose to display 4 representative distribution curves (0 mm, 1-2 mm, 8-10 mm, and 20-30 mm) from all forecast intervals on this kind of diagrams, which follow

after each other always from the top left to the right). The differences among the three sets of curves are significant. In this case the results overlap with our expectations, the shortest range (06–30) gives the sharpest distribution of the observations. For small forecast values a bigger and bigger proportion of the observations are above a threshold as the forecast range increases. For higher forecasts this effect is reversed. After about two weeks, the skill of the forecast system would probably disappear, and the distribution curves would lie on the top of each other for every forecast interval. In the section 4 some comparison among the verification results of these different forecast ranges, 06–30 h, 18–42 h, and 90–114 h will be shown.

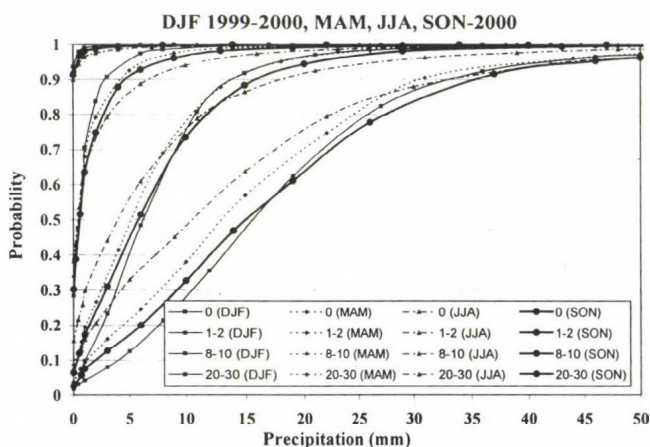


Fig. 5. Comparison of the PDF-s for DJF of 1999–2000, MAM, JJA, and SON of 2000, Northern Hemisphere, 06–30 h, for four different forecast intervals.

The next step in the investigation was to study the interannual and spatial characteristics of the probability distribution curves. In order to accomplish this task, we calculated the PDF curves for each season from MAM 1999 until summer 2001. These seasonal differences can be seen in Fig. 5. The curves for the same forecast interval do not match. The possible reasons for these differences are the convection and existence of different weather patterns. As it might be expected, spring and autumn are quite similar, while winter with largescale precipitation, and summer with large proportion of convective rain differ significantly. For small forecast values, the PDF curves for winter indicate just a slight chance of having large amount of precipitation (more than 5 or 10 mm), while regarding big values of forecasts the probability is relatively high. During summer, probably due to the uncertain convection, the opposite can be deduced.

There is another interesting aspect in the behavior of the PDFs, namely the interannual variability. During the seasons from spring of 1999 until the summer of 2001, two basic model changes could have strongly effected the PDFs. First, in October 1999 a change in the cloud and convection scheme took place, and in November 2000, T511 was put into operation. Analyzing the diagrams in *Figs. 6-9* we may conclude, that the change in the precipitation scheme affected the distributions quite strongly. While the latter change in resolution seem to cause just a slight modification. Results from the two winters with different resolution almost exactly overlap. In contrast, the spring and summer show much bigger differences, but the pattern of the deviation is rather similar.

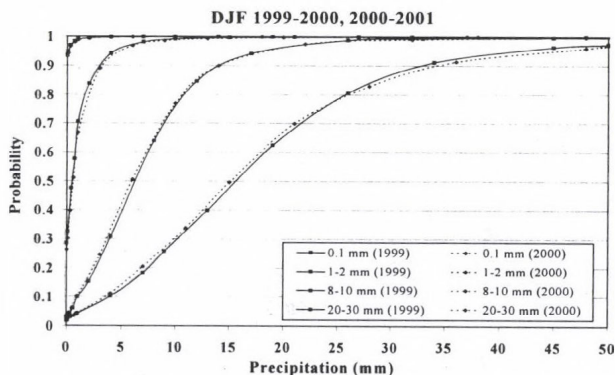


Fig. 6. Comparison of the annual variability of the PDF curves for winter, for four different forecast intervals.

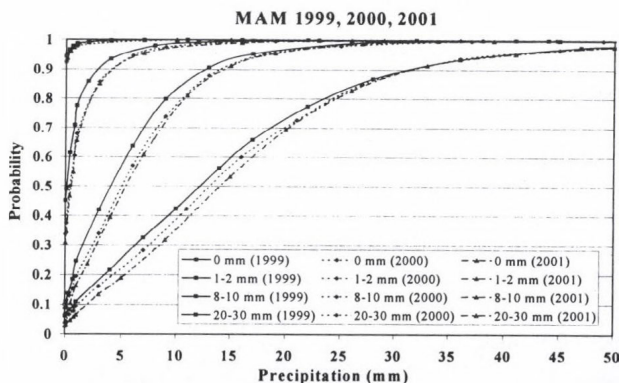


Fig. 7. Comparison of the annual variability of the PDF curves for spring, for four different forecast intervals.

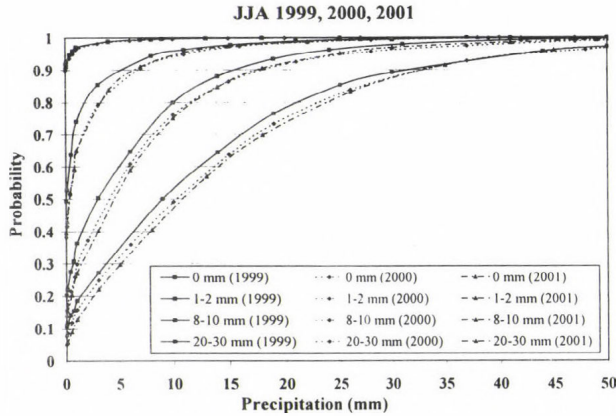


Fig. 8. Comparison of the annual variability of the PDF curves for summer, for four different forecast intervals.

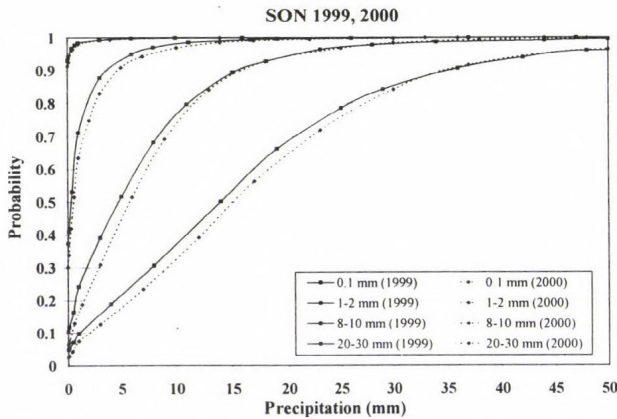


Fig. 9. Comparison of the annual variability of the PDF curves for autumn, for four different forecast intervals.

The curves are quite close in year 2000 and 2001, but during the summer of 1999 – the one with different precipitation scheme – we got significantly different distributions. The frequencies are consequently smaller for every forecast interval.

The spatial variability of the PDF curves is also important. To test the regional differences, we defined three regions besides Northern Hemisphere (NH): the European area (EU), the Northwest part of Europe (NWEU), and Central Europe (CE) (Fig. 10).

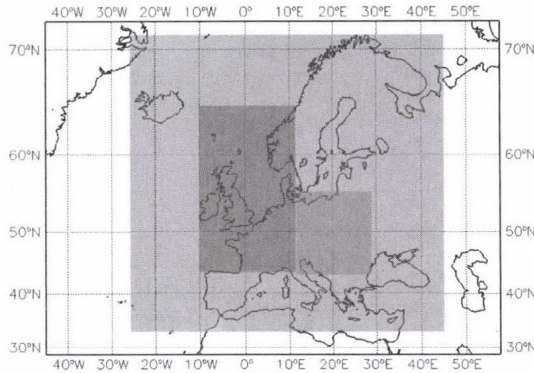


Fig. 10. Location of the geographical regions that are used in the study: Europe, Northwest Europe, and Central Europe.

We had about 80,000 observations for Europe, 25,000–30,000 for NWEU, and 20,000 for CE (as we stated above it is about 130,000–140,000 for NH). Because of the small sample size, for this comparison two years of data sets were put together. The results for the winter and summer periods can be seen in Figs. 11 and 12, respectively.

For winter the forecast distributions are represented by almost the same curves, and the differences are really small. However, regarding the summer PDFs, we could see larger deviations, but the curves still do not lie too far from each other. We could draw almost the same conclusion that we came to on the annual variability of the PDFs. Winter has the best, and summer has the worst overlapping property amongst the seasons.

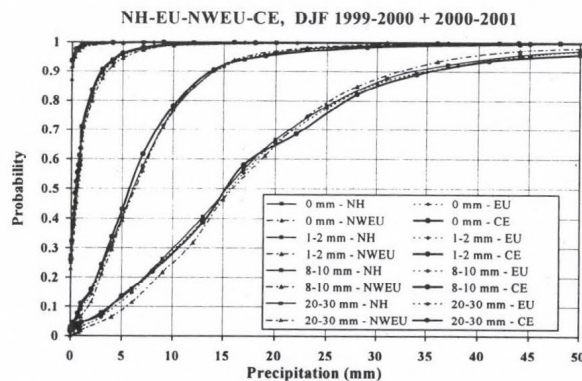


Fig. 11. Comparison of the spatial variability of the PDF curves for 4 regions – Northern Hemisphere (NH), Europe (EU), Northwest Europe (NWEU), and Central Europe (CE) – for winter season with two years data together, for 4 different forecast intervals.

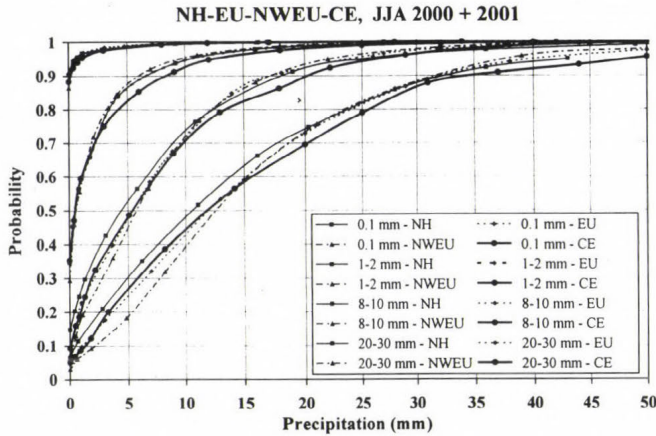


Fig. 12. Comparison of the spatial variability of the PDF curves for 4 regions – Northern Hemisphere (NH), Europe (EU), Northwest Europe (NWEU), and Central Europe (CE) – for summer, with two years data together, for 4 different forecast intervals.

3. The new probability fields

For the generation of the new probability fields defined by Eq. (3), the precipitation thresholds of 1, 5, 10, 20, and 50 mm were defined. First the individual forecast values had to be transformed to probabilities for every threshold and season. These probability values can be easily determined from the PDF diagrams presented in Fig. 3. All we have to do is to read the frequency values of every curve (belonging to different forecast intervals) at a certain threshold. This is also highlighted in Fig. 3 with vertical lines marking the thresholds. The required values are the crossing points of these lines and the PDF curves. Originally the cumulative functions show the probability of the observation below the threshold, thus a subtraction has to be done from 1. These frequencies concern the whole forecast intervals, thus we had to assign them an individual forecast value. The middle value of the forecast bins had been chosen. Finally, to get the desired probabilities for a precipitation forecast, we undertook a linear interpolation between the assigned discrete points. This simple method seemed to be sufficient enough even for higher forecasts, where the density of the function points are small.

To determine the seasonal relationship between forecast values and probabilities, the PDF sets of winter 1999–2000 and spring, summer, and autumn of year 2000 were taken. For the forecast intervals above 30 mm, the data sets of two years were combined to have sufficiently large sample sizes (2000+2001 for MAM and JJA, 1999+2000 for SON, and 1999–2000+

2000–2001 for DJF). The transform curves for every season and threshold can be seen in *Fig. 13*. The curves were not smoothed, so occasional jumps may be present.

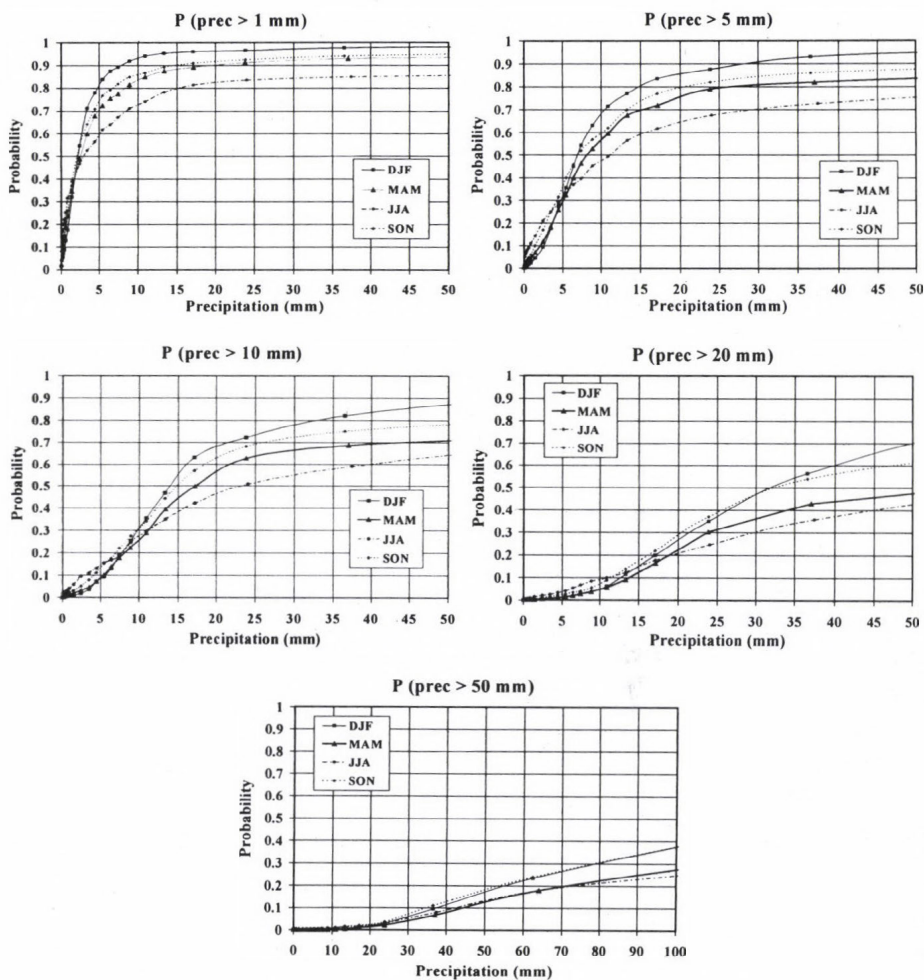


Fig. 13. Functions of the transformation of forecast values to probabilities for the thresholds of 1, 5, 10, and 50 mm.

During the experiments, probability fields were generated for all four seasons from September 2000 until August 2001. An example of the two probability fields is shown in *Fig. 14*. On the new forecast map the probabilities are spread further than on the old fields, and the maximum of the probabilities over wet regions is significantly lower with the new method.

These new features can be highlighted by two simple examples, when all members predict exactly 4 mm and secondly when 6 mm (the averaging of the 50 members contribution does not have any effect now). Let us consider the threshold of 5 mm. Now the operationally calculated probabilities differ sharply, namely in the first case we got 0%, and in the second case 100%. The new procedure distinguishes continuously between forecast values, and thus we have a same order of probabilities for these two cases. Moreover there is a chance of 5 mm rain even for the case when no rain was forecasted at all. For example, in the PDFs for autumn the probability of 4 mm is 28%, and for 6 mm it is 43%. With the new method there is an overall tendency of increasing the operational probability values around their minimum, while decreasing around the maximum.

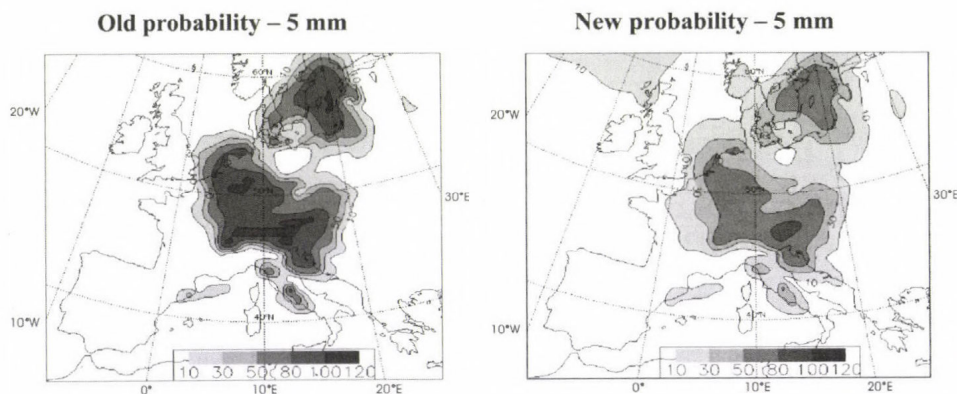


Fig. 14. Comparison of the probability fields (24 h PoP) created by the traditional democratic voting method (left), and by the new procedure (right), forecast of September 3, 2001, valid for: D+2, threshold: 5 mm.

4. Verification of experimental runs

We wanted to test the quality of this new type of PoP from as many aspects as possible. First, the probability fields for every full seasonal period had to be produced. We chose the seasons starting with SON 2000, and ending up with JJA 2001. Both the operational probabilities and our newly constructed probabilities had to be derived. The timing was chosen according to the users' needs, so we decided to prepare the probability fields for 06-06 UTC (24 hours period) consecutively for each day. Our target intervals thus have been selected as the following forecast ranges: 18-42 h, 42-66 h, 66-90 h, 90-114 h, 114-138 h, 138-162 h, 162-186 h, 186-210 h, 210-234 h (denoted from the forecasters point of view as D+1, D+2, ..., D+9).

As verification area, Europe has been chosen, focusing on the region where we have the largest number of available observations (only data in GTS). For qualitative evaluation we have chosen the most frequently used scores regarding probability forecasts (for a comprehensive overview of the scores and for the exact definitions see *Stanski et al.*, 1989; *Persson*, 2001):

- Brier score ($BrSc = BSrel - BSrsl + Uncertainty$),
- Brier score of the sample climate ($= Uncertainty$),
- Reliability ($BSrel$),
- Resolution ($BSrsl$),
- Brier skill score with respect to the sample climate

$$(BCBrSkSc = 1 - \frac{BrSc}{SCBrSc}),$$

- Brier reliability skill score ($BSSrel = 1 - \frac{BSrel}{SCBrSc}$),
- Brier resolution skill score ($BSSrsl = \frac{BSrsl}{Uncertainty}$),
- Relative operating characteristics (ROC).

We mainly present results for DJF and JJA, but the results for the other two seasons are very similar. Our primary interests were the reliability tables, ROC, and time series of Brier skill score with respect to sample climate and also time series of Brier resolution skill score.

Some results for JJA 2001 can be seen in *Fig. 15*. With the application of the new method, the operational overforecasting tendency turned to underforecasting for this summer period. The two pairs of curves are almost symmetrical to the diagonal line. Having analyzed the whole range of forecast steps and thresholds, we can summarize that the reliability is significantly better with the new probabilities for 1 mm. However, for bigger thresholds this is only true for D+1, afterwards there is no characteristic signal. The above stated underforecasting feature for probabilities greater than 20% is stronger for higher thresholds. It can also be seen from the figures, that the maximum of the predicted probabilities are significantly less for the new method than it was for the operational forecasts. This is just another evidence supporting our result with reference to the example of the two probability fields, as showed above.

Significant improvement in Brier skill score can only be seen for 1 mm, while for higher thresholds there is rapidly decreasing increment. In general the biggest difference can be detected for D+1. In resolution there is no significant improvement, but also there is no deterioration. If there is any increment it is only detectable during the first one or two days.

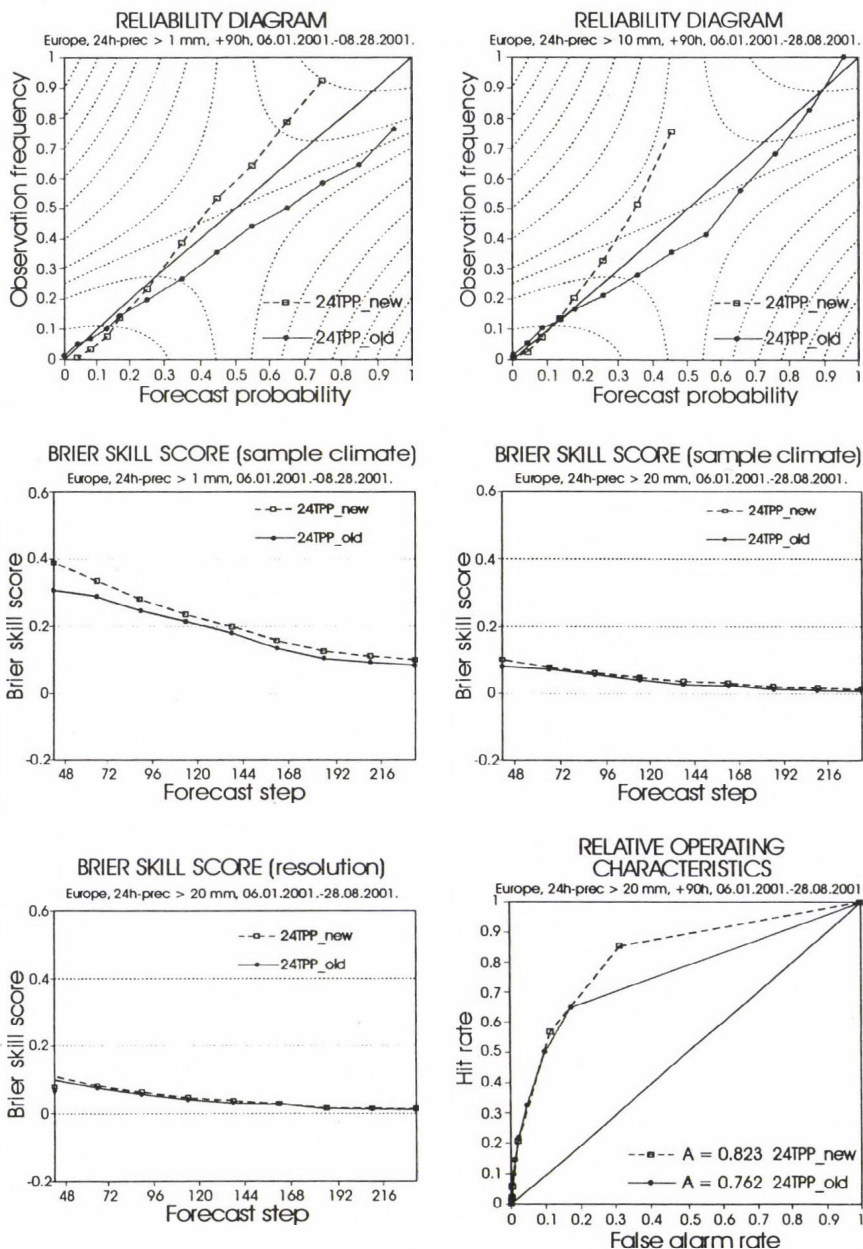


Fig. 15. A few verification diagrams for JJA 2001: reliability diagrams (first row; left: D+2, 1 mm; right: D+2, 10 mm), time series of Brier Skill Score with respect to sample climate (middle row; left: 1 mm; right: 10 mm), time series of Brier resolution skill score (3rd row; left: 20 mm), ROC (3rd row; right: D+2, 20 mm).

For ROC curves the area under the curves, is the same for 1 mm, but there is greater improvement for higher thresholds, which is better emphasized for short range. The improvement is due to the higher hit rates gained with the new method.

As can be seen in *Fig. 16*, much better results were attained for winter. In general larger increments could have been obtained than for summer. The reliability is very good with the new probabilities, especially for small thresholds. For 1 and 5 mm after D+4 we could see some underconfidence, no significance bias for 10 mm, while for 20 mm and 50 mm there is overconfidence similarly to summer but with less magnitude.

The difference between the maximum of the forecasted probability values for a certain threshold and time step we had for summer is smaller here. The reason for this is the significant variability over seasons, as winter and summer are the opposite extremes (summer with lower, winter with higher frequencies), as we have already seen it in *Fig. 5*. In Brier skill score quite massive increment can be seen. For higher thresholds the difference decreases quickly again. With bigger time steps the curves are relatively closer to each other. In resolution there is slightly bigger difference compared to summer case, but still these increments, presented mainly for short range, are not significant. For ROC curves, very similar conclusions could be stated as we did for summer. The difference is just that we have some improvement here for 1 mm, for the first 1–2 days as well, and that for every other thresholds the increments are enhanced, and the differences in terms of ROC areas are more emphasized.

Regarding the season of MAM 2001, every aspect of the verification is impressively similar to JJA 2001: only a slightly larger overall improvements could be detected for spring (not shown). The results of the two other seasons, SON 2000 and DJF 2000–2001 are also similar to each other. In autumn the new probability fields deliver slightly smaller improvement over the operational probabilities, than it was for DJF. Increments for reliability are moderately smaller for SON, and the overforecasting tendency for 1 and 5 mm after D+4 is less emphasized.

Earlier we have shown some comparisons regarding the PDF curves for different accumulation periods of the forecasts, tested in JJA 2001. As we can see in *Fig. 17*, the best results were achieved with the forecast range of 06–30 h. The probability forecasts lost skill in every aspects of the verification consistently, as the lead time got longer and longer.

As an interesting aspect of this new PoP generation procedure, the variability of the forecast quality with respect to utilization of different years PDF set has also been tested. The summer period have been chosen again, during 1999 and 2000, where the PDF curves differed significantly.

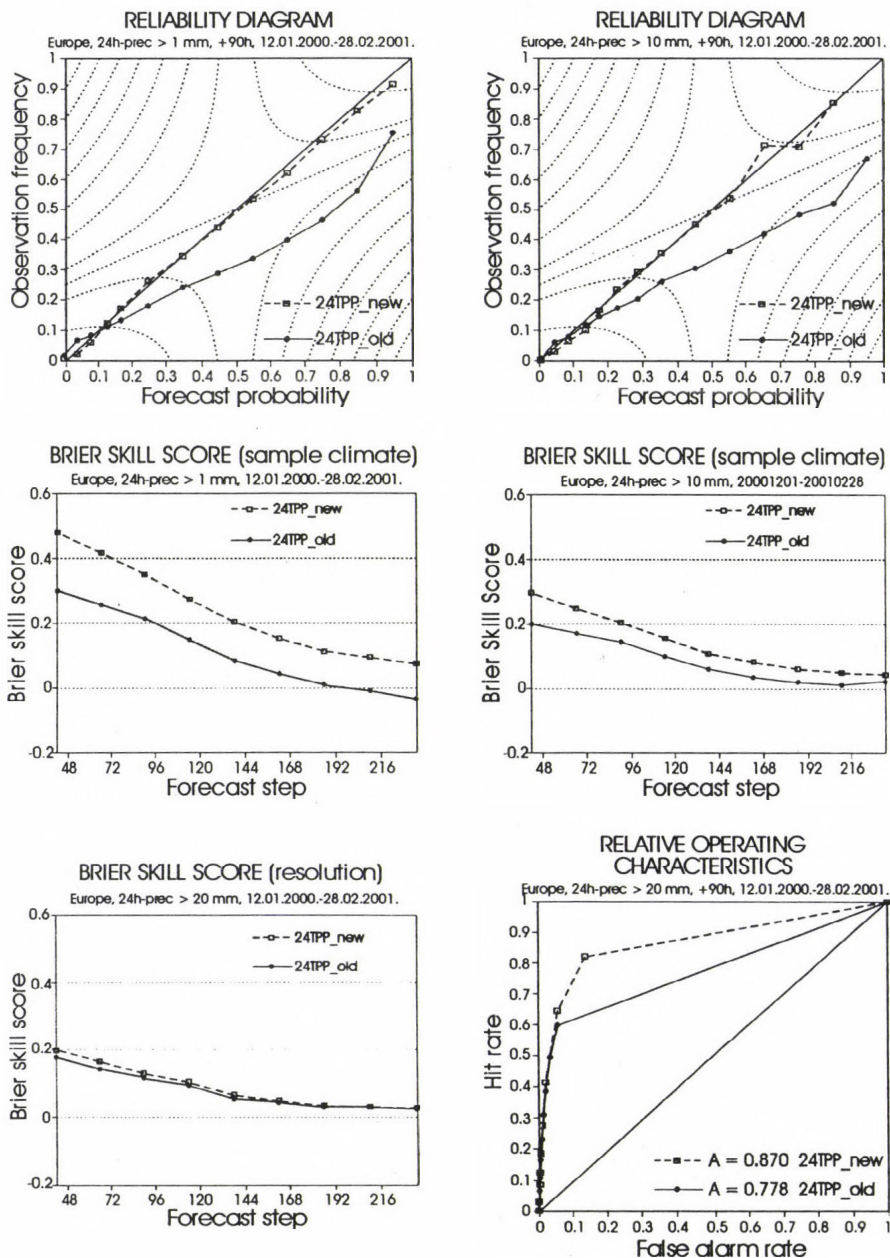


Fig. 16. A few verification diagrams for DJF 2000–2001: reliability diagrams (first row; left: D+2, 1 mm; right: D+2, 10 mm), time series of Brier skill score with respect to sample climate (middle row; left: 1 mm; right: 10 mm), time series of Brier resolution skill score (3rd row; left: 20 mm), ROC (3-rd row; right: D+2, 20 mm).

According to *Fig. 18*, moderate but systematic difference can be found between the quality performance of the two PDF sets. For resolution and ROC curves the results were almost identical, while there is slight and constant deterioration in Brier skill score and reliability for every threshold and time step. On the reliability diagram some shifts towards under-forecasting can also be seen, relative to the curve of 06–30 h. This is probably caused by the smaller frequencies of occurrence in the 1999's PDF sets (see *Figs. 6–9*).

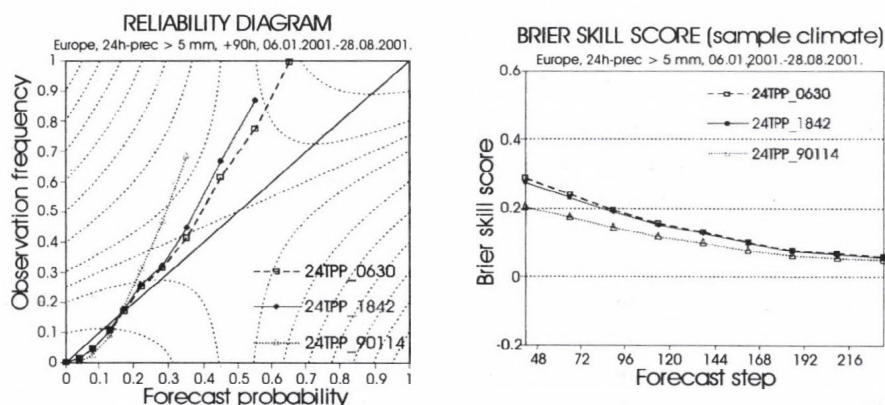


Fig. 17. Two examples of the comparisons between verification results of new probability fields, calculated by PDF-s of the forecast interval 06–30 h, 18–42 h and 90–114 h, verification period is JJA 2001.

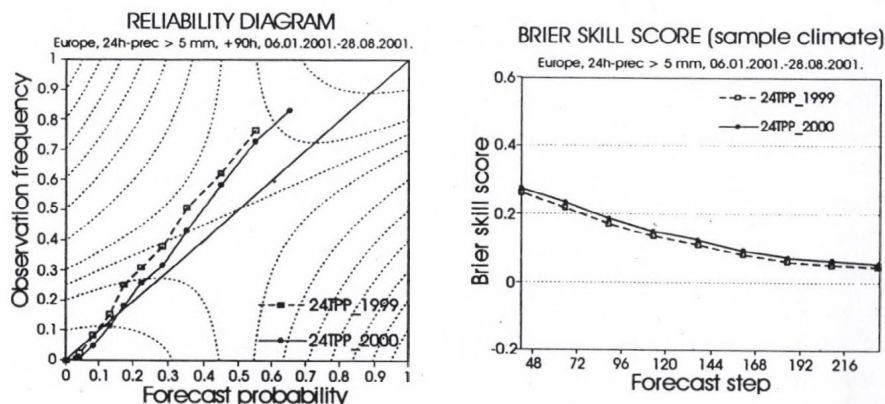


Fig. 18. Two examples of the comparisons between verification results of new probability fields, calculated by PDF-s of JJA 1999 and 2000, verification period is JJA 2001.

5. Summary, conclusions

In this paper we presented and tested a new and complex method for downscaling precipitation probabilities. Our basic idea – to calibrate the ensemble forecasts with conditional probability distributions of the forecasts-observation space – has produced promising results.

The generation of the probability distribution functions (PDF) was the first step in order to create the new probability fields. The PDFs were derived consistently for 22 different forecast intervals, for the forecast range of 06–30 h (24 hours period). Because of sample size requirements, the area of Northern Extra tropics was chosen, and the statistical analyses were performed for three months (seasonal) periods. Only a very small difference between two or three years seasonal PDFs could have been found, as long as the model environment was consistent. In addition, the geographical variability was also tested, without being able to demonstrate significant differences between smaller areas – like Central Europe. Thus, the geographical choice of the whole Northern Extra tropics seemed to be appropriate to be the basis for the statistical creation of the new probabilities for areas with significantly different climate.

The new fields that were calculated with probabilities for the local scale looked quite differently, in comparison with the operational probabilities. Because of the statistical calibration, the new fields are much smoother, the wet areas are spread out, and meanwhile the maximum value of the new probabilities is usually significantly smaller.

For testing the seasonal quality of the forecast, the new probability fields have been verified for different seasons (SON 2000, DJF 2000–2001, MAM 2001, and JJA 2001). The new method, in general, delivered better results than the operational one. The best results could have been obtained for winter, while the least improvement was attained for summer. While the old probabilities were underconfident for most of the cases, the new probabilities showed some overconfidency. In general, there is no significant improvement in the resolution, but as an important result there is no deterioration at all. The greatest improvement was gained for the Brier skill score, especially for the thresholds of 1 mm and 5 mm. Concerning ROC curves, some improvements (higher hit rates) were also present, mainly for bigger thresholds. Strong similarities were found between the results for JJA and MAM, and also in the case of DJF and SON, which can probably be explained by local scale convection.

In the future we would like to make verification with data from other years, as well. Preparing the PDFs using Control forecast data (EPS run starting from the deterministic model's initial state) instead of the T319 operational run, the model inconsistencies between the EPS forecasts, and the

statistically investigated forecasts could be eliminated. We also are planning to verify this new method of downscaling with very high density observational network.

Acknowledgements—This research has been done at the European Centre for Medium-Range Weather Forecasts (ECMWF), during my visit in summer 2001. Many thanks to Francois Lalaurette for his kind supervising, and also to everybody else who helped me during this work at ECMWF.

References

- Ehrendorfer, M., 1997: Predicting the uncertainty of numerical weather forecasts: A review. *Meteorol. Z.* 6, 147-183.
- Ghelli, A. and Lalaurette, F., 2000: Verifying precipitation forecasts using upscaled observations. *ECMWF Newsletter*, No. 87 [Available from ECMWF, Reading, England].
- Hamill, T. M., 2001: Interpretation of Rank Histograms for Verifying Ensemble Forecasts. *Mon. Weather Rev.* 129, 550-560.
- Palmer, T.N., Molteni, F., Mureau, R., Buizza, R., Chapelet, P., and Tribbia, J., 1992: Ensemble prediction. *ECMWF Research Department Tech. Memo.* No. 188 [Available from ECMWF, Reading, England].
- Persson, A., 2001: User Guide to ECMWF forecast products. [Available from ECMWF, Reading, England].
- Stanski, H.R., Wilson, L.J., and Burrows, W.R., 1989: Survey of common verification methods in meteorology. *World Weather Watch, Technical Report* No. 8, WMO/TD. No. 358.

IDŐJÁRÁS

Quarterly Journal of the Hungarian Meteorological Service
Vol. 109, No. 2, April–June 2005, pp. 111–122

General characterization of the lightnings in the Carpathian Basin

Ferenc Wantuch^{1*} and Sándor Szonda²

¹*Hungarian Meteorological Service,
P.O. Box 38, H-1525 Budapest, Hungary; E-mail: wantuch.f@met.hu*

²*Hungarian Power Companies Ltd,
P.O. Box 15, H-1255 Budapest, Hungary; E-mail: sszonda@vmv.hu*

(Manuscript received in final form August 6, 2004)

Abstract—The paper is a review of the general features of lightning records produced by the System d'Alerte Foudre par Interferometrie Radio-electrique (SAFIR) lightning detection system used in Hungary over the recent 5 years. The intra-cloud (IC) and cloud-to-ground (CG) lightnings were distinguished. Lots of information was generated with the help of this system. The electrical parameters were collected and processed. The time and spatial distributions of the lightnings and different type of lightning characteristics were computed. As the first discharges appear in the early time of the forming of a cumulonimbus cloud, the application of data generated by the lightning detection system is a good tool in the every day meteorological short range forecasting. Understanding of the lightning physics leads to the more effective meteorological and industrial application.

Key-words: SAFIR lightning detection system, interferometria, intra-cloud, cloud-to-ground, electrical parameters

1. Introduction

Thunderstorms are composed of convective cells developed due to the thermal instability of moist air. These cells usually fasten the growth process of each other. The horizontal size of thunderstorms can be of several tens of kilometers, while their lifetime can reach several hours. Convective cells are developing very fast, they can reach the height of 10 km in just several tens of

* Corresponding author

minutes. A strong updraft is present in the developing phase of the cells, which carries up ice crystals, overcooled water drops, and snowflakes. The basic processes of the loading of thunderclouds with electricity are the charge separation for both water drops and ice crystals and the separation of oppositely charged particles due to the irregular updraft. Usually, a triple electric pole develops inside the thundercloud as a result of these processes: a large negatively charged zone in a height of about 6 km, a positive zone at 8–12 km, and a weak positive layer at the cloud base level. A weaker electric field develops at the lower parts of the cloud, while in the upper part the electric field strength is several 100 kV/m. The time necessary for electric charge for one cell is less than ten minutes.

A very complicated process takes place as soon as the electric field strength reaches the air's capacity of electrical penetration. First, charges are concentrated by short jumps of several hundred meters and halts of several dozens of μs , and the air becomes pre-ionized along the jump paths. On the ground, charges with opposite polarity are gathering due to the big field strength produced by the approaching charges and good electric conductance of the ground, and they are moving upwards forming a counter discharge. When the two oppositely directed channels meet, the main discharge of the lightning forms. The whole process takes several hundred milliseconds, while the lightning itself takes only several tens of μs . Lightning is a self-destructive process, because the lightning channel is continuously narrowing due to the electric fields caused by the lightning current, and it breaks eventually. If all charges were not neutralized till the breaking of the channel, then new and new lightnings may occur with several hundred ms of delay (multiple lightning) in the previous channel, which still remains ionized after the discharge.

The process mentioned above is accompanied by electromagnetic radiation on a broad frequency spectrum, which is radiated out by the lightning channel as if it were a huge antenna. The frequency spectrum ranges from several kHz to 1–2 GHz. The dynamics of the movement of electric charges and, therefore, the spectra of the produced radiation differs significantly if the lightning occurred inside the cloud or if it has reached the ground. This gives us the possibility of distinguishing the cloud lightnings from the cloud-to-ground lightnings.

2. Installing the lightning detection system

The high-frequency VHF radiation of lightnings offers the possibility of observing the thunderstorm activity. The SAFIR lightning detection and forecasting system used in Hungary was developed by a French office,

ONERA (Office National d'Etudes et de Recherches Aéronautiques), for warning purposes of the rocket launching pad in French Guyana against thunder stroke (*Larosche et al.*, 1991). The system was produced for civil application purposes by the firm Vaisala-Dimension.

The SAFIR system is able to determine the position of lightning with an accuracy of several kilometers based on interferometric direction measurement. The direction measurement is based on the dislocation of phase between the electromagnetic waves reaching the four or eight closely mounted dipole antennas belonging to the sensor unit. The accuracy of the measurement depends on the number of antennas. The Hungarian system consists of five dipole antennas. The chosen frequency range for observation is 108–118 MHz. The high sensitivity of the system makes possible the detection of the low energy cloud-to-cloud lightnings, which can warn the user several 10 minutes before the first lightning reaches the ground. Let us see an example. *Fig. 1* shows the changes in the numbers of cloud and ground lightnings registered on August 1, 1999 with a 5-minute integration time. During this afternoon thunderstorm the cloud lightnings began 30 s earlier and ended 45 s later than the ground lightnings.

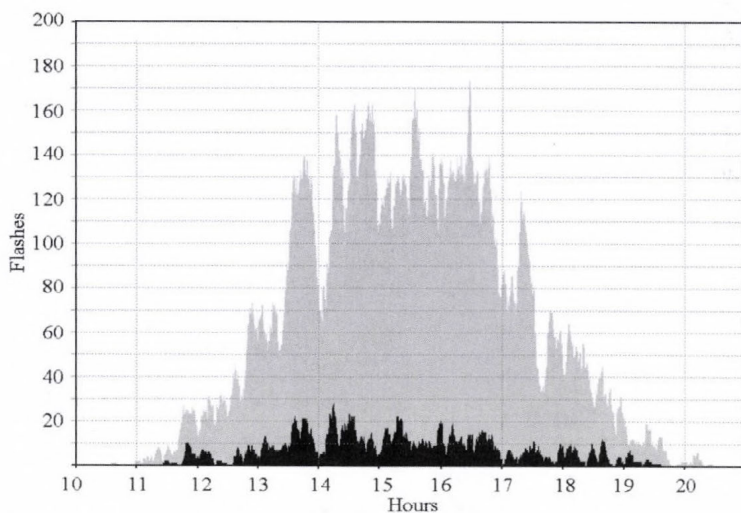


Fig. 1. IC (grey) and CG (black) lightnings registered on August 1, 1999 with a 5-minute integration time over Hungary.

The SAFIR system also has a low frequency (0.3–3 MHz) antenna, which is able to detect the strength of the produced electric field and the shape of the indication of lightnings. Based on these measurements it is possible to define

whether the lightning has reached the ground. With the use of propagation models, the following lightning parameters can also be derived:

- peak current (kA),
- rise time (μs),
- decay time (μs),
- steepness (kA/ μs),
- polarity,
- electric charge (As),
- the energy of the impulse (kA²s).

The sensors of the SAFIR system have a GPS based synchronizing time of 100 ns, and they are able of doing a localization every 100 μs . The centre and the sensors are in continuous touch – they are sending data in every second, so the system can follow the events in real-time mode.

The intention of installing a lightning detection system for Hungary first occurred in 1995. After a long period of preparation and organization, the establishment of the system began in 1997 using the elements of the SAFIR system as an investment of the Hungarian Meteorological Service. As a first step, three stations were established (Budapest (later moved to Bugyi), Sárvár, and Véménd) which provided a 60% coverage of the country. In 1998 two more stations were added (Zsadány and Várboc). Finally, in September 1998 the system was replaced by the newly developed product of Vaisala-Dimension, which had an entirely digital data processing system, and additional sensors were installed, which are able to measure the electric characteristics of lightnings. Due to the strict requirements, like horizon limitation, a spectrum with low background noise, available communication lines, power supply, etc., the sensors were mounted on the high communication towers of the T-Mobile Phone Ltd. The area under continuous observation is about 200,000 km² with the detection criteria set by the Vaisala-Dimension, and it also covers some parts of the neighboring countries. The system can localize the lightning with an accuracy of 1–2 km over Hungary, the probability of detection is above 98% (*Richard, 1998*). Both the accuracy of location measurement and the probability of detection decrease towards the limits of the area under observation.

The system can distinguish the ground strokes from cloud lightnings based on the following parameters:

- rise time: 0.125–15.0 μs ,
- decay time 15–255 μs ,
- peak current intensity: minimum 3 kA,
- detected electric field strength: minimum 1 V/m,
- time coherence: 200 ns,
- number of detecting stations: 3 – sometimes 2.

If these criteria are satisfied simultaneously, then the system assumes that the lightning is a groundstroke. Further statistical analyses are dealing only with these groundstrokes.

3. Evaluation of lightning data registered in 1999–2003

The observational network worked continuously, but in 2002 the SAFIR system was out of work by technical reasons. Thus 4 years of lightning database was collected. The system has registered 3,920,083 lightnings over the whole territory. The summarized lightning distribution – calculated for cells of 5×5 km – can be seen in Fig. 2. It happened several times that a station was out of work for shorter or longer time periods. The effect of this can easily be recognized in the cigar shaped NW-SE directed stripe between Sárvár and Véménd. Sárvár is located in the western, while Véménd is located in the south-western part of Hungary.

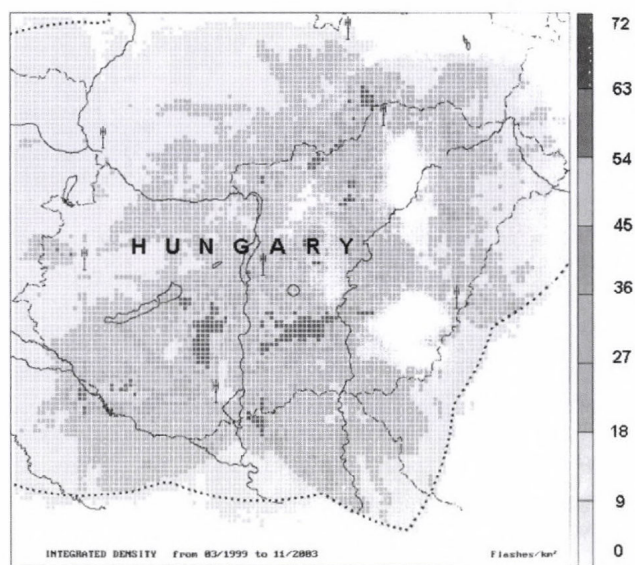


Fig. 2. CG and IC lightnings (flashes/ km^2) in the time period of 1999–2003 (except 2002).

The most frequent occurrence of cloud lightnings consists of three parts. First one was observed at the central part of Hungary, the second is in the southern part of Mátra Mountains next to the northern border. Third one is located near the SW border.

The examined 4 years are too short to establish any climatological features, but in the future we can generalize a very detailed new lightning climatological database of Hungary. Such database would be very useful for the industrial lightning protection.

After the spatial occurrence, the time distribution was generalized for the mentioned years. Two maximum were observed, the first in afternoon, the second in nighttime. Less lightning was observed in the morning time (*Fig. 3*). These results are harmonized with earlier climatological maps.

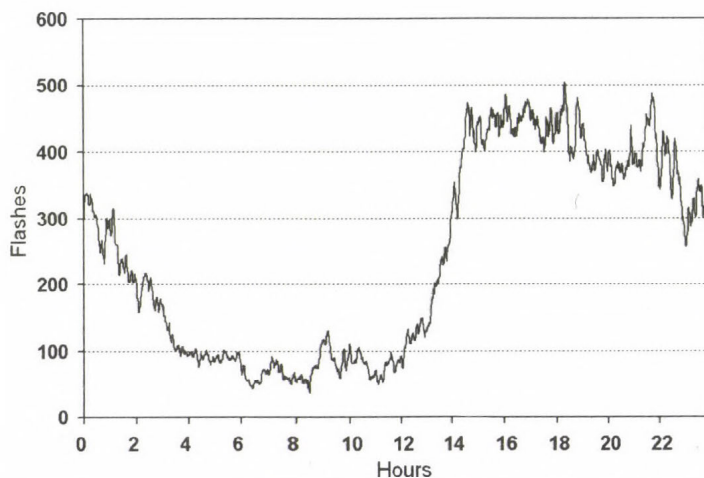


Fig. 3. Average number of CG lightnings in 5-minute over Hungary in 1999–2003 (except 2002).

Fig. 4 illustrates the composite picture of SAFIR data and radar echo. The idea was based on *Sonoi et al.* (1999). This visualization and comparison have two advantages. A larger part of bad observations, caused by interference and background noise, was filtered. On the other hand, the forecaster can distinguish electrical active part of cumulonimbus from the territories represented by intensive precipitation and radar signal. The IC lightning is a very good marker to find developing thunderstorm cells. The shape of active thunderstorm cell is well defined with the IC lightnings (*Weber et al.*, 1998).

The first IC discharges appear in the early time of the forming of a cumulonimbus cloud. The application of observed data generated by the lightning detection system is a good tool in the short range forecasting (*Kononov et al.*, 2000). The rate of CG and IC lightning in the whole data set is about 10% (*Fig. 5*). It means that from a statistical point of view ~ 1 CG lightning/km²/year is a good estimation for Hungary.

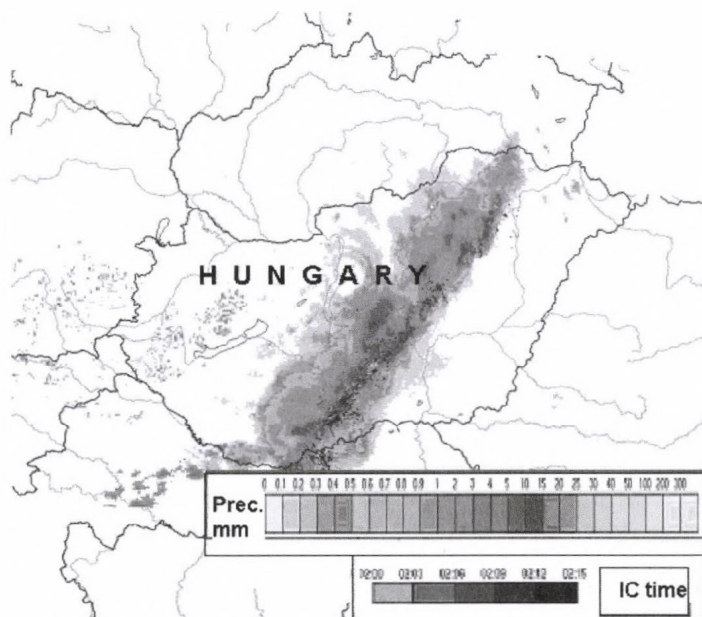


Fig. 4. Combined SAFIR and radar observation visualization on August 30, 2003, 02:00–02:15 UTC.

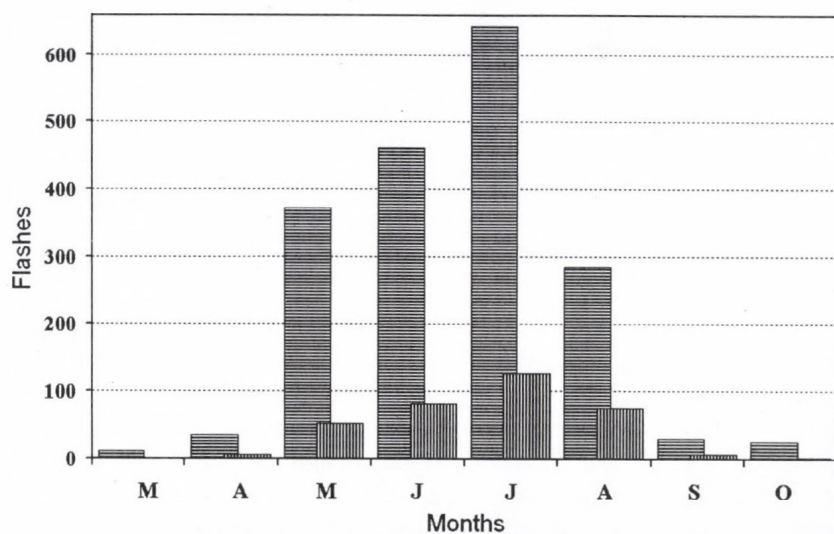


Fig. 5. Monthly IC and CG distribution in 1999–2003 (except 2002) (IC is striped horizontally, CG is striped vertically).

3.1 Polarity

The next electrical parameters are based on the 349,609 CG lightnings registered on the territory of Hungary in 1999–2003. Most of the lightnings (90%) had a negative polarity (*Fig. 6*). This fact is well known from other studies (*Szonda and Wantuch, 2001*). The negative lightnings belong to the individual convective process in the atmosphere. The registered database shows that the ratio of positive lightnings decreases during summer. The positive lightnings belong to the weather frontal effects with probably large ice crystals. In wintertime the positive lightnings are the dominant ones.

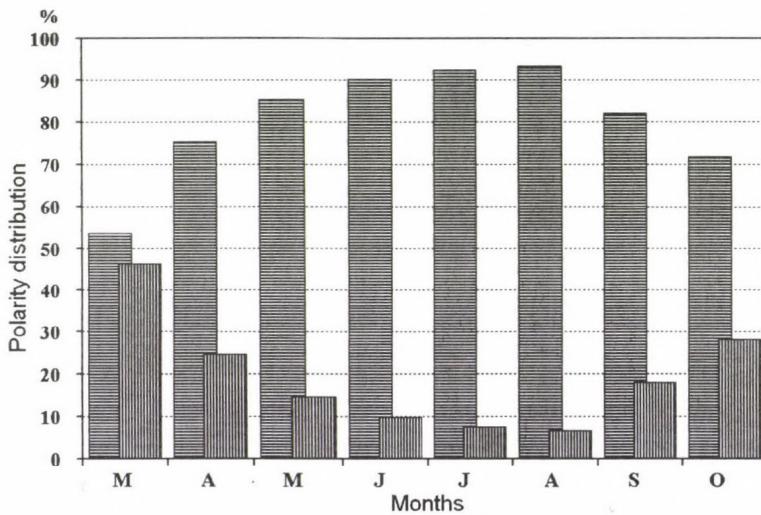


Fig. 6. Monthly current polarity distribution in 1999–2003
(negative polarity is striped horizontally, positive polarity is striped vertically).

3.2 Multiple lightnings

The system assumes that different lightnings belong to a multiple lightning if they occur at the same place or in a predefined distance (5 km) and time sequence (0.5 s). The statistical analysis shows that 79,6% of the positive lightnings are single, and 60,6% of negative lightnings are single. In case of double lightnings this effect is turned. It is in accordance with the result of scientific literature. So, negative discharges are more likely to produce multiple lightnings. The distribution of the positive, negative, and the total multiple lightnings of 1–6 strokes is presented in *Fig. 7*.

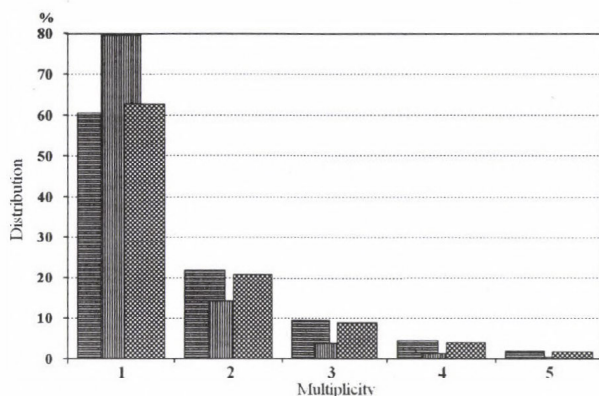


Fig. 7. Probability of multiple lightnings (negative lightnings are striped horizontally, positive lightnings are striped vertically, total lightnings are dotted striped).

3.3 Peak current

The peak current intensity (kA) can be calculated from the strength of the electric field (V/m) at the antenna location and the distance (m) of the lightning. In the next figure (Fig. 8), the characteristic distribution function of positive (+) and negative (-) lightnings is presented together with the number of lightnings in each discrete current intensity interval. One can observe a significant difference between the current intensities of the lightnings with different polarity. The average value for positive lightnings is ~ 25 kA, while for negative lightnings it is ~ 38 kA. On the other hand there are more positive lightnings which are stronger than ~ 70 kA. The largest registered values were +623 kA and -590 kA.

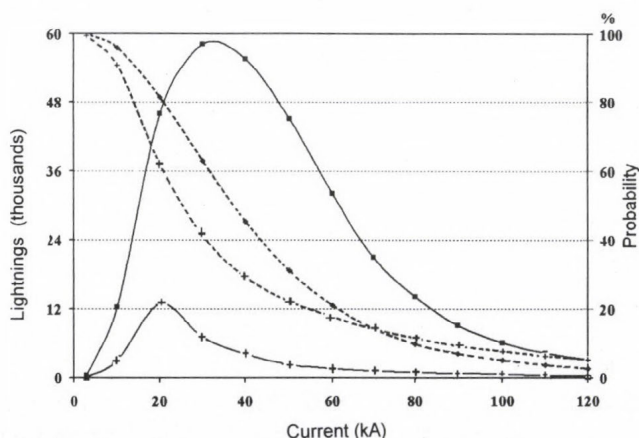


Fig. 8. Distribution of peak current.

3.4 Rise time

Measuring of the rise time with the SAFIR system (Fig. 9) is possible between 0.125 and 16.0 μs . The lowest registered value is 0.3 μs , the most frequent value is 6.2 μs . The average value is $\sim 7.2 \mu\text{s}$.

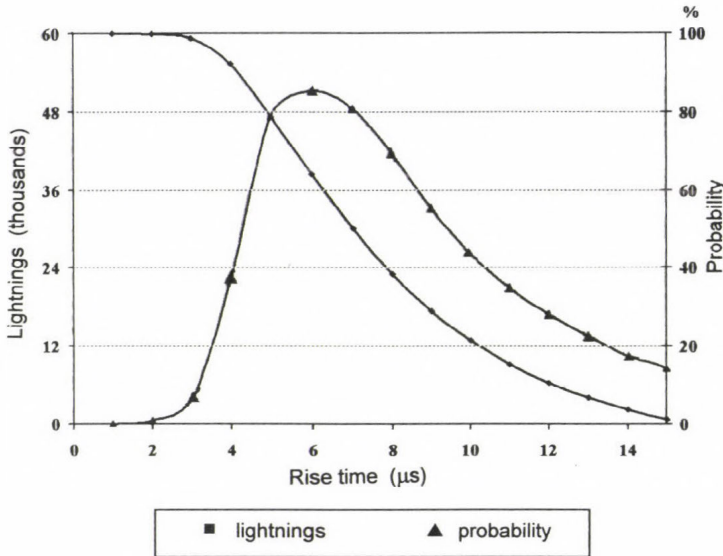


Fig. 9. Distribution of rise time.

3.5 Decay time

Unusually, instead of the half time, the system gives the so-called decay time (that is the time between the peak value and the lower limit of 3 kA). The measuring range for this parameter is set for 16–255 μs . The average value is $\sim 28 \mu\text{s}$, the most frequent value is 25 μs . The distribution curve looks much more equalized than in the case of rise time.

3.6 Steepness of rising phase

The very interesting value of current steepness from electrotechnical point of view can be calculated from the current intensity and rise time. The lowest steepness determined by the predefined limit values (3 kA and 15 μs) is 0.2 kA/ μs , the lowest registered value for both negative and positive lightnings is 0.5 kA/ μs . The maximum steepness differs for the differently polarized

discharges: for positive lightnings it is 509 kA/ μ s, while for negatives it is less than half of it: 237 kA/ μ s. These values are very large for the 90% of front steepness values, which are below 13 kA/ μ s.

3.7 Electric charge

The charge of lightnings can be calculated from the rise time, decay time, and peak current values. The predefined lower limit (0.125/15 μ s and 3 kA) allows the calculation of the lowest charge beginning with 56×10^{-9} As. The lowest registered value is many times larger than this, it is 0.068 As. There is a significant difference between the charge of the positive and negative lightnings. The average value for positive lightnings is ~ 0.5 As, for negative lightnings it is much larger: ~ 0.7 As. There is almost no difference between the maximum charge values, for positive lightnings it is 37 As, for negatives it is 39 As. These values are extremely high, because 90% of charge values are below 1.8 As.

3.8 The energy of the impulse

The integration of the current square – time values gives a number that is proportional to the energy content of the lightning. Similar to the charge, the lower limit determined by the predefined parameters is small. The lowest registered value is 0.00029 kA² s, the largest is 10.55 kA² s. The distribution function on the next figure shows that the average value is only 0.02 kA² s, and the 90% of the values are below 0.06 kA² s.

It can be said that the first test years of the Hungarian lightning detection system were successful. Registered data meet the historical data from literature both in the case of the number of lightnings and the lightning parameters.

4. Conclusion

In 1999, the installation of a lightning detection system was completed in Hungary. This system is suitable not only for detecting and registering intra cloud (IC) and cloud-to-ground (CG) discharges, but it is also capable of identifying major lightning parameters in case of the latter. This paper introduces the SAFIR system, and also includes the most significant statistical data on discharges registered during 1999–2004. The observed information is useful for everyday meteorological work and industrial application.

References

- Kononov, I.I., Petrenko, I., and Yusupov, I.E., 2000: Space-temporal variations of electromagnetic radiation of thunderstorms in the process of their evolution. *25th International Conference on Lightning Protection*. Sept 18, 2000, Rhodes, Greece.
- Laroche, P., Malherbe, C., Bondiou, A., Weber, M., Engholm, C., and Coel, V., 1991: Lightning activity in microburst producing storm cells. *25th International Conference on Radar Meteorology*. June 1991, Paris, France.
- Richard, P., 1998: Propositions of methods of validation of lightning localisation systems performances. *International Conference on Lightning Protection*. September 1998, Birmingham, U.K.
- Sonoi, Y., Kawasaki, Z.I., Maekawa, Y., Fukao, S., and Takashi, T., 1999: Observations of thunderclouds and lightning activity in winter by dual polarization radar and SAFIR. *11th International Conference on Atmospheric Electricity*. June 7-11, 1999, Guntersville, Alabama.
- Szonda, S. and Wantuch, F., 2001: Examination of lightnings detected by SAFIR system in 1999 (in Hungarian). *Elektrotechnika* 94, No. 2, 54-57.
- Weber, M.E., Williams, E.R., and Wolfson, M.M., -Group 43-, Goodman, S.J., 1998: An assessment of the operational utility of GOES lightning mapping sensor. NASA/Marshall Space Flight Center. *Project Report NOAA-18*.

IDŐJÁRÁS

Quarterly Journal of the Hungarian Meteorological Service
Vol. 109, No. 2, April–June 2005, pp. 123–138

A study of ultraviolet solar radiation at Cairo urban area, Egypt

S. M. Robaa

*Astronomy and Meteorology Department, Faculty of Science, Cairo University,
P.O. Box 12613, Giza, Egypt; E-mail: d_robba@hotmail.com*

(Manuscript received in final form February 6, 2004)

Abstract—Monthly mean daily values of global (G) and ultraviolet (UV) solar radiation incident upon a horizontal surface at Cairo urban area during two different periods (1969–1973 and 1993–1997) are presented, analyzed, and compared. The effect of urbanization processes on the solar radiation components is investigated and discussed. It was found that the total amount of the two radiation components, G and UV, received at the urban area of Cairo during the period 1969–1973 highly exceeds the total amount received during the period 1993–1997 for all months of the year. The mean relative reduction of G and UV reached 17.4% and 27.4%, respectively. A significant correlation between G and UV radiation has been found, and the recommended correlation equation has been stated to estimate the values of UV radiation which is difficult to measure at any site in the zone of Lower Egypt. Also, a comparative study of the two radiation components, G and UV, at urban (Cairo) and rural (Bahtim) areas during the period 1993–1997 revealed, that the urban area always has values of G and UV radiation distinctly lower than values found in rural area for all months of the year. Urban-rural mean reduction of G and UV reached 7.0% and 17.9%, respectively. The ratio of the ultraviolet to global radiation (UV/G) are calculated and compared with other sites in the Arabian Peninsula. The effect of atmospheric dust on the measured solar radiation components is also investigated and discussed.

Key-words: urbanization, industrialization, atmospheric dust, ultraviolet solar radiation, global solar radiation, urban areas, rural areas

1. Introduction

Ultraviolet solar radiation either at the edge of the atmosphere or at the Earth's surface, accounts for only a small fraction of the total radiation flux. In outer space, UV radiation accounts for only about 8.73% of the total solar radiation (Al-Aruri *et al.*, 1988), while at any location on the Earth's surface, the UV

radiation value depends on solar zenith angle, atmospheric ozone content, and transparency of the atmosphere (Kylling *et al.*, 2000; Kirchhoff *et al.*, 2002; Luccini *et al.*, 2003). UV radiation wavelength range has been divided into three sub-ranges; UV-A (400–315 nm), UV-B (315–290 nm), and UV-C (290–220 nm). The mentioned lower limit of UV-C (220 nm) is valid only when it is studied in air, but in fact, the wavelength of the shortest wave ultraviolet beams is shorter than 100 nm. The earth surface receives only UV-A and UV-B, while the UV-C component is removed not only by absorption through the protective ozone layer (O₃) but also because it provides energy for several photoionization processes. UV-B is partially absorbed by the ozone layer, while UV-A is transmitted (McKenzie *et al.*, 1995). There are many beneficial and damaging effects of UV-A and UV-B radiation on humans, the ecosystem, animals, plants, and materials (Parrish *et al.*, 1978; Biswas, 1979; Giese, 1982). High doses of ultraviolet radiation, especially band B, causes skin diseases, eye cataract, photo-decomposition, degradation of materials, and may also harm crops (Som, 1992). Inverse relation is known between the ozone density in the atmosphere and the amount of UV reaching the Earth's surface. From this point of view, the UV radiation is highly affected by the ozone which is destroyed by pollutants such as freon refrigerants, spray, and atomic bomb tests (Elhadidy *et al.*, 1990; Fiester and Grasnack, 1992; Tang *et al.*, 1998; Zerefos *et al.*, 2001; Wuttke *et al.*, 2003).

In Egypt, measurements of UV radiation have been taken for last few years. Measurements of global solar radiation began in 1969 at both Cairo and Bahtim using an Eppley pyranometer (Model PSP). The ultraviolet radiation has been measured in Egypt since 1990 at only two meteorological stations of Cairo in the north and Aswan (23°58'N; 32°47'E) in the south, using an Eppley radiometer which is sensitive to radiation in the wavelength band 290–385 nm (Salem, 2000). Although the study of UV radiation is very important because of its dramatic biological effects on humans, animals, plants, the earth's surface, and surrounding atmosphere, the concerned studies of UV radiation is very rare in Egypt. Therefore, the main objective of this paper is to study the characteristics and behavior of UV radiation, and the impact of urbanization on its values at Cairo urban area.

2. Geography and description of the study area

In this study, two Egyptian meteorological stations, namely Bahtim and Cairo, have been selected to represent rural and urban areas, respectively. The two selected stations lie inside the greater Cairo region. Brief description of these two stations is given below.

1. Bahtim agrometeorological station (30°08'N; 31°15'E) lies about 13 km to the northwest of central Cairo near the border between urbanized and cultivated area. It has been established at the end of 1966 in the field of the Agricultural Research Station of the Agricultural Society at Bahtim and has been working on a routine basis up till now (2003). Bahtim area was dominated by vegetation and characterized by clearness of its atmosphere. The surrounding area was also cultivated land, and it was considered to be a good example of the rural area. Unfortunately, the population and human activities started to increase rapidly in Bahtim area during the last few years.

2. Cairo meteorological station (main building of the Egyptian Meteorological Authority) (30°05'N; 31°17'E) lies on the east bank of River Nile near central Cairo on the road leading from the city to the suburb of Heliopolis, to the northeast part of Cairo city. Much of factories exist in the near-by area also, where high density of buildings and population exists in addition to thousands cars and buses. Streets are covered by asphalt and gardens are not abundant. The local soil is originally desert sand. Generally, air quality in Cairo station represents the typical urbanization effects in and around Cairo City.

3. Results and discussion

3.1 Relationship between G and UV solar radiation

Because the measurements of UV radiation are not available at any location in Egypt, except of the two stations of Cairo and Aswan, the estimation of UV at the rural area of Bahtim is of real benefit, especially for the present study.

Clear linear correlation between the ultraviolet and global solar radiation has been found in many studies (*Fiester and Grasnich, 1992; Koronakis et al., 2002*). Therefore, many types of correlations were tried to get out the best fit between G and UV radiation at Cairo using all available monthly mean values of the two parameters for nine years from 1990 to 1998. A significant positive correlation between G and UV radiation has been found in the form

$$UV = a G \pm b, \quad (1)$$

where a and b are the regression coefficients depending on the weather parameters of the location. Data has been processed using an advanced computer program, and the obtained values of a and b were 0.0349 and 0.0261 for Cairo, which represents the typical weather conditions of Lower Egypt. The obtained values of the correlation coefficient is 0.98 and the standard error

of estimate is 0.0023 (Fig. 1). The deduced empirical relationship (Eq. (1)) becomes

$$UV = 0.0349 G - 0.0261. \quad (2)$$

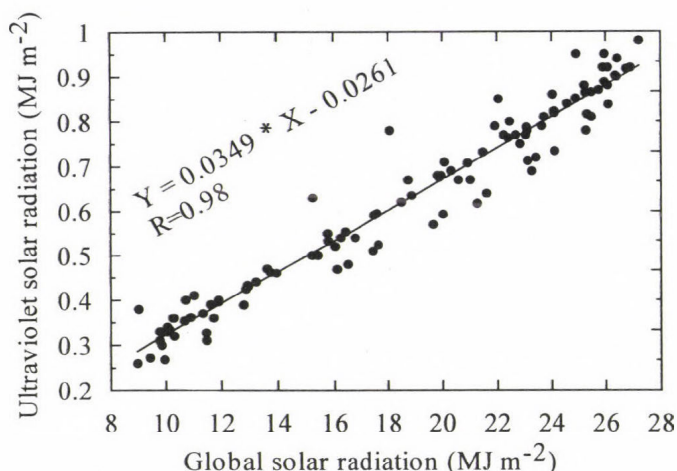


Fig. 1. Correlation between global and ultraviolet solar radiation at Cairo.

3.2 Verification of the empirical equation

To verify the deduced empirical equation (Eq. (2)), the monthly mean values of UV have been calculated for two years, 1999 and 2000, at Cairo using the corresponding values of the measured G radiation and applying Eq. (2). The estimated UV radiation was compared with the corresponding measured data during the same two years, 1999 and 2000. The results are listed in *Table 1*. It can be seen, that the estimated values of UV radiation are in a good agreement with the measured values for all months of the year. The percentage error was found ranged from -2.4 to +5.9, and from -3.7 to +5.1 during the two years, respectively, and from -3.0 to +5.2 for the average data of the two years. The annual mean values of the percentage error of the two years and their average values have been found +1.06, +1.27, and +1.16, respectively (see *Table 1*).

Therefore, it is concluded, that the empirical formula (Eq. (2)) could be used to make the determining of the UV radiation more precise at any location inside Lower Egypt, where there are no measured data of UV radiation or there are instrumental and other difficulties encountered in measuring of UV radiation.

Table 1. Comparison between the measured (UV_m ; MJ m⁻²), and estimated (UV_s ; MJ m⁻²) values of ultraviolet radiation, the percentage error of the estimated values (E%), and the measured global radiation (G_m ; MJ m⁻²) at Cairo during the two years of 1999 and 2000, and the average of the two years

Month	1999				2000				Average of the two years			
	G_m	UV_m	UV_s	E%	G_m	UV_m	UV_s	E%	G_m	UV_m	UV_s	E%
Jan	11.22	0.374	0.365	2.2	10.44	0.345	0.338	2.0	10.83	0.359	0.352	2.1
Feb	13.63	0.446	0.450	-0.8	14.56	0.483	0.482	0.2	14.10	0.465	0.466	-0.3
Mar	18.70	0.620	0.626	-1.0	19.13	0.624	0.642	-2.8	18.91	0.622	0.634	-1.9
Apr	22.89	0.814	0.773	5.1	23.80	0.848	0.805	5.1	23.34	0.831	0.789	5.1
May	25.71	0.926	0.871	5.9	26.02	0.923	0.882	4.4	25.86	0.924	0.877	5.2
Jun	27.44	0.962	0.932	3.1	27.12	0.959	0.920	4.0	27.28	0.960	0.926	3.5
Jul	26.52	0.936	0.899	3.9	26.48	0.927	0.898	3.1	26.50	0.931	0.899	3.5
Aug	23.69	0.794	0.801	-0.9	23.51	0.804	0.794	1.2	23.60	0.799	0.798	0.2
Sep	21.53	0.712	0.725	-1.9	20.36	0.679	0.684	-0.8	20.95	0.695	0.705	-1.4
Oct	15.94	0.519	0.530	-2.2	15.48	0.496	0.514	-3.7	15.71	0.507	0.522	-3.0
Nov	12.94	0.433	0.426	1.7	11.39	0.381	0.371	2.5	12.17	0.407	0.398	2.1
Dec	11.28	0.359	0.368	-2.4	9.81	0.316	0.316	0.0	10.55	0.338	0.342	-1.2
Mean	19.29	0.658	0.647	1.06	19.01	0.649	0.637	1.27	19.15	0.653	0.642	1.16

3.3 Impact of urbanization on G and UV radiation values received at Cairo urban area

Urbanization and industrialization processes have increased very rapidly in and around Cairo city. These processes cause not only an increase of atmospheric pollutants, which are harmful to human health and comfort, but also create several serious environmental problems. One of these problems is the attenuation of solar radiation components received at the Earth's surface especially the ultraviolet radiation. In order to investigate the effect of urbanization processes on the total global and ultraviolet solar radiation received at the urban area of Cairo, the monthly mean values of G and UV radiation for the old period (1969–1973) have been compared with the corresponding values of the recent period (1993–1997). The above two equal periods were selected for this study, because the measurements of G and UV radiation began at Cairo in 1969 and 1990, respectively. Furthermore, the monthly mean values of the total column ozone (O_3) retrieved from DOBSON surface observations at Cairo for the above two periods are also compared and taken into consideration to avoid the defects of neglecting effect of

stratospheric ozone on the modification of G and UV radiation values. The values of the old period (1969–1973) have been taken as reference base values for the non-urbanized period, while the values of the recent period (1993–1997) have also been taken to represent the heavy urbanized period. The used data of G, UV radiation, and O₃ have been obtained from the Egyptian Meteorological Authority, except UV radiation values for the non-urbanized period (1969–1973), where there are no measured values for UV radiation. Therefore, the monthly mean values of UV radiation have been estimated for the period (1969–1973) using the corresponding values of G for the same period and applying the deduced empirical formula (Eq. (2)). Furthermore, the monthly mean values of the percentage reduction (E%) of G, UV radiation, and O₃ values have been calculated for the recent urbanized period. The results and used data are presented and illustrated by *Figs. 2–5*. Also, the seasonal mean values of the G, UV radiation, and O₃ have been calculated for both non-urbanized and urbanized periods, and the results are given in *Table 2* with their percentage reductions.

Table 2. The seasonal mean values of G, UV radiation (MJ m⁻²), and O₃ (DU) at Cairo urban area during the two periods (1969–1973 and 1993–1997), as well as the relative percentage reduction of their values, E%

Season	G			UV			O ₃		
	1969– 1973	1993– 1997	E%	1969– 1973	1993– 1997	E%	1969– 1973	1993– 1997	E%
Winter	14.83	11.14	24.9	0.492	0.313	36.3	298	294	1.2
Spring	24.38	21.00	13.9	0.825	0.625	24.2	316	307	2.8
Summer	28.63	24.84	13.2	0.973	0.779	19.9	297	294	0.9
Autumn	19.13	15.86	17.1	0.642	0.463	27.8	283	275	2.6
Annual mean	21.74	18.21	17.3	0.733	0.545	27.1	298	293	1.9

A high variability of G and UV radiation values from month to month can be clearly seen in *Figs. 2* and *3*. This variability is caused not only by cloudiness but also the changing aerosol load. The monthly mean values of both G and UV radiation rise very regularly from a minimum value in December to a maximum value in July in both periods (1969–1973 and 1993–1997). Furthermore, during the non-urbanized period (1969–1973), the maximum values of G and UV radiation were 29.32 and 0.997 MJ m⁻² and the minimum values were 13.35 and 0.440 MJ m⁻², respectively, while in the recent urbanized period (1993–1997), the maximum values of G and UV

radiation were 26.09 and 0.820 MJ m⁻² and the minimum values were 9.95 and 0.268 MJ m⁻², respectively (Figs. 2 and 3). It could be also noticed, that the radiation values of the non-urbanized period are always higher than the values found in the recent urbanized period throughout the months of the year. The annual mean values of G and UV radiation (21.83 and 0.736 MJ m⁻² for G and UV, respectively) during the non-urbanized period have been found higher than those of the urbanized period (18.21 and 0.548 MJ m⁻² for G and UV, respectively) (Table 2). This is ascribed to the serious combined effects of the recently increased atmospheric pollution as sequence of increasing population, urbanization, and industrialization, as well as stationary and mobile sources of combustion in and around Cairo city.

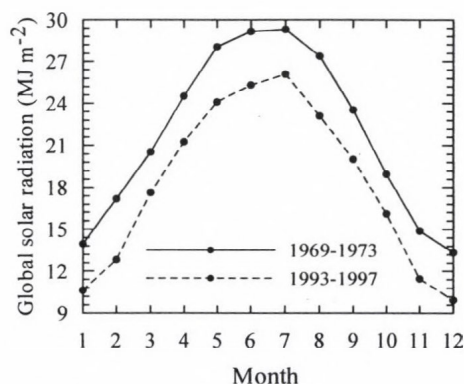


Fig. 2. The monthly variation of G radiation during the non-urbanized period (1969-1973) and urbanized period (1993-1997) at Cairo urban area.

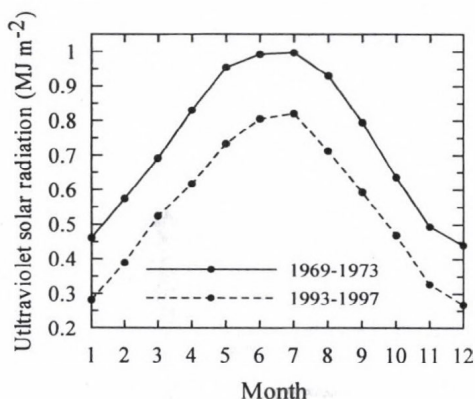


Fig. 3. Same as Fig. 2, but for UV radiation.

On the other hand, in Fig. 5 and Table 2, the relative percentage reduction (E%) of both G and UV radiation at the urban area, induced by recent urbanization processes, varies from month to month and from season to season. The heavy maximum reduction of the two radiation components occurred in December (winter season) (E=25.5% and 39.1% for G and UV, respectively), while the minimum reduction occurred in July (summer season) (E=11.0% and 17.8% for G and UV, respectively). This is due to the fact, that the winter season has recently higher levels of aerosol and atmospheric pollutants than the summer season. This result agrees with the findings of Robaa (1999), who found that the pollutant and aerosol concentrations, liberated recently from urbanization and industrialization processes, have been increased for more than threefold in the winter season and around double in

the summer season. The annual mean relative reduction of G and UV were 17.4% and 27.4%, respectively. It is also clearly noticed, that the UV radiation is more attenuated than the G radiation during all months of the year (Fig. 5). This is due to the fact that radiation loss due to pollutant aerosols is strongly wavelength-dependant, and the shorter wavelengths are much more seriously affected than the longer wavelengths. This means that the UV component of solar radiation is subjected to the greatest atmospheric scattering obeying the well-known Rayleigh scattering process (Rizk *et al.*, 1985; Sami and Al-Aruri, 1990).

On the other hand, it can be seen that the annual variation of the values of stratospheric ozone, O_3 , are irregular at Cairo, and the values of non-urbanized period (1969–1973) are always higher than the values found in the recent urbanized period (1993–1997), throughout the year months (Fig. 4). This is due to effect of the released pollutant gases, which increase the content of chlorine in the stratosphere with a consequent depletion of ozone (Watson, 1988). Furthermore, it was found that O_3 attained its maximum value (316 and 307 DU for non-urbanized and urbanized periods, respectively) in the spring season, mainly March, while the minimum value (283 and 275 DU for non-urbanized and urbanized periods, respectively) occurred in the autumn season, mainly in October and November.

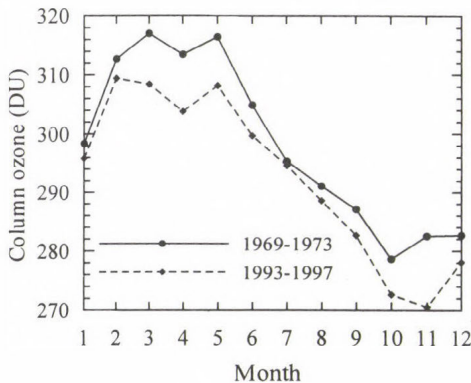


Fig. 4. Same as Fig. 2, but for ozone amount.

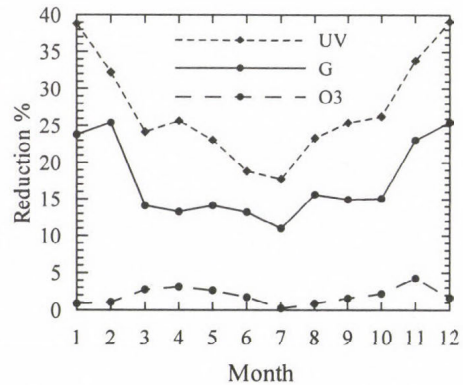


Fig. 5. Monthly variation of the calculated percentage reduction of G, UV, and O_3 during the urbanized period (1993–1997).

It is also noticed, that the ozone values have been weakly attenuated during the recent urbanized period (Figs. 4 and 5 and Table 2). The monthly mean values of the reduction of O_3 are also irregular and ranged between -0.25% in July to 4.25% in November, while the annual mean value was 1.89% . This result agrees with the finding of Shaltout *et al.* (1994) and Salem (2000), who

found that the stratospheric ozone is stable and has normal density over Cairo City. Although the attenuation in the stratospheric ozone at any place causes increase of UV radiation values, the reverse process occurred at Cairo urban area and the UV radiation values are attenuated. This has two reasons: first, as motioned above, the percentage values of ozone attenuation are small. Second, the increased UV values, as a result of the attenuation in ozone amounts, could be lost by the significant effects of urbanization processes. Therefore, it could be concluded, that the urbanization and industrialization processes are considered the distinct main reason in the reduction of the solar radiation component values at the urban area of Cairo.

3.4 Comparative studies on G and UV radiation at rural and urban areas

Five years mean G and UV solar radiation data (1993–1997) for both urban (Cairo) and rural (Bahtim) areas are presented and compared. The used G and UV radiation data have been obtained from the Egyptian Meteorological Authority, except UV radiation values at the rural area of Bahtim, where there are no measurements for UV radiation. Therefore, for the comparative purposes, the values of UV radiation have been estimated using the corresponding values of G radiation and applying the deduced empirical formula (Eq. (2)). The monthly mean values of the urban-rural percentage reduction (E%) for G and UV radiation have also been calculated. The results and used data are presented and illustrated by Figs. 6–8.

In Figs. 6 and 7, it was found that both urban and rural areas have similar annual variation of G and UV radiation with higher values at rural area throughout the months of the year. This is attributed to an urban area, which is characterized by highly polluted air and fine particulate grains. Consequently, a loss in the energy of solar beam received by the surface due to backscattering and absorption, while high radiation values over the rural area is attributed to its rural site dominated by vegetation and characterized by clearness of its atmosphere. The values of G radiation at the rural area ranged between 10.72 MJ m^{-2} in December and 27.74 MJ m^{-2} in June, while UV radiation ranged between 0.348 MJ m^{-2} in December and 0.942 MJ m^{-2} in June.

It could be noticed, that the urban-rural global and ultraviolet reduction values vary from month to month according to the exchanged effects of cloud cover and air pollution intensities induced by urbanization processes. E% values ranged between 3.3% and 9.0% for G radiation and between 10.4% and 23.0% for UV radiation (Fig. 8). Generally, the urban area receives 7.0% less G and 17.8% less UV radiation compared to rural area, as annual average. This result agrees with finding of Galindo (1962), who found that the global radiation attenuation is 10% for Mexico city compared to rural surroundings,

and *Padmanabhamurty* and *Mandal* (1981), who also found significant urban and rural radiation differences for Delhi city. In our study, the relatively lower G radiation attenuation for urban area (Cairo) compared to rural surrounding (Bahtim) is perhaps due to the effect of surface wind, which causes rapid transportation of pollutants from the urban complex to neighboring rural area.

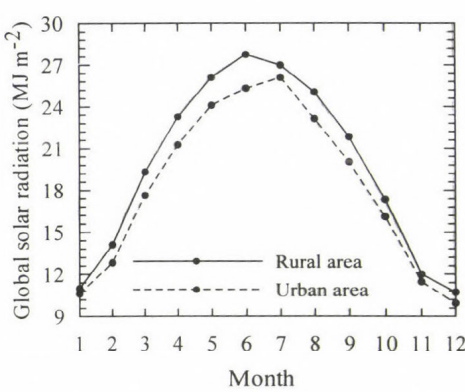


Fig. 6. Monthly variation of G radiation at both urban (Cairo) and rural (Bahtim) areas during the urbanized period (1993–1997).

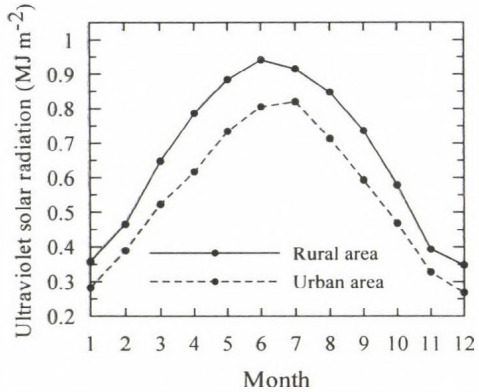


Fig. 7. Same as Fig. 6, but for UV radiation.

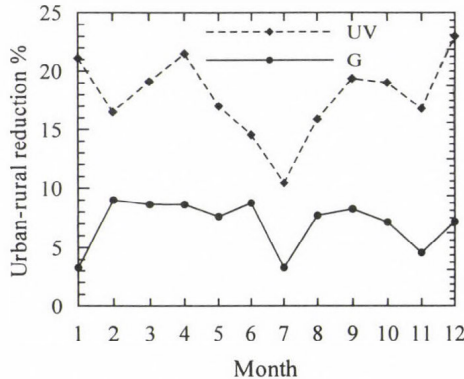


Fig. 8. Monthly variation of the calculated urban-rural percentage reduction of G and UV radiation during the urbanized period (1993–1997).

In Fig. 8, one can notice that the monthly mean percent reduction in the received UV radiation is higher than in G radiation in the urban area of Cairo. This is due to the UV component of solar radiation, which is a subject to the greatest atmospheric scattering obeying, the well-known Rayleigh scattering process (*Sami* and *Al-Aruri*, 1990). A large drop in the reduction of urban-

rural global and ultraviolet radiation is well noticed in July (Fig. 8). The reason of this drop is that the summer season (mainly July) is characterized by cloudless skies and lower levels of aerosol and atmospheric pollutants (Robaa, 1999).

3.5 Seasonal variation of the ratio UV/G

Fig. 9 shows the monthly variation of the ratio UV/G for Cairo during the non-urbanized (1969–1973) and urbanized periods (1993–1997) compared with UV/G values of two sites in the Arabian peninsula: Kuwait city in Kuwait (Al-Aruri et al. 1988) and Makkah in Saudi Arabia (Khogali and Al-Bar, 1992).

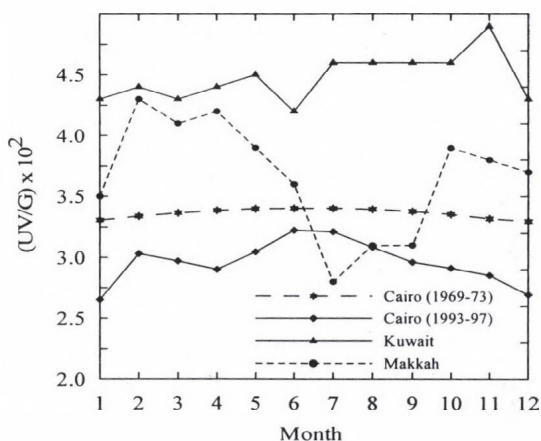


Fig. 9. Monthly variation of UV/G ratio for Cairo during the two periods (1969–1973 and 1993–1997) compared with UV/G for Kuwait and Makkah.

From this figure we can deduce the following:

- At all sites the ratio UV/G ranged between 2.7% and 4.9%.
- The lower values of UV/G occurring in winter are caused by lower solar elevation during this season.
- Cairo ratio of the urbanized period (1993–1997) is the lowest value compared to all other sites most of the year. This is due to the high air pollution in Cairo city produced by traffic and industrial activities. The curve of the non-urbanized period (1969–1973) has higher values than those of the urbanized period (1993–1997), and characterized by a very slight seasonal variation. This may be caused by the fact that the attenuation of UV that occurs during the recent period (1993–1997) is

higher than the attenuation of G as shown in *Fig. 8*, while the higher ratios UV/G during the non-urbanized period can be explained by the stronger absorption of G , that has longer wavelength than UV , due to the water vapor droplets of cloud. Similar features were also observed at Potsdam by *Fiester and Grasnack (1992)*.

- Kuwait ratio is the highest compared to all other sites most of the year. It is possibly due to the effect of Iraq-Iran war during the 1980's on the stratosphere over Kuwait, where G and UV radiation measurements in Kuwait is performed from July 1985 to June 1987 during the war (*Al-Aruri et al. 1988*).
- Makkah ratio has relatively higher values most of the year. This is due to the population (over one million people) and transporting vehicles gathered in July and August in the pilgrimage season of 1987. A large drop in the ratio UV/G is also observed in Makkah from July to September. This may be because of the attenuation of UV by dust and low tropospheric ozone during these months (*Khogali and Al-Bar, 1992*).
- The values of UV/G are higher for Kuwait and Makkah than for Cairo due to the stronger absorption of G and weaker absorption of UV at these two sites. This may be due to the difference in size and amount of the fine particles at both Kuwait and Makkah, or disturbances in the ozone layer at Kuwait due to Gulf war, or both (*El-Hadidy et al. 1990*).

3.6 The effect of atmospheric aerosols on G and UV solar radiation at Cairo

To study the effect of atmospheric aerosols on both G and UV solar radiation at Cairo, we selected the dusty days of the five years period from 1990 to 1994 for the urban area of Cairo, and only five days were available. The mentioned period (1990–1994) was selected for availing this data. During the same period, an equal number of dust free days were chosen. The chosen dust free days were in the same year and month that the dusty ones. It is of value to note here, that the dusty days were chosen with visibility less than 10 km, while dust free days had a visibility of more than 20 km. It must be noted that: (a) the technique, by which we selected clear days, is a draft method using horizontally measured visibility, and thus gives approximative estimation, (b) the ozone content is not considered for the above calculations and the quantitative establishments are valid solely for the days used, thus the percentage values cannot be considered characteristic or normal values. Under this choice, percentage of reduction in the received G and UV components were calculated and listed in *Table 3*. It was found, that the reduction in the received G and UV radiation due to the effects of the aerosol particles ranged between 26% and 45% for G and between 33% and 59% for UV . One can

also notice, that the maximum percentage reduction in the received G (45%) and UV (59%) radiation is higher than such reduction in the G and UV radiation induced by urbanization processes at Cairo (*Table 3*). This is due to the simultaneous combined effects of aerosol particles, urbanization, and industrialization processes during the dusty days.

Table 3. Calculated percentage reduction in the received total daily G and UV solar radiation due to the effect of atmospheric aerosols at the urban area of Cairo

Days	Reduction (%)	
	G	UV
March 05, 1990**	43	58
March 22, 1990*		
March 18, 1991**	26	33
March 05, 1991*		
April 22, 1992**	32	47
April 15, 1992*		
May 10, 1993**	45	59
May 25, 1993*		
April 03, 1994**	38	46
April 17, 1994*		

* Clear day

** Dusty day

One can also notice, that the percentage reduction in the received UV radiation is always higher than such reduction in G radiation during all dusty days (*Table 3*). This result can be attributed to, as mentioned before, the absorption by solid particles and to the known Rayleigh scattering, which varies with the inverse fourth power of the wavelength (λ^{-4}). Consequently, the UV component of solar radiation is a subject to the greatest atmospheric scattering. These results agree with the findings of both *Sami* and *Al-Aruri* (1990) and *Salem* (2000).

3. Conclusions

Although the study of ultraviolet, UV, solar radiation is very important because of its dramatic biological effects on humans, animals, plants, the earth's surface, and the surrounding atmosphere, the concerned studies of UV radiation is very rare in Egypt. Therefore, the present study is an attempt to study the characteristics and behavior of UV beside the total global, G,

radiation and the impact of urbanization on their received values at Cairo urban area. The measured and estimated values of G and UV radiation beside stratospheric ozone, O_3 , over urban (Cairo) and rural (Bahtim) areas during a non-urbanized (1969–1973) and urbanized period (1993–1997) have been used. Also, the effect of atmospheric dust on G and UV radiation is also investigated and discussed. The results could be summarized in the following:

- A significant correlation between G and UV radiation has been found with correlation coefficient 0.98 and the standard error was close to zero. The recommended correlation equation has been stated to estimate the values of UV radiation which is difficult to measure at any site in the zone of Lower Egypt.
- The monthly mean values of G and UV received at Cairo urban area during the non-urbanized period highly exceeds the values received during the urbanized period for all months of the year.
- At Cairo urban area, the annual mean values of G and UV radiation were 21.83 and 0.736 MJ m⁻² during the non-urbanized period and 18.21 and 0.548 MJ m⁻² during the urbanized period, while the mean relative reduction of G and UV were 17.4% and 27.4%, respectively. The UV radiation is more attenuated than G radiation during all months of the year. This is due to the radiation loss caused by pollutant aerosols, which is strongly wavelength-dependant, and the shorter wavelengths are much more seriously affected than longer wavelengths.
- The increase in UV values, as a result of the attenuation in ozone amount at Cairo, was lost by the significant effects of urbanization processes, that reduce the solar radiation amounts. Therefore, it could be concluded, that the urbanization and industrialization processes are considered the distinct main reason in the reduction of the values of the solar radiation components at Cairo urban area.
- A comparative study for G and UV radiation at both urban and rural areas during the urbanized period (1993–1997) revealed, that the urban area always has values of G and UV radiation distinctly lower than that found in rural area for all months of the year. Urban-rural mean reduction of G and UV were 7.0% and 17.9%, respectively.
- The ratio UV/G of the non-urbanized period (1969–1973) has higher values than those of the urbanized period (1993–1997), and characterized by very slight seasonal variation caused by the attenuation of UV. The attenuation of UV in the urbanized period is higher than that of G, while the higher values of the non-urbanized period can be explained by the stronger absorption of G, that has longer wavelength than UV, due to the water vapor droplets of cloud.

- In the dusty days, the reduction in the received G and UV radiation due to the effects of atmospheric aerosol particles ranged between 26% and 45% for G and between 33% and 59% for UV. The maximum percent reduction in the received G (45%) and UV (59%) radiation was higher than the same reduction in the G and UV radiation induced by urbanization processes at Cairo. This is due to the simultaneous combined effects of aerosol particles and urbanization processes during the dusty days. The quantitative establishments are valid solely for the days used, and the percentage values cannot be considered characteristic or normal values.

References

- Al-Aruri, S., Rasas, M., Al-Jamal, K., and Shaban, N., 1988: An assessment of global ultraviolet radiation in the range (0.290-385 μm) in Kuwait. *Sol. Energy* 41, 159-162.
- Biswas, A.K., 1979: *The Ozone Layer*. Vol. 4. Pergamon Press, Oxford.
- El-Hadidy, M.A., Abdel-Nabi, D.Y., and Kruss P.D., 1990: Ultraviolet solar radiation at Dhahran, Saudi Arabia. *Sol. Energy* 44, 315-319.
- Fiester, U. and Grasnack, K.H., 1992: Solar UV radiation measurements at Potsdam (52°22'N; 31°5'E). *Sol. Energy* 49, 541-548.
- Galindo, I., 1962: La radiacion en Mexico en 1957 (Global radiation in Mexico city). Instituto de Geafisica, UNAM.
- Giese, A.C., 1982: *Living with our Suns' Ultraviolet Rays*. Plenum Press, New York.
- Khogali, A. and Al-Bar, O.F., 1992: A study of solar ultraviolet radiation at Makkah solar Station. *Sol. Energy* 48, 79-87.
- Kirchhoff, V.W., Silva, A., and Pinheiro, K., 2002: Wavelength dependence of aerosol optical thickness in the UV-B band. *Geophys. Res. Lett.* 29, 1620, doi:10.1029/2001.
- Koronakis, P.S., Sfantos, G.K., Paliatsos, A.G., Kaldellis, J.K., Farofalakis J.E., and Koronaki, I.P., 2002: Interrelations of UV-global/global/diffuse solar irradiance components and UV-global attenuation on air pollution episode days in Athens, Greece. *Atmos. Environ.* 36, 3173-3181.
- Kylling, A., Dahlback, A., and Mayer, B., 2000: The effect of clouds and surface albedo on UV irradiances at a high latitude site. *Geophys. Res. Lett.* 27, 1411-1414.
- Luccini, E., Cede, A., and Piacentini, R.D., 2003: Effect of clouds on UV and total irradiance at Paradise Bay, Antarctic Peninsula, from a summer 2000 campaign. *Theor. Appl. Climatol.* 75, 105-116.
- McKenzie, R.L., Blumthaler M., Booth C.R., Diaz S.B., Frederick J.E., Ito T., Madronich S., and Seckmeyer, G., 1995: Surface ultraviolet radiation. In *Scientific Assessment of Ozone Depletion: 1994. WMO Global Ozone Research and Monitoring Project Report*, No. 37, 9.1-9.22.
- Padmanabhamurty, B. and Mandal, B.B., 1981: Urban-rural radiation differences. *Mausam* 33, 509.
- Parrish, J.A., Rox Anderson, R., Urbach, F., and Pitts, D., 1978: *UV-A*. Plenum Press, New York.
- Rizk, H.F., Farag, S.A., and Ateia, A.A., 1985: Effect of pollutant aerosols on spectral atmospheric transmissivity in Cairo. *J. Environ. Int.* 11, 487-492.
- Robaa, S.A., 1999: Impact of urbanization on meteorology and human comfort in Greater Cairo, Egypt. *Ph.D. Thesis*. Astronomy and Meteorology Dept., Faculty of Science, Cairo University.

- Salem, A.I., 2000: Analysis and correlation of ultraviolet solar radiation from routine meteorological measurements over Egypt. *Mausam* 51, 275-280.
- Sami, D. and Al-Aruri, 1990: The empirical relationship between global radiation and global ultraviolet (0.290-0.385 μm) solar radiation components. *Sol. Energy* 45, 61-64.
- Shaltout, M.A., Ghonim, M.M., Trabea, A.A., and Allam, H., 1994: Ultraviolet solar radiation over Egypt. *World Renewable Energy Congress - III*. Reading University, U.K., 5, 2, 1506-1509.
- Som, A.K., 1992: Solar UV-B radiation measurements over Bahrain. *Renew. Energ* 2, 93-98.
- Tnag, X., Madronich, S., Wallington, T., and Calamari, D., 1998: Changes in tropospheric composition and air quality. *J. Photoch. Photobio. B* 46, 83-95.
- Watson, R.T., 1988: Present state of knowledge of the upper atmosphere. *An assessment report*. NASA RP-1208, Washington D.C.
- Wuttke, S., Verdebout, J., and Seckmeyer, G., 2003: An improved algorithm for satellite derived UV Radiation. *Photochem. Photobiol.* 77, 52-57.
- Zerefos, C.S., Balis, D., Tzortziou, M., Bais, A., Tourpali, K., Meleti, C., Bernhard, G., and Herman, J., 2001: A note on the interannual variation of UV-B erythral doses and solar irradiance from ground - based and satellite observations. *Ann. Geophys.* 19, 115-120.

BOOK REVIEW

András Gelencsér: Carbonaceous Aerosol. Springer, 2004, Dordrecht, The Netherlands, 350 pages, with a rich reference list, and several figures and tables.

Hungarian aerosol research started about forty-five years ago. The original aim was to determine the nature of atmospheric aerosol particles serving as condensation nuclei during cloud formation. For this reason great efforts were devoted to identify water-soluble substances and the size distribution of particles consisting of these materials. At that time this obviously meant *inorganic ions*. This was due to the fact that practically nobody believed that organic compounds existing in the aerosol also contains water-soluble species. Secondly, analytical methods for detecting such materials were rather scanty. Organic compounds in the particles were investigated solely in air pollution studies after dissolving the aerosol samples in organic solvents. However, these studies clearly showed that species analyzed give only a small fraction of the total mass of organic substances. Since the natural solvent in atmospheric environment is water, it became clear that the study of possible water-soluble *organic species* is obviously needed if we want to understand cloud and precipitation formation in the atmosphere.

Such research began ten years ago at the University of Veszprém, partly in European cooperation, by the workers of the Air Chemistry Group sponsored by the Hungarian Academy of Sciences. Their efforts have given important results in the field outlined. At the same time a new generation of young scientists with background in chemistry was formed, who are able to do this complicated research. In this respect the author of this book is a good example. As the chapters show, he and his associates not only have made an excellent research, but also his knowledge gained made it possible to write the first book on carbonaceous aerosol.

The volume consists of five chapters. After the first introductory part, the sampling and analytical techniques making the observation of carbonaceous particles of different types in the air possible are summarized. The third chapter is devoted to the presentation of major carbonaceous particle types and their sources. The classification of carbon containing species (excluding carbonates of negligible significance) is not an easy task. Except soot particles of various types (black carbon, elemental carbon), a major part of carbonaceous materials is composed of organic matter of different kind and nature. The organic particles can be directly emitted into the air by natural

sources (vegetation, living organism, soil and oceans) as well as by human activity. The latter includes biomass and fossil fuel burning. The total global release of these primary particles is around 10 Tg yr^{-1} expressed in carbon equivalents. At least the same amount of organic particulate mass (secondary organic particles) is produced yearly by chemical reactions and condensation in the air of organic gases and vapors liberated by biogenic and anthropogenic processes. The study of secondary organic particle formation is rather difficult. It seems, however, that ozone and hydroxyl radicals play an important part in the control of the oxidation of organic precursor gases, which leads to condensable species. The estimation of the partition of gaseous and aerosol phases also an essential, but not well-solved problem. Although the formation of organic compounds with relatively low carbon number is possible in this way, the production of humic-like substances (HULIS), composed of macromolecules, is determining in particular. This is due to the observational fact indicating that the concentration of this group of compounds is very substantial in the air, and a part of them is soluble in water. It is to be noted that the author of this volume, and the group in Veszprém, carried out important work concerning this new subject.

The fourth chapter is entitled "Organic chemistry of aerosol". In this chapter the chemical and physical properties of organic aerosol are summarized, including such essential properties as the concentration, size distribution, and scavenging by cloud and rain of organic particles. The possibility of using organic particles as tracers is also outlined. From meteorological point of view, the last chapter is particularly interesting. The reader understands from this chapter: why the study of organic particles is so important. Thus, the optical properties of organic aerosol are presented and discussed from the point of view of radiation transfer in the atmosphere. Further, the hygroscopic behavior of particulate organic species is also described. Their possible effects on condensation and ice nucleation are explained in a very convincing manner. Since the organic particles influence the cloud structure, it is evident that they play an important part not only in the control of water cycle, but also in the indirect aerosol climatic forcing. Finally, a subchapter deals with the role of carbonaceous particles in the heterogeneous reaction in the atmosphere.

In summary we can conclude that *Gelencsér* wrote a very precious book. First, it gives an excellent review of a new branch of atmospheric aerosol chemistry. Secondly, the volume indicates the development of atmospheric chemistry. It makes it obvious that professional chemists can make an important contribution to the evolution of atmospheric science. The last chapter also proves that such chemical studies are very useful to a deeper understanding of such classical meteorological problems as cloud and

precipitation formation, solar and terrestrial radiation transfer, and climate in general.

The volume, published in the Atmospheric and Oceanographic Science series of the editor, is thus proposed to everybody, for example meteorologists and chemists, interested in up-to-date art of state of the science of atmospheric environment.

E. Mészáros

Wilford Zdunkowski and Andreas Bott: Dynamics of the Atmosphere. A Course in Theoretical Meteorology. Cambridge University Press, Cambridge, 2003. 719 pages, 187 figures.

Wilford Zdunkowski and Andreas Bott: Thermodynamics of the Atmosphere. A Course in Theoretical Meteorology. Cambridge University Press, Cambridge, 2004. 251 pages, 37 figures.

There are many "classical" schools of theoretical meteorology, one of them is the German School. There were many highlights of the activity of German meteorologists in the last one and a half centuries, and the influence generated by the meteorological reference books and university textbooks of the German School is very strongly perceptible in the meteorological communities of the Central and Eastern European countries.

Wilford Zdunkowski, retired professor of the Johannes Gutenberg University in Mainz and *Andreas Bott*, professor of the Rheinische Friedrich Wilhelms University in Bonn, former lecturer of the Mainz University have declared in the preface to their book to be determined by the activity of legendary predecessors like professors *K. H. Hinkelmann* and *J. G. Korb*.

The structure and way, the various topics of the dynamics and thermodynamics of the atmosphere are discussed, are similar to the methods of the German School.

The dynamics of the atmosphere is discussed in two independent parts in one book. It is quite common in university textbooks of dynamic meteorology to treat basic mathematics in the introductory chapters, but it is novel to divide the book into two independent parts: one dealing with pure mathematics and one with applied mathematics, i.e., the dynamics of the atmosphere. The most important mathematical tools of vector algebra, vector function theory, differential and integral calculus are presented in Part I. Even the concept of nonlinear dynamics is discussed here.

Part II of this heavy textbook gives all the basic elements of dynamic meteorology in 27 chapters. Such rarities like the usage of the natural coordinate system can also be found in the book. A detailed and profound discussion of atmospheric wave motions, especially Rossby wave motions, are given by the authors. The description of boundary layer processes is also a valuable part of the book. The chapters dealing with the role of baroclinic instability, atmospheric modeling, and predictability summarize the results of theoretical meteorology of the last couple of decades.

The coursebook on thermodynamics gives a broad spectrum of the knowledge of physical thermodynamics applied to atmospheric processes. After the basic concepts the fundamental laws of thermodynamics are discussed. Thermodynamic potentials and stability conditions, thermodynamic diagrams and special adiabats are presented in full details. Chapters presenting thermal radiation, constitutive equations for irreversible fluxes, and state functions for cloud air are further substantial parts of the book.

Sets of exercises (160 in the first and 80 in the second volume) make the books profitable both for undergraduate and graduate students of meteorology.

Hungarian readers of the volumes, who are familiar with the footprints of the classical German meteorological school in the traditional textbooks of *Frigyes Dési*, *Ferenc Rákóczi*, and *Gusztáv Götz*, will most probably welcome the new results of the last quarter of a century on the dynamics and thermodynamics of the atmosphere, worked into these fine volumes.

Gy. Gyuró

GUIDE FOR AUTHORS OF *IDŐJÁRÁS*

The purpose of the journal is to publish papers in any field of meteorology and atmosphere related scientific areas. These may be

- research papers on new results of scientific investigations,
- critical review articles summarizing the current state of art of a certain topic,
- short contributions dealing with a particular question.

Some issues contain "News" and "Book review", therefore, such contributions are also welcome. The papers must be in American English and should be checked by a native speaker if necessary.

Authors are requested to send their manuscripts to

Editor-in Chief of IDŐJÁRÁS

P.O. Box 39, H-1675 Budapest, Hungary

in three identical printed copies including all illustrations. Papers will then be reviewed normally by two independent referees, who remain unidentified for the author(s). The Editor-in-Chief will inform the author(s) whether or not the paper is acceptable for publication, and what modifications, if any, are necessary.

Please, follow the order given below when typing manuscripts.

Title part: should consist of the title, the name(s) of the author(s), their affiliation(s) including full postal and E-mail address(es). In case of more than one author, the corresponding author must be identified.

Abstract: should contain the purpose, the applied data and methods as well as the basic conclusion(s) of the paper.

Key-words: must be included (from 5 to 10) to help to classify the topic.

Text: has to be typed in double spacing with wide margins on one side of an A4 size white paper. Use of S.I. units are expected, and the use of negative exponent is preferred to fractional sign. Mathematical formulae are expected to be as simple as possible and numbered in parentheses at the right margin.

All publications cited in the text should be presented in a *list of references*,

arranged in alphabetical order. For an article: name(s) of author(s) in Italics, year, title of article, name of journal, volume, number (the latter two in Italics) and pages. E.g., *Nathan, K.K.*, 1986: A note on the relationship between photo-synthetically active radiation and cloud amount. *Időjárás* 90, 10-13. For a book: name(s) of author(s), year, title of the book (all in Italics except the year), publisher and place of publication. E.g., *Junge, C. E.*, 1963: *Air Chemistry and Radioactivity*. Academic Press, New York and London. Reference in the text should contain the name(s) of the author(s) in Italics and year of publication. E.g., in the case of one author: *Miller* (1989); in the case of two authors: *Gamov* and *Cleveland* (1973); and if there are more than two authors: *Smith et al.* (1990). If the name of the author cannot be fitted into the text: (*Miller*, 1989); etc. When referring papers published in the same year by the same author, letters a, b, c, etc. should follow the year of publication.

Tables should be marked by Arabic numbers and printed in separate sheets with their numbers and legends given below them. Avoid too lengthy or complicated tables, or tables duplicating results given in other form in the manuscript (e.g., graphs)

Figures should also be marked with Arabic numbers and printed in black and white in camera-ready form in separate sheets with their numbers and captions given below them. Good quality laser printings are preferred.

The text should be submitted both in manuscript and in electronic form, the latter on diskette or in E-mail. Use standard 3.5" MS-DOS formatted diskette or CD for this purpose. MS Word format is preferred.

Reprints: authors receive 30 reprints free of charge. Additional reprints may be ordered at the authors' expense when sending back the proofs to the Editorial Office.

More information for authors is available: antal.e@met.hu

Information on the last issues: http://omsz.met.hu/irodalom/firat_ido/ido_hu.html

Published by the Hungarian Meteorological Service

Budapest, Hungary

INDEX: 26 361

HU ISSN 0324-6329

IDŐJÁRÁS

QUARTERLY JOURNAL
OF THE HUNGARIAN METEOROLOGICAL SERVICE

CONTENTS

<i>Roger Randriamampianina</i> : Radiance-bias correction for a limited area model.....	143
<i>Roland Steib and Krisztina Labancz</i> : Regulatory modeling in Hungary – the AERMOD model. Part I. Description and application	157
<i>Tamás Ladics</i> : Analysis of the splitting error for advection-reaction problems in air pollution models.....	173
<i>Sándor Cseh and Pál Bencze</i> : Long-term variations of temperature, wind, and precipitable water in the troposphere and lower stratosphere over Budapest, Hungary	189
Book review	203

http://omsz.met.hu/omsz.php?almenu_id=omsz&pid=references&pri=2

IDŐJÁRÁS

Quarterly Journal of the Hungarian Meteorological Service

Editor-in-Chief
LÁSZLÓ BOZÓ

Executive Editor
MARGIT ANTAL

EDITORIAL BOARD

- | | |
|--|--|
| AMBRÓZY, P. (Budapest, Hungary) | MIKA, J. (Budapest, Hungary) |
| ANTAL, E. (Budapest, Hungary) | MERSICH, I. (Budapest, Hungary) |
| BARTHOLY, J. (Budapest, Hungary) | MÖLLER, D. (Berlin, Germany) |
| BATCHVAROVA, E. (Sofia, Bulgaria) | NEUWIRTH, F. (Vienna, Austria) |
| BRIMBLECOMBE, P. (Norwich, U.K.) | PAP, J.M. (Greenbelt, MD, U.S.A.) |
| CZELNAI, R. (Dörcicse, Hungary) | PINTO, J. (R. Triangle Park, NC, U.S.A.) |
| DÉVÉNYI, D. (Boulder, U.S.A.) | PRÁGER, T. (Budapest, Hungary) |
| DUNKEL, Z. (Budapest, Hungary) | PROBÁLD, F. (Budapest, Hungary) |
| FISHER, B. (Reading, U.K.) | RADNÓTI, G. (Budapest, Hungary) |
| GELEYN, J.-Fr. (Toulouse, France) | ROCHARD, G. (Lannion, France) |
| GERESDI, I. (Pécs, Hungary) | S. BURÁNSZKY, M. (Budapest, Hungary) |
| GÖTZ, G. (Budapest, Hungary) | SZALAI, S. (Budapest, Hungary) |
| HANTEL, M. (Vienna, Austria) | TAR, K. (Debrecen, Hungary) |
| HASZPRA, L. (Budapest, Hungary) | TÁNCZER, T. (Budapest, Hungary) |
| HORÁNYI, A. (Budapest, Hungary) | TOTH, Z. (Camp Springs, U.S.A.) |
| HORVÁTH, Á. (Siófok, Hungary) | VALI, G. (Laramie, WY, U.S.A.) |
| KONDRATYEV, K.Ya. (St. Petersburg, Russia) | VARGA-HASZONITS, Z. (Moson- |
| MAJOR, G. (Budapest, Hungary) | magyaróvár, Hungary) |
| MÉSZÁROS, E. (Veszprém, Hungary) | WEIDINGER, T. (Budapest, Hungary) |

*Editorial Office: P.O. Box 39, H-1675 Budapest, Hungary or
Gilice tér 39, H-1181 Budapest, Hungary
E-mail: bozo.l@met.hu or antal.e@met.hu
Fax: (36-1) 346-4809*

Subscription by

*mail: IDŐJÁRÁS, P.O. Box 39, H-1675 Budapest, Hungary;
E-mail: bozo.l@met.hu or antal.e@met.hu; Fax: (36-1) 346-4809*

IDŐJÁRÁS

Quarterly Journal of the Hungarian Meteorological Service
Vol. 109, No. 3, July–September 2005, pp. 143–155

Radiance-bias correction for a limited area model

Roger Randriamampianina

Hungarian Meteorological Service
P.O. Box 38, H-1525 Budapest, Hungary; E-mail: roger@met.hu

(Manuscript received in final form August 1, 2005)

Abstract—Direct assimilation of satellite measurements requires correction of biases caused by both measurement problems and errors in the radiative transfer model. The bias correction is based on finding the difference between the observed radiances and those simulated from the model states. Since the bias correction method was originally developed for global models, its adaptation to limited area models (LAMs) raises further questions. The quality of the bias correction coefficients – scan-angle biases and coefficients for air-mass predictors – depends on the sample of the observation-minus-model-first-guess, obtained at each satellite (AMSU-A) scan position. The amount of satellite measurements along the scan line is much smaller in case of a limited domain (LAM) compared to global models. This can cause problems when evaluating the scan-angle biases for a limited area model. This paper investigates different bias correction coefficients in order to find the best method for processing satellite data in the ALADIN limited area model. Bias correction coefficients, computed for the French global (ARPEGE) model, and one computed for the ALADIN limited area model, and many of their combinations were tested. The impact of the bias correction coefficients computed for the ALADIN limited area model was found to be more “stable” in both the analysis and short-range forecasts. The impact of the bias correction coefficients computed for the global model depended on the synoptic situation of the investigated period, especially in the important for the synoptic meteorology 850 to 500 hPa layer.

Key-words: limited area model, radiance-bias correction, data assimilation, ATOVS/AMSU-A.

1. Introduction

In most numerical weather prediction (NWP) centres, satellite data are assimilated in the form of raw radiances. For the efficient use of raw radiances (in our case from ATOVS), biases between the observed radiances and those simulated from the model states (first-guess) must be removed.

Many investigations were carried out on the removal of these biases. *Eyre* (1992) introduced the radiance bias as the combination of the scan-angle dependent (originating from the measurement quality) and air mass dependent errors. *Harris and Kelly* (2001) showed that scan angle biases vary with the geographical latitude bands. *Dee* (2004) proposed an adaptive bias correction scheme that can automatically sense the change in the bias of a given channel and responses correspondingly. The bias parameters are then updated jointly and simultaneously with the model state during the variational analysis, and are fully consistent with all observational information available to the analysis. *Watts and McNally* (2004) introduced a bias correction scheme, which is based on a modification of the transmittance coefficients in the radiative transfer model (RTTOV), involving two global parameters for each channel that can be adjusted to reduce the systematic errors in the RTTOV calculations.

The proposed bias correction schemes, however, were developed for global models. Thus, their adaptation to limited area models (LAMs) raises further questions. The quality of the bias correction coefficients – scan-angle biases and coefficients for air-mass predictors – depends on the amount of the observation-minus-model-first-guess, obtained at each satellite (AMSU-A) scan position. The amount of satellite measurements along the scan line is much smaller in case of a limited domain (LAM) compared to global models, because satellite paths are likely to be cut at different scan positions during their pre-processing. This can cause problems when evaluating the scan-angle biases for a limited area model.

In ARPEGE/ALADIN model (*Horányi et al.*, 1996), the method described by *Harris and Kelly* (2001) is used for correcting radiance-biases (see Section 2.2). Scan-angle biases depend on the number of samples obtained at each scan position. When computing scan angle biases using a limited area model (LAM), it is not likely to have the same number of samples for all scan positions in a given channel. To illustrate this, two satellite paths – a complete one on the right and a portion of a second path on the left side of the domain – are shown in *Fig. 1*. The inadequacy in the number of samples leads to fluctuating bias curves along the scan-lines (*Fig. 2a*) instead of well-smoothed ones. Due to sufficient number of samples, this problem does not appear when computing the scan-angle biases for global models.

Fig. 2a demonstrates the statistics computed for a one month period for the old domain (*Fig. 3a*) of the ALADIN Hungary (ALADIN/HU) model, which is relatively small compared to the new one (*Fig. 3b*). Enlarging the domain, smoother curves were obtained (*Fig. 2b*). Less but valuable fluctuation, however, was still observed for several channels – see, for example, the curve representing the scan-angle bias for channel 9 of AMSU-A

(triangles in Fig. 2b). This indicates, that further efforts have to be done to improve the bias correction method for the ALADIN/HU LAM model.

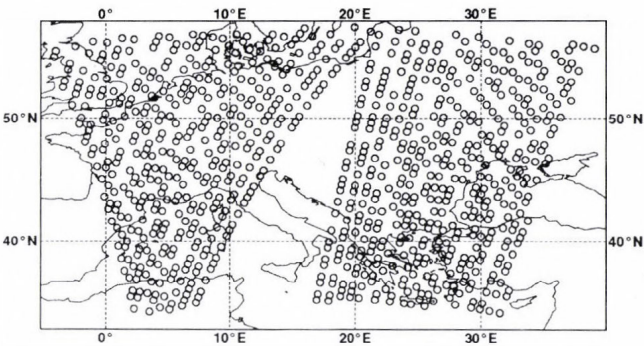


Fig. 1. Example of satellite paths inside the ALADIN/HU domain observed on April 23, 2003, 00 UTC.

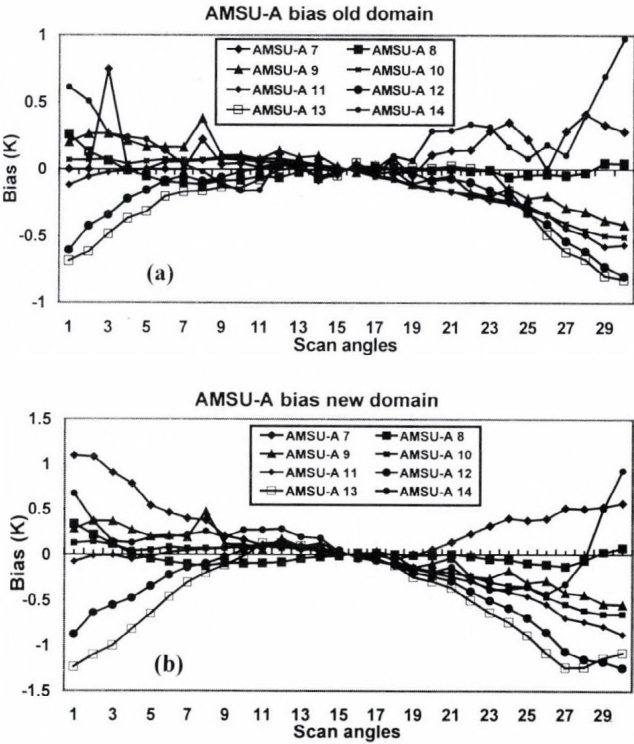


Fig. 2. Scan-angle bias computed for the old (a) and new (b) ALADIN/HU domains. Note that the domains of the ALADIN/HU model are presented in Figs. 3a and 3b.

This paper investigates different bias correction coefficients in order to find the best method for processing raw radiance satellite data in the ALADIN limited area model.

Bias correction coefficients, computed for the French global (ARPEGE) model and for the ALADIN limited area model, and many of their combinations were tested. Bias-correction coefficients computed for the restricted LAM domain were then compared with those, calculated for the coupling¹ global model. The need on removing air-mass related biases when assimilating the ATOVS observations in a limited area model was also investigated.

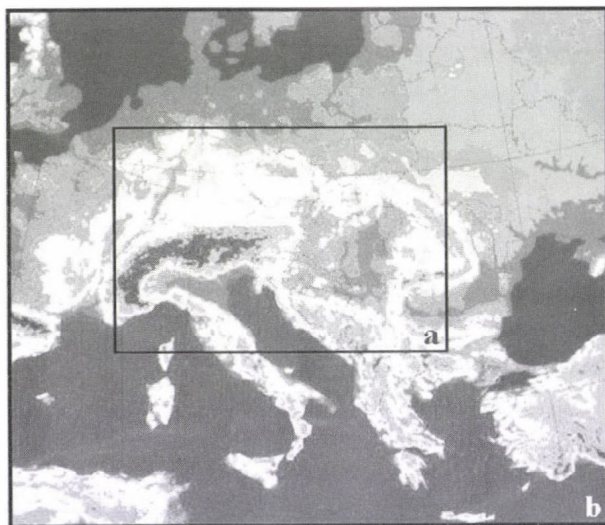


Fig. 3. Topography of the old (a) and new (b) ALADIN/HU domains, respectively.

Section 2 describes the main characteristics of ALADIN/HU model and its assimilation system. Section 2.1 illustrates the local pre-processing of satellite data, while Section 2.2 provides a short description of the bias correction method used in ALADIN/HU. Section 3 gives a detailed description of the experiments performed with various bias correction files. Section 4 reviews the results of the experiments, and in Section 5 we draw some conclusions of the results presented in this paper.

1 The integration of a limited area model needs information about its lateral boundary conditions – the coupling files. In the case of ALADIN model, we use a file from the global ARPEGE model, which is referred here as a coupling model.

2. The ALADIN/HU model and its assimilation system

At the Hungarian Meteorological Service (HMS), the ALADIN/HU model runs in its hydrostatic version. The model used in this investigation was the al15/cy24t1 version of the ARPEGE/ALADIN codes (<http://www.cnrm-meteo.fr/aladin/concept/historycycles.html>). In this study we used the model with 12 km horizontal resolution (*Fig. 3b*) and 37 vertical levels from the surface up to 5 hPa. The three-dimensional variational data assimilation (3D-Var) system was applied to assimilate both conventional (SYNOP and TEMP) and satellite (ATOVS) observations. As the variational technique computes the observational part of the cost function in the observational space, it is necessary to simulate radiances from the model parameters. In ARPEGE/ALADIN (al15/cy24t1) we use the RTTOV6 radiative transfer code to perform this transformation (*Saunders et al.*, 1998), which has 43 vertical levels. Above the top of the model, an extrapolation of the profile is performed using a regression algorithm (*Rabier et al.*, 2001). Below the top of the model, profiles are interpolated to RTTOV pressure levels. A good estimation of the background error covariance matrix is also essential for the variational technique to be successful. The background error covariance – the so-called “B” matrix – is computed using the standard NMC method (*Parrish and Derber*, 1992; *Široká et al.*, 2003). The specific humidity was assimilated in univariate form to avoid certain problems, related to its assimilation (see *Randriamampianina and Szoták*, 2003 for more details). An optimal interpolation scheme was used to analyze the surface fields (*Radi and Issara*, 1994). The AMSU-A data were assimilated at 80 km resolution. The 3D-Var is running in 6-hour assimilation cycle generating an analysis at 00, 06, 12, and 18 UTC. In this study, we performed a 48-hour forecast once a day, starting from 00 UTC.

2.1 Pre-processing of satellite data

The ATOVS data are received through our HRPT antenna and pre-processed with the AAPP (ATOVS and AVHRR Pre-processing Package) software package. We used AMSU-A, level 1-C radiances in our experiments.

For technical reasons our antenna is able to receive data only from two different satellites. To acquire the maximum amount of satellite observations, the NOAA-15 and NOAA-16 satellites were chosen, which have orbits perpendicular to each other and pass over the ALADIN/HU domain at about 06 and 18 UTC, and 00 and 12 UTC, respectively.

For each assimilation time we used the satellite observations that were measured within ± 3 hours. The number of paths over the ALADIN/HU domain within this 6-hour interval varied up to three.

2.2 Bias correction

The direct assimilation of satellite measurements requires the correction of biases computed as differences between the observed radiances and those simulated from the model first guess. These biases, arising mainly from instrument characteristics or inaccuracies in the radiative transfer model, can be significant. The method developed by *Harris and Kelly* (2001) was used to remove this systematic error. This scheme is based on separation of the biases into scan-angle dependent bias and state dependent components. The air-mass dependent bias is expressed as a linear combination of the set of state-dependent predictors.

Four predictors computed from the first-guess fields were selected (p1 – the 1000–300 hPa thickness, p2 – the 200–50 hPa thickness, p3 – the skin temperature, and p4 – the total column water) for the AMSU-A data used in our experiments.

A carefully selected sample of background departures for the AMSU-A and channel set was used to estimate the bias, in a two-step procedure. First, scan bias coefficients were computed by separating the scan-position dependent component of the mean departures in latitude bands. Secondly, after removing the scan bias from the departures, the predictor coefficients for the state-dependent component of the bias were obtained by linear regression. At the end of this estimation procedure, bias coefficients for the AMSU-A were stored in a file. The data assimilation system could then access the coefficients in order to compute bias corrections for the latest observations, using update state information for evaluating the air-mass dependent component of the bias. The brightness temperatures were corrected accordingly, just prior to assimilation.

As ARPEGE model uses every second pixel of ATOVS measurements, it has zero scan-angle coefficients at non-used pixels, which may cause a large remaining bias when using one by one field of view of the AMSU-A data. To overcome this problem, the values of the two adjacent pixels were interpolated into pixels with zero coefficients.

3. Description of the experiments

In order to estimate the impact of different bias correction coefficients on the model analysis and forecasts, the scores of different experiments were compared with those from the run (NT80U) performed using the bias correction file, computed for the ALADIN/HU LAM model. The scores of each run were evaluated objectively. The bias and root-mean-square error

(RMSE) were computed from the differences between the analysis/forecasts and observations (surface and radiosondes).

A twenty-day period (April 18, 2003–May 07, 2003 – denoted as first period later on) was used for the first impact study that consisted of four experiments. A fifteen-day period (February 20, 2003–March 06, 2003 – denoted as second period later on) was chosen for the second impact study in order to confirm the main results of the first one by repeating some of the experiments.

The radiosonde (TEMP), surface (SYNOP), and AMSU-A observations were used in all the experiments, applying different bias correction methods:

- NT80U:** The bias correction coefficients were computed for the ALADIN/HU domain (control run).
- T8B1I:** The bias correction coefficients were computed for the ARPEGE model.
- T8B2I:** The scan angle coefficients were computed for the ARPEGE model, but no air-mass correction was applied.
- T8B3I:** The ARPEGE scan-angle coefficients and the air-mass bias correction coefficients computed for the ALADIN/HU were used.
- NOT8U:** The same as NT80U for the second period.
- OT8B1I:** The same as T8B1I for the second period.
- OT8B3I:** The same as T8B3I for the second period.

4. Results and discussion

Bias correction coefficients computed for the global ARPEGE and limited area ALADIN/HU models and their combinations were compared in order to find the best solution for processing the AMSU-A data in the ALADIN/HU model. Almost neutral impact of bias correction methods on the analysis and forecast of relative humidity, geopotential height, and wind speed was found.

Concerning the impact on the temperature, the results are classified as follows.

4.1 Comparison of biases using different bias correction files

The particularity of the data assimilation system at the HMS is that it has different (positive or negative) bias on temperature profile at different model levels. For example, clear positive and negative bias can be observed at the 1000 hPa and 850 hPa levels, respectively (*Fig. 4*). The bias on humidity profile is slightly positive for all the model levels (not shown).

According to our results, the bias coefficients for the global ARPEGE model (mentioned as global bias correction file later on) have a heating effect above and a cooling effect under the 500 hPa level (*Fig. 4*) compared to the control run. Our verification concerns only the levels below 100 hPa.

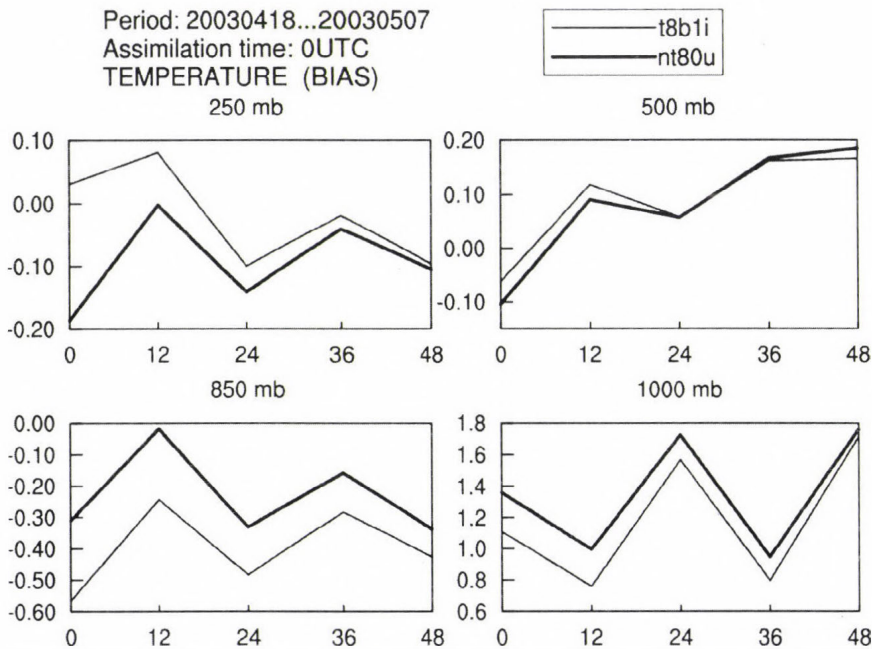


Fig. 4. Temperature biases, computed using the global (ARPEGE) bias correction coefficients (T8B1I) against biases, computed using the LAM coefficients (NT80U) for the first period.

4.2 Impact of the global bias correction file

Though the ALADIN/HU model has different biases of temperature in different model layers, the systematic cooling or heating does not necessarily yield an overall positive impact on temperature forecasts. For example, a clear positive impact on the forecast of temperature can be observed in the troposphere (500 hPa level) during the second period, although there was a negative impact at 850 hPa during the first period (*Fig. 5*). Thus, the behavior of the limited area model is not fully “controllable” when applying the global bias correction file in the assimilation system to process satellite observations. Consequently, no stable impact on the model analysis and forecast can be obtained.

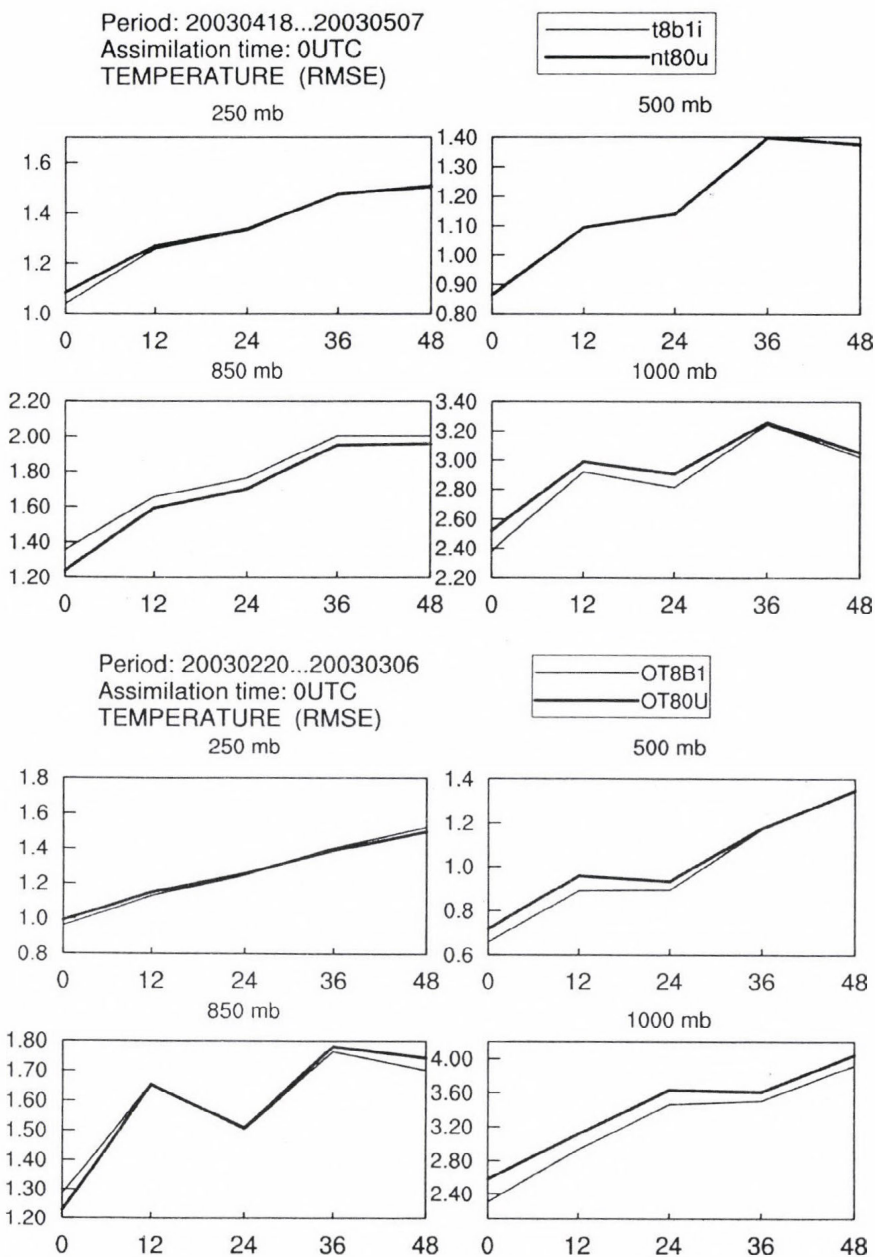


Fig. 5. Temperature root-mean-squares errors (RMSEs) for run with global bias correction coefficients (ARPEGE) (T8B1I and OT8B1I, for the first and the second period, respectively) against run with LAM coefficients (NT80U and OT80U, for the first and the second period, respectively).

4.3 Impact of no air-mass bias correction in the processing of AMSU-A

In order to assess the importance of air-mass bias correction, model runs with and without application of air-mass correction were compared. Thus, in the experiment T8B2I, no more than the interpolated ARPEGE scan-angle bias correction was used, since using a global model we can compute better representation of the scan-angle bias.

Without air-mass bias correction, satellite measurements warmed the model fields to a larger extent, which indicates that there was a residual bias in the temperature field shifted by satellite data (not shown). Accordingly, the verification scores showed a slightly negative or neutral impact on all the variables, including temperature forecast, in which the positive impact completely disappeared (*Fig. 6*). It seems likely that we need air-mass bias correction to assimilate radiances, since the ARPEGE scan-angle bias correction itself was not satisfactory.

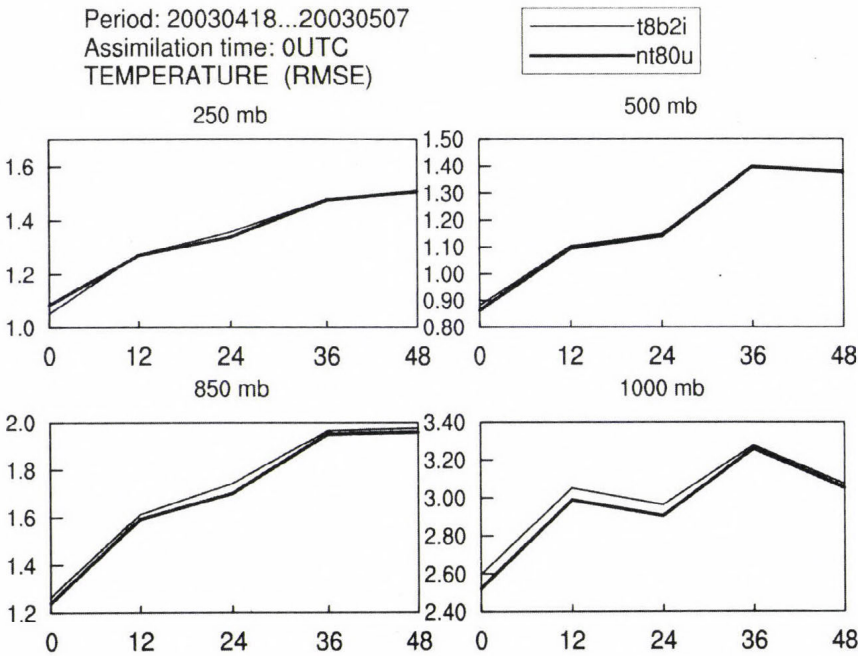


Fig. 6. Temperature root-mean-square errors (RMSEs) for run with global bias correction coefficients (ARPEGE) (T8B2I – no air-mass bias correction) against run with LAM coefficients (NT80U).

4.4 Combining the scan-angle bias correction of the global model with the air-mass bias coefficients of the LAM

Assuming that the air-mass bias correction is important, we combined the interpolated ARPEGE scan-angle bias correction with the ALADIN/HU air-mass bias correction in the experiment T8B3I. The combination of the global and local bias correction coefficients showed structurally similar results to those obtained in the experiment with ARPEGE bias correction file only (see Fig. 5), but both negative and positive impacts were negligible (Fig. 7). This reveals that using the global scan-angle bias correction with LAM air-mass bias correction coefficients did not improve the impact significantly.

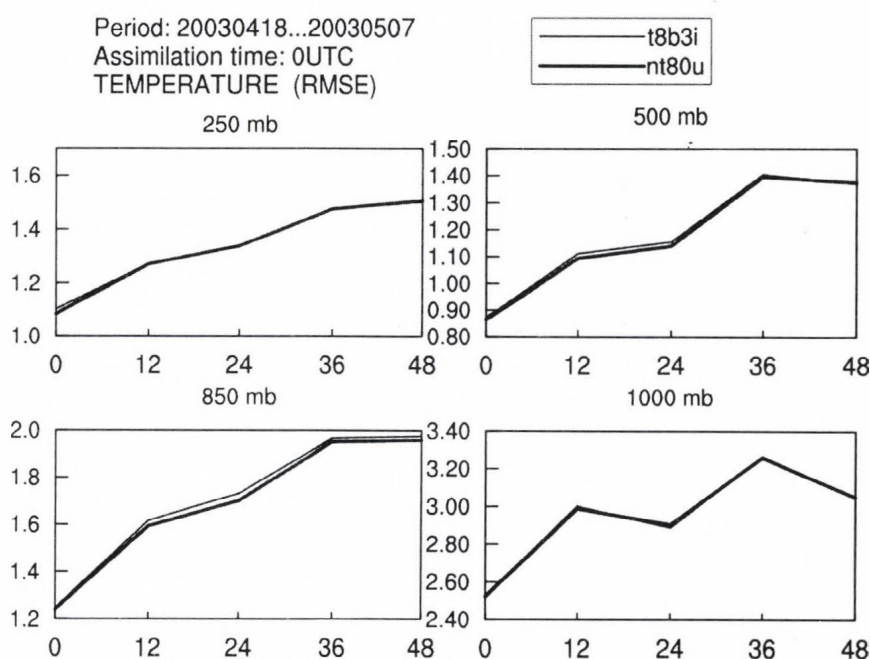


Fig. 7. Temperature root-mean-square errors (RMSEs) for run with global (ARPEGE) scan-angle bias correction coefficients and with LAM air-mass bias correction coefficients (T8B3I) against run with LAM bias correction coefficients (NT80U).

The sensitivity of channels 5, 6, 7, 10, 11, and 12 to the bias correction files was evaluated analyzing the number of assimilated satellite data (Fig. 8). More observation was available in the troposphere (channels 5, 6, and 7), while less data were used for channels 10, 11, and 12 when applying the

global air-mass bias coefficients in data processing. We assume, that the use of channels 5–7 was more efficient when applying the global bias coefficients compared to the local ones, probably because the analysis of the surface fields in the ARPEGE model is more accurate than that in the LAM.

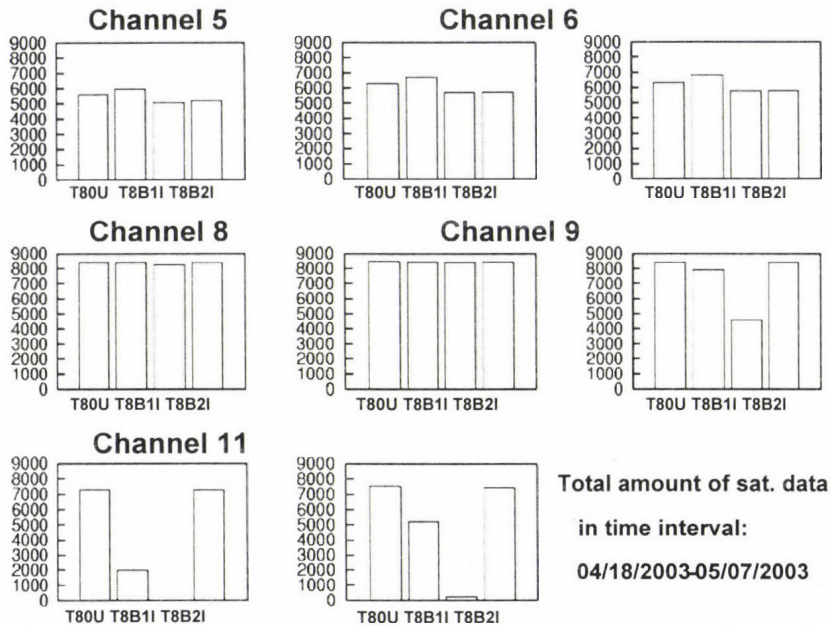


Fig. 8. Total number of assimilated satellite observations (active data) for the period April 18, 2003–May 07, 2003.

5. Conclusions

Our experiments show the importance of bias correction coefficients in the processing of AMSU-A data in the ALADIN/HU limited area model.

The use of the global bias correction file showed different impacts on short-range forecasts, especially in the lower troposphere, which is very important for synoptic meteorology. LAM bias correction coefficients provide a “stable” impact on the analysis as well as on the short-range forecasts.

Although the ARPEGE and the ALADIN models use basically the same parameterization of physical processes, and the bias correction coefficients are available from the global model, it is recommended to use bias correction, computed separately for the ALADIN model to ensure better processing of the AMSU-A data in the analysis system. It was found, that despite of smaller observation-

minus-first-guess samples, bias correction coefficients computed for the limited area are more suitable and reliable when assimilating radiances in a LAM.

It was proved, that the air-mass bias correction must be included in the processing of AMSU-A data in the limited area model.

It seems that the processing of the channels 10–12 in LAM is very sensitive to the bias coefficients computed for a global model.

At the Hungarian Meteorological Service, a 3D-Var system became operational this year (from May 17, 2005). In this system the pre-processing of the AMSU-A data uses bias correction coefficients computed locally according to the method, presented in this paper.

Acknowledgements—The research for this paper was supported by the János Bolyai Research Scholarship of the Hungarian Academy of Sciences and by the Hungarian National Scientific Foundation (OTKA T049579). The helps from *Philippe Caille* and *Élisabeth Gérard* of the Météo France and the fruitful discussion with colleagues of the numerical prediction division, department research and development of the Hungarian Meteorological Service are highly acknowledged. The author recognizes and appreciates the participation of *Regina Szoták* in this investigation.

References

- Dee, D.P., 2004: Variational bias correction of radiance data in the ECMWF system. *Proc. of the ECMWF Workshop on Assimilation of High Spectral Resolution Sounders in NWP*. 28 June – 1 July 2004, Reading, U.K.
- Eyre, J.R., 1992: A bias correction scheme for simulated TOVS brightness temperatures. *ECMWF Technical Memorandum*, 176.
- Harris, B.A. and Kelly, G., 2001: A satellite radiance-bias correction scheme for data assimilation. *Q. J. Roy. Meteor. Soc.*, 1453–1468.
- Horányi, A., Ihász, I., and Radnóti, G., 1996: ARPEGE/ALADIN: A numerical weather prediction model for Central-Europe with the participation of the HMS. *Időjárás* 100, 277–301.
- Parrish, D.F. and Derber, J.C., 1992: The National Meteorological Centre's spectral statistical interpolation analysis system. *Mon. Weather Rev.* 120, 1747–1763.
- Rabier, F., Gérard É., Sahlaoui Z., Dahoui M. and Randriamampianina R., 2001: Use of ATOVS and SSMI observations at Météo-France. *11th Conference on Satellite Meteorology and Oceanography*. Madison, WI, 15–18 October 2001 (preprints). Boston, MA, American Meteorological Society. 367–370.
- Radi, A. and Issara, S., 1994: Introduction de l'analyse canari du modèle global arpège dans le modèle à domaine limité aladin. *Master's Thesis*. Ecole Nationale de la Météorologie, Toulouse.
- Randriamampianina, R. and Szoták, R., 2003: Impact of the ATOVS data on the Mesoscale ALADIN/HU Model. *ALADIN Newsletter*, N24, also at <http://www.cnrm.meteo.fr/aladin/newsletters/newsletters.html>.
- Saunders, R., Matricardi, M., and Brunel, P., 1998: An improved fast radiative transfer model for assimilation of satellite radiance observations. *Q. J. Roy. Meteor. Soc.* 125, 1407–1425.
- Šíroká, M., Fischer, C., Cassé, V., Brožková, R., and Geleyn, J.-F., 2003: The definition of mesoscale selective forecast error covariances for a limited area variational analysis. *Meteor. Atmos. Phys.* 82, 227–244.
- Watts, P.D. and McNally, A.P., 2004: Identification and correction of radiative transfer modelling errors for atmospheric sounders: AIRS and AMSU-A. *Proc. of ECMWF Workshop on Assimilation of High Spectral Resolution Sounders in NWP*. 28 June – 1 July 2004, Reading, UK.

IDŐJÁRÁS

Quarterly Journal of the Hungarian Meteorological Service
Vol. 109, No. 3, July–September 2005, pp. 157–172

Regulatory modeling in Hungary – the AERMOD model Part I. Description and application

Roland Steib and Krisztina Labancz

Hungarian Meteorological Service
P.O. Box 39, H-1675 Budapest, Hungary; E-mail: steib.r@met.hu

(Manuscript received in final form July 22, 2005)

Abstract—This paper presents the adaptation of a second-generation local-scale dispersion model, called AERMOD, at the Hungarian Meteorological Service (HMS). The aim of this work is to develop a method suitable for calculations of air pollutant concentrations for regulatory purposes. AERMOD was designed to introduce current planetary boundary layer concepts into regulatory dispersion models. In this paper the main features of the AERMOD modeling system are described. New developments, implemented during the adaptation work, are discussed in detail. Finally, our experiences running the model and modeling results are described. Test runs and the validation of the model will be described in Part II of this paper, where the sensitivity of the model to the meteorological and surface parameters will be examined, and with some case studies we would like to show how the stability of the atmosphere influences the distribution of this pollutants, calculated by the model.

Key-words: regulatory modeling, local-scale dispersion model, planetary boundary layer, bi-Gaussian distribution, elevated terrain, terrain height scale, dividing streamline height.

1. Introduction

In 1991, the American Meteorological Society (AMS) and the U.S. Environmental Protection Agency (EPA) initiated a formal collaboration with the goal of introducing current planetary boundary layer (PBL) concepts into regulatory dispersion models. A working group (AMS/EPA Regulatory Model Improvement Committee, AERMIC) comprising AMS and EPA scientists was formed for this collaborative effort.

EPA's regulatory platform for near-field modeling, during 25 years, has with few exceptions, remained fundamentally unchanged. During this period,

the Industrial Source Complex Model (ISC3) was the workhorse regulatory model. Therefore, AERMIC selected the EPA's ISC3 Model for a major overhaul. AERMIC's objective was to develop a complete replacement for ISC3 by: (1) adopting ISC3's input/output computer architecture; (2) updating, where practical, antiquated ISC3 model algorithms with newly developed or current state-of-the-art modeling techniques; and (3) insuring that the source and atmospheric processes presently modeled by ISC3 will continue to be handled by the AERMIC Model (AERMOD), albeit in an improved manner.

AERMOD underwent a comprehensive performance evaluation (*Brode et al.*, 1998) designed to assess how well AERMOD's concentration estimates compare against a variety of independent data bases, and to assess the adequacy of the model for use in regulatory decision making. AERMOD was evaluated against five independent data bases (two in simple terrain and three in complex terrain), each containing one full year of continuous SO₂ measurements. Additionally, AERMOD's performance was compared against the performance of four other applied regulatory models: ISC3 (*U.S. Environmental Protection Agency*, 1995), CTDMPPLUS (*Perry*, 1992), RTDM (*Paine and Egan*, 1987), and HPDM (*Hanna and Paine*, 1989; *Hanna and Chang*, 1993). The performance of these models against AERMOD has been compared using the procedures in EPA's "Protocol for Determining the Best Performing Model" (*U.S. Environmental Protection Agency*, 1992). In April 21, 2000, EPA proposed that AERMOD be adopted as a replacement to ISC3 in Appendix A of the Guideline on Air Quality Models (*Code of Federal Regulations*, 1997). As such, upon final action, AERMOD would become EPA's preferred regulatory model for both simple and complex terrain. The newest performance of AERMOD is documented in *Perry et al.* (2003).

In 2002, the Hungarian Meteorological Service decided to replace its old dispersion model, a very simple Gaussian model by AERMOD. The new model, working with modern concepts of boundary layer and treating complex terrain, is a much more effective tool in regulatory modeling calculations.

2. The AERMOD modeling system

The AERMOD modeling system consists of three pre-processors and the dispersion model. The AERMIC meteorological preprocessor (AERMET) provides AERMOD with the meteorological information it needs to characterize the planetary boundary layer (PBL). The AERMIC terrain preprocessor (AERMAP) both characterizes the terrain, and generates receptor grids for the dispersion model (AERMOD). INTERFACE, which is inside AERMOD is a preprocessor, that makes connection between AERMET and

AERMOD. Fig. 1 shows the flow and processing of information in AERMOD, where NWS means National Weather Service, ONSITE means on-site measurement, PASS OBS means passing observation, PBL PARAM means planetary boundary layer parameters, u is wind-vector, $turb$ is turbulence, dT/dz is temperature gradient, X , Y , Z are coordinates of the receptor points, and h_c is the effective height scale.

MODELING SYSTEM STRUCTURE

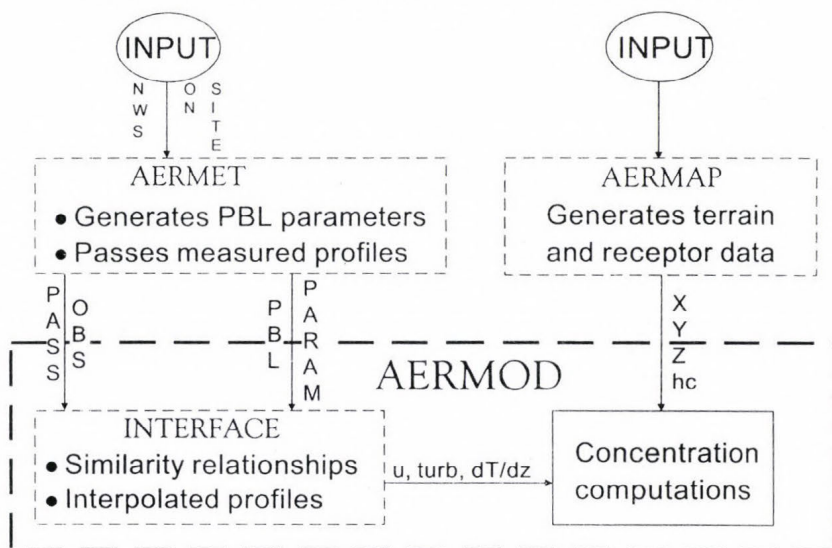


Fig. 1. Data flow in the AERMOD modeling system.

2.1 AERMOD – the dispersion model

AERMOD is a steady-state plume model. In the stable boundary layer (SBL), it assumes the concentration distribution to be Gaussian in both the vertical and horizontal. In the convective boundary layer (CBL), the horizontal distribution is also assumed to be Gaussian, but the vertical distribution is described with a bi-Gaussian probability density function (pdf). This behavior of the concentration distributions in the CBL was demonstrated by Willis and Deardorff (1981) and Briggs (1993).

Using a relatively simple approach, AERMOD incorporates current concepts about flow and dispersion in complex terrain. Where appropriate, the plume is modeled as either impacting and/or following the terrain. This

approach has been designed to be physically realistic and simple to implement while avoiding the need to distinguish among simple, intermediate, and complex terrain, as required by other regulatory models. As a result, AERMOD removes the need for defining complex terrain regimes. All terrain is handled in a consistent and continuous manner while considering the dividing streamline concept (*Snyder et al.*, 1985) in stably stratified conditions.

One of the major improvements that AERMOD brings to applied dispersion modeling is its ability to characterize the PBL through both surface and mixed layer scaling. AERMOD constructs vertical profiles of required meteorological variables based on measurements and extrapolations of those measurements using similarity (scaling) relationships. Vertical profiles of wind speed, wind direction, turbulence, temperature, and temperature gradient are estimated using all available meteorological observations. AERMOD is designed to run with a minimum of observed meteorological parameters. As a replacement for the ISC3 model, AERMOD requires only a single surface measurement of wind speed (measured in the layer between 7 times of the surface roughness height and 100 meters above the surface), wind direction, and ambient temperature. Like ISC3, AERMOD also needs observed cloud cover. However, if cloud cover is not available (e.g., from an on-site monitoring program), two vertical measurements of temperature (typically at 2 and 10 meters), and a measurement of solar radiation can be substituted. A full morning upper air sounding (RAWINSONDE) is required in order to calculate the convective mixing height throughout the day. Surface characteristics (surface roughness, Bowen ratio, and albedo) are also needed in order to construct similarity profiles of the relevant PBL parameters.

Unlike existing regulatory models, AERMOD accounts for the vertical inhomogeneity of the PBL in its dispersion calculations. This is accomplished by “averaging” the parameters of the actual PBL into “effective” parameters of an equivalent homogeneous PBL.

2.2 AERMET – the meteorological preprocessor

AERMOD requires a preprocessor that organizes and processes meteorological data and estimates the necessary boundary layer parameters for dispersion calculations. The meteorological preprocessor that serves this purpose is AERMET.

AERMET is designed to be run as a three-stage process (*Fig. 2*), where *QA* means quality assessment, *stage1n2* and *stage3* are the executable programs. AERMET operates on three types of data – hourly surface observations, daily upper air soundings, and data collected from an on-site measurement program such as an instrumented tower. The first stage extracts

data and assesses data quality. The second stage combines the available data for 24-hour periods and writes these data to an intermediate file. The third and final stage reads the merged data file and develops the necessary boundary layer parameters for dispersion calculations by AERMOD.

AERMET can extract data from several standard NCDC formats. These include the TD-6201 format for upper air sounding data, hourly surface weather observations in the CD-144 format, which is a time-based (i.e., by hour) format, and the TD-3280 format, which is an element-based (i.e., by variable) format for surface data.

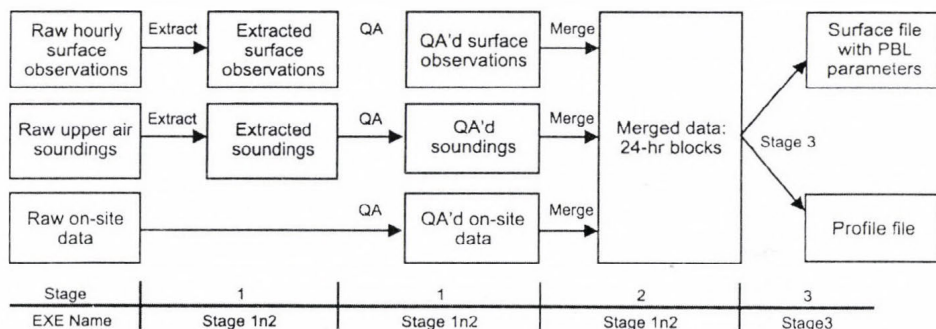


Fig. 2. The 3 stages of the AERMET processing.

The temperature structure of the atmosphere prior to sunrise is required by AERMET to estimate the growth of the convective boundary layer for the day. Currently, AERMET uses the 12:00 UTC upper air sounding for this purpose. A one-hour window of time in the search allows for the possibility of an early or late launch time. This search restricts the applicability of AERMET to those longitudes where the 12:00 UTC sounding corresponds to the early morning hours, i.e., the Western Hemisphere.

Surface characteristics in the form of albedo, surface roughness, and Bowen ratio, plus standard meteorological observations (wind speed, wind direction, temperature, and cloud cover), are input to AERMET. AERMET then calculates the PBL parameters: friction velocity (u^*), Monin-Obukhov length (L), convective velocity scale (w^*), temperature scale (θ^*), mixing height (z_i), and surface heat flux (H). These parameters are then passed to the INTERFACE (which is within AERMOD), where similarity expressions (in conjunction with measurements) are used to calculate vertical profiles of wind speed (u), lateral and vertical turbulent fluctuations (σ_v , σ_w), potential temperature gradient ($d\theta/dz$), and potential temperature (θ).

2.3 AERMAP – the terrain preprocessor

The AERMAP terrain pre-processor uses gridded terrain data to calculate a representative terrain-influence height (h_c), also referred to as the terrain height scale. The terrain height scale h_c , which is uniquely defined for each receptor location, is used to calculate the dividing streamline height. The gridded data needed by AERMAP is selected from Digital Elevation Model (DEM) data. AERMAP is also used to create receptor grids. The elevation for each specified receptor is automatically assigned through AERMAP. For each receptor, AERMAP passes the following information to AERMOD: the receptor's location (x_r , y_r), its height above mean sea level (z_r), and the receptor specific terrain height scale (h_c).

2.4 Output options

The AERMOD model provides various output options for regulatory purposes: summaries of high values (highest, second highest, etc.) by receptor for each averaging period (1-hour, 3-hour, 8-hour, 24-hour, monthly, yearly, average for the entire data period) and source group combination; summaries of overall maximum values for each averaging period and source group combination; tables of concurrent values summarized by receptor for each day of data processed.

Another output option of the AERMOD model is to give all occurrences when a concentration value equals or exceeds a user-specified threshold. Separate results are generated for only those combinations of averaging period and source group that are of interest.

In air quality dispersion modeling applications, there is a need to know the contribution that a particular source makes to an overall concentration value for a group of sources. The AERMOD model provides the option to perform the source attribution analyses. For example, the user can specify source groups for which the model calculates high values independently. In addition, when maximum values for individual sources are output, the user has the option of specifying whether the maximum source values are to be the maximum values for each source independently, or the contribution of each source to the maximum group values, or both.

3. Adaptation of the AERMOD system at the HMS

At the Hungarian Meteorological Service we do not have the data file formats, that AERMET and AERMAP can use as inputs. We had to create a program

that gives us the meteorological parameters in the extracted file formats for AERMET. So when we run stage1 of AERMET, we only have to run the second part (quality assessment) of this stage. Instead of AERMAP we also created our own terrain pre-processor to get the needed terrain parameters for AERMOD.

We had two other, major problems to solve. The first was that AERMET needs cloud cover to calculate planetary boundary layer parameters, but there are few stations with visual observations in Hungary. The second problem was that AERMET needs an early morning upper air sounding in order to calculate the convective boundary layer parameters. In Hungary we only have 00:20 LST (Budapest and Szeged) and 12:20 LST (Budapest) upper air soundings, which cannot be used in AERMET.

We thought that the best way to solve these problems is to use two- and three-dimensional analysis fields of the necessary meteorological parameters. The analysis fields are calculated by the MM5 model, a numerical weather prediction model developed especially for nowcasting purposes, which operationally runs at the Hungarian Meteorological Service. In these data files the meteorological parameters are represented in grid points. Cloud cover (SatCloudi) is calculated from MSG satellite data. Two and three-dimensional MM5 analysis data are available for every hour. We thought that the 05:00 UTC three-dimensional MM5 analysis data could represent well the early-morning vertical structure of the planetary boundary layer. In consequence, we had to change an original subroutine in AERMET (Mppbl.for). This original subroutine could read only the 11:00, 12:00, and 13:00 UTC upper air data. We changed the source code, so the new one is able to read the 05:00 UTC upper air data.

3.1 Structure of meteorological data

We construct the meteorological data files from the two- and three-dimensional MM5 analysis netCDF files. These netCDF files can be found on the *lamb* server of the Hungarian Meteorological Service. The resolution of the two dimensional files is $1/60 \times 1/50$ degrees, and that of the three dimensional files is 0.06×0.05 degrees. From the two-dimensional netCDF files we read the following parameters and store them in ASCII files: u-component of wind at 10 meters, v-component of wind at 10 meters, temperature at 2 meters, relative humidity at 2 meters, surface pressure, and cloud cover. From the three-dimensional netCDF files we read the following parameters (at the 1000, 950, 925, 900, 850, 800, 750, 700, 650, 600, 550, and 500 hPa isobaric levels) and store them in ASCII files: u-component of wind, v-component of wind, temperature, relative humidity, and geopotential height.

3.2 Constructing the meteorological inputs for AERMET

In our opinion, using the meteorological parameters from one grid point (nearest to the pollution source) of the MM5 analysis data files is not the best way to represent the meteorological situation in a bigger area, so we use meteorological parameters averaged over a grid, approximately 30×30 km. We have already seen that we have to construct the meteorological data in exactly that file format that the AERMET meteorological pre-processor gives after running stage1. We do this work in 3 steps. The first step is a small program which calculates the nearest grid point to the pollution source in the meteorological data with the help of the source coordinates. A 2D meteorological grid file consists of about 440 zonal points and 178 meridional points. A 3D grid file contains about 150 zonal points and 60 meridional points. The second step is a shell-script in which an awk-script is embedded. The shell-script does the following work: copies data files in the working directory, uncompresses them, runs the awk-script and writes the results in intermediate meteorological files. The awk-script reads the meteorological data from a 30×30 km domain around the source of the 2D and 3D files, and calculates the averages over this area. The third part is a program which reads the meteorological data from the intermediate files and converts them to the file format that AERMET can read.

3.3 Constructing the terrain inputs

The terrain preprocessor of AERMOD uses gridded terrain data to calculate the elevation and representative terrain-influence height (referred to as terrain height scale) for each specified receptor point. The gridded data originally was selected from the U.S. Digital Elevation Model (DEM) database. Because DEM does not contain terrain data for Europe, we used similar elevation data files consisting of a regular array of elevations referenced horizontally on the UTM longitude/latitude coordinate system calculated on the World Geodetic System (WGS-84) ellipsoid. Therefore, we had to write a new terrain preprocessor.

First, we have to define a modeling domain. A modeling domain is defined as the area that consists of all the receptors and sources being modeled. For regulatory purposes, we use a 30×30 km domain around the source point, where the minimal receptor point distance could be 500 m. Then we define the receptor point(s). The receptors are specified in a manner identical to the AERMOD dispersion model. One can specify discrete receptors as well as Cartesian and polar grid networks. However, there are some special considerations, e.g., when specifying discrete polar receptors, it

is necessary to specify the position of a source relative to which the receptor is assigned.

In addition to the location and height above mean sea level of each receptor, the AERMOD model requires the receptors' specific terrain height scale, which is used to calculate the critical dividing streamline height. Our terrain preprocessor contains a new calculation method for determining the height scale. First, the method calculates the maximum elevation difference in the domain, then the relief height of the terrain points with respect to the height of the receptor, and the slope are determined. If the slope is 10% or greater, the height scale for the receptor is updated.

3.4 Post-processing

The post-processing part of the AERMOD modeling system contains two programs. The first program constructs a tabular overview of the concentrations in the receptor points. First the period average concentrations, then the 24-hour maximum concentrations, and at last the 1-hour maximum concentrations are constructed. This program also defines the "efficient" area. The "efficient" area is a domain around the pollutant source where the concentration is higher than the 80% of the maximum 1-hour concentration or the concentration is higher than the 10% of the maximum 1-hour threshold value of a pollutant. The second program constructs the graphical overview of the period average, the 24-hour maximum and the 1-hour maximum concentration distribution. This step is done with the DISLIN graphical program, which produces three pictures in PNG file format.

4. Results

In this paper we present the results of two different test runs to illustrate the benefits of adaptation of the AERMOD modeling system at the Hungarian Meteorological Service. In the first test we made a comparison between AERMOD and the formal dispersion model, called TRANSMISSION 1.0 (Szepesi *et al.*, 1995), which is a very simple Gaussian model. Since TRANSMISSION can not treat complex terrain, in the first test we made calculations over flat terrain to compare the basic characteristics of the two models. In the second test we examined the effects of complex terrain on the results of AERMOD. In all our tests we used the following parameters:

- one point source (stack),
- location of the source: 46.06°N, 18.26°E (south-western part of Hungary),

- type of pollutant: NO_x ,
- receptor resolution: ~ 500 m,
- number of receptors: 59×59 ,
- domain size: $\sim 30 \times 30$ km,
- emission rate: 28 g/s,
- release height above ground: 82 m,
- stack gas exit temperature: 373 K,
- stack gas exit velocity: 13 m/s,
- stack inside diameter: 6 m.

4.1 Test 1. Dispersion distribution over flat terrain

In our first test we wanted to examine AERMOD's behavior in case of flat terrain, because our former dispersion model could only treat flat terrain. We wanted to see the differences or similarities in the concentration distributions between the two models. The yearly average concentration distribution of the two models showed similarities. *Fig. 3* shows the yearly average NO_x concentration field calculated by the TRANSMISSION 1.0 model, and *Fig. 4* shows the yearly average NO_x concentration field calculated by the AERMOD model over the above characterized domain and source parameters. In all graphics the cross-shaped symbol represents the place of the source. When long averaging period (1 year) was used, we found that the concentration field was mostly governed by the average wind direction of the domain. In this area the wind usually blows from north-west, so we could find the highest concentration values in both cases to the south-east direction of the source. The difference between the two models was that the concentration field calculated by AERMOD spreaded over a smaller area around the source giving higher yearly average concentration values than TRANSMISSION. When we used short averaging period (1 hour), the results between the two models were much more significant. *Fig. 5* shows the maximum 1-hour NO_x concentration field of TRANSMISSION and *Fig. 6* the max 1-hour NO_x concentration field of AERMOD. The concentration distribution in *Fig 5* is totally concentric, while *Fig. 6* also shows some concentricity, but the concentration distribution is much more irregular. This characteristic of the concentration field can be explained by that over a short averaging period the direction of the local wind is fluctuating, and any direction of the wind can result in high concentration values. In our opinion the differences between the two models in the case of short averaging periods is not surprising. Probably it comes from the different structures of the two models. The simple Gaussian model calculates the planetary boundary layer parameters empirically, while AERMOD calculates unique

parameters of the planetary boundary layer for every hour, so the boundary layer changes continuously during the day. In case of the 1-hour averaging period both models gave almost the same maximum concentration values. The AERMOD model usually gave high concentration values in calm wind situations.

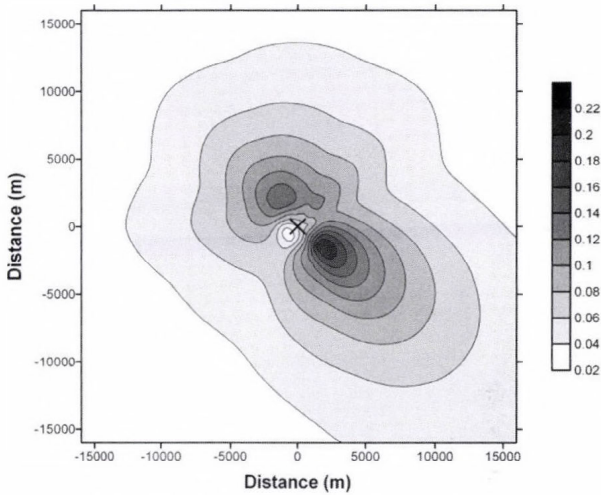


Fig. 3. Yearly average NO_x concentration of TRANSMISSION (flat terrain). Units: µg/m³.

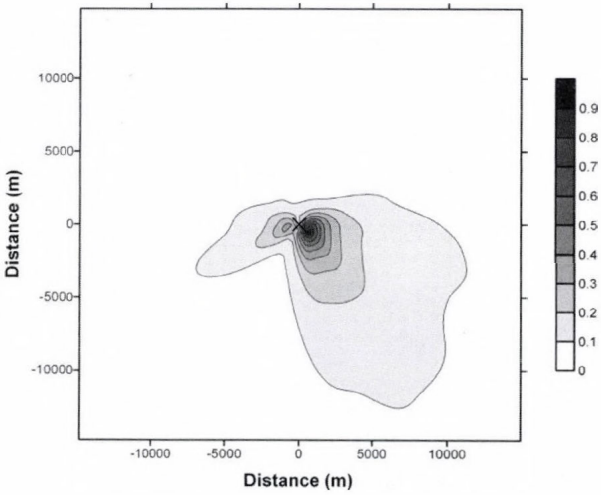


Fig. 4. Yearly average NO_x concentration of AERMOD (flat terrain). Units: µg/m³.

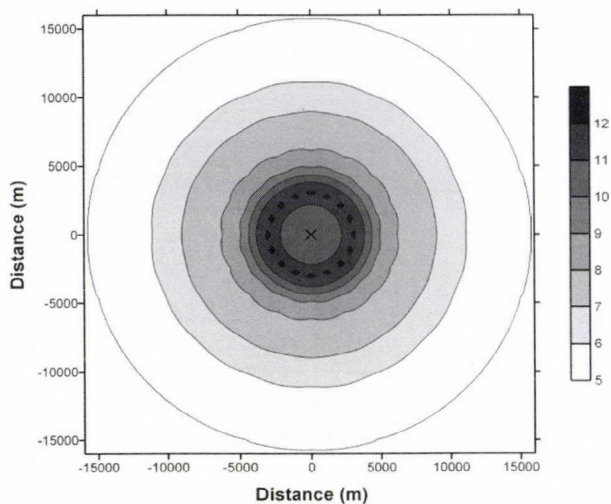


Fig. 5. 1-hour maximum NO_x concentration of TRANSMISSION (flat terrain). Units: $\mu\text{g}/\text{m}^3$.

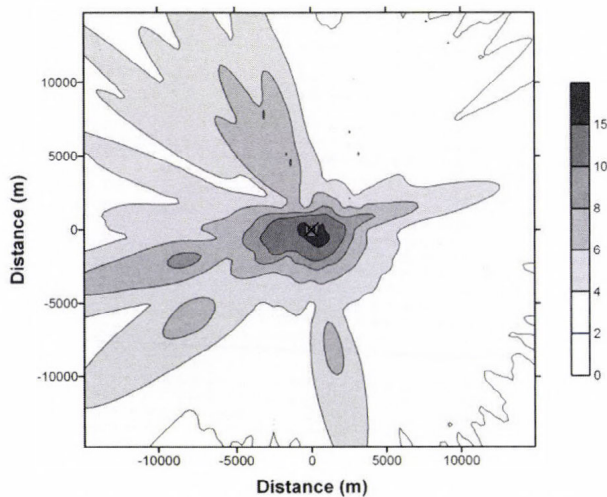


Fig. 6. 1-hour maximum NO_x concentration of AERMOD (flat terrain). Units: $\mu\text{g} / \text{m}^3$.

4.2 Test 2. Dispersion distribution over complex terrain

In this test we wanted to see the changes in the concentration field when the AERMOD model used elevated terrain. By short and also by long averaging periods we experienced big differences in the concentration fields between

calculations with elevated terrain and flat terrain. *Fig. 7* illustrates concentration distribution of AERMOD in the case of the yearly averaging period, while *Fig. 8* shows the same but with 1-hour averaging period. By long time averaging period we can notice two maximum places of the concentration distribution. The first maximum is at the same place as it was at the flat terrain. But also a second maximum can be seen at the place where the terrain begins to elevate at the feet of the mountains. This second maximum can be found near the centreline height of the plume. We can also see that the plume flows around the mountains, and at the top of the mountains (500–600 m) the concentration values are lower again.

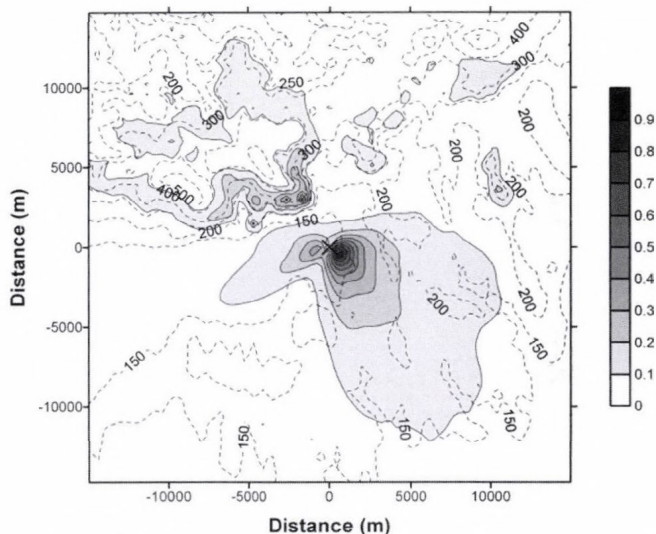


Fig. 7. Yearly average NO_x concentration of AERMOD (elevated terrain). Units: $\mu\text{g}/\text{m}^3$.
Dashed isolines represent the terrain height. Contour intervals are at every 50 m.

By the 1-hour averaging period, the highest concentration values can be found at the feet of the nearest mountain to the source, and also at the height of the plume centerline. Thus, when short averaging period was used, the elevated terrain had even more influence on the concentration distribution than by the yearly averaging period.

We also have to notice that the maximum value of the yearly average concentration of AERMOD is almost the same with flat- and elevated terrain, but the maximum value of the 1-hour concentration is about 10 times higher

with elevated terrain than with flat terrain. This result makes us clear that the elevated terrain can very much change the concentration distribution of a pollutant.

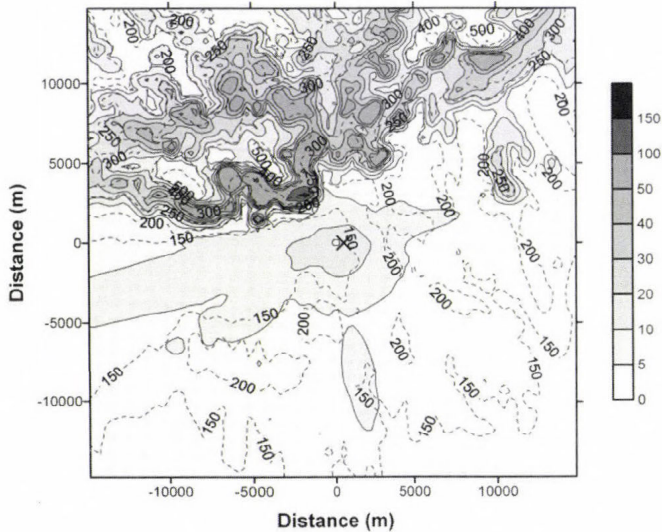


Fig. 8. 1-hour maximum NO_x concentration of AERMOD (elevated terrain).
Units: $\mu\text{g}/\text{m}^3$. Dashed isolines represent the terrain height.
Contour intervals are at every 50 m.

We have already mentioned in the abstract that in Part II of this paper we want to examine the model's sensitivity to meteorological and surface parameters. We also want to examine how the stability of the atmosphere influences the concentration distribution. We would like to show the differences in the concentrations between the stable and convective boundary layer. We also would like to examine in which way the height of the stable and convective boundary layer affects the concentration field.

5. Conclusions and future plans

In this paper a second-generation local-scale dispersion model was presented. The model, developed at the Environmental Protection Agency, U.S. for regulatory purposes, works with modern concepts of boundary layer and treats

complex terrain. The AERMOD model was adapted and tested at the Hungarian Meteorological Service, it was compared with the old Gaussian model TRANSMISSION 1.0. One of the advantages of AERMOD is that it can treat complex terrain giving much more realistic figures of the distribution of pollutants. In addition to this, AERMOD gave better concentration distributions over flat terrain for the 1-hour averaging period. The difference was remarkable in the case of short averaging periods caused by the different structure of the two models. The simple Gaussian model calculates the planetary boundary layer parameters empirically, while AERMOD calculates unique parameters of the planetary boundary layer for every hour, so the boundary layer changes continuously during the day.

So far we could not afford to evaluate the performance of AERMOD by using measured data. In the U.S., AERMOD underwent a comprehensive performance evaluation against five independent data bases (two in simple terrain and three in complex terrain), each containing one full year of continuous SO₂ measurements. On the basis of our co-operation with Hungarian environmental agencies, we hope to evaluate our model version against measured data bases in the future.

The Hungarian Meteorological Service co-operates with local Hungarian environmental agencies in air pollution regulatory tasks. Our dispersion models are run for local, special environmental problems, for which the AERMOD model system has been proven to be a very efficient tool. This model version of AERMOD does not take into account dry and wet deposition. This can be the reason why the model usually gives slightly higher concentration values than the measurements or other dispersion models. The next version of the model is under construction. The new version of the model will be able to handle dry and wet deposition of gases and particles, so we can hope that we will be able to make even better concentration estimations.

References

- Briggs, G.A., 1993: Plume dispersion in the convective boundary layer. Part II: Analysis of CONDORS field experiment data. *J. Appl. Meteorol.* 32, 1388-1425.
- Brode, R.W., Perry, S.G., Cimarelli, A.J., Weil, J.C., Venkatram, A., Paine, R.J., Wilson, R.B., Lee, R.F., and Peters, W.D. 1998: Model Evaluation Results of AERMOD. EPA web site (<http://www.epa.gov/scram001/tt26.htm#aermod>).
- Code for Federal Regulations, 1997: Service of the U.S. Government Printing Office, U.S. GPO web site (<http://www.gpoaccess.gov/cfr>).
- Hanna, S.R. and Paine, R.J., 1989: Hybrid Plume Dispersion Model (HPDM) development and evaluation. *J. Appl. Meteorol.* 28, 206-224.
- Hanna, S.R. and Chang, J.S., 1993: Hybrid Plume Dispersion Model (HPDM), improvements and testing at three field sites. *Atmos. Environ.* 27A, 1491-1508.

- Paine, R.J. and Egan, B.A., 1987: User's Guide to the Rough Terrain Diffusion Model (RTDM) - Rev. 3.20. ERT Document PD-535-585, ENSR, Acton, MA.
- Perry, S.G., 1992: CTDMPPLUS: A dispersion model for sources in complex topography. Part I: Technical formulations. *J. Appl. Meteorol.* 31, 633-645.
- Perry, S.G., Cimorelli, A.J., Weil, J.C., Venkatram, A., Paine, R.J., Wilson, R.B., Lee, R.F., and Peters, W.D., 2003: AERMOD: Latest Features and Evaluation Results. EPA web site (<http://www.epa.gov/scram001/tt26.htm#aermod>).
- Snyder, W.H., Thompson, R.S., Eskridge, R.E., Lawson, R.E., Castro, I.P., Lee, J.T., Hunt, J.C.R., and Ogawa, Y., 1985: The structure of the strongly stratified flow over hills: Dividing streamline concept. *J. Fluid Mech.* 152, 249-288.
- Szepesi, D.J., Fekete, K.E., Gyenes, L., 1995: Regulatory Models for Environmental Impact Assessment in Hungary. *Int. J. Environ. and Pollution* 5, 497-507.
- U.S. Environmental Protection Agency, 1992, Protocol for Determining the Best Performing Model. EPA-454/R-92-025, U.S. Environmental Protection Agency, RTP, NC.
- U.S. Environmental Protection Agency, 1995, User's Guide for the Industrial Source Complex (ISC3) Dispersion Models (revised) Volume I - User Instructions. EPA-454/b-95-003a, U.S. Environmental Protection Agency, Research Triangle Park, NC.
- Willis, G.E. and Deardorff, J.W., 1981: A laboratory study of dispersion in the middle of the convectively mixed layer. *Atmos. Environ.* 15, 109-117.

Analysis of the splitting error for advection-reaction problems in air pollution models

Tamás Ladics

*Department of Meteorology, Eötvös Loránd University
P.O. Box 32, H-1518 Budapest, Hungary
and*

*Department of Analysis, Budapest University of Technology and Economics
P.O. Box 91, H-1591 Budapest, Hungary
E-mail: tladics@math.bme.hu*

(Manuscript received in final form October 5, 2004)

Abstract—Operator splitting is a widely used method in the numerical solution of air pollution transport equations. This paper presents an analysis of splitting error for advection-reaction problems. Our investigations are focused on Molenkamp–Crowley advection and chemical reactions. A necessary and sufficient condition is derived under which the splitting error vanishes. Some numerical experiments are presented for two-dimensional models.

Key-words: Molenkamp–Crowley advection, chemical reactions, numerical solution of partial differential equations, splitting error, operator splitting, air pollution modeling.

1. Introduction

Air pollution has become one of the main environmental problems due to increasing human activity in the fields of transport and industry (Havasi *et al.*, 2001). Reducing the amount of air pollutants emitted into the atmosphere is an important task. The efficient treatment of this problem requires the study of the mathematical models of air pollution transport. In the description of this process, *advection-diffusion-reaction equations* are widely used. Models describing the evolution of pollutant concentrations are based on the mass conservation law and represent different processes acting in the atmosphere (namely advection, diffusion, emission, chemical reactions, and deposition) in the form of a system of partial differential equations. To find the symbolic

solution of these equations is practically impossible, therefore, we use a numerical method to obtain an approximate solution of the equations. However, even the numerical treatment of the problem is complicated. To get a sufficiently precise approximation in reasonable time, we apply the *splitting method* (see, e.g., Zlatev, 1995). Operator splitting is a tool to make the numerical treatment simpler and to use our numerical methods more efficiently.

The technique of splitting to help us solve this system of equations was used for a long time in different ways. A kind of special splitting was introduced by Marchuk (1968) and Strang (1968), which has higher order accuracy. A splitting method was used in the solution of the diffusion equation by McRae *et al.* (1984). For advection-diffusion-reaction problems Lanser and Verwer (1999) analyzed the error caused by splitting. A study on splitting techniques applicable for problems with stiff operators can be found in Sportisse (2000).

The theoretical background of operator splitting and a detailed study of the splitting error in the case of air pollution models have been presented by Havasi *et al.* (2001). Here we strongly rely on their results especially on the condition for the splitting error to be zero.

In this paper we focus on the advection-reaction problem. We apply the result of Havasi *et al.* (2001) on L-commutation, and we determine the condition of L-commutativity in the case of advection and reaction operators. Furthermore, we present the results of some numerical computation for advection-reaction models. Section 2 introduces the transport equation used in air pollution modeling. Section 3 contains a review of the splitting method and a definition of the splitting error. In Section 4 we give a characterization of the splitting error and derive the error for the advection-reaction problem in general. In Section 5 we derive a necessary and sufficient condition for a two-dimensional advection-reaction model with Molenkamp-Crowley advection under which the operators (advection and reaction) commute, i.e., the splitting error is zero. In Section 6 we present our numerical results for this advection-reaction model. Section 7 discusses results and further plans.

2. The air pollution transport equation

The system of partial differential equations to describe advection, diffusion, and reaction in air pollution modeling is as follows:

$$\begin{aligned} \frac{\partial c_i(\mathbf{x}, t)}{\partial t} = & -\nabla \cdot (\mathbf{u}(\mathbf{x}, t) c_i(\mathbf{x}, t)) + \nabla \cdot (\mathbf{K}_i(\mathbf{x}, t) \nabla c_i(\mathbf{x}, t)) + r_i(\mathbf{x}, t, \mathbf{c}(\mathbf{x}, t)) \\ & + E_i(\mathbf{x}, t) + \sigma_i c_i(\mathbf{x}, t), \quad i = 1, 2, \dots, n; \end{aligned} \quad (1)$$

see, e.g., Zlatev (1995). Here

- $\mathbf{c} = (c_1, \dots, c_n)$ is a vector-valued function and contains the concentration c_i of each species as a function of space (\mathbf{x}) and time (t);
- the function \mathbf{u} denotes the velocity of flow depending on space and time;
- \mathbf{K}_i is the diffusion coefficient matrix of pollutant i , it also depends on space and time;
- $r_i(\mathbf{x}, t, \mathbf{c})$ represents the formation rate of pollutant i as a result of chemical reactions at place \mathbf{x} and time t . The function r_i is usually nonlinear and may depend on the concentration of all species. (This dependence is polynomial, if *mass action type kinetics* is assumed, which is the most frequent case, or r_i are rational functions, e.g., in the cases when enzymatic or saturation processes are present, or if we are dealing with binding kinetics.) Therefore, r_i links the equations belonging to the different pollutants; further, this term leads to the greatest difficulties in handling the model equations;
- $E_i(\mathbf{x}, t)$ represents the emission of pollutant i ;
- $\sigma_i \leq 0$ is the sedimentation coefficient.

3. The splitting method

For simplicity we introduce the splitting procedure on a finite dimensional problem, i.e., on the example of a system of ordinary differential equations. Let us consider the initial value problem

$$\frac{d\mathbf{c}(t)}{dt} = A(\mathbf{c})(t) \quad \mathbf{c}(0) = \mathbf{c}_0, \quad (2)$$

where \mathbf{c} is the unknown vector function and A can be written as a sum of two simpler operators A_1 and A_2 : $A = A_1 + A_2$. Now let us take a short time τ , and let us split the problem into the following simpler problems:

$$\frac{d\mathbf{c}^{(1)}(t)}{dt} = A_1(\mathbf{c}^{(1)})(t) \quad \mathbf{c}^{(1)}(0) = \mathbf{c}_0, \quad (3)$$

and

$$\frac{d\mathbf{c}^{(2)}(t)}{dt} = A_2(\mathbf{c}^{(2)})(t) \quad \mathbf{c}^{(2)}(0) = \mathbf{c}^{(1)}(\tau). \quad (4)$$

The solution of the splitted problem at time τ is $\mathbf{c}_{sp}(\tau) = \mathbf{c}^{(2)}(\tau)$.

The basic idea of splitting is to decompose the operator on the right hand side into the sum of simpler operators, and to solve the subproblems corresponding to the operators successively in each time step. More accurately, we solve the equation only with operator A_1 until time τ (as if only the subprocess represented by A_1 were present), and the solution in time τ will be the initial condition of the equation with A_2 . It means that we return to the initial time and solve the equation with A_2 , as well. The solution of the second equation in time τ will be the approximate solution of the original problem in time τ . This procedure is then repeated on the interval, $[\tau, 2\tau]$, etc. Thus, the simpler subproblems are connected to each other through the initial conditions.

It is clear, that the numerical treatment of the separate subproblems is simpler. The most significant advantage of splitting is that we can exploit the special properties of different subproblems and apply the most suitable numerical method for each of them. Thus, we can obtain a more precise solution in a shorter time.

The splitting error at time τ can be defined as a norm of the difference between the solutions of the exact and splitted problems at time τ :

$$\text{Err}_{\text{sp}}(\tau) = \| \mathbf{c}(\tau) - \mathbf{c}_{\text{sp}}(\tau) \| . \tag{5}$$

An operator can obviously be splitted into more than two summands, and this way the method can be extended. If we apply the method to our more complicated Eq. (1), then a possible decomposition of the operator corresponding to the right hand side might correspond to terms describing advection, diffusion, formation rate (chemical reactions), emission, and sedimentation of pollutants.

In the case of partial differential equations like Eq. (1) the splitting procedure is formally the same, but the operators act on functions with values in an *infinite dimensional* (as opposed to finite dimensional above) space. If we consider the air pollution transport equation in Section 2, the operator A in Eq. (2) corresponds to the whole right hand side of Eq. (1), that is A represents all the effects in the transport process which are presented in Eq. (1). We can split A to more, simpler operators corresponding to the physical effects that are presented in the equation. One possible splitting is: advection (A_1), diffusion (A_2), emission (A_3), reaction (A_4), sedimentation (A_5); i.e., there will be 5 subproblems corresponding to the 5 subprocesses. Of course there are other possible splittings of the problem, but it is not our aim to go into details in this question.

4. Investigation of the splitting error

For the investigation of the splitting error, Lie-operators can give us some useful help. In this section we define the basic concepts of the theory of Lie-operators, which play role in the determination of the splitting error. With the help of Lie-operators we can give a condition for zero splitting error, which is the main result of *Havasi et al.* (2001). At the end of this section we analyze this condition for the special case of advection and chemistry operators, presented in Eq. (1).

4.1 The splitting error

The zero splitting error can be characterized via the Lie-operator, see also *Varadarajan* (1974). The *Lie-operator* \mathbf{A} of the operator A is a linear operator acting on the space of differentiable operators, and it is defined for a differentiable operator G as follows:

$$(\mathbf{A}(G))(\mathbf{c}) := (G'(\mathbf{c}) \circ A)(\mathbf{c}) \quad \text{for } \forall \mathbf{c} \in D_G \cap D_A,$$

where $'$ denotes differentiation with respect to \mathbf{c} . If evaluated at the identity operator, it is actually the original operator. It is not the aim of this paper to give a very detailed description of Lie-operators and their connection with the splitting error. A more detailed discussion of this issue can be found in *Havasi et al.* (2001). Here we just mention the main points of the argument for the condition of zero splitting error.

For the solution $\mathbf{c}(t)$ of Eq. (2) using the Taylor-series expansion, we can write:

$$\mathbf{c}(t + \tau) = (e^{\tau \mathbf{A}}(I))(\mathbf{c})(t). \quad (6)$$

For the solution of the splitted problem in the same way, we obtain:

$$\mathbf{c}_{\text{sp}}(t + \tau) = (e^{\tau \mathbf{A}_2} e^{\tau \mathbf{A}_1}(I))(\mathbf{c}_{\text{sp}})(t), \quad (7)$$

where \mathbf{A} , \mathbf{A}_1 , and \mathbf{A}_2 are the Lie-operators of the operators A , A_1 , and A_2 which are presented in Eqs. (1), (2), and (3). Taking the difference of Eqs. (6) and (7) and applying simple changes we get

$$\mathbf{c}(t + \tau) - \mathbf{c}_{\text{sp}}(t + \tau) = (e^{\tau(\mathbf{A}_1 + \mathbf{A}_2)}(I))(\mathbf{c} - \mathbf{c}_{\text{sp}})(t) + (e^{\tau(\mathbf{A}_1 + \mathbf{A}_2)} - e^{\tau \mathbf{A}_2} e^{\tau \mathbf{A}_1})(I)(\mathbf{c}_{\text{sp}})(t). \quad (8)$$

The second term of the right hand side is the *local splitting error*, which arises through the use of splitting on the time interval $[t, t + \tau]$. The first term expresses the error coming from the local splitting error of earlier time steps. Considering Eq. (7), we see that the splitting error vanishes for all functions \mathbf{c} if and only if

$$e^{\tau(\mathbf{A}_1 + \mathbf{A}_2)}(I) = e^{\tau\mathbf{A}_2}e^{\tau\mathbf{A}_1}(I). \quad (9)$$

Let us define the *commutator* of \mathbf{A}_1 and \mathbf{A}_2 as

$$[\mathbf{A}_1, \mathbf{A}_2] := \mathbf{A}_1 \circ \mathbf{A}_2 - \mathbf{A}_2 \circ \mathbf{A}_1,$$

where $\mathbf{A}_1 \circ \mathbf{A}_2$ denotes the composition of the operators \mathbf{A}_1 and \mathbf{A}_2 . *Havasi et al.* (2001) have shown by the investigation of the Baker–Campbell–Hausdorff-formula that Eq. (9) holds if and only if the commutator of the operators \mathbf{A}_1 and \mathbf{A}_2 evaluated at the identity operator I is zero, that is the operators \mathbf{A}_1 and \mathbf{A}_2 commute on the operator I . Applying the definition of the Lie-operator, we obtain the following form of the necessary and sufficient condition:

$$\begin{aligned} 0 &= ([\mathbf{A}_1, \mathbf{A}_2](I))(\mathbf{c}) = ((\mathbf{A}_1 \circ \mathbf{A}_2 - \mathbf{A}_2 \circ \mathbf{A}_1)(I))(\mathbf{c}) = \\ &= (A'_2(\mathbf{c}) \circ A_1)(\mathbf{c}) - (A'_1(\mathbf{c}) \circ A_2)(\mathbf{c}). \end{aligned}$$

Hereafter we will use this condition to analyze the splitting error of a given splitting procedure. Henceforth, if the Lie-operators of A_1 and A_2 commute, we say that the operators A_1 and A_2 L-commute, furthermore, we will use the notation:

$$[A_1, A_2]_L := [\mathbf{A}_1, \mathbf{A}_2](I).$$

We remark that if A_1 and A_2 are linear operators then the L-commutation is equivalent to the usual commutation, although $[A_1, A_2]_L = -[A_1, A_2]$.

4.2 L-commutativity of the advection and chemistry operators

Now we investigate the condition of L-commutativity in the case of advection and chemistry operators. We study the conditions under which the advection and chemistry operators presented in Eq. (1) L-commute. Related studies can be found in *Dimov et. al.* (1999, 2002), *Faragó and Havasi* (2001), and *Hundsdofer and Verwer* (1994). Let us denote the advection operator from now on by A . It is defined by

$$(A\mathbf{c})(\mathbf{x}, t) := -\left(\nabla \cdot (\mathbf{u}(\mathbf{x}, t)c_1(\mathbf{x}, t)), \nabla \cdot (\mathbf{u}(\mathbf{x}, t)c_2(\mathbf{x}, t)), \dots, \nabla \cdot (\mathbf{u}(\mathbf{x}, t)c_n(\mathbf{x}, t))\right).$$

Let the chemistry operator $R = (R_1, R_2, \dots, R_n)$ be defined by

$$(R(\mathbf{c}))(\mathbf{x}, t) := (r_1(\mathbf{x}, t, \mathbf{c}(\mathbf{x}, t)), r_2(\mathbf{x}, t, \mathbf{c}(\mathbf{x}, t)), \dots, r_n(\mathbf{x}, t, \mathbf{c}(\mathbf{x}, t))),$$

or using another notation emphasizing that R acts on the space of functions:

$$R(\mathbf{c}) := (r_1 \circ (\text{id}, \mathbf{c}), r_2 \circ (\text{id}, \mathbf{c}), \dots, r_n \circ (\text{id}, \mathbf{c})).$$

Since the operator A is linear, its derivative is A itself. The derivative of the operator R evaluated at the function \mathbf{c} is an $n \times n$ matrix, with the element $\frac{\partial r_i}{\partial c_j}$ in the i th row and j th column. Then

$$[A, R]_L(\mathbf{c}) = (R'(\mathbf{c}) \circ A)(\mathbf{c}) - (A'(\mathbf{c}) \circ R)(\mathbf{c})$$

is an n -dimensional vector valued function whose i th coordinate function is given by

$$([A, R]_L(\mathbf{c}))_i = -\sum_{j=1}^n \frac{\partial r_i}{\partial c_j} \nabla \cdot (\mathbf{u}c_j) + \nabla \cdot (\mathbf{u}r_i).$$

We remark that for the scalar function $r_i(\mathbf{x}, t, \mathbf{c}(\mathbf{x}, t))$ and vector function $\mathbf{u}(\mathbf{x}, t)$, the following relation holds

$$\nabla \cdot (\mathbf{u}r_i) = r_i \nabla \cdot \mathbf{u} + \mathbf{u} \cdot \left(\nabla_{\mathbf{x}} r_i + \sum_{j=1}^n \frac{\partial r_i}{\partial c_j} \nabla c_j \right),$$

where

$$\nabla_{\mathbf{x}} r_i(x, y, z, t, c_1, c_2, \dots, c_n) = \left(\frac{\partial r_i}{\partial x}, \frac{\partial r_i}{\partial y}, \frac{\partial r_i}{\partial z} \right).$$

Applying that identity, we obtain

$$\begin{aligned} ([A, R]_L(\mathbf{c}))_i &= -\sum_{j=1}^n \frac{\partial r_i}{\partial c_j} c_j \nabla \cdot \mathbf{u} - \sum_{j=1}^n \frac{\partial r_i}{\partial c_j} \mathbf{u} \cdot \nabla c_j + r_i \nabla \cdot \mathbf{u} + \mathbf{u} \cdot \nabla_{\mathbf{x}} r_i + \mathbf{u} \cdot \sum_{j=1}^n \frac{\partial r_i}{\partial c_j} \nabla c_j = \\ &= -\sum_{j=1}^n \frac{\partial r_i}{\partial c_j} c_j \nabla \cdot \mathbf{u} + r_i \nabla \cdot \mathbf{u} + \mathbf{u} \cdot \nabla_{\mathbf{x}} r_i. \end{aligned} \quad (10)$$

The operators L-commute if and only if the expression given by Eq. (10) is equal to zero. A sufficient condition for this is

$$\nabla \cdot \mathbf{u} = 0 \quad \text{and} \quad \mathbf{u} \cdot \nabla_{\mathbf{x}} r_i = 0,$$

which holds for all $i = 1, 2, \dots, n$. Obviously, if the flow is divergence free and the rate of chemical reactions depends only on the concentrations and time, the above sufficient conditions are satisfied.

5. An advection-reaction model with Molenkampf–Crowley advection

In this section we present our results for a specialized two-dimensional model, henceforth, \mathbf{x} denotes the two spatial coordinates (x, y) . We study a problem with special advection, called *Molenkampf–Crowley* advection and chemistry processes:

$$\frac{\partial c_i(\mathbf{x}, t)}{\partial t} = y \frac{\partial c_i(\mathbf{x}, t)}{\partial x} - x \frac{\partial c_i(\mathbf{x}, t)}{\partial y} + r_i(\mathbf{x}, t, \mathbf{c}(\mathbf{x}, t)), \quad i = 1, 2, \dots, n. \quad (11)$$

We give necessary and sufficient conditions under which the operator of the Molenkampf–Crowley advection and the operator of chemical reactions L-commute.

5.1 Molenkampf–Crowley advection

The operator A of the advection is linear, its derivative is A itself. For n species the operator is defined as

$$A\mathbf{c} = \begin{pmatrix} y \frac{\partial c_1}{\partial x} - x \frac{\partial c_1}{\partial y} \\ \vdots \\ y \frac{\partial c_n}{\partial x} - x \frac{\partial c_n}{\partial y} \end{pmatrix}$$

This is a special case of the general advection presented in Eq. (1). We obtain it if Eq. (1) is reduced into two spatial dimensions, and the function \mathbf{u} – which has now two coordinate functions u_1 and u_2 – equals to $(-y, x)$, that is $u_1(x, y, t) = -y$ and $u_2(x, y, t) = x$.

The Molenkampf–Crowley advection is often used as a test in the investigation of different methods, see, e.g., in Zlatev (1995). It is also known as *cone-test*. As a simple advection, it is suitable for us to investigate the behavior of the splitting error. The solution of the problem

$$\frac{\partial c_i}{\partial t} = y \frac{\partial c_i}{\partial x} - x \frac{\partial c_i}{\partial y}, \quad i = 1, 2, \dots, n, \quad (12)$$

with the initial condition $c_i(x, y, 0) = x^2 + y^2$, forms a cone for every $i = 1, 2, \dots, n$ and keeps its form during the time interval of the integration.

5.2 Main result: necessary and sufficient condition of L-commutativity

Now we show which special type of chemistry operators L-commute with the Molenkampf–Crowley advection. The operator of the chemical reactions R has the same form as defined before. Let us consider the i th coordinate of the L-commutator of A and R in two spatial dimensions:

$$([A, R]_L(\mathbf{c}))_i = u_1 \frac{\partial r_i}{\partial x} + u_2 \frac{\partial r_i}{\partial y} - \sum_{j=1}^n \frac{\partial r_i}{\partial c_j} \left(u_1 \frac{\partial c_j}{\partial x} + u_2 \frac{\partial c_j}{\partial y} \right). \quad (13)$$

The notation $\frac{\partial r_i}{\partial x}$ and $\frac{\partial r_i}{\partial y}$ can be misleading. The function r_i has $n+3$ variables $(x, y, t, c_1, \dots, c_n)$ and depends on space and time also through the concentrations (c_1, \dots, c_n) . Thus, the derivative of the function r_i with respect to x is $\frac{\partial r_i}{\partial x} + \sum_{j=1}^n \frac{\partial r_i}{\partial c_j} \frac{\partial c_j}{\partial x}$, where the notation $\frac{\partial r_i}{\partial x}$ is correct in a sense. So we study the expression

$$\begin{aligned} ([A, R]_L(\mathbf{c}))_i &= u_1 \left(\frac{\partial r_i}{\partial x} + \sum_{j=1}^n \frac{\partial r_i}{\partial c_j} \frac{\partial c_j}{\partial x} \right) + u_2 \left(\frac{\partial r_i}{\partial y} + \sum_{j=1}^n \frac{\partial r_i}{\partial c_j} \frac{\partial c_j}{\partial y} \right) - \\ &\quad - \sum_{j=1}^n \left(u_1 \frac{\partial r_i}{\partial c_j} \frac{\partial c_j}{\partial x} + u_2 \frac{\partial r_i}{\partial c_j} \frac{\partial c_j}{\partial y} \right) = \\ &= u_1 \frac{\partial r_i}{\partial x} + u_1 \sum_{j=1}^n \frac{\partial r_i}{\partial c_j} \frac{\partial c_j}{\partial x} + u_2 \frac{\partial r_i}{\partial y} + u_2 \sum_{j=1}^n \frac{\partial r_i}{\partial c_j} \frac{\partial c_j}{\partial y} - u_1 \sum_{j=1}^n \frac{\partial r_i}{\partial c_j} \frac{\partial c_j}{\partial x} - u_2 \sum_{j=1}^n \frac{\partial r_i}{\partial c_j} \frac{\partial c_j}{\partial y} = \end{aligned}$$

$$= u_1 \frac{\partial r_i}{\partial x} + u_2 \frac{\partial r_i}{\partial y}. \quad (14)$$

Substituting the functions $u_1(x, y, t) = -y$ and $u_2(x, y, t) = x$, we obtain that the splitting error is zero for any initial functions if and only if the equality

$$-y \frac{\partial r_i}{\partial x} + x \frac{\partial r_i}{\partial y} = 0 \quad (15)$$

holds for $i = 1, 2, \dots, n$. This is a first order homogeneous linear partial differential equation for r_i . A general solution of Eq. (15) can be obtained as:

$$r_i(x, y, t, \mathbf{c}) = \varphi_i(x^2 + y^2, t, \mathbf{c}), \quad (16)$$

where φ_i is an arbitrary continuously differentiable function. This provides a necessary and sufficient condition for the L-commutation of Molenkampf–Crowley advection and chemistry. As we have mentioned, the chemistry operator represents the rate of the reactions between the pollutants. It usually depends on the concentrations and on a coefficient, which is modeled by the Arrhenius-equation:

$$k = A e^{-\frac{E_a}{RT}}, \quad (17)$$

where T is the temperature and A, R, E_a are physical constants (see in *Atkins*, 1998; *Seakins* and *Pilling*, 1996). Hence, the coefficient k depends on the spatial coordinates and time through temperature. Thus, the condition of L-commutativity of the operators A and R is

$$T(x, y, t) = f(x^2 + y^2, t). \quad (18)$$

This means geometrically that the isotherms form concentric circles in space.

6. Numerical examples

In this section we present some numerical results for models with Molenkampf–Crowley advection and chemistry operators. Thus, the problem is two-dimensional and we have only one species, so $\mathbf{c} = (c_1, \dots, c_n)$ reduces to c . We study the following initial value problem:

$$\frac{\partial c(x, y, t)}{\partial t} = y \frac{\partial c(x, y, t)}{\partial x} - x \frac{\partial c(x, y, t)}{\partial y} + r(x, y, t, c(x, y, t)) \quad c(x, y, 0) = c_0. \quad (19)$$

We will call this full equation since both operators are present. The splitting problem in the first time step will be as follows:

$$\frac{\partial c^{(1)}(x, y, t)}{\partial t} = y \frac{\partial c^{(1)}(x, y, t)}{\partial x} - x \frac{\partial c^{(1)}(x, y, t)}{\partial y}, \quad c^{(1)}(x, y, 0) = c_0,$$

and

$$\frac{\partial c^{(2)}(x, y, t)}{\partial t} = r(x, y, t, c^{(2)}(x, y, t)), \quad c^{(2)}(x, y, 0) = c^{(1)}(x, y, \tau). \quad (20)$$

We solve both the full and splitting problems numerically on a bounded domain: on a square. We choose three different functions r to present the chemical reactions, and solve the problem with each of them. However, our r functions typically do not represent real-life processes, but they are adequate to analyze the splitting error arising in the solution of the problems. We choose the functions for r in such a way that we know the exact solution of the problem, hence, we can compare it with the approximate solutions. Thus, we can calculate the errors of the approximations, which are the maximum norm of the difference between the exact solution and the approximation in every given case. We compare the solution of the full and splitting problems to the exact solution in each time step.

6.1 Numerical experiments

The numerical treatment requires temporal and spatial discretisation of the equations. See *Stoer and Bulirsch (1993)*. Let us consider the following division of our domain:

$$\{x_i = ih, i = 1, 2, \dots, 10; y_j = jh, j = 1, 2, \dots, 10\}.$$

Hence, we obtain a 10×10 square grid. The grid parameter h was 1.0 in each problem. The time step of the numerical scheme and the time step of the splitting were equal to 0.015. We approximated the derivatives with first order finite differences. To approximate the spatial derivatives, in the advection term we used central scheme, and on the boundary of the domain we used the appropriate *forward* or *backward* Euler scheme. To approximate the time derivative on the left side, we used the *Euler forward* scheme. We solved the

equations by applying both explicit and implicit schemes. As initial value, we chose the value of the exact solution at time $t = 0$. In every problem we calculated the relative error as the maximum norm of the difference between the exact and the numerical solution. We compared these errors in different ways to analyze the effect of splitting. In the figures we plotted the errors against time steps.

In the first problem we had $r(x, y, t, c) = c - xy + x^2 - y^2 - t + 1$. The exact solution is $c(x, y, t) = xy + t$, with the corresponding initial condition $c(x, y, 0) = xy$. As we can see it easily, the condition of L-commutativity does not hold in this problem. In the figures we can see that the error in the solution of the splitting problem is greater than in the solution of the full problem. Fig. 1 shows the relative errors of the solutions of the *full* and *splitting* problems. Both of the problems were solved numerically by an *explicit Euler* scheme. Fig. 3 shows the same calculations by *implicit Euler* schemes. Figs. 2 and 4 show the difference between the relative errors of the splitting and full solutions in order generated by an explicit scheme and implicit schemes. The implicit scheme provides a more accurate solution compared to the explicit scheme. We can observe that the implicit scheme equilibrates the effect of splitting and its error much more than the explicit scheme. Fig. 5 shows the difference between the relative error of the full and splitting problem solutions generated by explicit and implicit schemes. In Fig. 5 we can see how the splitting affects the accuracy with implicit and explicit schemes. See also Fig. 6, which shows the relative error of the solution of the splitting problem generated by explicit and implicit schemes.

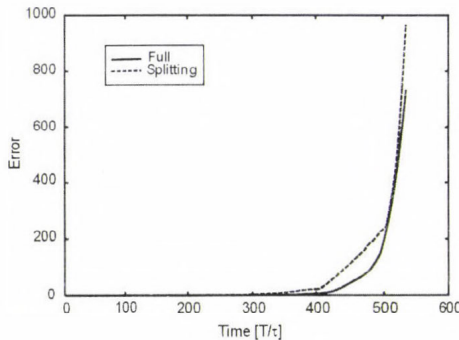


Fig. 1. The relative errors of the numerical solutions of the first problem are plotted against the number of time steps.

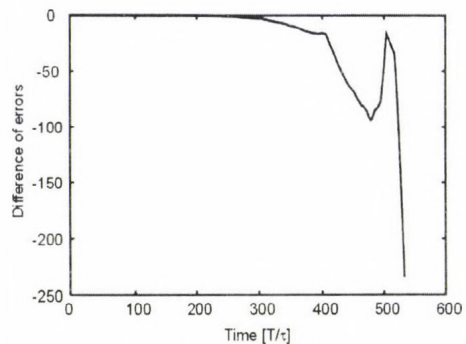


Fig. 2. The difference between the relative errors of the numerical solutions of the *full* and *splitting* problems is plotted against the number of time steps.

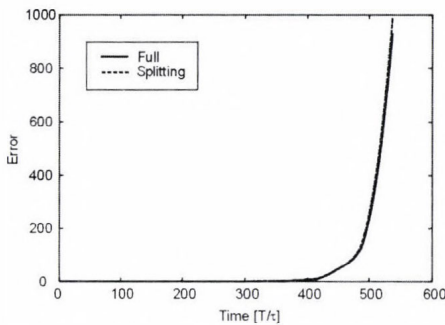


Fig. 3. The relative errors of the numerical solutions of the first problem are plotted against the number of time steps.

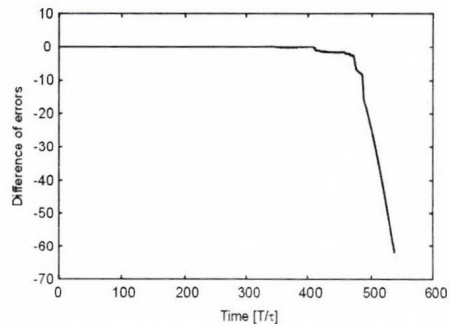


Fig. 4. The difference between the relative errors of the numerical solutions of the *full* and *splitting* problems is plotted against the number of time steps.

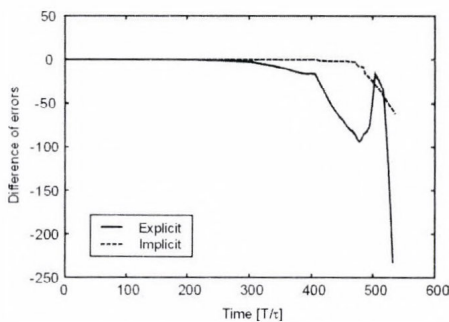


Fig. 5. The differences between the relative errors of the numerical solutions of the *full* and *splitting* problems are plotted against the number of time steps.

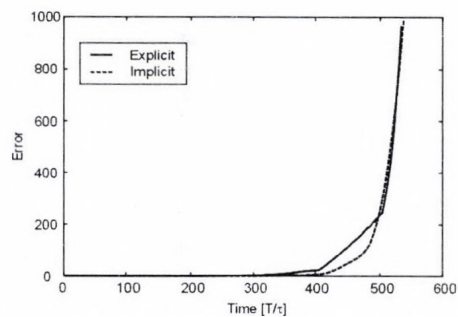


Fig. 6. The relative errors of the numerical solutions of the splitting problem are plotted against the number of time steps.

In the second problem we had $r(x, y, t, c) = c - 2y$. The splitting error is not zero. The exact solution of this problem is $c(x, y, t) = x + y$. In this special case, the applied finite difference schemes provide the exact solution for the full problem. Using an implicit scheme we obtain the exact solution with splitting, too. The explicit scheme provides a solution different from the exact solution. See Fig. 7, which shows the relative errors of the solutions of the full and splitting problems. Both of the problems were solved numerically by an explicit Euler scheme. The solution of the full problem was equal to the exact solution; so its relative error is constantly zero. We may observe significant

the splitting problem. We can say that the splitting procedure is sensitive to the choice of the applied numerical scheme. The splitting error does not appear in the solution generated by the implicit scheme.

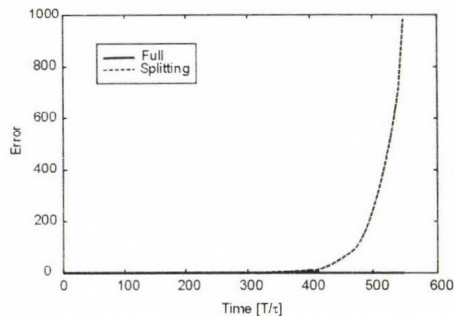


Fig. 7. The relative errors of the numerical solutions of the second problem are plotted against the number of time steps.

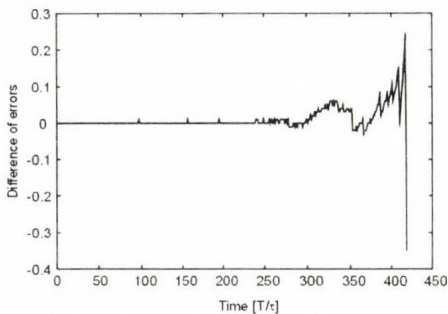


Fig. 8. The difference between the relative errors of the numerical solutions of the *full* and *splitting* problems is plotted against the number of time steps.

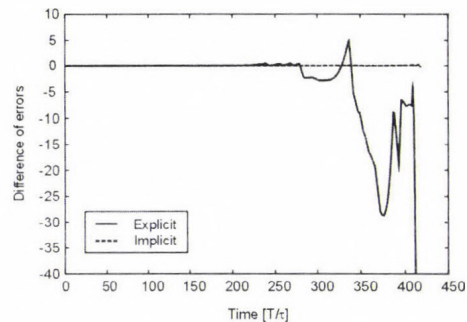


Fig. 9. The differences between the relative errors of the numerical solutions of the *full* and *splitting* problems are plotted against the number of time steps.

In the third problem we had $r(x,y,t,c)=c-x^2-y^2-t+1$. Note that in this problem the condition of L-commutativity is satisfied. The function of chemical reaction rate has a form $f(x^2+y^2,t,c)$. The exact solution of the problem is $c(x,y,t)=x^2+y^2+t$. Comparing to the previous problems, we can see that we obtain more accurate solutions of the splitting problem compared to the full one than before. There are intervals in which the solution of the splitting problem is closer to the exact solution than the solution of the full problem. See Fig. 8, which shows the difference between the relative errors of the solutions of the full and splitting problems. Both of the problems were solved numerically by an implicit Euler scheme. Also, in this third problem we

can say that the implicit scheme provides a more accurate solution than the explicit scheme. Furthermore, the implicit scheme equilibrates the effect of splitting and its error much more than the explicit scheme. See also *Fig. 9*, which shows the difference between the relative error of the full and splitting problem solutions generated by explicit and implicit schemes.

6.2 Conclusion of the numerical experiments

The solutions of different problems show that the errors generated by splitting are sensitive to the choice of the numerical method. We can say in general that the implicit scheme equilibrates the effect of splitting and its error much more than the explicit scheme. We also obtained a result, where the theoretically non-zero splitting error did not appear in the solution.

7. Discussion and perspectives

In this paper the general result by *Havasi et al.* (2001) was on zero splitting error. The condition of L-commutativity was investigated in the case of Molenkampf–Crowley advection and chemistry operators. A necessary and sufficient condition on the L-commutation of the advection and chemistry operators was derived. Numerical experiments were performed with Molenkampf–Crowley advection and different chemistry operators.

After splitting the problem, a numerical method is used to solve the subproblem. It means, that the subproblem is not solved exactly, so the L-commutativity does not provide direct information about the error of the obtained solution. To have a quantitative estimation of the error we need to study the approximation operators defined by the numerical methods. In all of the three studied problems we obtained very different results regarding the effect of splitting when using different numerical methods.

Our future plan is to make a systematic study on reaction diffusion equations. We would like to study the effect of splitting in reaction diffusion equations. Our main aim is to characterize the splitting error if it is not zero to map the advantages of splitting in running time and accuracy.

Acknowledgement—The present work has partially been supported by the National Science Foundation, Hungary (T037491).

References

- Atkins, P.W.*, 1998: *Physical Chemistry* (6th ed.), Vol. III., *Change*. W.H. Freeman Co., New York.
- Dimov, I., Faragó, I., and Zlatev, Z.*, 1999: Commutativity of operator splitting methods for air pollution models. *Technical Report 04/99*. Bulgarian Academy of Sciences.

- Dimov, I., Faragó, I., Havasi, Á., and Zlatev, Z., 2002: L-commutativity of the operators in splitting methods for air pollution models. *Annal. Univ. Sci. Sec. Math.* 44, 127-148.
- Faragó, I. and Havasi, Á., 2001: The mathematical background of operator splitting and the effect of non-commutativity. *Proc. of the Conference on Large-scale Scientific Computations*. Springer, 264-271.
- Havasi, Á., Bartholy, J., and Faragó, I., 2001: Splitting method and its application in air pollution modeling. *Időjárás* 105, 39-58.
- Hundsdorfer, W. and Verwer, J.G., 1994: A note on splitting errors for advection-reaction equations. *Appl. Math.* 18, 191-199.
- Lanser, D. and Verwer, J.G., 1999: Analysis of operator splitting for advection-diffusion-reaction problems from air pollution modelling. *J. Comput. Appl. Math.* 111, 201-216.
- Marchuk, G.I., 1968: Some application of splitting-up methods to the solution of mathematical physics problems. *Applik. Mat.*, 13.
- McRae, G.J., Goodin, W.R., and Seinfeld, J.H., 1984: Numerical solution of the atmospheric diffusion equations for chemically reacting flows. *J. Comput. Phys.* 45, 1-11.
- Seakins, P.W. and Pilling, M.J., 1996: *Reaction Kinetics*. Oxford University Press, Oxford.
- Sportisse, B., 2000: An analysis of operator splitting techniques in the stiff case. *J. Comput. Phys.* 161, 140-168.
- Stoer, J. and Bulirsch, R., 1993: *Introduction to Numerical Analysis*. Springer-Verlag.
- Strang, G., 1968: On the construction and comparison of difference schemes. *SIAM J. Numer. Anal.* 5, 505-517.
- Varadarajan, V.S., 1974: *Lie-groups, Lie-Algebras and Their Representations*. Prentice-Hall, Inc., Englewood Cliffs, New Jersey.
- Zlatev, Z., 1995: *Computer Treatment of Large Air Pollution Models*. Kluwer Academic Publishers, Dordrecht-Boston-London.

IDŐJÁRÁS

Quarterly Journal of the Hungarian Meteorological Service
Vol. 109, No. 3, July–September 2005, pp. 189–202

Long-term variations of temperature, wind, and precipitable water in the troposphere and lower stratosphere over Budapest, Hungary

Sándor Cseh¹ and Pál Bencze²

¹*Apáczai Csere János Teacher's Training Faculty, University of Western Hungary,
P.O. Box 204, H-9002 Győr, Hungary*

²*Geodetic and Geophysical Research Institute, Hungarian Academy of Sciences,
P.O. Box 5, H-9401 Sopron, Hungary; E-mail: bencze@ggki.hu*

(Manuscript received in final form May 27, 2005)

Abstract—Long-term variations of the height of different isobaric levels, temperature, wind, and precipitable water in the troposphere and lower stratosphere have been studied for determination of the temporal trend of these parameters at mid-latitudes over Budapest, Hungary. One of the reasons of this study was to establish the height, where the trend of temperature changes sign from positive (increasing) in the lower troposphere due to the global warming to negative (decreasing) in the upper part of the troposphere over Budapest, Hungary. For the analyses of the behavior of temperature with increasing altitude, radiosounding data were used. It has been found that the trend of temperature is positive from the ground to the height of the 500 hPa isobaric level (~ 5.6 km), then it turns into negative. The trend has been determined by using linear regression. The results show that the lower troposphere is warming from the ground to a height of about 6 km, while the region above this height is cooling. The precipitable water in a column of unit area extending from 850 hPa (1.5 km) to 200 hPa (12 km) indicates a significant negative (decreasing) trend, suggesting a drying tendency in the troposphere.

Key-words: temperature in the troposphere, precipitable water, warming of the atmosphere, long-term change of meteorological parameters.

1. Introduction

The atmosphere is a continuous substance. Effects of atmospheric processes taking place in the lower atmosphere are not limited to the lower atmosphere, and inversely, consequences of atmospheric phenomena in the upper

atmosphere are not limited to the upper atmosphere. Such phenomena are, e.g., the origin of the atmospheric waves, which can also be observed in the upper atmosphere, or absorption of the solar electromagnetic radiation in the upper atmosphere, as well as modification of the energy spectrum of energetic particles of galactic origin by the upper atmosphere. This circumstance should also be considered, if regional climate scenarios are drawn up, as it is done in case of the Carpathian Basin (*Mika*, 1988, 1994).

An important issue of the study of climate change is the determination of the proportion, by which different processes can affect the global change. These processes generally considered are the greenhouse effect, aerosol particles, cloudiness, solar radiation (solar activity), geomagnetic activity, and galactic cosmic rays. Investigations are partly carried out taking into account one of the processes. There is also difference in the length of time, to which these investigations are extended, short period or long-term changes of the processes.

Concerning the greenhouse effect, it is due to the so-called greenhouse gases, which absorb and reradiate the long wave temperature radiation of the Earth's surface and the overlying atmospheric layers in all directions. First of all, these greenhouse gases are responsible for global warming (*Lean and Rind*, 1999). The climate is especially sensible to enhancement of the concentration of carbon dioxide. This circumstance is related to the coincidence of the wavelength of the maximum long wave radiation of the ground with the main wavelength band of absorption of CO₂. A study of the effect of greenhouse gases extending to both of the middle and upper atmosphere has been carried out by *Roble and Dickinson* (1989). Model results of these authors predicted a long-term decrease of the NO concentration, which indicated a shrinking of the atmosphere that is cooling at stratospheric and mesospheric heights. Decrease of the NO concentration has been experimentally proved by analysis of the reflection height of low frequency (LF) radio waves (*Bremer and Berger*, 2002). Model results have shown that the experimental temperature trends can qualitatively be explained by an increasing atmospheric greenhouse effect (*Bremer and Berger*, 2002; *Bremer*, 2003). According to a review of the results referring to long-term changes in the upper atmosphere (*Bremer et al.*, 2004), an increasing atmospheric greenhouse effect can also be shown in the height range of 90–150 km. An increasing effect of greenhouse gases can be traced at altitudes from 150 to 180 km, too. However, above these altitudes no sure effect of greenhouse gases could be revealed. It is obvious that this circumstance is related to the decreasing concentration (rarefaction) of greenhouse gases.

The role of the cloudiness is a complex problem. Clouds can influence the global change by extension of the cloud cover depending on optical thickness, reflectivity, and height of the clouds. The extension of the cloud cover depends

on temperature and humidity of near surface atmospheric layers, as well as on many other factors, as, e.g., topography, instabilities.

Concerning the solar radiation, the total solar irradiance changes over periodicities from minutes to the eleven-year solar cycle (*Pap and Fröhlich, 1999; Rottman, 1999*). Observations of the intensity of solar radiation carried out during solar flares in the past have shown that the intensity of radiation in the EUV and X-ray bands increases for a period of about one hour, and the extent of the increase is reduced with increasing wavelength. The enhancement of radiation due to solar flares may not have a significant effect on the atmosphere because of the short time and changes limited to the EUV and X-ray bands, which can only penetrate to the height of about 60 km. Thus, this radiation increase is insignificant from point of view of the total irradiation. Intensity of the ultraviolet irradiance is varying due to the solar rotation related to the non-uniform distribution of active areas on the solar disk. In this case the magnitude of irradiance also decreases with increasing wavelength to about 300 nm (*Rottman, 1999*). The solar cycle variation of the irradiance is also limited to a wavelength of less than 300 nm. The 27-day variation expressed by the ratio of the solar spectrum referring to an active day to the spectrum related to a less active day shows a value of about 20% at the Lyman α wavelength. The ratio of the solar spectrum in the maximum solar activity period to the spectrum in the minimum period indicates an enhancement about 70% at the Lyman α wavelength (*Rottman, 1999*). Nevertheless, assuming a climate sensitivity of $1\text{ }^{\circ}\text{C W}^{-1}\text{ m}^{-2}$, the enhancement of the total solar irradiance of 0.14% from 1900 to 1990 can only be responsible for 0.25 $^{\circ}\text{C}$ of the 0.6 $^{\circ}\text{C}$ surface warming (*Lean and Rind, 1999*).

Geomagnetic activity plays also an indirect role in the change of the global climate. Geomagnetic activity is the consequence of the solar activity in the Earth's environment. As a consequence of heat input during geomagnetic disturbances, the atmosphere may also be affected by creating and strengthening the reverse circulation at high latitudes in the middle atmosphere, as well as extending it to mid-latitudes. The heat input related to geomagnetic disturbances is due to precipitation of energetic electrons ($> 30\text{ keV}$) into the auroral zone, increasing ionization there, and thus, increasing electric conductivity in the height range of 90–120 km. Enhancement of the conductivity results in the intensification of the auroral electrojet and in the enhancement of the Joule heat by the increased current intensity.

Effect of the galactic cosmic rays are taken into account, since they are the main ionization radiation below about 90 km in the atmosphere. The flux of galactic cosmic radiation depends on the state of the interplanetary magnetic field. On the other hand, the state of the interplanetary magnetic field is controlled by the solar activity increasing the production of magnetic field

irregularities (piling up of magnetic field lines in front of plasma clouds and production of shock fronts ahead and behind corotating high speed plasma streams). Galactic cosmic ray particles are scattered by these irregularities, and thus, their flux decreases, which is called Forbush decrease. The effect of irregularities of the interplanetary magnetic field is the greater, the smaller is the particle energy, and it is inversely proportional to the solar activity. Galactic cosmic rays may affect the global change indirectly by ionization influencing the effectiveness of the transformation of supercooled drops into ice (tropospheric aerosols).

On the one hand, supercooled drops are thermodynamically unstable, because they are in transitional state between the liquid and solid states. As the transformation of supercooled drops to ice is finished, these particles begin to grow by the deposition of water vapor to the surface of ice crystals. Both transition of the supercooled drops to ice and deposition of the water vapor to ice crystals are related to the release of latent heat. The ice grains begin to sink as soon as they reach the corresponding dimension. Thus, on the other hand, this system is also gravitationally unstable. Ice grains may decrease the water vapor concentration in the middle part of clouds, too, by deposition of water vapor to ice grains during their fall causing further release of latent heat.

The above described process would mean no unusual matter as compared with processes known so far. However, theoretical and experimental investigations have shown that if supercooled drops have electrical charge, transition of the supercooled drops into ice is accelerated (*Pruppacher and Klett, 1997*). Supercooled drops originating in the upper part of the clouds become positively charged due to the positive charge accumulation as a result of polarization of the clouds. Polarization of clouds embedded in the atmospheric electric circuit is produced by the vertical air-earth current. Electric conductivity of the clouds is smaller than that of the environment. Charge accumulation in the upper part of the clouds depends on the intensity of the vertical air-earth current. However, intensity of the vertical air-earth current is also proportional to the electric conductivity of the air, which is determined by the ion concentration and mobility of ions. Thus, the degree of the charge accumulation can be changed by the effect of the galactic cosmic rays on the ionization, affecting the ion concentration. Estimations referring to the latent heat released in course of the above discussed cloud physical processes have shown the following results. The water leaving the cloud, as precipitation is only about 10% of the total cloudwater. The remaining part of the cloudwater evaporates again. By the increase of the effectivity of the precipitation formation, the water leaving the cloud as precipitation increases from 10% to 11%, taking a speed of the rainfall of 1 cm hour^{-1} , and it would produce an energy flux of about $10^{-1} \text{ W cm}^{-2}$ for the heating of the atmosphere. Considering

the limited spatial extension and period of the rainfall, this energy flux would represent an increase of the energy flux supplied to the atmosphere by the galactic cosmic ray flux of $10^{-10} \text{ W cm}^{-2}$ by a factor of 10^9 (Tinsley, 1996).

2. Method and data

Monthly mean values of pressure, temperature, humidity, and wind are measured by radiosounding at different altitudes at the Aerological Observatory of the Hungarian Meteorological Service, Budapest (47°26'N; 19°11'E). Measured profiles are published in yearbooks. Yearly means were calculated from the monthly mean values using the data of midday ascents. Linear regression analyses were used for determination of the trend of the different parameters. Correlation between the yearly mean values and the regression line has also been computed and indicated in the figures. The data series comprised data of 33 years from 1962 to 1994, referring to the middle atmosphere. Thus, trends of the height of selected isobaric levels, that of the temperature and wind at these levels, and the trend of precipitable water were determined. In case of such a long interval, it must be considered that the measuring equipment and data processing have been changed, furthermore, the measured data include smaller or larger errors, however, computation of yearly means may significantly decrease the errors.

According to previous investigations aimed at the determination of reliable trends, it is necessary to have a data series comprising at least three solar cycles (Bremer, 1992). Bremer (1992) found that the sign of the trend fluctuated strongly between positive and negative values, if the length of the data series is less than three solar cycles. The length of the period, within which the sign of the trend does not change already, depends on the season. Sign of the trend is most quickly stabilized in the summer months (less than two solar cycles), and the final value is most slowly reached in the winter months. This difference might be attributed to the variability of the data within the data series.

Concerning the significance of the correlation coefficient, it is to be noted that monthly mean values of 33 years are used, that is, nearly 400 values. The value of the significant correlation coefficient decreases with increasing magnitude of the sample (Taubenheim, 1969). In this case all correlation coefficients are significant at the 95% level of confidence, if their values are greater than 0.18. The coefficient of determination, R^2 , is shown in the figures. The coefficient of the determination is equal to the square of the correlation coefficient. Thus, the correlation coefficient is simply its square root.

3. Results and discussion

The trend of the height of isobaric levels is positive. This means increasing height with time at the isobaric levels of 850, 500, 250 hPa, and at the tropopause (*Fig. 1*). The sign of the trend changes above the isobaric level 150 hPa, this level is indicating the transition. The trend of the height of isobaric levels is already negative, the height decreases with time in case of the isobaric levels of 150, 30, 20, and 10 hPa (*Fig. 2*). If we study the trend of the temperature at different isobaric levels, it may be established that trends of the height of isobaric levels follow the behavior of the trends of temperature at levels to a height of about 250 hPa. It can be seen in *Fig. 3*, that the temperature shows positive trend at the ground and at the isobaric levels of 900, 850, 700, 600, and 500 hPa. Change of the sign of the trend occurs below about 250 hPa, at this height the trend of the temperature is already negative, the temperature decreases with time (*Fig. 3*). Trends of the temperature are negative at the isobaric levels of 150, 100, 50, 30, and 20 hPa, but positive at the isobaric level of 10 hPa (*Fig. 4*).

The approximately similar behavior of the trends of the height of isobaric levels and temperature may be explained by the change of temperature resulting in the expansion or contraction of the atmosphere. The height of the isobaric levels increases with time, where the temperature rises with time, as in the troposphere. Similarly, the height of the isobaric levels decreases with time, where the temperature sinks, as in the lower stratosphere. Change of the positive sign of the trends below about 250 hPa into negative sign and then, its changing into positive sign at heights above 20 hPa hints at a possible effect of ozone. The heating in the stratosphere is associated with absorption of the solar electromagnetic radiation by ozone, mainly in the wavelength band of 200–300 nm. It may be assumed that the reduced ozone concentration is attributable to the human activity, and the decreased heating due to the lowered ozone concentration in the past century results in the negative trend of temperature in the lower stratosphere from the isobaric level of 250 hPa (10 km) to about 20 hPa (27 km). It is to be noted that the ozone depletion is the largest in the lower stratosphere (*Bencze, 1991*).

In the troposphere the height of isobaric levels increases with time, but in different degree. The positive trend decreases with decreasing pressure, the height difference between isobaric levels diminishes with time. This means that the vertical pressure gradient is growing with time. According to the equation of pressure of the kinetic gas theory, the vertical gradient of pressure is proportional to the vertical gradient of temperature. As we have seen, the degree of the trend of the temperature at isobaric levels decreases also with decreasing pressure in the troposphere. Thus, the vertical gradient of

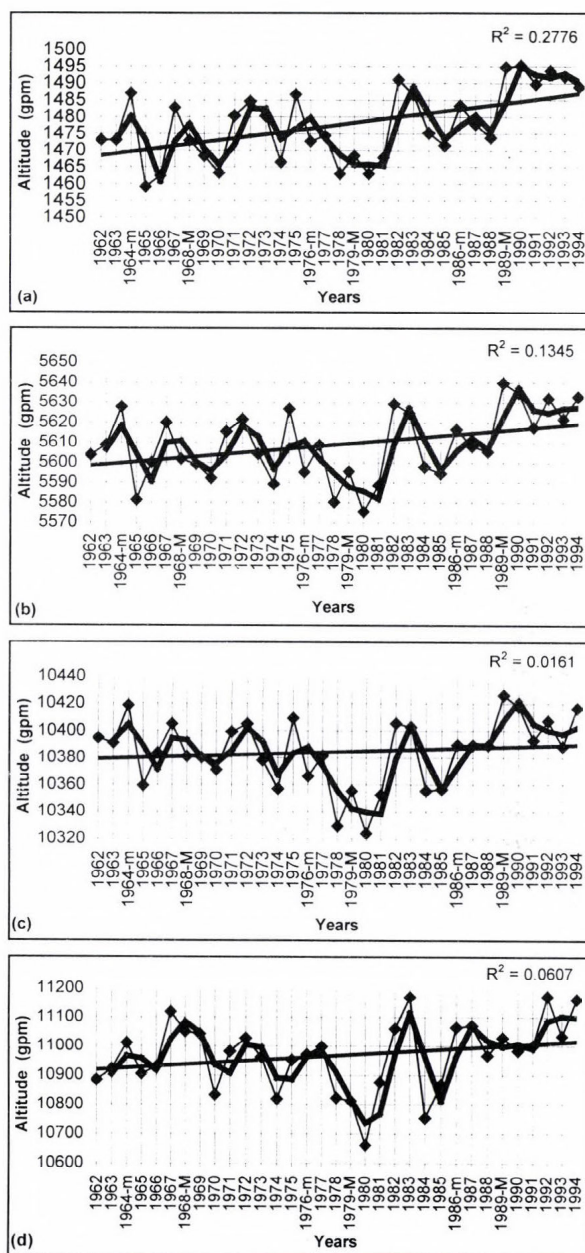


Fig. 1. Long-term change of the altitude of the 850 hPa (a), 500 hPa (b), 250 hPa (c) isobaric levels, and the tropopause (d) above Budapest. Square of the correlation coefficient is printed in the right upper corner. Thick curve shows the two-year sliding average. *m* and *M* indicate solar activity minimum and maximum, respectively.

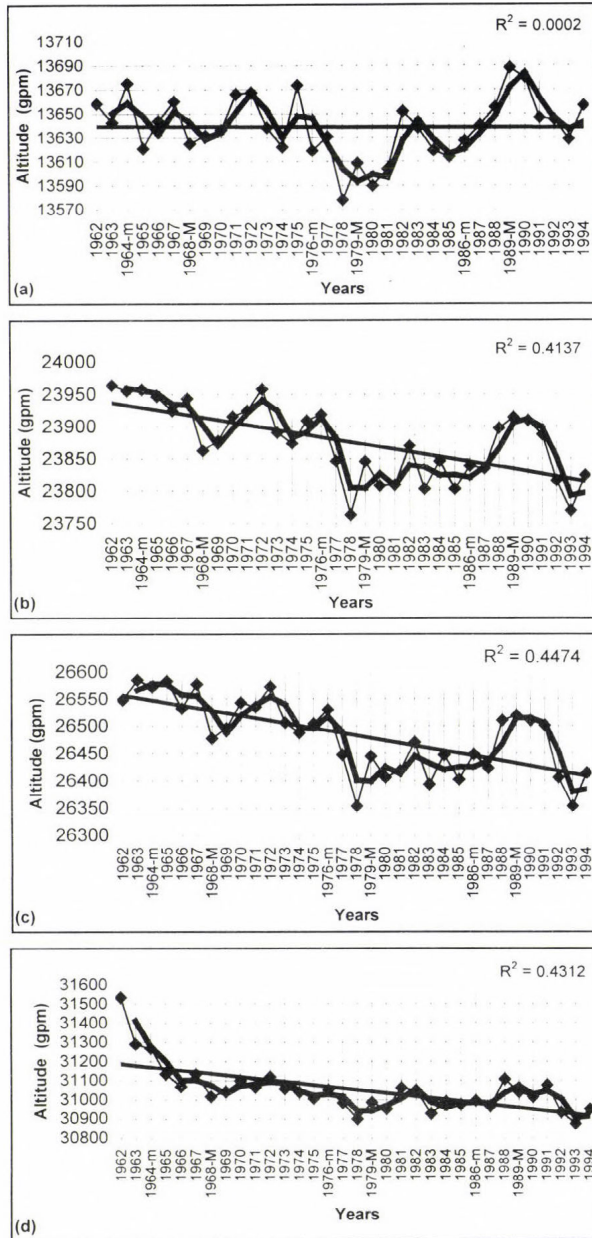


Fig. 2. Long-term change of the altitude of the 150 hPa (a), 30 hPa (b), 20 hPa (c), and 10 hPa (d) isobaric levels above Budapest. Square of the correlation coefficient is printed in the right upper corner. Thick curve shows the two-year sliding average. *m* and *M* indicate solar activity minimum and maximum, respectively.

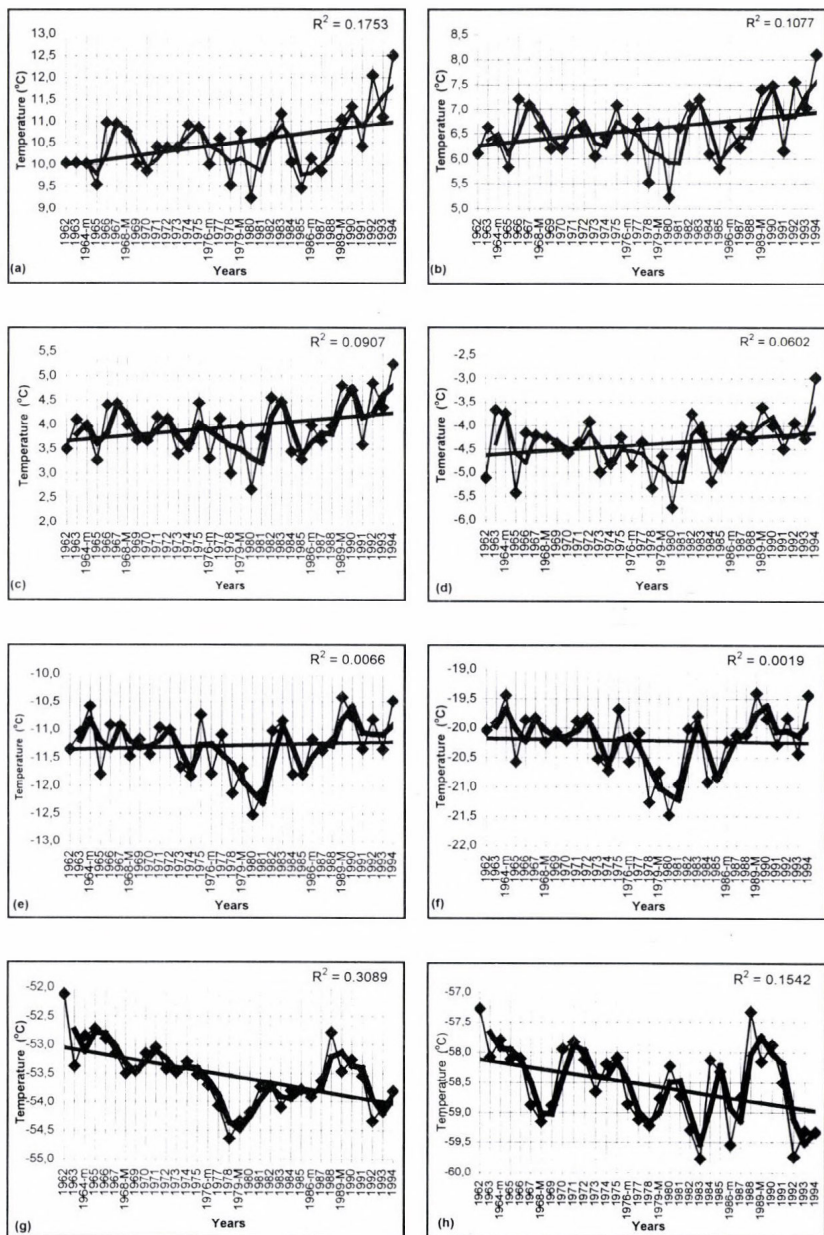


Fig. 3. Long-term change of the temperature at the ground (a), at the isobaric levels of 900 hPa (b), 850 hPa (c), 700 hPa (d), 600 hPa (e), 500 hPa (f), 250 hPa (g), as well as at the tropopause (h) above Budapest. Square of the correlation coefficient is printed in the right upper corner. Thick curve shows the two-year sliding average. *m* and *M* indicate solar activity minimum and maximum, respectively.

temperature increases in accordance with growing vertical pressure gradient. Considering the lower stratosphere, both the trend of the height of the isobaric levels and trend of the temperature are negative, the degree of the trend is increasing with falling pressure. This means that both the vertical gradient of pressure and that of the temperature decrease with time in accordance with the equation of pressure of the kinetic gas theory.

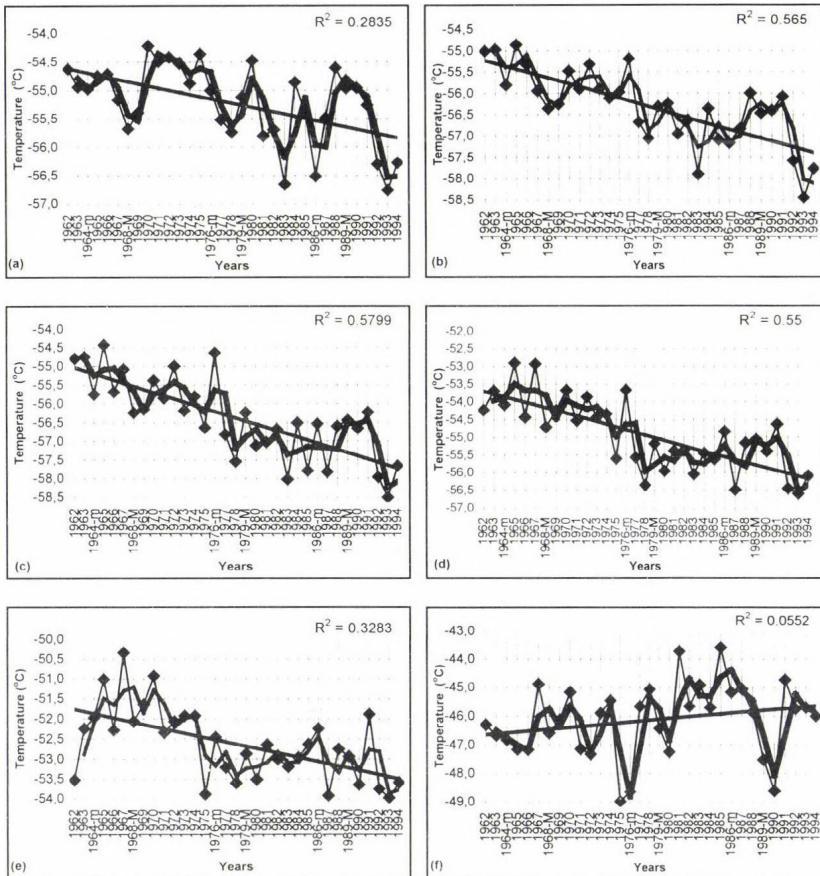


Fig. 4. Long-term change of the temperature at the isobaric levels of 150 hPa (a), 100 hPa (b), 50 hPa (c), 30 hPa (d), 20 hPa (e), and 10 hPa (f) above Budapest. Square of the correlation coefficient is printed in the right upper corner. Thick curve shows the two-year sliding average. *m* and *M* indicate solar activity minimum and maximum, respectively.

Trends of the wind at the isobaric levels also show some regularities. In the troposphere, for example, at the isobaric level of 500 hPa, the trend of the wind speed (speed of the prevailing wind) is positive, speed increases with

time (Fig. 5). Though, the change of the wind speed is not significant, nevertheless, it indicates an enhancement. However, in the lower stratosphere, at the isobaric level of 150 hPa, the trend of the wind speed is already negative, indicating a decrease of the wind speed with time (Fig. 6). In this case, the decrease of the wind speed with time is significant at the 95% level of confidence, according to both the t-test and F-test of the level of confidence for correlation coefficients. The behavior of the trend of the wind speed may be explained by considering the trend of the wind speed at different isobaric levels. The trend of the wind speed at different isobaric levels in the troposphere decreases with increasing height, thus, the vertical gradient of the wind speed is enhanced with time. This might be related to the similar change of the meridional temperature gradient (thermal wind equation), that is the latitudinal gradient of temperature increases with time increasing the speed of the zonal wind component with time. In the lower stratosphere one can meet the opposite situation.

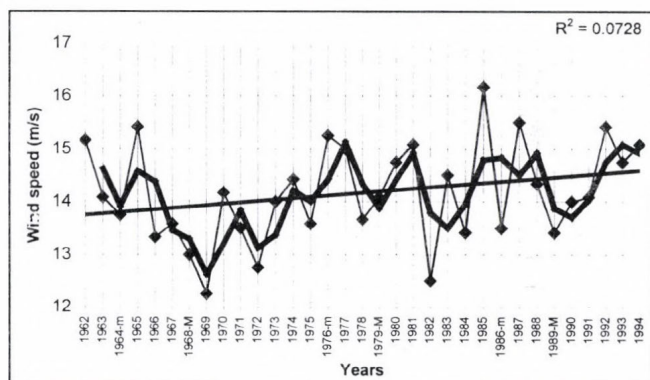


Fig. 5. Long-term change of the wind speed at the isobaric level of 500 hPa above Budapest. Square of the correlation coefficient is printed in the right upper corner. Thick curve shows the two-year sliding average. *m* and *M* indicate solar activity minimum and maximum, respectively.

The study of the precipitable water can be limited to the troposphere, since the predominant part of the water vapor is concentrated in the troposphere. Thus, the precipitable water in a column of unit area between the levels of 850 hPa and 200 hPa has been determined. The trend of the precipitable water is negative indicating the decrease of precipitable water in the troposphere with time (Fig. 7). This trend is significant according to both the t-test and F-test of the significance level of correlation coefficients. Though

the measuring equipments and data processing could be changed during this interval, as well as measurements include smaller or larger errors, yearly means enable us at least to determine the trend of the long-term variation. This would show the drying out of the troposphere. Other investigations related to the precipitable water indicate both positive and negative trends referring largely to the same period (1973–1995) (Ross and Elliot, 2001). Increase of the precipitable water from the surface to 500 hPa has been found over North America except of the north-eastern part of Canada. In Eurasia only China and the Pacific Islands show a regional increase of precipitable water. However, Europe, extending to the Ural Mountains, is an area of decreasing precipitable water. Thus, there are significant regional differences in the trends of precipitable water. Our results referring to Budapest (Hungary) fit very well into the spatial distribution of the trend of precipitable water.

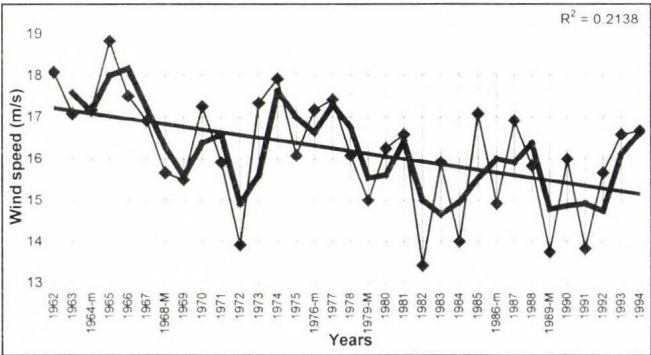


Fig. 6. Long-term change of the wind speed at the isobaric level of 150 hPa above Budapest. Square of the correlation coefficient is printed in the right upper corner. Thick curve shows the two-year sliding average. *m* and *M* indicate solar activity minimum and maximum, respectively.

Drying out of the troposphere might be attributed to the long-term changes of the total cloud amount over land (IPCC, 2001). Growing total cloud amount may be accompanied, on the one hand, by increasing precipitation reducing the precipitable water in the troposphere. On the other hand, the solar activity has been indicating an upward tendency since the end of the 19th century (Reid, 1999). This assumption is also in agreement with the enhanced sea-surface temperature (Reid, 1999). According to relevant investigations, increase of the sea-surface temperature is accompanied also by growth of the global thunderstorm activity. Thus, it may be assumed that drying out of the troposphere is also related in this way to enhancement of the global thunderstorm activity.

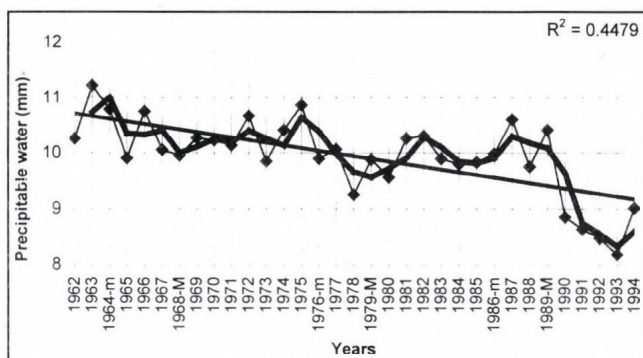


Fig. 7. Long-term change of the precipitable water referring to a column of unit area extending between the isobaric levels of 850 hPa and 200 hPa above Budapest. Square of the correlation coefficient is printed in the right upper corner. Thick curve shows the two-year sliding average. *m* and *M* indicate solar activity minimum and maximum, respectively.

The relation between trends of the height of isobaric levels, temperature, and wind, as well as solar activity might also be studied. Earlier investigations have shown that the solar activity may affect indirectly the meteorological parameters. Correlations of atmospheric dynamics with solar activity evidenced by a connection via the solar wind (interplanetary magnetic field), atmospheric electricity, and cloud microphysics have been found (*Tinsley and Heelis, 1993*). This is confirmed by finding the solar wind modulation of the global electric circuit and apparent effects on cloud microphysics, latent heat release, and tropospheric dynamics (*Tinsley, 1996*), by demonstrating the signal of the 11-year solar cycle in the global stratosphere (*Labitzke and van Loon, 1998*) and in the total ozone content (*Labitzke and van Loon, 1995*). As a further indirect effect of the solar activity, the work of *Svensmark and Friis-Christensen (1997)* might be mentioned, who revealed relation between variations of the cosmic ray flux and the global cloud coverage – as a missing link in solar-climate relationship. According to these results, long-term change of the meteorological parameters studied in this paper might partly also be influenced by solar activity, though the main reason seems to be the greenhouse effect. Studies related to estimation of the magnitude of the effects attributed to various sources of a global temperature increase indicate that the solar variability may be responsible for 0.25 °C of the 0.6 °C warming from 1900 to 1990 (*Lean and Rind, 1999*).

Acknowledgements—The authors thank to the Hungarian Meteorological Service for using the radiosonde data. Also, thanks to the two unknown referees for their useful comments.

References

- Bencze, P., 1991: Development of the concentration of ozone in the middle atmosphere (in Hungarian). *Időjárás* 95, 77-93.
- Bremer, J., 1992: Ionospheric trends in mid-latitudes as a possible indicator of the atmospheric greenhouse effect. *J. Atmos. Terr. Phys.* 54, 1505-1511.
- Bremer, J., 2003: Mesospheric temperature trends at mid-latitudes derived from LF radio propagation experiments. *Adv. Space Res.* 32, 1653-1662.
- Bremer, J. and Berger, U., 2002: Mesospheric temperature trends derived from ground-based LF phase-height observations at mid-latitudes: comparison with model simulations. *J. Atmos. Sol.-Terr. Phys.* 64, 805-816.
- Bremer, J., Alfonsi, L., Bencze, P., Lastovička, J., Mikhailov, A.V., and Rogers, N., 2004: Long-term trends in the ionosphere and upper atmosphere parameters. *Ann. Geophys.* 47, 1009-1029.
- IPCC, 2001: Climate Change 2001: The Scientific Basis. Contribution of Working Group I to the Third Assessment Report of the Intergovernmental Panel on Climate Change (eds.: J.T. Houghton, Y. Ding, D.J. Griggs, M. Noguer, P.J. van der Linden, X. Dai, K. Maskell, C.A. Johnson). Cambridge University Press, Cambridge, U. K.
- Labitzke, K. and van Loon, H., 1995: Total ozone and the 11-year sunspot cycle. *J. Atmos. Sol.-Terr. Phys.* 59, 9-19.
- Labitzke, K. and van Loon, H., 1998: The signal of the 11-year solar cycle in the global stratosphere. *J. Atmos. Sol.-Terr. Phys.* 61, 53-61.
- Lean, J. and Rind, D., 1999: Evaluating sun-climate relationships since the Little Ice Age. *J. Atmos. Sol.-Terr. Phys.* 61, 25-36.
- Mika, J., 1988: Regional features of global warming in the Karpathian-Basin (in Hungarian). *Időjárás* 92, 178-189.
- Mika, J., 1994: Regional climate change scenaria. In *Climate and Agroclimatic Variability in Central and Southeastern Europe* (ed.: N.R. Delazios). University of Thessaly, Volos, Greece, pp. 53-81.
- Pap, J.M. and Fröhlich, C., 1999: Total solar irradiance variations. *J. Atmos. Sol.-Terr. Phys.* 61, 15-24.
- Pruppacher, H.R. and Klett, J.D., 1997: *Microphysics of Cloud and Precipitation*. Kluwer, Dordrecht, The Netherlands.
- Reid, G.C., 1999: Solar variability and its implications for the human environment. *J. Atmos. Sol.-Terr. Phys.* 61, 3-14.
- Roble, R.G. and Dickinson, R.E., 1989: How will changes of carbon dioxide and methane modify the mean structure of the mesosphere and thermosphere? *Geophys. Res. Lett.* 16, 1441-1444.
- Ross, R.J. and Elliott, W.P., 2001: Radiosonde-based Northern-Hemisphere tropospheric water vapour trends. *J. Climate* 14, 1602-1612.
- Rottman, G., 1999: Solar ultraviolet irradiance and its temporal variation. *J. Atmos. Sol.-Terr. Phys.* 61, 37-44.
- Svensmark, H. and Friis-Christensen, E., 1997: Variations of cosmic ray flux and global cloud coverage – a missing link in solar-climate relationships. *J. Atmos. Sol.-Terr. Phys.* 59, 1225-1232.
- Taubenheim, J., 1969: *Statistische Auswertung geophysikalischer und meteorologischer Daten*. Akademische Verlagsgesellschaft Geest & Portig K.-G., Leipzig.
- Tinsley, B.A., 1996: Solar wind modulation of the global electric circuit and apparent effects on cloud microphysics, latent heat release and tropospheric dynamics. *J. Geomagn. Geoelectr.* 48, 165-175.
- Tinsley, B.A. and Heelis, R.A., 1993: Correlations of atmospheric dynamics with solar activity: evidence of a connection via the solar wind, atmospheric electricity and cloud microphysics. *J. Geophys. Res.* 98, 10375-10384.
- Yearbooks of the Central Institute of Meteorology of the Hungarian Meteorological Service. Upper-Air Observations, Budapest, 1962-1994.

BOOK REVIEW

Houghton, J., 2002: **The Physics of Atmospheres. Third Edition.** Cambridge University Press, Cambridge. 320 pages, 135 figures.

It is not easy to explain all the basic principles of a scientific area to non-professionals, and it is especially a challenging task in the case of meteorology because of the stereotypes haunting the “science of weather-wises”. Even some experts of physics and mathematics believe that the science of the atmosphere lacks established theoretical foundations. These facts will no doubt give a lot to the importance of meteorological textbooks dedicated to non-meteorologists.

The first version of *The Physics of the Atmospheres* was published by Professor Houghton in 1976. It was recommended for students of physics both undergraduate and graduate. The material of the book had been collected since 1958 at the University of Oxford, where Dr. Houghton served as Lecturer, later Reader, and since 1976 as Professor of Atmospheric Physics. Professor Houghton's monograph became very soon an internationally acknowledged volume of the scientific literature of meteorology. The second edition was published in 1986, and in 2002, the Cambridge University Press published a third, revised and extended edition.

Even in the first edition, Professor Houghton drew attention to the increase of interest in the atmospheric sciences. The book gives fundamental material on atmospheric radiation, radiation transfer, thermodynamics, statics, and the dynamics of the lower, middle, and upper atmosphere, turbulence, and atmospheric waves as well. The second edition was extended by chapters on general circulation, numerical modeling, observation, and climate, highlighting the modern developments and the increasing interest in these topics. The publication of the third edition was motivated by the large scientific and political interest in the possibility of an anthropogenic climate change on a global scale. Substantially, new chapters have been added to the monograph – on predictability and climate change. In the new chapters the author gives the basic physical foundations for these “hot topics”, and discusses all questions addressed to the meteorological community in our days.

The Physics of Atmospheres can be recommended not only for undergraduate and graduate students of physics and meteorology, but also for physicists, meteorologists, geographers, and anyone interested in the foundations of meteorology determining the possibility of atmospheric and, especially, climate predictions.

Gy. Gyuró

GUIDE FOR AUTHORS OF *IDŐJÁRÁS*

The purpose of the journal is to publish papers in any field of meteorology and atmosphere related scientific areas. These may be

- research papers on new results of scientific investigations,
- critical review articles summarizing the current state of art of a certain topic,
- short contributions dealing with a particular question.

Some issues contain "News" and "Book review", therefore, such contributions are also welcome. The papers must be in American English and should be checked by a native speaker if necessary.

Authors are requested to send their manuscripts to

Editor-in Chief of IDŐJÁRÁS

P.O. Box 39, H-1675 Budapest, Hungary

in three identical printed copies including all illustrations. Papers will then be reviewed normally by two independent referees, who remain unidentified for the author(s). The Editor-in-Chief will inform the author(s) whether or not the paper is acceptable for publication, and what modifications, if any, are necessary.

Please, follow the order given below when typing manuscripts.

Title part: should consist of the title, the name(s) of the author(s), their affiliation(s) including full postal and E-mail address(es). In case of more than one author, the corresponding author must be identified.

Abstract: should contain the purpose, the applied data and methods as well as the basic conclusion(s) of the paper.

Key-words: must be included (from 5 to 10) to help to classify the topic.

Text: has to be typed in double spacing with wide margins on one side of an A4 size white paper. Use of S.I. units are expected, and the use of negative exponent is preferred to fractional sign. Mathematical formulae are expected to be as simple as possible and numbered in parentheses at the right margin.

All publications cited in the text should be presented in a *list of references*,

arranged in alphabetical order. For an article: name(s) of author(s) in Italics, year, title of article, name of journal, volume, number (the latter two in Italics) and pages. E.g., *Nathan, K.K.*, 1986: A note on the relationship between photo-synthetically active radiation and cloud amount. *IDőjárás* 90, 10-13. For a book: name(s) of author(s), year, title of the book (all in Italics except the year), publisher and place of publication. E.g., *Junge, C. E.*, 1963: *Air Chemistry and Radioactivity*. Academic Press, New York and London. Reference in the text should contain the name(s) of the author(s) in Italics and year of publication. E.g., in the case of one author: *Miller* (1989); in the case of two authors: *Gamov and Cleveland* (1973); and if there are more than two authors: *Smith et al.* (1990). If the name of the author cannot be fitted into the text: (*Miller*, 1989); etc. When referring papers published in the same year by the same author, letters a, b, c, etc. should follow the year of publication.

Tables should be marked by Arabic numbers and printed in separate sheets with their numbers and legends given below them. Avoid too lengthy or complicated tables, or tables duplicating results given in other form in the manuscript (e.g., graphs)

Figures should also be marked with Arabic numbers and printed in black and white in camera-ready form in separate sheets with their numbers and captions given below them. Good quality laser printings are preferred.

The text should be submitted both in manuscript and in electronic form, the latter on diskette or in E-mail. Use standard 3.5" MS-DOS formatted diskette or CD for this purpose. MS Word format is preferred.

Reprints: authors receive 30 reprints free of charge. Additional reprints may be ordered at the authors' expense when sending back the proofs to the Editorial Office.

More information for authors is available: antal.e@met.hu

Information on the last issues: http://omsz.met.hu/irodalom/firat_ido/ido_hu.html

Published by the Hungarian Meteorological Service

Budapest, Hungary

INDEX: 26 361

HU ISSN 0324-6329

IDŐJÁRÁS

QUARTERLY JOURNAL
OF THE HUNGARIAN METEOROLOGICAL SERVICE

CONTENTS

<i>Judit Kerényi and Mária Putsay: Extreme flood monitoring in Romania and Hungary using Earth Observation Data</i>	205
<i>Zsuzsanna Dezső, Judit Bartholy and Rita Pongrácz: Satellite-based analysis of the urban heat island effect.....</i>	217
<i>Steluța Vasiliu and András Horányi: An evaluation of the performance of the three-dimensional variational data assimilation scheme for the ALADIN/HU spectral limited area model.....</i>	233
<i>Dezső Szepesi, Katalin Fekete, Richárd Büki, László Koncsos and Endre Kovács: Development of regulatory transmission modeling in Hungary</i>	257
Book review	281

http://omsz.met.hu/omsz.php?almenu_id=omsz&pid=references&pri=2

IDŐJÁRÁS

Quarterly Journal of the Hungarian Meteorological Service

Editor-in-Chief
LÁSZLÓ BOZÓ

Executive Editor
MARGIT ANTAL

EDITORIAL BOARD

- | | |
|--|---|
| AMBRÓZY, P. (Budapest, Hungary) | MIKA, J. (Budapest, Hungary) |
| ANTAL, E. (Budapest, Hungary) | MERSICH, I. (Budapest, Hungary) |
| BARTHOLY, J. (Budapest, Hungary) | MÖLLER, D. (Berlin, Germany) |
| BATCHVAROVA, E. (Sofia, Bulgaria) | NEUWIRTH, F. (Vienna, Austria) |
| BRIMBLECOMBE, P. (Norwich, U.K.) | PAP, J.M. (Greenbelt, MD, U.S.A.) |
| CZELNAI, R. (Dörgicse, Hungary) | PINTO, J. (R. Triangle Park, NC, U.S.A) |
| DÉVÉNYI, D. (Boulder, U.S.A.) | PRÁGER, T. (Budapest, Hungary) |
| DUNKEL, Z. (Budapest, Hungary) | PROBÁLD, F. (Budapest, Hungary) |
| FISHER, B. (Reading, U.K.) | RADNÓTI, G. (Budapest, Hungary) |
| GELEYN, J.-Fr. (Toulouse, France) | ROCHARD, G. (Lannion, France) |
| GERESDI, I. (Pécs, Hungary) | S. BURÁNSZKY, M. (Budapest, Hungary) |
| GÖTZ, G. (Budapest, Hungary) | SZALAI, S. (Budapest, Hungary) |
| HANTEL, M. (Vienna, Austria) | TAR, K. (Debrecen, Hungary) |
| HASZPRA, L. (Budapest, Hungary) | TÁNCZER, T. (Budapest, Hungary) |
| HORÁNYI, A. (Budapest, Hungary) | TOTH, Z. (Camp Springs, U.S.A.) |
| HORVÁTH, Á. (Siófok, Hungary) | VALI, G. (Laramie, WY, U.S.A.) |
| KONDRATYEV, K.Ya. (St. Petersburg, Russia) | VARGA-HASZONITS, Z. (Moson- |
| MAJOR, G. (Budapest, Hungary) | magyaróvár, Hungary) |
| MÉSZÁROS, E. (Veszprém, Hungary) | WEIDINGER, T. (Budapest, Hungary) |

*Editorial Office: P.O. Box 39, H-1675 Budapest, Hungary or
Gillice tér 39, H-1181 Budapest, Hungary
E-mail: bozo.l@met.hu or antal.e@met.hu
Fax: (36-1) 346-4809*

Subscription by

*mail: IDŐJÁRÁS, P.O. Box 39, H-1675 Budapest, Hungary;
E-mail: bozo.l@met.hu or antal.e@met.hu; Fax: (36-1) 346-4809*

Extreme flood monitoring in Romania and Hungary using Earth Observation Data

Judit Kerényi and Mária Putsay

Hungarian Meteorological Service
P.O. Box 38, H-1525 Budapest, Hungary; E-mail: kerenyi.j@met.hu

(Manuscript received in final form September 19, 2005)

Abstract—In the recent years, large and extreme floods occurred frequently in many parts of the world. One region, which suffers from flood damages on a regular basis, is the transboundary area of the Fehér-Körös and Fekete-Körös rivers flowing from Romania to Hungary. For further improvement of flood management in this area, an international team was formed. The paper provides a brief overview of the whole project and a more detailed description of the satellite data processing tools elaborated for the project, developed at the Hungarian Meteorological Service (HMS). Both the ASTER and MODIS instruments are flying on the Terra and Aqua satellites. Our tasks were to produce a high-resolution land use map about the study area and to develop a method for floodwater detection. Land use map was used as background information with topographical, physiographical, and hydrological parameters in the GIS database. It was derived by applying 15 m spatial resolution ASTER images. At the water detection, the data of the MODIS instrument were used. This instrument measures in 36 channels and the spatial resolutions of these are 250 m, 500 m, and 1000 m depending on the channel. Two methods were developed for water detection. Both methods are based on threshold techniques. One is automatic, quick, but less accurate, as it may contain misdetected cloud shadow pixels. The other algorithm is a more accurate semi-automatic method, but interactive correction is needed if the investigated area is partly cloudy. Water masks were derived for the days of the flood event in spring of 2000.

Key-words: flood management, remote sensing, land use map, detecting flood water, ASTER, MODIS.

1. Introduction

The cost of natural disasters is increasing; their impact is invariably higher in developing countries and where people are concentrated. Many factors contribute to increasing vulnerability, such as unsustainable development practices,

degradation of natural resources, weak disaster management and forecasting techniques, or inadequate communications and transport infrastructure.

At the same time there are several technological trends that can serve to decrease the vulnerability to disasters. These include: better understanding of hazardous processes, improved analytical methods and communications. The use of modern and appropriate technologies like remote sensing and GIS can lead to the reduction of social and economic impact of natural disasters, and many technologically advanced nations are today investing heavily in such technology for this purpose.

In the recent years, large and extreme floods occurred frequently in many parts of the world. In the last few years several related projects were launched. For example, the SIREN project, funded by the European Union with the participation of France, Spain, Italy, and Germany (*Rabaute et al.*, 2002), mainly aims at working on “user services” aspects in order to imagine, define, validate specific concepts, and solutions to make the use of Earth observation derived information easier and more effective for potential users (disaster management services, public services at national and local level, environmental agencies).

One region, which suffers from flood damages on a regular basis, is the transboundary area of the Fehér-Körös and Fekete-Körös rivers flowing from Romania into Hungary. Floods in this area typically start in the mountainous terrain of the upper parts of the Transylvanian Basin in Romania and propagate to the plains in Hungary. Recent floods in this area include the two spring 2000 floods, which caused damages in the Romanian territory. In the Hungarian territory, a particularly notable flood occurred in the summer of 1980.

There exists a close co-operation between Romania and Hungary concerning flood defense. The information provided by Romania to Hungary (downstream) is presently based entirely upon ground based data, mainly collected from the non-automatic hydrometeorological stations. Such data are somewhat limited in respect of spatial distribution, temporal resolution, and speed of collection and transmission.

Recognizing the need for further improvement of flood management in this area, an international team was formed, with representatives of Hungary, Romania, and the USA, and a project started on “Monitoring of Extreme Flood Events in Romania and Hungary Using Earth Observation (EO) Data” in the framework of NATO Science for Peace (SfP) Program. The project concerns the region between 46.5–47.5°N and 20.5–22°E.

Success of risk management largely depends on the availability, dissemination, and effective use of timely information. Remote sensing technologies and the numerical hydrological prediction calculations using the traditional means can greatly improve the management of flood hazards. The

SfP project aims to provide such an efficient and powerful flood monitoring tool. A GIS (Geographic Information System) database is organized merging the surface and remote sensing data, to handle them together.

The paper provides a brief overview of the whole project and a more detailed overview of the satellite data processing tools. This work was done at the Satellite Research Laboratory of the Hungarian Meteorological Service (HMS). Our tasks were to produce a high-resolution land use map about the study area and to develop a method for floodwater detection.

2. The project objectives

The main goal of the project is to provide an efficient and powerful flood-monitoring tool based on new MODIS satellite data to the local and river authorities and to other key organizations. A new flood management system is being established, based on hydrological models, GIS technology with hydrological and meteorological database, traditional surface and satellite remote sensing tools. A database, containing EO data, hydrological and meteorological parameters related to significant flood events, was developed and used to test the processing and analytical algorithms, in order to establish an operational methodology for the detection, mapping, and analysis of flooding. The proposed hydrological forecasting model will increase the lead time and thereby provide additional time for implementing the measures needed to protect the human life and property in the study area. This will lead to direct and indirect reduction of economic losses and an earlier flood warning for the Hungarian territory of the Fehér-Körös and Fekete-Körös rivers.

Finally, the project results described here could also help in restoration and rehabilitation of some river sections, which were adversely altered by floods, and also in future analysis and selection of structural flood protection works.

3. Image processing for flood analysis

In the framework of the project, HMS produced land cover/land use map and detected floodwater. In this work medium spatial resolution MODIS and high resolution ASTER images are applied.

3.1 Land use map using ASTER images

To get information about the land cover for the investigated area, a land use map was derived applying ASTER images. This information will be used as

background information with topographical, physiographical, and hydrological parameters in the GIS database.

ASTER is a sensor onboard the Terra (EOS AM) and Aqua (EOS PM) satellites. The ASTER measures in 14 spectral bands. ASTER images were found suitable for producing detailed maps of land cover/land use. The 15 m spatial resolution visible and near infrared bands were used: band 1–0.56 μm , band 2–0.66 μm , and band 3–0.8 μm .

The spectral characteristics of the water, land (bare soil, different types of vegetation: agriculture, forest, meadows) and cloud surfaces in these three bands are quite different, which allow to separate them by classification. Most land surfaces (including bare soil and vegetation) are brighter in band 3 than band 1, but it is not true for water surfaces and clouds. The water is darker in the near infrared than in the visible part of the spectrum. Clouds are similarly bright in both spectral regions. The two visible bands help to separate the different vegetation types.

For the land classification we used the ENVI software. The land use maps were derived from images taken in 2002–2003.

The method for the land cover/land use mapping included two steps: (a) geo-referencing and (b) data classification. For the classification both supervised and unsupervised methods were tested. Following *Pinilla et al.* (2000), we investigated how many iterations were needed in the unsupervised classification. Better results were obtained with the unsupervised classification, in which different numbers of classes and iterations were tested (90 classes and 40 iterations were chosen). At the post-processing the classes were merged into 8 groups: 4 different agriculture areas, forest, water, cloud, shadow. The urban area could not be separated in a discrete class so they had to be classified manually.

The classification was performed for four ASTER images to cover the Hungarian part of the investigated area, and a mosaic land use map was made from them.

The raster type images are vectorized and evaluated for the GIS data base. The land use maps will be utilized for evaluating the damage of the inundation.

3.2 Short description of MODIS images

In 1999 the Terra (EOS-AM), in 2002 the Aqua (EOS-PM) new satellites were launched. The key instrument flying on both Terra and Aqua satellites is the Moderate Resolution Imaging Spectroradiometer (MODIS). Both Terra and Aqua view the entire Earth's surface every day. For detection of the flooded area, MODIS images were applied. The new satellite data can be applied in

several other fields of meteorology. For example, in the EUMETSAT Hydrology SAF (http://www.eumetsat.int/en/area4/saf/Internet/ain_safs/hwm/NEW-HSFWG2-SummaryReport-rev23-FINAL.html), MODIS data will be used for precipitation estimation, snow detection, surface moisture calculation. MODIS is a passive imaging spectroradiometer, acquiring data in 36 spectral bands. Spatial resolution of the images is 250 m (bands 1–2), 500 m (bands 3–7), and 1000 m (bands 8–36), respectively.

Fig. 1 shows a MODIS visible image received on April 21, 2001, which covers the middle part of Europe. As we can see in *Table 1*, several parameters for land, ocean, and atmosphere in good spatial resolution can be derived.

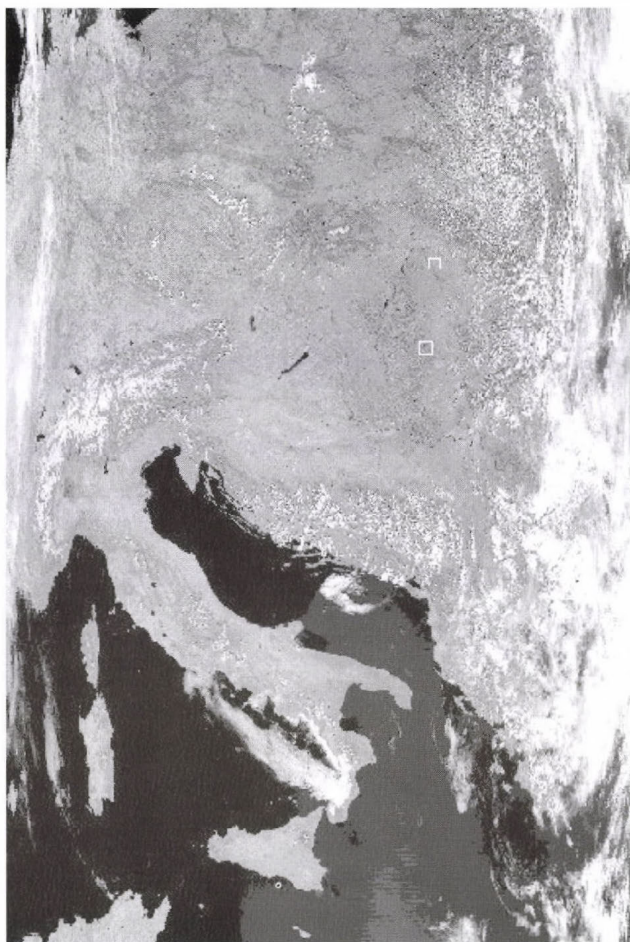


Fig. 1. A TERRA/MODIS image (channel 2) taken on April 21, 2001.

Table 1. Information about the MODIS instrument

Primary use	Bands	Bandwidth
Land/cloud boundaries	1	620–670 nm
	2	841–876 nm
Land/cloud properties	3	459–479 nm
	4	545–565 nm
	5	1230–1250 nm
	6	1628–1652 nm
	7	2105–2155 nm
Ocean color/phytoplankton/ biogeochemistry	8	405–420 nm
	9	438–448 nm
	10	483–493 nm
	11	526–536 nm
	12	546–556 nm
	13	662–762 nm
	14	673–683 nm
	15	743–753 nm
	16	862–877 nm
Atmospheric water vapor	17	890–920 nm
	18	931–941 nm
	19	915–965 nm
Surface/cloud temperature	20	3.660–3.840 μm
	21	3.929–3.989 μm
	22	3.929–3.989 μm
	23	4.020–4.080 μm
Atmospheric temperature	24	4.433–4.498 μm
	25	4.482–4.549 μm
Cirrus clouds	26	1.360–1.390 μm
Water vapor	27	6.535–6.895 μm
	28	7.175–7.475 μm
	29	8.400–8.700 μm
Ozone	30	9.580–9.880 μm
Surface/cloud temperature	31	10.780–11.280 μm
	32	11.770–12.770 μm
Cloud top altitude	33	13.185–13.485 μm
	34	13.485–13.785 μm
	35	13.785–14.085 μm
	36	14.085–14.385 μm

The data available from MODIS are suitable for many different tasks concerning water surfaces, for example investigation of ocean color, water quality monitoring (*Guangyu*, 2005), to detect land cover changes such as

floods, deforestation and burnt scars (Zhan *et al.*, 2002), or flooded area detection (Kameyama *et al.*, 2003).

3.3 Water detection using MODIS data

The MODIS data are highly suitable for flood warning and management, as well, because they are available in real time (or nearly real time), can be rapidly processed and disseminated, cover a wide area, and are abundant and inexpensive, which is important when dealing with longer duration floods. MODIS provides very accurate geo-coding, clouds can be removed by composition techniques, and the data are distributed via the EOS Gateway.

TERRA/MODIS satellite data were used to determine the flood-prone areas. For our purpose we used Level 1B data, channel 1 (0.66 μm) and 2 (0.87 μm) with 250 m spatial resolution, and channel 3 (1.6 μm) with 500 m spatial resolution. The MODIS Level 1B data from the Terra Satellite were downloaded from the EOS Data Gateway, Land Processes Distributed Active Archive Center (LP DAAC) World-Wide Web site is <http://edcimswww.cr.usgs.gov/pub/imswelcome/>.

One way to detect the flooded area is based on the supervised classification of the actual image considering from the differences from a monthly cloud free image derived in the normal season (Low *et al.*, 2004). This method is work- and time-consuming. Our aim was to develop an automatic method to create water mask in a faster, easier, and more objective way.

Usually NDVI (Normalized Difference Vegetation Index) and/or the 0.87 μm reflectance are used for water detection, as those have low values at flooded surfaces (and these data have the highest spatial resolution among the MODIS data).

$$NDVI = (R_{0.87} - R_{0.66}) / (R_{0.87} + R_{0.66}), \quad (1)$$

where $R_{0.66}$ and $R_{0.87}$ are the reflectance values in channel 2 and 1.

The 0.87 μm reflectance and the NDVI are much lower for water surfaces than for vegetation or bare soil, so this is a good tool for detecting pixels fully covered by clear water. But, unfortunately, for mixed pixels partly covered by vegetation, the NDVI and the 0.87 μm reflectance value can strongly increase, they are sensitive to vegetation portion or turbid water.

Only one test for NDVI is not sufficient, application of more tests is certainly needed if we want to detect not only 100% clear water pixels far from snow, clouds, and cloud shadows. The aim was to find an automatic algorithm to detect pixels that were either 100% water or partially water covered.

At HMS, an automatic cloud detection method for NOAA images was developed (Kerényi *et al.*, 1995). This algorithm has been routinely used at the Hungarian Meteorological Service for years. As an analogue for this cloud detection algorithm, a method for water detection using multispectral MODIS images was developed.

The threshold technique works for each pixel separately. It investigates spectral characteristics of the pixels individually, without taking into account the adjacent pixels. The method consists of more tests, each test examines whether the measured value in a channel (or a value calculated from more channels) is larger (or smaller) than a predefined threshold. If a given combination of the tests fulfils, then the pixel is considered as covered by water.

The main thing is to find the appropriate tests (with physical meaning) and the appropriate thresholds. The thresholds should be general in the meaning that they should not vary from image to image (some seasonal variation may occur, but this should also be predetermined).

For finding general thresholds, the most important thing is to use calibrated (not raw) data. Water detection algorithm works with channels measuring reflected solar radiation, so it is very important to eliminate the effects of illumination conditions. This elimination can be performed by using calibrated values, namely solar zenith angle corrected reflectances. So, the next step was to find the tests, and their accurate combination.

As we have already stated, the NDVI and the 0.87 μm reflectances are useful for clear water detection. The channel 1.6 μm is also very useful for water detection, because it is characterized by the lowest water reflectance and mostly independent of turbidity, which is typical for flood waters. The reflectance in 1.6 μm channel is less affected by vegetation, than the 0.87 μm channel reflectance. Oancea and her colleagues (Oancea *et al.*, 2003) made reflectance measurements at several wavelengths and they confirmed this behavior. The spatial resolution in the 1.6 μm channel is only half as much, as for the 0.87 μm channel, but it is so informative, that we decided to use it for the main test: (i) For water, the 1.6 μm reflectance should be less than a threshold. The problem is that this 1.6 μm channel test can not be used alone. The 1.6 μm channel allows separating water from low-land areas, but not from snow in mountainous areas. Snow is bright in 0.87 μm channel, but dark in 1.6 μm channel. To mask out snowy areas, the 0.87 μm channel was used additionally; (ii) The 0.87 μm reflectance should be less than this threshold. For water both test-conditions should be fulfilled at the same time.

Other problems encountered were caused by orographic and cloud shadows, and by melting snow. Their spectral characteristics were quite similar to those of water, so only partial separation could be achieved. Large, clear water surfaces without vegetation have NDVI values less than -0.2, and

they can be easily separated from shadows. However, using this threshold would mask out not only the shadows but also many pixels containing water, such as the pixels with high vegetation fractions, turbid waters, and mixed pixels along the coasts. To avoid the loss of such pixels, an NDVI threshold greater than -0.2 had to be used.

As a conclusion, three tests were decided to use: first for channel $1.6 \mu\text{m}$, a second for channel $0.87 \mu\text{m}$ and a third for NDVI. For water all the tests should be fulfilled (Putsay, 2003). The thresholds can have seasonal variations. Good thresholds must be tested on many images under many circumstances, in different seasons.

We had to make a compromise (Putsay, 2004), considering it was not fully possible to separate the water and cloud shadow pixels automatically. In a few cases, cloud shadows were misdetected as water pixels.

The water detection method was developed in two ways:

- The first one is an automatic method, which is quick, but it can misdetect some shadow pixels as water, and it does not detect some water pixels.
- The other method is semi-automatic, which is more accurate, but it needs more time and interactive correction.

3.3.1 The automatic method

The thresholds of the automatic method can be used if there is no time for *a posteriori* manual correction. The following thresholds were derived:

$$(R_{1.6} < 1\%) \text{ or } [(R_{1.6} < 5\%) \text{ and } (R_{0.87} < 13\%) \text{ and } (NDVI < T)], \quad (2)$$

where T varies between -0.2 and $+0.2$ depending on the seasons and the cloudiness, $R_{1.6}$ and $R_{0.87}$ are the reflectance in channel $1.6 \mu\text{m}$ and $0.87 \mu\text{m}$, respectively. If the $1.6 \mu\text{m}$ reflectance is very low (less than 1%), then no additional tests are needed.

3.3.2 The semi-automatic method

The semi-automatic method is more accurate, but it needs interactive correction (removal of misdetected cloud shadow vectors manually). For the investigation solar zenith, bow-tie, and geo-corrected MODIS images were used at the time of the flood event in spring 2000 on Körös rivers. A semi-automatic method has been developed by modifying the thresholds and the equation. After the automatic method there is more shadow, but an accurate water mask is got. First, the water mask raster image is derived, then it is

converted to vectors, and third, the misdected cloud shadow vectors are removed manually.

The new equation and the thresholds are the following:

$$(R_{1.6} < 1\%) \text{ or } [(R_{1.6} < 10\%) \text{ and } (R_{0.87} < 18\%) \text{ and } (NDVI < 0.4)] \text{ or } [(R_{1.6} < 15\%) \text{ and } (R_{0.87} < 15\%) \text{ and } (NDVI < 0.0)]. \quad (3)$$

For a lower $NDVI$ value, higher $R_{1.6}$ values are permitted to keep pixels with less water portion.

In *Figs. 2* and *3* water masks derived for three successive flooded days are seen. In *Fig. 1* the lower small white box represents this investigated area. Two-two water vectors are visualized corresponding to different days together to see the variation of the inundated area. In *Fig. 2* water vectors were overlaid on a channel $0.87 \mu\text{m}$ image as a background (which was taken on April 21), while in *Fig. 3* the vectors were visualized on ASTER land use map.

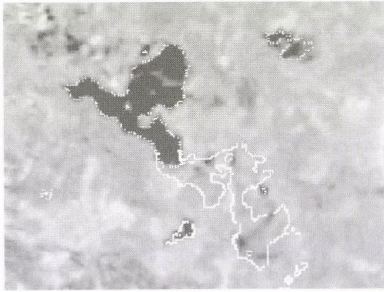


Fig. 2. Water masks derived for two days using MODIS images, visualized on a channel $0.87 \mu\text{m}$ image (taken on April 21, 2000). The solid line water mask corresponds to the 9th, the dotted line water mask to the 21st of April.



Fig. 3. Water masks derived for two days using MODIS images, visualized on land use map derived from ASTER images. The gray water mask corresponds to April 21, and the black one to May 2, 2000.

4. Validation of water mask

To validate the satellite based water detection method, it was compared with a flood map made by Water Resources Research Center (VITUKI, Hungary) using aerial images. As they had air photos only for Tisza river, the validation was done for the upper Tisza region, for the flood event on March 7, 2001. The investigated area is represented by the upper white box in *Fig. 1*. The VITUKI-map is a flood map, it shows only the flooded area, but it does not

contain the river itself, while the MODIS water mask contains the overflowed rivers, as well. *Fig. 4* shows the water-covered area, flooded rivers derived from the MODIS images (black), and flooded area performed from the air photo (light gray). The medium gray patches are the settlements. In *Fig. 4a* the flooded area derived from aerial images are over the water covered area derived from the MODIS images, while in *Fig. 4b* the MODIS water mask is over. As we can see, the MODIS water covered area shows good agreement with the flooded area derived from air photos. Only at the edge of the flooded area we can see difference. The reason of the misdetection is the different spatial resolution between the MODIS and the air photo. At the edge of the flooded area, the MODIS pixels contain water and surface as well, while in the air photo – because of the resolution – they can be separated much better.

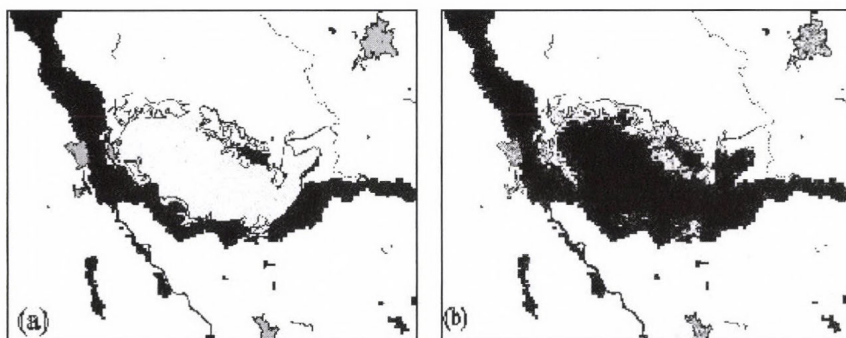


Fig. 4. Water mask (containing flooded area and river) based on MODIS images (black) and flooded area map derived from air photo (light gray) for the Tisza river on March 7, 2001. Medium gray patches are the settlements. The flood map derived from air photos is put over the other on map (a) and below on map (b).

5. Conclusions

The paper gave a brief overview of the satellite data processing techniques needed for the “Monitoring of Extreme Flood Events in Romania and Hungary Using Earth Observation (EO) Data” in the framework of NATO Science for Peace (SfP) project developed at the Hungarian Meteorological Service (HMS). Our task was to produce a high-resolution land use map about the study area and to develop a method for floodwater detection.

Land use map will be used as background information with topographical, physiographical, and hydrological parameters in the GIS database. It is derived by applying 15 m spatial resolution ASTER images.

Two methods were developed for water detection using multispectral MODIS images. Both methods are based on thresholds techniques. One is automatic, quick, but less accurate, it may contain misdetected cloud shadow pixels. The other algorithm is a semi-automatic method, more accurate, but interactive correction is needed if the investigated area is partly cloudy. The results were compared with air photo. The flooded areas derived from MODIS data and air photo showed good agreement, except at the edge of the flooded, area because of the spatial resolution of MODIS images.

Acknowledgements—This work was supported by the NATO Science for Peace (SfP) Program by the project “Monitoring of Extreme Flood Events in Romania and Hungary Using Earth Observation (EO) Data”. We are grateful for the staff of Dartmouth Flood Observatory (Hanover, USA), *G. Robert Brakenridge, Emily S. Bryant, and Elaine Anderson*, who helped our work with advices and data. We also thank the staff of VITUKI, *János Szekeres, Béla Zóka, and Béla Licskó*, who helped at the validation.

References

- Guangyu, W., 2005: Seasonal Change Detection of Water Quality in Texas Gulf Coast. Available on-line from <http://www.ucgis.org/summer03/studentpapers/guangyuwu.pdf>. Accessed March, 2005.
- Kameyama, S., Zhang, J., Wang, Q., Xu, K., Katoh, T., and Watanabe, M., 2003: An Approach to Estimate the Water Level and Volume of Dongting Lake by using Terra/MODIS data . *The 2nd APEIS Capacity Building Workshop, November 24-29, Sydney, Australia*. Available on-line from http://www.word-craft.net/nies/english/products/2nd_Sydney/1st-day_2003-11-28/10_kame.pdf.
- Kerényi, J., Szentján, I.G., Putsay, M., and Wantuch, F., 1995: Cloud detection on a threshold technique for NOAA/AVHRR images for the Carpathian Basin. *Proc. of the 1995 Meteorological Satellite Data Users' Conference*. Winchester, United Kingdom, 4-8 Sept 1995, 565-569.
- Low, J., Liew, S.C. and Kwok, L.K., 2004: Automated Near-realtime Flood Detection and Mapping Using Terra Modis. *Proc. of the 25th Asian Conference and 1th Asian Space Conference on Remote Sensing*, November 22-26, 2004, Chiang Mai, Thailand. Available on-line from http://www.gisdevelopment.net/aars/acrs/2004/b_change/acrs2004_b2001pf.html.
- Oancea, S., Alecu, C., and Bryant, E., 2003: MODIS water classification report. *Report prepared at the Dartmouth Flood Observatory*, 2003.
- Pinilla, C., Ariza, F.J., and Sánchez de la Orden, M., 2000: Unsupervised classification's optimization. *Proc. of the 19th EARSeL Symposium on Remote Sensing in the 21st Century*. Valladolid, 31 May–2 June 1999: *Remote Sensing in the 21st Century, Economic and Environmental Applications*, Balkema Rotterdam, 2000, 19-22.
- Putsay, M., 2003: Creating a Water Mask using a Threshold Technique on Multispectral MODIS Images. *Report of Visit of Maria Putsay to Dartmouth Flood Observatory*, November 25, 2003. http://nato.inmh.ro/Download/putsay_report.zip.
- Putsay, M., 2004: Creating Water Mask using a Threshold Technique on Multispectral MODIS Images. http://nato.inmh.ro/MEDIA/nato2_presentations.html.
- Rabaute, Th., Gonzales, Gh., Dupouyet, J.P., Vidal, J.J., Colin, Y., and Denave, B., 2002: Space technologies for flood risk management: from images to products and services. *Proc. of the 21st EARSeL Symposium*. Paris, 14-16 May, 2001: *Observing our environment from Space, New solution for the new millennium*, Balkema Rotterdam, 2002, 227-235.
- Zhan, X., Sohlberg, R.A., Townshend, J.R.G., DiMiceli, C., Carroll, M.L., Eastman, J.C., Hansen, M.C., and DeFries, R.S., 2002: Detection of land cover changes using MODIS 250 m data. *Remote Sens. Environ.* 83, 336-350.

IDŐJÁRÁS

Quarterly Journal of the Hungarian Meteorological Service
Vol. 109, No. 4, October–December 2005, pp. 217–232

Satellite-based analysis of the urban heat island effect

Zsuzsanna Dezső, Judit Bartholy* and Rita Pongrácz

Department of Meteorology, Eötvös Loránd University
P.O. Box 32, H-1518 Budapest, Hungary
E-mail: tante@nimbus.elte.hu, bari@ludens.elte.hu, prita@elte.hu

(Manuscript received in final form September 10, 2005)

Abstract—Analysis of the urban heat island (UHI) effects for the Budapest agglomeration area and other nine cities located in Hungary has been accomplished. Remotely sensed information (namely, observations of sensor MODIS on satellites Terra and Aqua) serve as a basic tool to this analysis. Day-time and night-time surface temperature time series have been considered in order to define the UHI intensity as the difference between spatially averaged surface temperature of the urban and surrounding pixels. Spatial structures of the UHI have been determined and compared depending on seasons. The most intense UHIs occur in day-time during the summer months in case of all the selected cities.

Key-words: urban heat island effect, surface temperature, satellite imagery, sensor MODIS, Budapest agglomeration area, Hungarian large cities.

1. Introduction

Increasing human presence and intense anthropogenic activity have a considerable impact on the environment resulting in global change. One of the main aspects includes the increase of artificial covers (e.g., concrete, asphalt) and dense urban areas. Urban conditions significantly modify the surface-atmosphere energy budget and produce the so-called urban heat island (UHI) effect (Howard, 1833; Oke, 1982). Traditionally, UHI analysis uses air temperature data observed at standard height (1.5–2 m above the ground), while remotely sensed information is often available at ground-level. UHI effect has been investigated using satellite imagery for three decades. The early studies (e.g., Rao, 1972) evaluated coarse resolution satellite data (7–8 km per

* Corresponding author

pixel), and used very simple methods to calculate the surface temperature from the spectral observations (*Carlson et al.*, 1977; *Price*, 1979). These investigations in the 1970s and 1980s concluded that satellite measurements can be applied to detect the UHI effect in case of clear sky conditions. The thermal differences between urban and rural areas appear even in case of relatively small towns (*Matson et al.*, 1978; *Price*, 1979). Ground-based measurements require either the installation of a dense station network or the introduction of a measuring equipment mounted on a moving vehicle. Moving measurements can be arranged in a relatively small city, where the difference between observation times may be handled by following the designed path back and forth. In case of several Hungarian cities (e.g., Szeged, Debrecen, Szombathely), *Unger et al.* (2001) and *Bottyán et al.* (2005) accomplished such observations. However, for larger agglomerations, i.e., Budapest, these methods cannot be implemented due to economical constraints. An alternate method using satellite imagery providing spatially continuous and simultaneous observations may be applied to analyze UHI effect of large urban areas as well as smaller cities (*Bartholy et al.*, 2001, 2004; *Rigo and Parlow*, 2004). The maximum of the UHI intensity occurs a few hours after sunset using the ground-based air temperature data, while it can be detected during day-time in case of using satellite images (*Roth et al.*, 1989). Nowadays, the main objectives of the UHI investigations include (i) to determine the detailed structure of the UHI (*Nichol*, 1996), (ii) to use this information in the urban planning and human comfort studies (*Scherer et al.*, 1999; *Gómez et al.*, 2001), and (iii) to model wind and temperature patterns of cities (*Herbert et al.*, 1998; *Voogt and Grimmond*, 2000). In this paper, the UHI effects for the Budapest agglomeration area and the other nine largest cities of Hungary are analyzed. Besides the capital, the nine most populated Hungarian cities include Debrecen, Miskolc, Szeged, Pécs, Győr, Nyíregyháza, Kecskemét, Székesfehérvár, and Szombathely. First, the satellite data is described and the methodology is presented. Then, results of the analysis are presented separately for the capital and the other nine Hungarian cities.

2. Data and methodology

As part of the Earth Observing System Program of the American National Aeronautics and Space Administration (NASA), satellites Terra and Aqua were launched to polar orbit in December 1999, and May 2002, respectively. Satellite Terra is on a descending orbit (10:30 a.m.), while satellite Aqua is on an ascending orbit (1:30 p.m.), both at 705 km height above the surface. Main goal of remote measurements of these missions is to improve our under-

standing of global dynamics and processes occurring on the land, in the oceans, cryosphere, and lower atmosphere (NASA, 1999). These measurements and their use play an important role in the development of validated, global, interactive earth system models being able to predict global climate and environmental change accurately enough to assist policy makers worldwide in making decisions concerning the protection and management of our environment and natural resources. The planned lifetime of satellites is about 15 years. The first observations of satellite Terra started in February 2000, and regular validated measurements are available from July 2000. Numerous climatic and environmental parameters are accessible via Internet at the Earth Observing System Data Gateway.

Five instruments are included in satellite Terra (NASA, 1999): (1) ASTER (Advanced Spaceborne Thermal Emission and Reflection Radiometer), (2) CERES (Clouds and the Earth's Radiant Energy System), (3) MISR (Multi-Angle Imaging Spectroradiometer), (4) MODIS (Moderate Resolution Imaging Spectroradiometer), and (5) MOPITT (Measurements of Pollution in the Troposphere). Satellite Aqua carries six instruments: (1) AIRS (Atmospheric Infrared Sounder), (2) AMSU-A (Advanced Microwave Sounding Unit), (3) HSB (Humidity Sounder for Brazil), (4) AMSR-E (Advanced Microwave Scanning Radiometer for EOS), (5) MODIS (Moderate Resolution Imaging Spectroradiometer), and (6) CERES (Clouds and the Earth's Radiant Energy System).

The measurements of sensor MODIS of the above two satellites have been analyzed in this paper. MODIS measures biological and physical processes on the land and ocean using a cross-track scanning multi-spectral radiometer with 36 electromagnetic spectral bands from visible to thermal infrared (Barnes *et al.*, 1998). From the measurements of MODIS the following parameters are determined: surface temperature (both land and ocean), ocean color, global vegetation, cloud characteristics, snow cover, temperature, and moisture profiles. MODIS is capable of viewing the entire globe daily at high resolution, namely 250 m per pixel in the visible and 1 km per pixel in the infrared channels.

In this paper, day-time and night-time surface temperature time series measured in Hungary are analyzed. Surface temperature is strongly related to surface energy budget, especially, to latent and sensible heat flux. Calculation of surface temperature data is based on thermal infrared measurements of MODIS that are quality controlled and calibrated by surface observations (NASA, 1999). In order to determine the surface temperature output, seven spectral bands are used: 3660–3840 nm (channel 20), 3929–3989 nm (channel 22), 4020–4080 nm (channel 23), 8400–8700 nm (channel 29), 10780–11280 nm (channel 31), 11770–12270 nm (channel 32), and 13185–13485 nm (channel 33).

Wan and Snyder (1999) developed a model to calculate surface temperature from the spectral observations that can be applied in case of clear weather. This so-called Day/Night MODIS LST (Land Surface Temperature) Method enables us to determine surface temperature and emissivity without preliminary knowing of air temperature and water vapor profiles. The problem is underdetermined, when we attempt to solve temperature and surface emissivity in N bands simultaneously, solely from one-time observation (even if the exact atmospheric conditions are known). We have $2N$ observations using one set during the day and another one during the night. The unknown variables are N bands emissivities, day-time surface temperature, night-time surface temperature, four atmospheric variables: air temperature and water vapor profiles during day and night, and the anisotropic factor. Altogether we have $N+7$ unknown variables, thus the radiation transfer equations can be solved if $N \geq 7$.

A linear approximation of the radiation transfer equation in the proximities of reference values of surface temperature and band emissivities results in a simplified form (Strahler *et al.*, 1999). Combining 14 equations together (2×7 bands), the solution for surface temperature and band emissivities should be a linear combination of the band brightness temperatures, each of which corresponds to one of the 14 observations. Components of \mathbf{x} vector (x_i) can be written as follows:

$$x_i = \sum_{j=1}^{14} w_{i,j} \cdot y_j + w_{i,0}, \quad (1)$$

where \mathbf{x} is a vector of the 14 variables including surface temperature and band emissivities, y_j is the band brightness temperature for observation j , $w_{i,j}$ ($i=1, \dots, 14$ and $j=1, \dots, 14$) and $w_{i,0}$ are the regression coefficients.

In order to separate urban and rural pixels, the MODIS Land Cover Product (LCP) have been used. The LCP values are based on a 1 km gridded database composited from different MODIS products, namely, land/water mask, albedo, spatial texture, directional reflectance, enhanced vegetation index, snow cover, land surface temperature, and terrain elevation information. These data are composited over a one-month time period to produce a globally consistent, multitemporal database on a 1 km grid as input to classification characterization algorithms. The LCP recognizes 17 categories of land cover following the International Geosphere-Biosphere Program scheme (Belward *et al.*, 1999). Land cover classes are produced by processing the 32-day database, using decision tree and artificial neural network classification algorithms to assign land cover classes based on training data (Strahler *et al.*, 1999).

Since the topography significantly affects UHI, hilly regions have to be eliminated. To this process, the GTOPO30 global digital elevation model (DEM) has been used. This global data set was developed by the U.S. Geological Survey's (USGS) Earth Resources Observation System Data Center (USGS, 1996). The horizontal grid spacing of this database is 30 arc seconds (approximately 1 km). GTOPO30 is based on data derived from different sources of elevation information, e.g., Digital Terrain Elevation Data, USGS 1-degree DEM's, International Map of the World 1:1,000,000-scale maps, Digital Chart of the World (Danko, 1992).

In the present analysis, the ten largest cities of Hungary with more than 80 thousands inhabitants (Budapest, Debrecen, Miskolc, Szeged, Pécs, Győr, Nyíregyháza, Kecskemét, Székesfehérvár, and Szombathely) have been selected according to the population data of the *Hungarian Ministry of Interior* (2000). Pixel representations of the selected urban settlements (including their rural environment) have been determined from the total 1200×1200 pixels containing the Carpathian Basin at the upper half of the satellite image. Since 20% of the country population live in Budapest (which means ten times more inhabitants in the capital than in any other large cities), furthermore, the differences between the spatial extensions of Budapest and other cities are of similar rate, therefore, the agglomeration of the capital is represented by 50×50 pixels (covering 2500 km^2) from the entire satellite image, while other selected cities are represented by only 30×30 pixels (covering 900 km^2). The representative areas have been divided into urban and rural pixels in case of each city. First, the MODIS LCP is applied to separate urban built-up and rural surrounding areas (upper left panel of *Fig. 1*). Urban part of the total area is defined within the 15 km radius circle around the city center in case of Budapest, while 5 km in case of other Hungarian cities. Rural pixels may be found within a 15–25 km or 5–15 km radius ring around the city center in case of Budapest and the other cities, respectively. Furthermore, hilly regions have been eliminated using the global DEM (upper right panel of *Fig. 1*) when calculating the UHI intensity. The finally separated areas are demonstrated in the lower part of *Fig. 1* in case of the Budapest agglomeration area. *Table 1* summarizes the total number of pixels representing the urban and rural areas in case of each city. Cities located in hilly regions are represented by less pixels than expected because of their real spatial extension. On the base of the spatial averages of observed values converted to urban and rural surface temperature, UHI effects have been analyzed for the selected large cities.

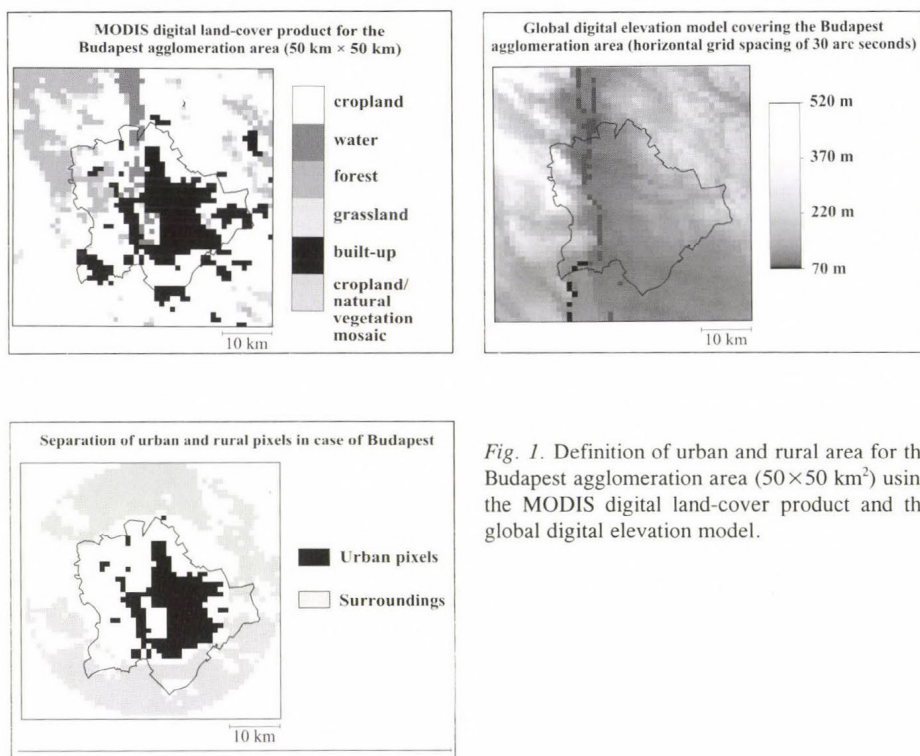


Fig. 1. Definition of urban and rural area for the Budapest agglomeration area ($50 \times 50 \text{ km}^2$) using the MODIS digital land-cover product and the global digital elevation model.

Table 1. Number of pixels representing urban and rural area in case of the ten most populated Hungarian cities. The satellite image granule of Budapest contains 2500 pixels, while the granules of the other nine cities contain 900 pixels

City	Urban pixels	Rural pixels
Budapest	237	831
Debrecen	25	621
Miskolc	21	525
Szeged	19	622
Kecskemét	12	624
Nyíregyháza	13	621
Pécs	6	433
Szombathely	10	626
Győr	11	621
Székesfehérvár	7	617

3. Urban heat island effect of the Budapest agglomeration area

In this section monthly and seasonal mean spatial structure of the Budapest UHI is presented and compared on the base of the MODIS observations between 2001 and 2004.

Time series of spatial averages of the observed surface temperature in cloud-free urban and rural pixels are determined for each satellite image. Those satellite images, where more than half of the urban pixels were cloud-covered, have been eliminated. In the Carpathian Basin winter days are more often cloudy or foggy than summer days, therefore, less satellite images could be used in winter to calculate the monthly mean UHI intensity, as the difference between the urban and rural average surface temperature, than in summer. *Fig. 2* presents the monthly mean UHI intensity of the Budapest agglomeration area based on remotely sensed surface temperature observed by Terra/MODIS and Aqua/MODIS in 2004. Annual variation of UHI intensity is larger in day-time than in night-time due to larger variance of the energy balance. The most intense UHI effect (4–5 °C on monthly average) occurs during day-time in the summer months in case of both satellites. Direct solar radiation and thermal inertia can be considered as possible reasons.

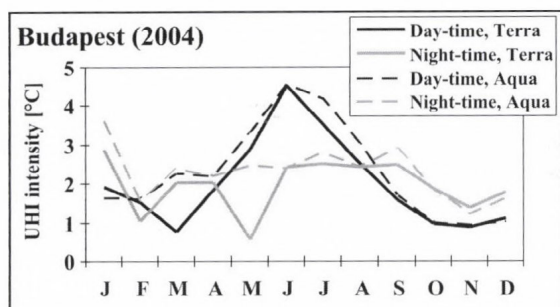


Fig. 2. Monthly mean UHI intensity of the Budapest agglomeration area based on Terra/MODIS and Aqua/MODIS observations, 2004.

The detailed spatial structure is illustrated in *Fig. 3*, where seasonal mean UHIs of day-time and night-time are presented based on Aqua/MODIS thermal information observed in 2004. The seasonal mean difference between the surface temperature of each pixel and the rural mean is presented on the maps. The largest anomaly values and consequently, the most intense UHI occur in summer. UHI intensity is large also in spring, however, smaller anomalies can be detected than in summer.

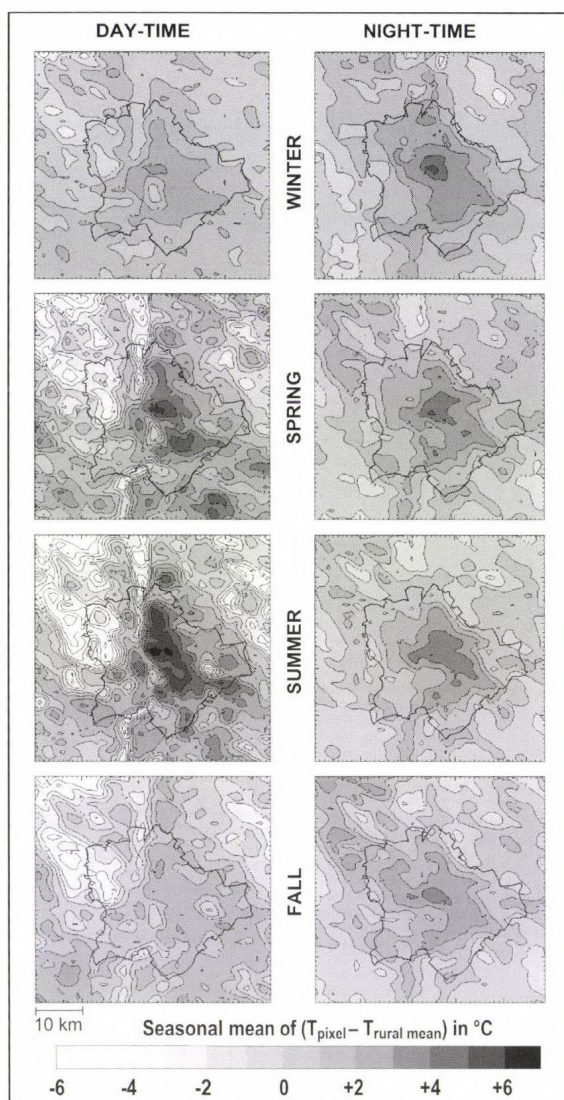


Fig. 3. Annual variation of the seasonal mean UHI structure in Budapest (50 × 50 km²) based on Aqua/MODIS observations, 2004.

The maps of *Fig. 3* suggest, that night-time structures of UHI are quite similar to each-other, while UHI structures significantly differ from one another in day-time. The warmest part of the city is the downtown area

(administrative and commercial center) on the left bank of the river Danube (which is on the right side of the presented maps). The western part of the city is hilly and covered by forests, so its surface is relatively cold. The difference between the warmest and coldest surface temperature exceeds 12 °C in summer, and 8 °C in spring. The downtown warm spots are 4–5 °C colder on winter days than on summer days, while the seasonal difference is considerably smaller during nights (less than 1 °C).

In order to analyze the temporal variation of the UHI structure of the Budapest agglomeration area, time series of the monthly mean differences of surface temperature of each pixel and the rural mean along the major cross-sections (i.e., N-S, W-E, NW-SE, NE-SW) have been compared. In this paper, the NW-SE cross-section is selected and shown in *Fig. 4*, because it represents the orographical variability of the capital and its surroundings the most. Since the validated, good-quality measurements are available from 2001, the previous year is not presented here. The four-year-long time series (2001–2004) are calculated from the Terra/MODIS observations. The downtown region can be clearly recognized due to the positive anomaly values that are greater than +5, +6 °C, and +3, +4 °C in day-time and night-time, respectively. Annual variation of the monthly means is more pronounced in day-time than in night-time, which was expected. The maximum anomaly occurs in summer months in both cases. Although record temperature values were detected in Europe in summer 2003 (*Vidale et al.*, 2004), the time series of remotely sensed surface temperature do not show this extreme hot weather. On the contrary, day-time UHI of summer 2003 is weaker than in the other three years analyzed in this paper.

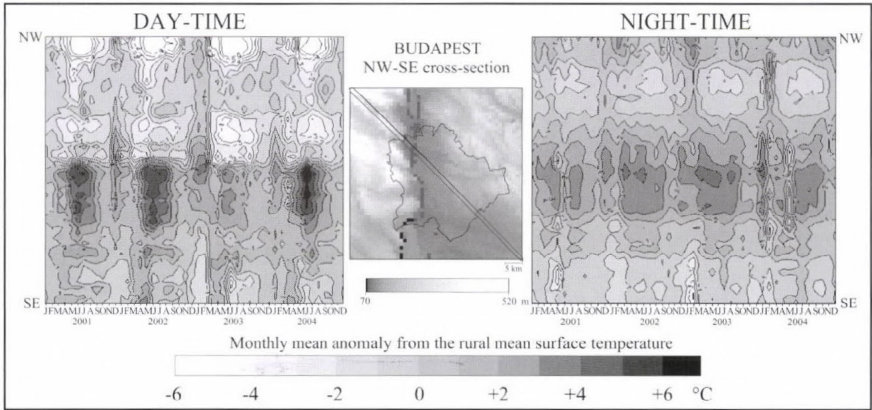


Fig. 4. Monthly mean surface temperature anomaly in the NW-SE cross-section of Budapest agglomeration area based on Terra/MODIS observations, 2001–2004.

Verification of our satellite-based results was accomplished using ground-based observations at the urban climate station installed at the Eötvös Loránd University in 1999 (with the supervision of the Hungarian Meteorological Service). Satellite-based surface temperature and ground-based temperature observations (i.e., 12 UTC, grass minimum, daily minimum, daily maximum, and daily mean temperature values) have been compared (Bartholy *et al.*, 2004). The linear relationship between the satellite- and ground-based temperature measurements were determined, and correlation coefficients of the time series were calculated. Our results suggest very strong relationships with correlation coefficients being larger than 0.91 (in some cases 0.97). Furthermore, other techniques are planned to make verification of the satellite data for larger areas (both in the capital and the other nine cities).

4. Urban heat island effect of the other Hungarian cities

Similarly to the analysis of the Budapest agglomeration area, UHIs of the other nine Hungarian cities are analyzed in this section. Fig. 5 presents the monthly mean UHI intensity observed in 2004.

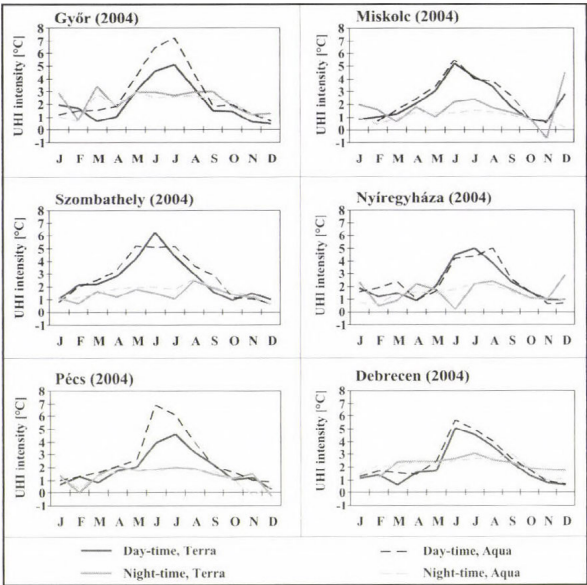


Fig. 5. Monthly mean UHI intensity of selected cities located in Transdanubia (on the left) and Eastern Hungary (on the right).

Graphs on the left side of the figure refer to cities located in Transdanubia, while those on the right side represent the Eastern Hungarian cities. The results suggest that the annual variation of monthly mean UHI intensity is larger in day-time than in night-time, as it was detected in *Fig. 2* in case of the capital, as well. The maximum UHI intensity exceeds 5 °C, and it occurs in day-time from May to August. Usually, day-time monthly mean UHI intensities calculated from the Aqua/MODIS observations are slightly greater than those from Terra/MODIS observations. This can be explained by the orbital parameters of the satellites, namely, the difference between the local times, when the path of the satellites allows to make remotely sensed measurements of the Carpathian Basin. Satellite Terra crosses our region earlier (around 8–11 o'clock) than satellite Aqua (around 10–13 o'clock). Therefore, thermal radiation values observed by satellite Terra are slightly less than those of satellite Aqua.

Temporal evolution of UHIs can be analyzed using different cross-sections of the surrounding region of the cities. Day-time and night-time monthly mean surface temperature anomalies relative to the monthly rural means are determined for each pixel in the 30×30 km² surrounding of the nine Hungarian cities. *Figs. 6* and *7* summarize the time series of pixels located in the N-S or W-E cross-sections of the selected regions for the Transdanubian and Eastern Hungarian cities, respectively. The presented cross-sections have been selected on the base of the representativeness of the geographical and orographical features in case of each city. According to the results, the most intense UHIs occur in summer day-time as in case of the Budapest agglomeration area. Another similarity between Budapest and the other nine cities can be recognized, namely, the day-time variation is greater than the difference between the monthly means during night-time. However, due to the evident difference between city sizes, spatial extension of UHI is smaller in case of these nine cities than in case of the capital. On the base of *Figs. 6* and *7*, besides the UHI effect, seasonal variation of other land cover types (e.g., river, forest) and orographical features (e.g., valleys, hills) can be evaluated. For instance, in case of the N-S cross-section of the satellite image subsection containing Győr (on the top of *Fig. 6*), the river Danube can be well identified due to the large seasonal variation of surface temperature anomalies in day-time. In the summer half-year, large negative values can be detected in these pixels. Other examples can be seen in case of Pécs and Miskolc (bottom of *Fig. 6* and top of *Fig. 7*, respectively), where hilly regions and valleys are located in the presented cross-sections. As an opposite of the positive anomaly values of the UHI, the hilly (mountain Mecsek) or the valley (valley of the creek Szinva in mountain Bükk) negative anomalies appear with large seasonal variation in day-time. The difference between the warm UHI and the cold hilly or valley region is the greatest in the summer months.

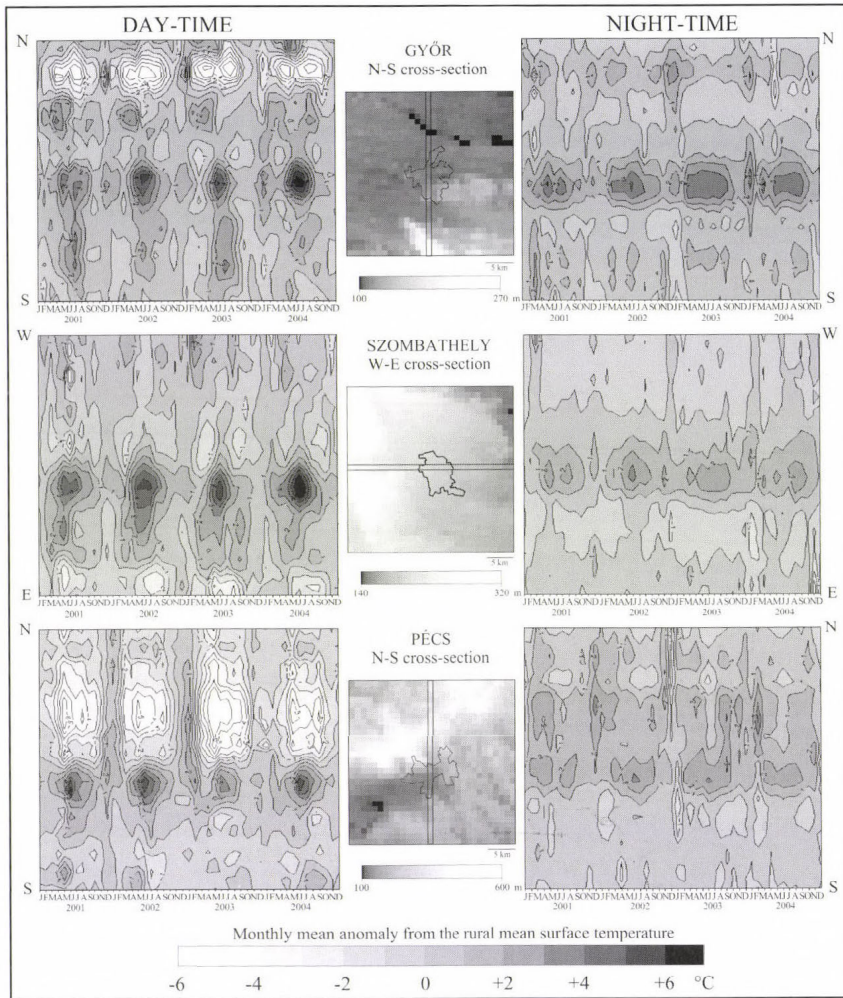


Fig. 6. Time series of monthly mean surface temperature anomaly in case of selected Transdanubian cities in the characteristic cross-sections based on Terra/MODIS observations, 2001–2004.

Mean UHI intensity is shown in Fig. 8, where the cities are ranked according to the number of their inhabitants starting with the capital. The UHI intensity presented here is calculated using the Terra/MODIS night-time observations between 2001 and 2004. Basically, more populated cities exhibit more intense heat island, and only orographical modification disturbs this relationship by decreasing the UHI intensity. Since Budapest, Miskolc, and

Pécs are located in hilly regions, partly or entirely, their mean UHI is less intense than expected. Although the city of Kecskemét is small, its central location on the Great Plains may explain the larger mean difference between the temperature of urban and rural areas. Finally, in case of Győr, the surroundings contain several cold spots because of the large floodplain of the river Danube that results in more intense UHI than expected.

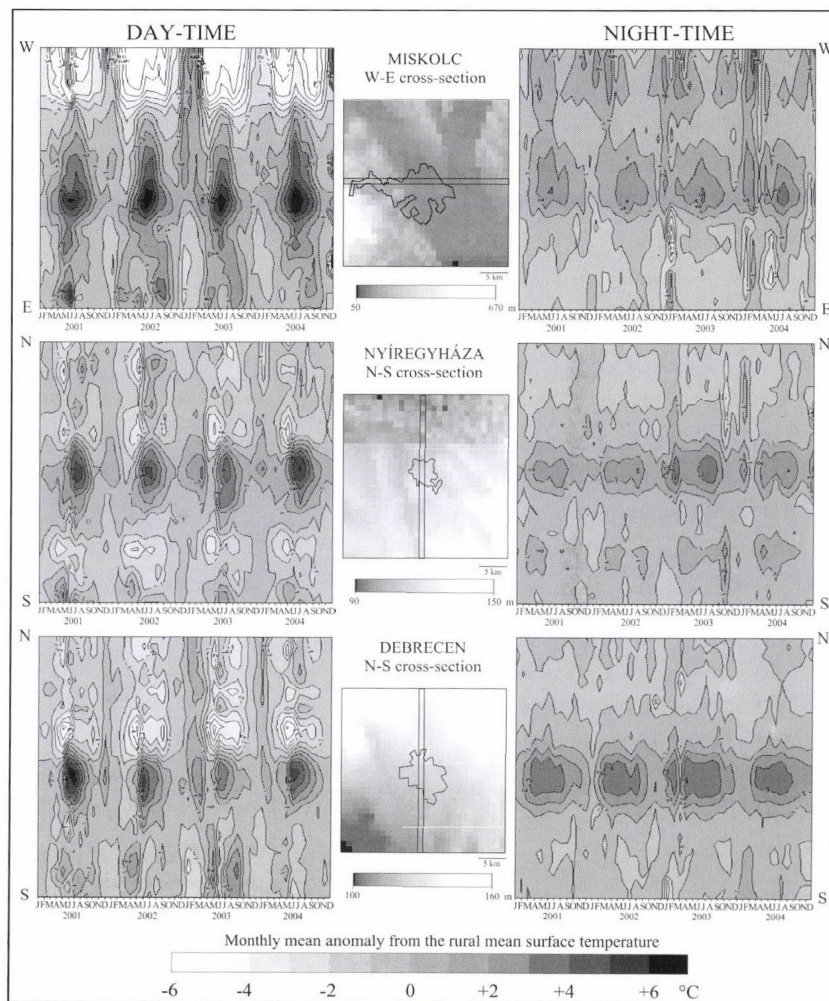


Fig. 7. Time series of monthly mean surface temperature anomaly in case of selected Eastern Hungarian cities in the characteristic cross-sections based on Terra/MODIS observations, 2001–2004.

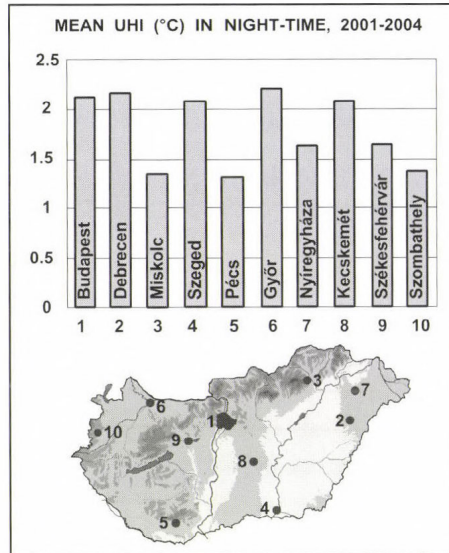


Fig. 8. Mean night-time UHI intensity of the ten most populated cities of Hungary, 2001–2004.

5. Conclusions

In order to find potential mitigation strategies that facilitate the urban population to adapt to new environmental conditions, UHI and other climatological impacts of urbanization should be investigated. In this paper, the ten most populated cities of Hungary (including the capital) have been selected, and their urban and rural pixel representations have been determined. Day-time and night-time surface temperature time series measured by the instrument MODIS of satellites Terra and Aqua have been analyzed. Urban and rural spatial averages have been calculated and compared for each selected city. Monthly and seasonal mean spatial structures of UHI have been determined. On the base of the results the following conclusions can be drawn:

- No significant difference can be detected between the UHI intensity values based on the MODIS-observations of the two satellites (Terra and Aqua).
- Day-time UHIs exhibit greater monthly variation than night-time UHIs in case of both the Budapest agglomeration area and the other nine Hungarian cities. The maximum UHI effect can be detected in day-time.

- The most intense UHI occurs in the summer period (May-June-July-August) for all the urban sites. Monthly mean UHI intensity in these months exceeds 5 °C.
- In the Budapest agglomeration area, the difference between the warmest and coldest surface temperature exceeds 12 °C in summer, and 8 °C in spring. The downtown warm spots are 4–5 °C colder on winter days than on summer days. The seasonal difference is much smaller during night-time.

Acknowledgements—The authors wish to thank NASA for producing the satellite surface temperature data in their present form and the Earth Observing System Data Gateway for distributing the data. Research leading to this paper has been supported by the *Hungarian National Science Research Foundation* under grants T-034867, T-038423, and T-049824, also by the AEROCARB and CHIOTTO projects of the *European Union* Nr. 5 program under grants EVK2-CT-1999/0013, EVK2-CT-2002/0163, and the *Hungarian National Research Development Program* under grants NKFP-3A/0006/2002 and NKFP-3A/082/2004.

References

- Barnes, W.L., Pagano, T.S., and Salamonson, V.V., 1998: Prelaunch characteristics of the Moderate Resolution Imaging Spectroradiometer (MODIS) on EOS-AM1. *IEEE T. Geosci. Remote* 36, 1088-1100.
- Bartholy, J., Pongrácz, R., and Dezső, Zs., 2001: Evaluation of urban heat island effect for large Hungarian cities using high resolution satellite imagery. *Proc. of the Fifth European Conference on Applications of Meteorology, ECAM 2001* (ed.: M. Hunkár). Kiadó? Budapest.
- Bartholy, J., Pongrácz, R., Barcza, Z., and Dezső, Zs., 2004: Aspects of urban/rural population migration in the Carpathian Basin using satellite imagery. In *Environmental Change and its Implications for Population Migration* (eds.: J.D. Unruh, M.S. Krol, and N. Klot) Book series "Advances in Global Change Research" Vol. 20. Kluwer Academic Publishers, Dordrecht and Boston, 289-313.
- Belward, A.S., Estes, J.E., and Kline, K.D., 1999: The IGBP-DIS 1-Km Land-Cover Data Set DISCover: A Project Overview. *Photogramm. Eng. Rem.* 65, 1013-1020.
- Bottyán, Zs., Kircsi, A., Szegedi, S., and Unger, J., 2005: The relationship between built-up areas and the spatial development of the mean maximum urban heat island in Debrecen, Hungary. *Int. J. Climatol.* 25, 405-418.
- Carlson, T.N., Augustine, J.A., and Boland, F.E., 1977: Potential application of satellite temperature measurements in the analysis of land use over urban areas. *B. Am. Meteorol. Soc.* 58, 1301-1303.
- Danko, D.M., 1992: The digital chart of the world. *GeoInfo Systems* 2, 29-36.
- Gómez, F., Tamarit, N., and Jabaloyes, J., 2001: Green zones, bioclimatic studies and human comfort in the future development of urban planning. *Landscape Urban Plan.* 55, 151-161.
- Herbert, J.M., Johnson, G.T., and Arnfield, A.J., 1998: Modelling the thermal climate in city canyons. *Environ. Modell. Softw.* 13, 267-277.
- Howard, L., 1833: *Climate of London Deduced from Meteorological Observations*. Vol. 1-3. Harvey and Darton, London.
- Hungarian Ministry of Interior, 2000: *Local Authorities Database*. <http://web.bm.hu/proba/-cimtar.nsf/lakossag>.
- Matson, M., McClain, E.P., McGinnis D.F., and Pritchard, J.A., 1978: Satellite detection of urban heat island. *Mon. Weather Rev.* 106, 1725-1734.

- NASA, 1999: *Science Writers' Guide to Terra*. NASA Earth Observing System Project Science Office, Greenbelt, MD.
- Nichol, J.E., 1996: High-resolution surface temperature patterns related to urban morphology in a tropical city: a satellite-based study. *J. Appl. Meteorol.* 35, 135-146.
- Oke, T.R., 1982: The energetic basis of the urban heat island. *Q. J. Roy. Meteor. Soc.* 108, 1-24.
- Price, J.C., 1979: Assessment of the heat island effect through the use of satellite data. *Mon. Weather Rev.* 107, 1554-1557.
- Rao, P.K., 1972: Remote sensing of urban heat islands from an environmental satellite. *B. Am. Meteorol. Soc.* 53, 647-648.
- Rigo, G. and Parlow, E., 2004: Multitemporal analysis of the urban surface temperature – Heat island of the city of Basel. In *New Strategies for European Remote Sensing* (ed.: M. Oluic) Milpress, Rotterdam, 679-683.
- Roth, M., Oke, T.R., and Emery, W.J., 1989: Satellite-derived urban heat island from three coastal cities and the utilization of such data in urban climatology. *Int. J. Remote Sens.* 10, 1699-1720.
- Scherer, D., Fehrenbach, U., Beha, H.-D., and Parlow, E., 1999: Improved concepts and methods in analysis and evaluation of the urban climate for optimizing urban planning processes. *Atmos. Environ.* 33, 4185-4193.
- Strahler, A., Muchoney, D., Borak, J., Friedl, M., Gopal, S., Lambin, E., and Moody, A., 1999: *MODIS Land Cover Product Algorithm Theoretical Basis Document, Version 5.0*. Center for Remote Sensing, Department of Geography, Boston University. Boston, MA.
- Unger, J., Sümeghy, Z., and Zoboki, J., 2001: Temperature cross-section features in an urban area. *Atmos. Res.* 58, 117-127.
- USGS, 1996: GTOPO30 documentation. <http://edcdaac.usgs.gov/gtopo30/>.
- Vidale, P.L., Lüthi, D., Frei, C., Häberli, C., Liniger, M.A., and Appenzeller, C., 2004: The role of increasing temperature variability in European summer heatwaves. *Nature* 427, 332-336.
- Voogt, J.A., Grimmond, C.S.B., 2000: Modeling surface sensible heat flux using surface radiative temperatures in a simple urban area. *J. Appl. Meteorol.* 39, 1679-1699.
- Wan, Z. and Snyder, W., 1999: *MODIS Land-surface Temperature Algorithm Theoretical Basis Document*. Institute for Computational Earth Systems Science, Univ. of California, Santa Barbara.

IDŐJÁRÁS

Quarterly Journal of the Hungarian Meteorological Service
Vol. 109, No. 4, October–December 2005, pp. 233–256

An evaluation of the performance of the three-dimensional variational data assimilation scheme for the ALADIN/HU spectral limited area model

Steluța Vasiliu¹ and András Horányi²

¹*National Meteorological Administration of Romania*
97, Sos. Bucuresti-Ploiesti, 013686 Bucharest, Romania
E-mail: steluta.vasiliu@meteo.inmh.ro

²*Hungarian Meteorological Service*
P.O. Box 38, H-1525 Budapest, Hungary; E-mail: horanyi.a@met.hu

(Manuscript received in final form November 10, 2005)

Abstract—In this paper, the three-dimensional variational (3D-Var) data assimilation scheme for the ALADIN/Hungary model is described and its performance is evaluated by comparing the resulting forecast scores with those from the reference model running in dynamical adaptation. Experiments with different assimilation strategies have been studied, in order to establish the general framework for further research. The verification scores show a better short-range performance of the 3D-Var system. More results are presented for two individual synoptic cases, corresponding to interesting meteorological situations. One was selected based on the poor performance of the reference model, where the model using the 3D-Var scheme is found to perform better. The other was an example, when the operational model did well, and it was shown that the 3D-Var scheme is able to keep the good performance of the reference model.

Key-words: variational data assimilation, 3D-Var, mesoscale limited area model

1. Introduction

Numerical weather prediction (NWP) is a modern discipline in meteorology, which makes the prediction of future states of the atmosphere numerically feasible. In order to produce an accurate weather forecast, a realistic description of the initial atmospheric conditions is required. This is achieved basically by using observational information from the atmosphere together with

its assimilation into the numerical model. High quantity of observations is available with large temporal and spatial resolution about the atmosphere from a variety of observing types. Anyway, in spite of the relatively high volume of the observations, they are still considered to be sparse and heterogeneous having in mind the number of all state variables at all model grid points. In other words, the assimilation problem is highly under-determined. Therefore, beside the observations, one must use additional past and current information to improve the initial conditions. The most important such information is the *background* or *first guess*, which is nothing else, than a short range forecast of a numerical weather prediction model valid at the analysis time (i.e., the time instant, when the initial conditions for the NWP model are to be determined).

The ultimate goal of the atmospheric data assimilation is to produce a regular, dynamically consistent four-dimensional representation of the atmospheric states from observations irregularly distributed in space and time, taking into account first guess information and considering all the error characteristics of the applied information sources. This latter is needed for the evaluation of the reliability of the information source in the assimilation process. Since all information has to be represented within the NWP model, it is important, that the model has a sufficiently high resolution, with physically realistic detail.

In 1987, ECMWF together with Météo-France established the basis of a new forecasting system. The main goals of this project were to develop efficient global data assimilation tools (4D-Var system), and also to have numerical weather prediction models at every spatial and time scales (*Courtier et al.*, 1991). Thus, the project is named IFS (Integrated Forecasting System) at ECMWF, and ARPEGE (Action de Recherche Petite Echelle Grande Echelle) at Météo-France. In the literature, it is often referred as "ARPEGE/IFS". The models are global spectral primitive-equation models, with a triangular spectral truncation in the horizontal, and a hybrid coordinate in the vertical.

In 1990, Météo-France started a collaboration with several weather services, mainly from Central and Eastern Europe, in order to develop a limited area version of the ARPEGE/IFS model, in the framework of the existing global code, for dynamical adaptation at the limit of the hydrostatic approximation. The new model, called ALADIN (Aire Limitee Adaptation dynamique Developpement InterNational), is a spectral mesoscale limited area model (LAM), using bi-Fourier horizontal spectral representation. An important part of the ARPEGE dynamics is kept and its physics is basically identical with the ARPEGE's one (*Horányi et al.*, 1996; *Pailleux*, 1997).

A data assimilation system had been under development since 1996 for the ALADIN LAM, based on a three-dimensional variational (3D-Var) scheme. Being counterpart of the global model ARPEGE, the ALADIN 3D-Var system

basically follows the specifications of the ARPEGE version. ALADIN has specific code only in the horizontal part (because of the geometry), but in the vertical part, the observation operators and vertical grids are identical for both models. The main goal of the ALADIN 3D-Var system with the analyses of such high density observations, which are not assimilated by the ARPEGE assimilation system, is to analyze better the small scales of the atmosphere, without touching the large scales already analyzed in the global model.

Our work was devoted to the development and application of the ALADIN 3D-Var scheme to the ALADIN/HU version of the model applied at the Hungarian Meteorological Service. Thus, the first experiments of the 3D-Var data assimilation scheme for the ALADIN/HU model were aiming to get a general impression of the applicability of the scheme and, moreover, to establish the best possible strategy for such a mesoscale data assimilation system. Many experiments were performed in this framework in order to choose, beside others, the lateral boundary conditions to provide the large scale information, the first guess to be used, the optimal initialization method to be applied, the way to incorporate the lateral boundary conditions, etc. These experiments provided the framework for a more detailed study of the application of the 3D-Var scheme. The next set of experiments was performed by choosing special meteorological situations, where on the one hand, the reference version (without data assimilation) failed to provide a good prediction, and on the other hand, where the operational (reference) forecast was reasonably good. For the first synoptic case the improvements were checked, and in the latter one, whether the new scheme is able to keep the good performance of the model.

The present paper describes the latest results obtained using the 3D-Var scheme for a spectral mesoscale limited area model. A brief overview of the formulation of the 3D-Var scheme in the ALADIN model is given in Section 2. Section 3 presents the experiments, which helped to establish an optimal assimilation strategy. Afterwards, the results of two case studies are illustrated in Section 4. The conclusions are summarized at the end, and finally some plans for the future are presented briefly.

2. Data assimilation method for the ALADIN model

The limited area model ALADIN is running in dynamical adaptation mode in many European countries. This means that no independent objective analysis is performed in order to obtain initial conditions for the limited area model, instead the large scale forecasts, provided by the global model ARPEGE, are adapted to the high-resolution local characteristics (whence the name

“dynamical adaptation”). The lateral boundary coupling is carried out using the Davies relaxation technique (*Davies, 1976*), where the relaxation zone of the domain ensures the continuous transition between the boundary conditions and the ALADIN solution obtained every time-step.

Another algorithm to be used for the ALADIN model is the 3D-Var data assimilation scheme for providing initial conditions of the model. The code for the 3D-Var scheme for the ALADIN model is basically the same as for the ARPEGE global model, with some differences because of the applied geometries (spherical for the global model, and plane Cartesian grid for the limited area model). Thus, the horizontal interpolations from the model grid to the observation position, and also some required physical transformations, are performed in a different way. This split presents the advantage that allows introducing the geometrical specificities to the horizontal operators (especially the ALADIN domain aspects), while retaining all the ARPEGE code in the vertical part, since the vertical grids and observational operators are identical for ARPEGE and ALADIN.

The 3D-Var cost function for the ALADIN/HU model is a sum of the background term and observation term. No constraint term was introduced so far in the ALADIN/HU 3D-Var system. The observation term might take into account different types of observations: conventional (SYNOP, AMDAR/aircraft data, radiosondes, PILOT balloons) and remote sensed (for instance satellite winds, ATOVS radiances) ones. For the background term, the standard NMC statistics are considered. The NMC (National Meteorological Center, now is called National Centers for Environmental Prediction) method estimates the background error statistics using a set of differences between forecasts valid at the same time, but at different ranges (usually 36h–12h differences) (*Parrish and Derber, 1992*). Statistical balance is considered between the model variables (vorticity ξ , divergence η , temperature T , logarithm of surface pressure P_s , and specific humidity q), where the empirical balance coefficients are obtained from multiple regressions over the set of those NMC differences, and provide a set of uncorrelated variables used as predictors in the analysis, instead of the model variables. This method was used first for the global model (ARPEGE), and then it was adapted for the high-resolution limited area model with an additional balance relation for humidity. Thus, for the ALADIN model, the relationships between predictors and predictands are as follows:

$$\begin{aligned}\xi &= \xi, \\ \eta &= \mathbf{M}\mathbf{H}\xi + \eta_u, \\ (T, P_s) &= \mathbf{N}\mathbf{H}\xi + \mathbf{P}\eta_u + (T, P_s)_u, \\ q &= \mathbf{Q}\mathbf{H}\xi + \mathbf{R}\eta_u + \mathbf{S}(T, P_s)_u + q_u,\end{aligned}$$

where ξ , η , (T, P_s) , and q are the forecast errors of vorticity, divergence, temperature and surface pressure, and specific humidity, on models levels. The subscript u stands for unbalanced (total minus balanced) fields. \mathbf{M} , \mathbf{N} , \mathbf{P} , \mathbf{Q} , \mathbf{R} , and \mathbf{S} are the vertical balance operators. They are block-diagonal matrices relating spectral vertical profiles of predictors and those of the predictands. \mathbf{H} is the horizontal geostrophic balance operator. It transforms vorticity ξ into the so-called balanced geopotential $P_b = \mathbf{H}\xi$ (Berre, 2000).

The 3D-Var system of the ALADIN/HU model particularly performs four analysis steps each day, with observation window of six hours, centred on the observing times at 00, 06, 12, and 18 UTC. Each analysis step begins with the observation pre-processing, when a quality control for the observation format and position, for the climatological and hydrostatic limits, and for the temporal consistency is realized. Another criterion to check the observation is to compute and compare the innovation vector of each observation to its expected values defined by the diagonal of the observational error covariance matrix. In this way the best-quality and unique observations close to the analysis time are selected.

Further, the 3D-Var analysis is performed, using the background information, the observation file prepared by the screening (quality control) and the background error statistics. The ALADIN/HU 3D-Var system is using a quasi-incremental procedure, only that the analysis increment and the first guess have the same resolution. The pre-conditioning is used for a faster convergence of the minimization of the cost function. So first the differences between the background field and the observations are calculated. The analysis increments are estimated using the observation increments. Afterwards, these increments are used to update the background field in order to create the analysis. The minimization is based on a variable-storage quasi-Newton algorithm (Gilbert and Lemaréchal, 1989). Because the 3D-Var data assimilation scheme is acting only for the upper-air meteorological fields, after the variational analysis step, the optimal interpolation method is applied for the surface variables. In principle, this step can be performed prior to the upper-air variational analysis step as well. Each analysis is used to initialize the forecast model, which is integrated for a six-hour range (at least for the assimilation runs). However, for production mostly 24-hour and 48-hour forecasts are carried out. The six-hour forecast is used as first guess of the following analysis. The refreshment of the lateral boundary conditions is done every 6 hours in our case. During these experiments the horizontal resolution of the ALADIN/HU model is 8 km.

The experiments described below have been performed with the 3D-Var data assimilation scheme for the *double-nested limited area model*, ALADIN/HU. Double nesting means that the boundary conditions of the

model are provided by another limited area model, ALADIN/LACE (Limited Area modelling for Central Europe), which has a larger domain, and a lower resolution. At its turn, this limited area model is driven by the global model ARPEGE. The idea of the double-nested models is to get a fine scale resolution in the area of interest, and to analyze better the physical processes from the smaller scales with a reasonable computational cost.

3. General evaluation

A general evaluation of the ALADIN/HU 3D-Var system was realized, before any other detailed studies were performed, especially because there were so many choices in order to establish the optimal strategy for the 3D-Var scheme.

In the assimilation process, both the information from the first guess and from the observations are important for the quality of an analysis. For the global models (in intermittent data assimilation cycles), the first guess is always the 6-hour forecast from the previous model integration. But for the mesoscale models, different possibilities can be chosen: the 6-hour forecast from the previous model integration (the classical choice), which contains information from the small scales, the analysis provided by the global model, which contains information mainly from the large scales, or the mixture of the first two information, with the help of some kind of *blending* procedure, which merges the fine-mesh information from the limited area model, and the synoptic scale information from the analysis of the global model. For the time being, the 6-hour forecast from the previous integration of the model as first guess for ALADIN/HU 3D-Var system has been considered a natural choice. A blending between the ALADIN/HU forecast, using the 3D-Var data assimilation scheme, and the ARPEGE analysis is considered in a later stage.

3.1 Coupling strategies

Another question was the way in which the information from the lateral boundary conditions (LBC) should be incorporated into the data assimilation cycle. Two different strategies were tested. The first one is the so-called “time-consistency” coupling technique, when the lateral boundary conditions, necessary for the integration of the limited area model, contain time consistent tendency information, being provided by the same integration of the coupling model. The second strategy, named “space-consistency”, differs from the previous one, that the 3D-Var analysis replaces the first lateral boundary condition, thus the information for the integration of the model is consistent in space. In practice it means that the initial field and the first LBC field are the

same. The first experiments were performed for a period of one week, when the two coupling techniques have been systematically compared in terms of verification scores.

For the experiments, the background error statistics are determined by the standard NMC method, and the observation term takes into account surface and upper-air (radiosounding) observations. Thus, the relative humidity, geopotential, and temperature measurements are assimilated from the surface data, and geopotential, wind, temperature, and relative humidity variables from the radiosondes.

All the data assimilation experiments were run with a six-hour cycle (the integration length of the background field), and 24 hours in production (for the short-range forecast of the model). Digital filter initialization (DFI) has been applied both in cycling and production. Analyses and forecasts were verified against radiosondes, using mainly simple statistical measures, as mean error (BIAS) and root mean square error (RMSE). These objective scores are calculated for the results of the model using 3D-Var scheme, and also of the operational one (in dynamical adaptation), with respect to the observations. The compared fields are the temperature, geopotential, zonal and meridional wind, relative humidity, direction and speed of the wind. Also other objective measures, as time-evolution of the fields at different levels of the model, have been examined. For subjective evaluation, maps with analysis increments and representation of different meteorological fields were drawn.

During the evaluation of the verification scores, we have to keep in mind, that the 6-hour forecast (from 00 UTC and 12 UTC model runs) is compared with the data from 06 UTC and 18 UTC, respectively. For these moments of time, the number of observations is much smaller than at 00 UTC and 12 UTC. This means that the statistical scores for 06 UTC, as an example, do not have the same precision, as those for 00 UTC. But even in this situation, the scores give a general idea about how the forecast using the 3D-Var data assimilation scheme is behaving compared to the operational one.

The vertical cross section of RMSE scores for relative humidity and geopotential are plotted in *Fig. 1*, for the analysis of the operational model, and of the model using 3D-Var scheme, in time-consistency and space-consistency. The most significant improvements, meaning better scores of the analyses, have been obtained for the relative humidity (*Fig. 1*, left panel) and wind (not shown). There is a slight advantage for the 3D-Var scheme for temperature (not shown) and geopotential (*Fig. 1*, right panel) for some upper levels, otherwise the scores are almost neutral. Comparing the curves, when the two different coupling techniques have been applied, it reveals that the model using the 3D-Var scheme with the time-consistency coupling technique has slightly better scores.

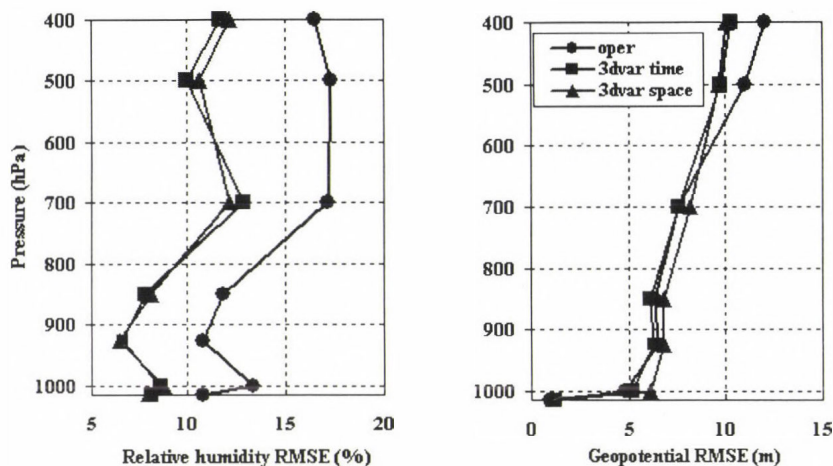


Fig. 1. Vertical profile of the RMSE of the operational analysis (*oper* – line with circles) and using 3D-Var scheme in time-consistency (*3dvar time* – line with squares), and space-consistency (*3dvar space* – line with triangles), for relative humidity (left panel) and geopotential (right panel).

Verifications of the 6-hour forecasts illustrate, that when the 3D-Var scheme has been used, the forecasts lost from the initial improvements, especially for wind and relative humidity (Fig. 2, left panel). But still the model using the 3D-Var scheme was able to provide a better forecast for relative humidity especially up to the middle troposphere. For the other upper levels, the operational model has been slightly improved the six-hour forecast. Verification of geopotential (Fig. 2, right panel) and wind generally showed a more positive impact of the 3D-Var scheme, than those of temperature, for which the scores were neutral. Wind forecasts are sometimes better for some upper levels using the 3D-Var scheme than in dynamical adaptation, and sometimes it is the reverse. Regarding the two coupling techniques, the verification scores for the six-hour forecast show again that the results of the 3D-Var system using the time-consistency technique were improved mainly for the relative humidity and wind fields.

After 24-hour integration, the scores are very similar to those in dynamical adaptation, with small variations near the surface (not shown). This means that the information is coming mainly from the lateral boundary conditions, as for the operational forecast, and the impact of the observational data assimilated at the beginning of the forecast period becomes negligible.

In conclusion, the scores showed that the 3D-Var analysis fits the observations for all the fields reasonably well, as it was expected of a data

assimilation scheme. The 6-hour forecast of the model using 3D-Var scheme is losing from the initial improvement, but not for all levels. After 24-hour integration, the scores start to be very close to each other. These verification scores and also other objective measures helped us to choose “time-consistency” as coupling technique for the experiments using the 3D-Var scheme for the ALADIN/HU model.

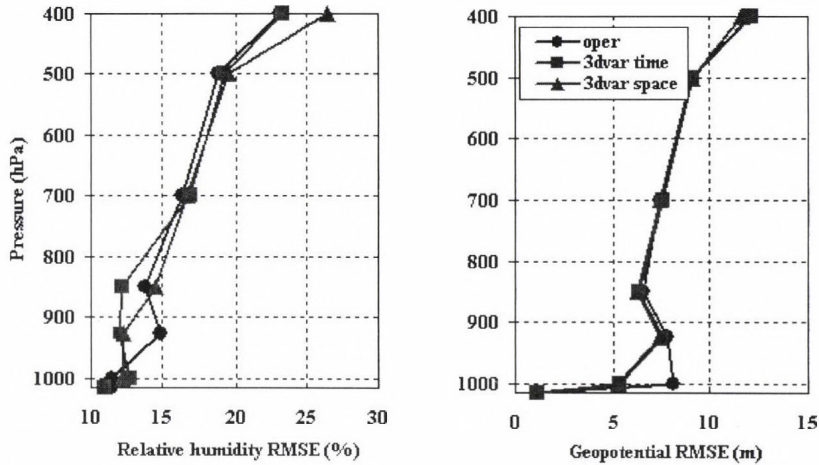


Fig. 2. Vertical profile of the RMSE of the operational 6-hour forecast (*oper* – line with circles) and using 3D-Var scheme in time-consistency (*3dvar time* – line with squares), and space-consistency (*3dvar space* – line with triangles), for relative humidity (left panel) and geopotential (right panel).

3.2 Initialization methods

Further we tried to decide which initialization method is better for application both in cycling and production. As it was mentioned before, the ALADIN model is using the digital filter initialization (DFI) technique, to suppress the unrealistic high-frequency gravity oscillations from the initial conditions. A variation of the classical DFI method has been tested, namely the incremental digital filter initialization (IDFI), when it is assumed that the first guess is already balanced and the analysis increment (the difference between the analysis and the first guess) should be filtered. The third choice was not to apply any initialization method in the 6-hour assimilation cycle. The same time period was selected as for the previous experiments.

Similarly to the previous experiments, first the verification scores have been examined, and they show a neutral impact of the different initialization

methods. Thus, it was difficult to select which method is better to be applied. So, further other objective measures were used, like the time evolution of some fields at different levels, in order to check the balance properties of the different fields. *Fig. 3* shows the time evolution of mean sea-level pressure checked during the 6-hour integration in cycling for a selected case (February 28, 2002, 00 UTC), for four different points on the domain. The selected points were chosen accordingly: two are over the mountains, one is in the middle of the domain, and the other one is in the left-bottom corner of the domain.

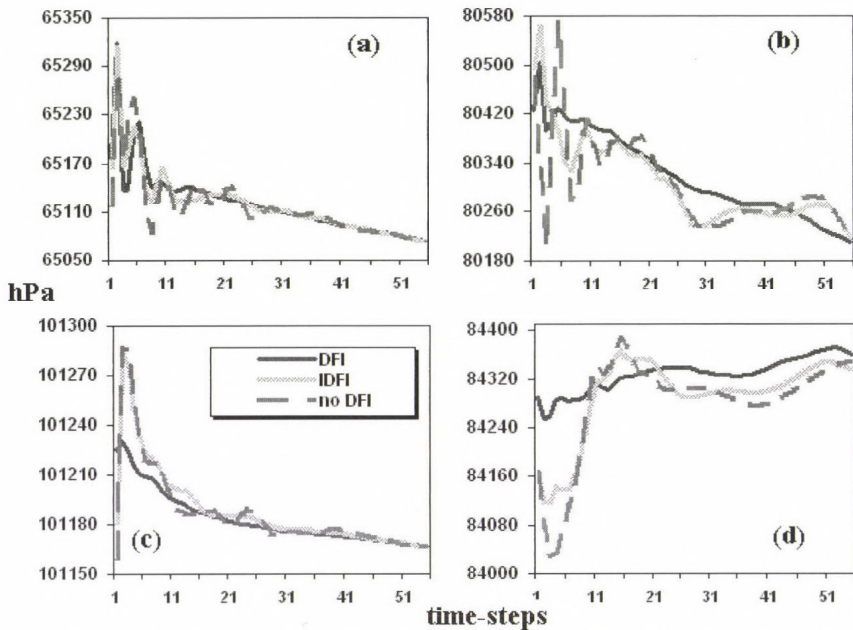


Fig. 3. Time evolution of the mean sea-level pressure using different initialization methods in cycling, DFI (solid line), IDFI (dotted line), no DFI (dotted-dashed line), for February 28, 2002, 00 UTC. (a) and (b) represent points in mountainous regions, (c) a corner point, and (d) a point in the middle of the domain.

The noise can be seen for the first time-steps of the integration, when no initialization or IDFI were used in the assimilation cycle. The curves when DFI was applied are rather smooth. At the end of the six-hour forecast, the level of noise looks relatively small, even without DFI or IDFI. But one can

see, that for some points, six hours are sometimes not enough to get a filtered forecast. So we could consider, that the final 6-hour forecast has bigger chance to be realistic if it results from a less noisy time evolution. In conclusion, the digital filter initialization has been selected to be applied in cycling.

The time evolution of the mean sea-level pressure was checked during the 6-hour integration in production (not shown), for the operational forecast and using 3D-Var scheme with different initialization methods in cycling and production. It seems that the fields are in balance, when DFI was used in production (for the operational model, and also with 3D-Var scheme). Without initialization, the noise appeared especially for the first time-steps. Following the same argument as before, it was decided that digital filter initialization has to be applied also in production (Alexandru, 2002).

3.3 Lateral boundary conditions

Another experiment was carried out using different lateral boundary conditions provided by the driving model (ALADIN/LACE) and global model (ARPEGE) in the assimilation cycle. The time period of these experiments was extended to one month.

The verification scores of analyses, provided by the operational model and using the 3D-Var scheme with different lateral boundary conditions, against observations are presented for temperature and zonal wind. The temperature scores show an advantage for the 3D-Var scheme for all the upper levels (*Fig. 4*, left panel). Comparing with the first experiments (for the one week period), one can say that the significant improvement in the analyses of wind is illustrated again (*Fig. 4*, right panel). Geopotential scores are almost neutral for the lower levels for both models (with and without data assimilation), but above 700 hPa, the 3D-Var scheme has a slight advantage (not shown). Another field estimated well by the model with the data assimilation was the relative humidity (not shown). Generally, the model using the 3D-Var scheme was able to provide a better analysis. Anyway, the main interest during these experiments was to see whether or not the choice of the lateral boundary conditions (from the ALADIN/LACE or ARPEGE models) is important. No large difference could be seen for the analysis verification, for all the fields (Alexandru, 2003).

The six-hour forecast scores for temperature (*Fig. 5*, left panel) show that the models, using the 3D-Var scheme and in dynamical adaptation perform equally well, with very small differences near the surface. In terms of the wind, the scores look slightly better using data assimilation than the reference, at almost every upper level (*Fig. 5*, right panel). The verification for relative humidity shows an improvement using the 3D-Var scheme especially near the

surface, whereas for the upper levels, the operational forecast is slightly better (not shown). Compared to the analysis, the forecast of the geopotential, with data assimilation, was improved especially in the lower levels (also not shown). The only difference between the results of the verification of the model using the 3D-Var scheme with different LBCs appeared in the upper levels for the zonal wind, where the LBCs from the ALADIN/LACE model seems to provide a slight improvement.

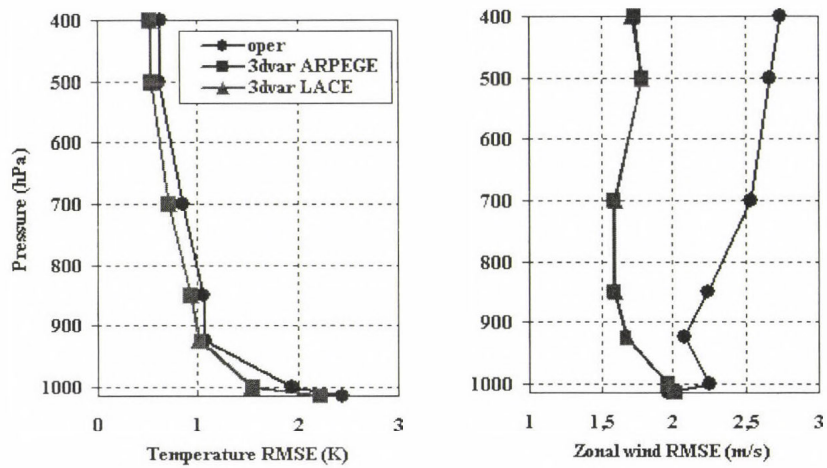


Fig. 4. Vertical profile of the RMSE of the operational analysis (*oper* – line with circles) and using 3D-Var scheme with ARPEGE (*3dvar ARPEGE* – line with squares), and LACE LBCs (*3dvar LACE* – line with triangles), for temperature (left panel) and zonal wind (right panel).

Other objective measures showed small differences on results, when the lateral boundary conditions from the two coupling models were used in the assimilation cycle. Also maps with the representation of some meteorological fields were checked, but again the differences for the experiments with 3D-Var scheme and different LBCs were not visible (not shown).

So far, the general evaluation of the 3D-Var scheme permitted us to conclude, that the optimal choices are as follows: lateral boundary conditions to come from the same integration of the coupling model, thus the information to be consistent in time, and digital filter initialization to be applied both in cycling and production, in order to have a filtered forecast. The choice of the lateral boundary conditions from the global or limited area model is indifferent.

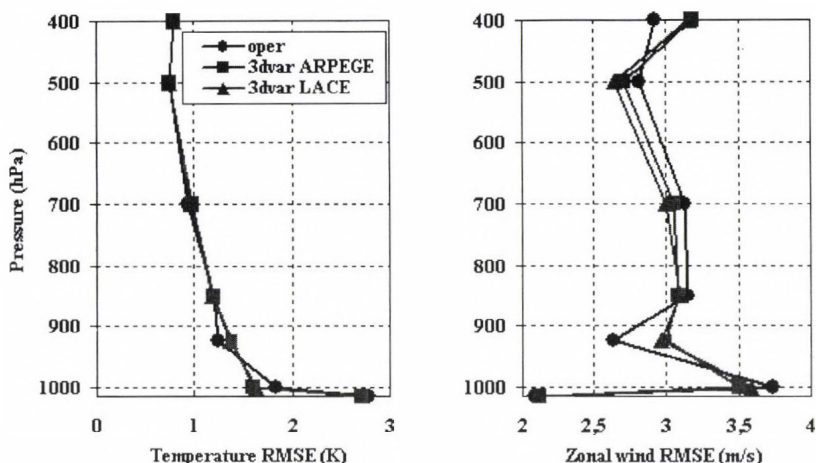


Fig. 5. Vertical profile of the RMSE of the operational 6-hour forecast (*oper* – line with circles) and using 3D-Var scheme with ARPEGE (*3dvar ARPEGE* – line with squares), and LACE LBC (*3dvar LACE* – line with triangles), for temperature (left panel) and zonal wind (right panel).

4. Case studies

Once the best possible scientific strategy of the ALADIN/HU 3D-Var system was established, some interesting meteorological situations have been selected in order to study the performance of the model using the 3D-Var scheme in more details. Thus, two types of cases are presented in this paper: one, when the operational model failed to provide a reasonable forecast, and the second one, when the operational forecast was very accurate. The lateral boundary conditions were provided by the ALADIN/LACE model, using time-consistency as coupling technique, and digital filter initialization was applied in cycling and production (see the previous chapter).

4.1 Summer case (July 17–18, 2002)

A short description of the synoptic situation of this case is as follows. On July 13, a cold trough spread over Western Europe on the 500 hPa isobaric surface. From this, a cold drop isolated on July 14, moved to east, whirled over Northern Italy on July 16, at noon, and filled slightly in between. From noon of July 17, it got a cold supply on the backside, which made the cyclone to strengthen again and to move to east from July 18. Between July 18 and 20, the cyclone moved over the Carpathian Basin. Thus on July 18, large amount of precipitation (up to 54 mm/24h) was measured over the central part of

Hungary, along the Danube river (*Fig. 6*). In the morning of July 18, a steady convergence evolved in the wind field that probably played an important role as a trigger effect in the rainstorm (with precipitation over a large area).

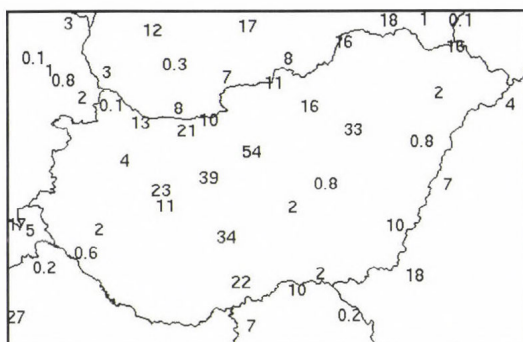


Fig. 6. The amount of precipitation (mm/24h) measured over Hungary between July 18, 06 UTC and July 19, 06 UTC.

For this case study, the results of the ALADIN/HU model, running in dynamical adaptation (the operational version) and using the 3D-Var scheme, were examined. The first one was kept as the reference for all the new experiments with data assimilation. The plots of different meteorological fields (except for the geopotential height forecasts) were zoomed over Hungary, in order to focus on the place of interest.

In *Fig. 7*, the geopotential height forecasts show that the cold air is streaming from north-west in the lower troposphere, bringing cooler air especially in the western part of Hungary. The operational forecast of relative humidity at 700 hPa indicates the availability of moisture in the south-western part of Hungary, and that the area of the Danubian Basin is partly cloudy (not shown). However, the vertical velocity field does not indicate any significant rising motion of the air masses through the 700 hPa surface (also not shown). So, heavy rainfall is not likely to occur in the central part of Hungary. The maximum of precipitation predicted by the model running in dynamical adaptation is located in the south-western part of the country, with a value around 36 mm/24h (*Fig. 8*, left panel). The location of this precipitation maximum is related to the area, where the moisture is available. Compared to real measurements, it can be seen that the operational model misforecasted this event, because no precipitation has been indicated over the Danubian Basin, and the maximum in the south-western part of Hungary was not more than 5 mm/24h.

Comparing the geopotential forecasts of the models with and without data assimilation, one can see the considerable differences, which appeared over Hungary (Fig. 7). The assimilation of observations helped the model, using the 3D-Var scheme, to predict a low-pressure system located over the Danubian Basin. The cyclone is well defined also in the altitude.

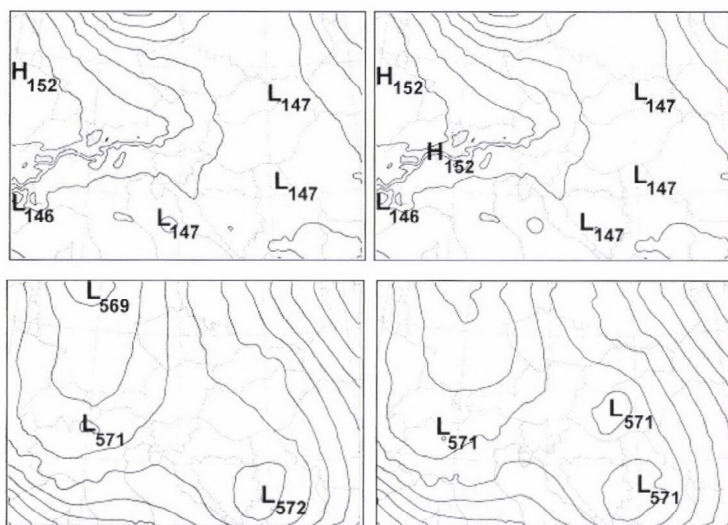


Fig. 7. 18-hour forecasts of the model in dynamical adaptation (left column) and using 3D-Var scheme (right column) for geopotential height (dam) at 850 hPa (upper row) and 500 hPa (lower row), valid on July 18, 18 UTC. For geopotential height the contour intervals are at every 1 dam.

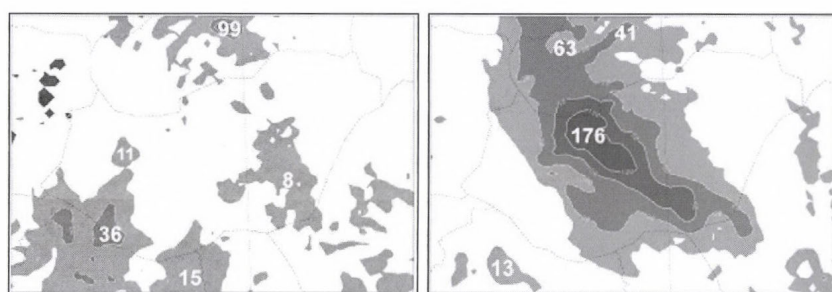


Fig. 8. The amount of precipitation (mm/24h) forecasted by the models in dynamical adaptation (left panel) and using 3D-Var scheme (right panel) over Hungary, between July 18, 06 UTC and July 19, 06 UTC. The contour values are 5, 20, 50, 100 mm/24h.

The area, where enough moisture is available, covers almost the entire country in the experiments when 3D-Var scheme has been used, with a high likelihood of precipitation in the central part, as it is illustrated in *Fig. 9*. Also, the forecast of the vertical velocity field at 700 hPa shows an intensive vertical motion. All these fields, together with the forecast of the low geopotential height gave an indication of the heavy rainfall to be occurred over the central part of Hungary.

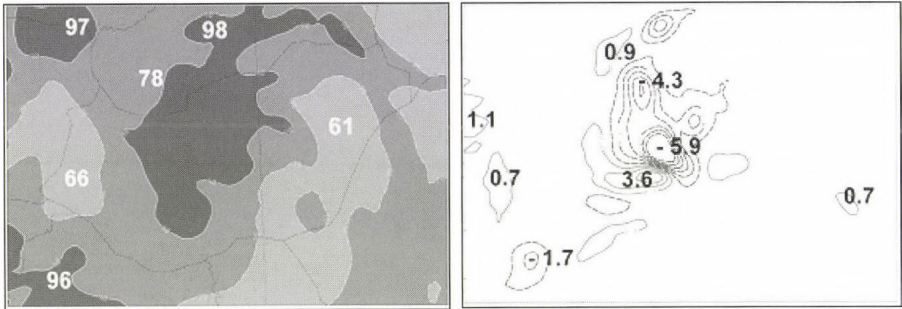


Fig. 9. 18-hour forecasts of the model using 3D-Var scheme, for relative humidity (left panel) and vertical velocity (right panel), at 700 hPa, valid on July 18, 18 UTC. For relative humidity, the contour values are 40, 60, 75, 90%, and for vertical velocity, the contour intervals are at every 0.9 Pa/s.

In *Fig. 10*, the divergence at different upper levels from the experiments with data assimilation is plotted. One can see the strong divergence at 300 hPa and the convergence at 850 hPa, located in the central part of Hungary. In this area the vertical velocity at 700 hPa is around -6 Pa/s, and also the moisture is available. Usually, strong divergence at upper levels, associated with large areas of rising air in the middle troposphere, indicates heavy rainfall.

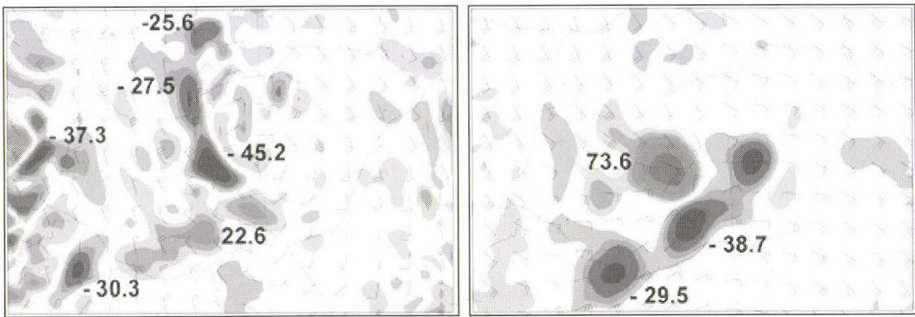


Fig. 10. 18-hour forecasts of wind (m/s) and divergence ($\cdot 10^5/s$) at 850 hPa (left panel) and 300 hPa (right panel), valid on July 18, 18 UTC.

The precipitation forecast of the 3D-Var experiments has a good location generally (*Fig. 8*, right panel), being predicted over the entire Danubian Basin, but the amount of rainfall (with the maximum around 176 mm/24h) is much greater than in reality (compared with values as 54 mm/24h). *Fig. 8* illustrates what a big difference was between the precipitation forecast of the two models. So, the assimilation of observations helped the ALADIN/HU 3D-Var system to realize a better prediction of this event, however, the amount of precipitation was overestimated.

Trying to understand how the observations have influenced the quantity and location of precipitation, some experiments were carried out using the 3D-Var scheme, and assimilating only the surface or upper-air (radiosounding) measurements available at the Hungarian Meteorological Service, all along the cycle. The results of these experiments showed, that such set of observations, which are uniquely responsible for the improved prediction of the rainfall event, cannot be identified. The most important features for the forecast are coming from the upper-air observations. However, for this case it is better to use observations from surface and upper-air together. Naturally, the positive influence of the observations over the forecast is bigger as the time is closer to the moment of the event, and as the location of the high resolution data is closer to the area of interest.

As a conclusion from this case study, it can be said that the operational model was unable to predict any features of the phenomenon. Neither the coupling model gave any indication about the rainfall to the coupled model through the lateral boundary conditions. However, the ALADIN/HU model, using 3D-Var scheme, forecasted large amount of precipitation (even too much) as it was in the reality. Therefore, the new information coming from the observations contributed to the improvement of the forecast of this event, in spite of the fact, that some of the applied observations for the limited area model was already used in the global ARPEGE analysis (4D-Var).

4.2 The Czech floods in August 2002

Another case study has been selected in order to be studied using the ALADIN 3D-Var scheme. The operational forecast of this event was considered a success by the forecasters. So the aim of the new experiments was to check whether or not the model using data assimilation can achieve similar performance as it is for the reference version.

In August 2002, disastrous floods hit Central-Europe. The floods proceeded in two waves and were caused by intensive rain from two deep cyclones and the related frontal systems, one following the other at a very short time interval. Both moved slowly, but only the second one was

remarkably well developed. On August 6, a high altitude low-pressure system from the Gulf of Genoa reached the area of the Alps causing rain showers and thunderstorms in Austria. As an effect of the moist air with unstable stratification in the cyclone, the amount of precipitation was high, 50–100 mm in the Alps, but in some places of the central part of Austria it exceeded even 200 mm during the two days.

Precipitation in the Alps begun to diminish temporarily between August 8 and 10. Rain showers, thunderstorms continued to occur, but significant quantity of precipitation fell only locally. A new active cyclone reached Northern Italy on August 11. Because an anticyclone was located over Eastern Europe, first the depression moved slowly in the northeast direction, and then more to the north. Thus, its occluded front spread over the central part of Austria and Bohemia for three days almost without any movement. As a consequence of this stationary front, the quantity of precipitation was again significant in Austria, Bavaria, and Bohemia, reaching 100–150 mm in 24-hour, and locally 200 or in some places even more than 300 mm (*Fig. 11*) (*Sopko, 2003*).

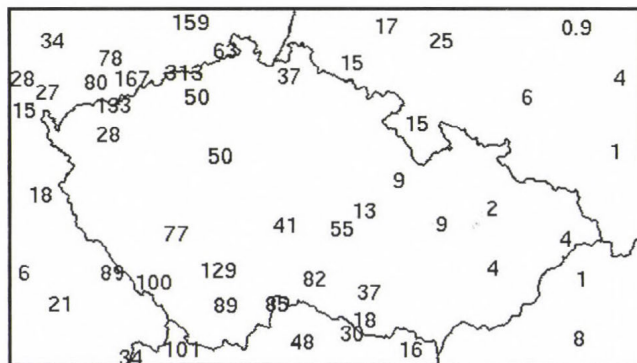


Fig. 11. The amount of precipitation (mm/24h) measured over the Czech Republic between August 12, 06 UTC and August 13, 06 UTC.

Both models, with and without data assimilation, succeeded to predict the slow motion of the cyclone, together with the heavy rainfall. On August 11, the cyclone moved from Northern Italy over Austria, progressing on a northward track. The area where enough moisture was available is very large, covering the western part of Austria, Bavaria, Saxony, and the western part of the Czech Republic. The air masses at that location have an intensive vertical motion (of around -6.5 Pa/s). So there is an increased likelihood that heavy precipitation will develop. Both models predicted almost the same pattern of

high humidity. The location of the rainfall and the very high quantity of precipitation (not shown) were well forecasted. Locally in Austria, the rainfall was overestimated (more than 200 mm/24h), comparing with measurements (100 mm/24h). Also, in the borderline areas of South Bohemia and Austria, the models predicted heavy rainfall.

On the following day, the centre of the low-pressure system moved towards the northern part of Bohemia. The depression has deepened in between, and the rainfall intensified. On the fronts the temperature forecasts showed sharp contrasts, and the air was very warm in the warm sector.

The operational and 3D-Var forecasts of the relative humidity at the 700 hPa isobaric surface showed the same shape of the areas, where the moisture is available (*Fig. 12*). One can see that the air was very humid, especially in the northern part of Austria, Bohemia, and Saxony, with a strong ascending vertical motion. These facts indicate that a heavy rainfall is likely to occur. In the southern part of Austria, the sky is partly cloudy and the air has descending motion (not shown), which are generally associated with areas of fair weather. So it is expected that the precipitation will end soon.

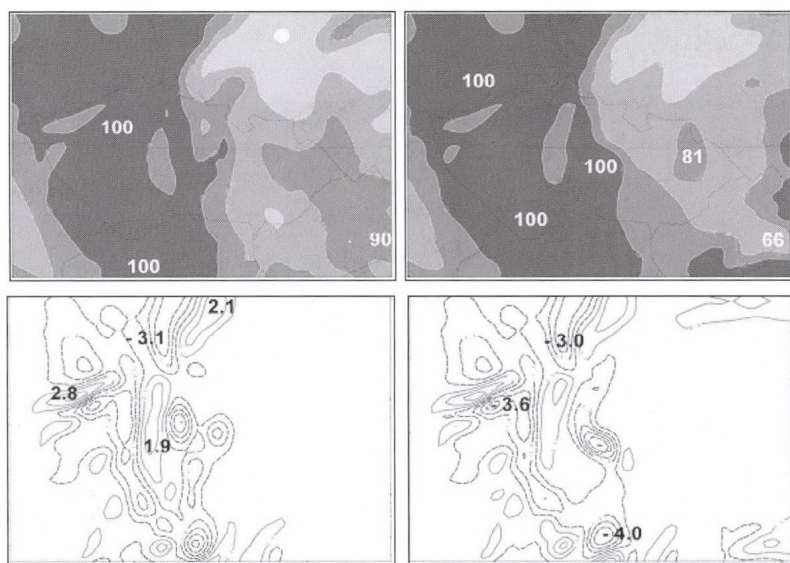


Fig. 12. 24-hour forecasts of the model in dynamical adaptation (left column) and using 3D-Var scheme (right column), for relative humidity (upper row) and vertical velocity (lower row) at 700 hPa, valid on August 13, 00 UTC. For relative humidity, the contour values are 40, 60, 75, 90%, and for vertical velocity, the contour intervals are at every 0.9 Pa/s.

Fig. 13 shows the precipitation accumulated in 24 hours between August 12, 06 UTC and August 13, 06 UTC. Both models predicted the right location of the rainfall in Saxony, where values up to 296 mm/24h are shown. The operational forecast had the closest value to reality. But also the 3D-Var experiments predicted an important quantity in that area. A good prediction of the rainfall over Bohemia has been performed also. A small area with 100 mm precipitation forecast in 24 hours, can be seen over the border of Poland and the Czech Republic. The quantity is overestimated, in reality it has not been more than 37 mm/24h, but it is an indication of the new place, where significant rainfall is expected.

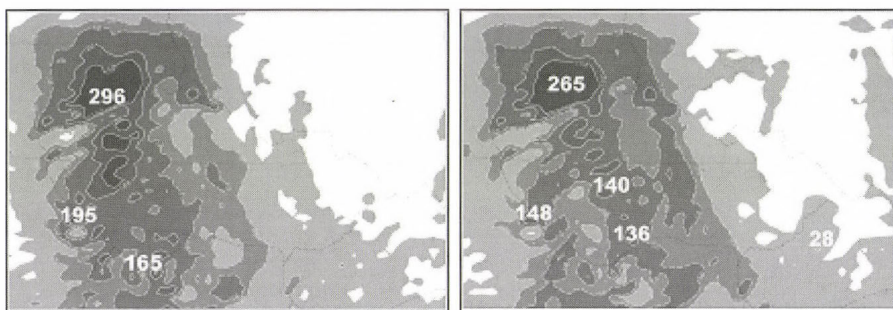


Fig. 13. The quantity of precipitation (mm/24h) forecasted by the models in dynamical adaptation (left panel) and using 3D-Var scheme (right panel) over the Czech Republic, between August 12, 06 UTC and August 13, 06 UTC. The contour values are 5, 25, 50, 100, 150 mm/24h.

On August 13, the forecasts of the models showed that the cyclone continued to move to a north-eastward direction, over Poland. The pressure gradients weakened and the winds subsided, so the cyclone began to fill. The differences between the operational forecasts for geopotential and those of the model using 3D-Var scheme are very small, less than 1 dam. The moisture was available in the south-western part of Poland, the Czech Republic, and the western part of Hungary. The vertical motion of the air masses is less intense, reaching values of 2.6 Pa/s (not shown).

The intensity of precipitation started to decrease, and the location of the rainfall moved towards the eastern part of the Czech Republic. Both models predicted almost the same quantity of rain (cumulated in 24 hours, between August 13, 06 UTC and August 14, 06 UTC), and the location was also similar. Comparing to reality, the models in dynamical adaptation and using the 3D-var scheme showed an underestimation of the amount of precipitation

in some places and an overestimation in others. However, the locations of the maximum values over the border of the Czech Republic and Poland, and in Moravia were well predicted. So the forecast still can be considered good with reasonable limits.

The successful forecast of the operational ALADIN/HU model is partly due to the correct information provided through the initial and more particularly through the lateral boundary conditions. Being a double-nested limited area model, it means that both ALADIN/LACE and mainly ARPEGE models provided a good forecast for the floods. The global model ARPEGE, using 4D-Var scheme, assimilates more types of observations, compared with the 3D-Var scheme for ALADIN/HU model. This is one explanation of the good performance of the global model.

The accurate information from the lateral boundary conditions, together with the assimilation of more surface observations, helped the model with 3D-Var scheme to obtain a good prediction of the event. It was concluded, that the 3D-Var system does not deteriorate the good performance of the reference model.

In this chapter, the results of two versions of the limited area model, with and without data assimilation, in different meteorological situations have been described. It was shown first, that the model using 3D-Var scheme was able to improve the forecast, when the operational model failed. Then, that the 3D-Var scheme can support the model to achieve the same good results, as the operational one succeeded.

5. Discussion and conclusions

In the present paper, the 3D-Var scheme for the double-nested limited area model, ALADIN/HU, has been described, and its performance has been compared to that of the operational version of the model, running in dynamical adaptation. Nevertheless, it is believed that the double-nesting aspect is not really important, while interpreting the obtained results. The experiments were realized in two parts. First, a general evaluation was carried out, in order to establish the best possible framework of the ALADIN/HU 3D-Var system. Then, some synoptic cases have been investigated, in order to study the scheme in greater detail.

For the general evaluation, different sets of experiments with the models in dynamical adaptation and using the 3D-Var scheme have been performed. The statistical scores for the analysis have shown large improvements for relative humidity and wind fields. Also, a positive impact for the temperature and geopotential has been achieved. These scores illustrate that the 3D-Var

analysis fits well to the observations, as it was expected of a data assimilation scheme. In the short range, geopotential and wind fields have been found to be slightly better with respect to the reference throughout the troposphere. Relative humidity kept its improvement also, as it is shown by the forecast scores. But the difference between the two models, in terms of the statistical scores, starts to decrease with respect to time. One explanation can be the deficiency of the verification procedure, due to the fact that the six-hour forecast is compared against a smaller number of the observations than the analysis. As the forecast range increases, the scores of both models are getting closer, which means that the information is provided mainly from the lateral boundary conditions, while the analysis has less influence on the forecast. Regarding the coupling strategy, it has been decided that using all the lateral boundary conditions from the coupling model (i.e., "time-consistency" technique), the fields show a better representation.

The impact of different initialization methods over the analysis and the short-range forecast has been found to be rather neutral in terms of the verification scores, computed with respect to observations. The time evolution of the mean sea-level pressure field during the first six-hour integration of the model using the 3D-Var scheme with different initializations revealed, that in order to obtain a balanced first guess, the digital filter initialization should be applied in cycling. Also, in production it was decided to use the initialization based on the digital filters, to reduce the inertia-gravity waves from the initial conditions.

The statistical scores from the experiments, when the lateral boundary conditions have been provided by different models (global or limited area model), illustrate the positive impact for almost every field when the 3D-Var scheme has been used, compared to the results of the reference model (running in dynamical adaptation). The objective and subjective evaluations revealed similar results between the experiments with the 3D-Var scheme, which means that the lateral boundary conditions can be used either from the intermediate limited area model (ALADIN/LACE) or from the global model (ARPEGE).

These general experiments have led us to conclude, that the optimal choices for the ALADIN/HU model using the 3D-Var scheme are: the lateral boundary conditions to be provided by the same integration of the coupling model, thus the information is consistent in time, digital filter initialization to be applied both in cycling and production, in order to have a filtered forecast, and finally, the choice of the lateral boundary conditions from the global or limited area model is not so important.

In view of these results, it was decided to continue the experiments with the 3D-Var scheme, for some individual synoptic cases. In that regard two case studies have been presented. In the first one, the operational model did

not predict a heavy rainfall, which happened over the Danubian Basin. It has been tried to demonstrate, how the assimilation of observations can improve the operational forecast. The results of different integrations of the model have been compared, and they revealed that the model using the 3D-Var scheme has a clear advantage over the dynamical adaptation. The location of the rainfall has been well predicted, however, the quantity of precipitation was overestimated. Since both models were using the same lateral boundary conditions, it means that the observations and data assimilation algorithm are responsible for the improvements of the model with the 3D-Var scheme. The second case presents the disastrous floods, which hit Austria, Germany, and the Czech Republic, in August 2002. Large amount of precipitation, more than 100 mm/24h, was measured in different locations. The intensive rainfall has been well predicted by the operational model, both as location and amount, which made us to conclude that the information from the coupling model was accurate. The results of the model using the 3D-Var scheme were investigated, and showed that the forecasts have been in accordance with the reality. Both models have been predicted areas with huge amount of rain and high humidity, which have the same pattern. Therefore, beside the accurate information from the lateral boundary conditions, the ALADIN/HU model using the 3D-Var scheme with some additional local measurements was performing equally well as the global 4D-Var data assimilation system of the ARPEGE model.

The two case studies highlighted that the information from the lateral boundary conditions should be accurate, in order to obtain a good short-range forecast. Also it has been presented that the current 3D-Var scheme benefits from the assimilation both of the surface observations and radiosounding data.

This paper emphasizes that the present framework of the ALADIN/HU 3D-Var system is appropriate to obtain an improved forecast. In the future, it is planned to try other background error statistics (computed by the lagged NMC constant coupling method or the ensemble method), more other types of observations to be assimilated (for instance, aircraft or satellite observations), and to obtain the first guess by using a simple, explicit blending algorithm.

Acknowledgements—This work was made possible thanks to the financial support provided through the European Community's Human Potential Programme under contract HPRN-CT-1999-00057, ALATNET. ALATNET is supported by the TMR/IHP Programme of the European Community, but the information provided here is the sole responsibility of the ALATNET team and does not reflect the Community's opinion. The Community is not responsible for any use that might be made of data appearing here. The authors are grateful to all the colleagues from the ALADIN community, who have contributed to the development of the data assimilation algorithms within the ALADIN model. Special thanks to *Claude Fischer* and *Loïk Berre* for fruitful discussions and collaboration. The first author would like to thank the 3D-Var team from the Hungarian Meteorological Service, for their useful advices. The support of the National Meteorological Administration of Romania was very much appreciated by the first author.

References

- Alexandru, S., 2002: 3D-VAR data assimilation experiments for the double-nested limited area model ALADIN/Hungary. *ALATNET Internal Note* (<http://www.cnrm.meteo.fr/alatnet/>).
- Alexandru, S., 2003: Further experiments with the 3D-VAR data assimilation scheme for ALADIN/Hungary model. *ALATNET Newsletter* 6 (<http://www.cnrm.meteo.fr/aladin/-newsletters/news23/news23-6.html>).
- Berre, L., 2000: Estimation of synoptic and mesoscale forecast error covariances in a limited area model. *Mon. Weather Rev.* 128, 644-667.
- Courtier, Ph., Freydlér, C., Geleyn, J.-F., Rabier, F., and Rochas, M., 1991: The ARPEGE project at Météo-France. *ECMWF Seminar Proceeding*, Reading, Vol. II, 193-231.
- Davies, H.C., 1976: A lateral boundary formulation for multi-level prediction models. *Q. J. Roy. Meteor. Soc.* 102, 405-418.
- Sopko, 2003: Model predictions of the floods in the Czech Republic during August 2002: The forecasters' perspective. *ECMWF Newsletter* 97, 2-6 (<http://www.ecmwf.int/publications/-newsletters/pdf/97.pdf>).
- Gilbert, J.C., and Lemaréchal, C., 1989: Some numerical experiments with variable storage quasi-Newton algorithms. *Math. Prog.* B25, 407-435.
- Horányi, A., Ihász, I., and Radnóti, G., 1996: ARPEGE/ALADIN: A numerical weather prediction model for Central-Europe with the participation of the Hungarian Meteorological Service. *Időjárás* 100, 277-301.
- Pailleux, J., 1997: 1987-1997: Ten years of research and operational activities with the Integrated Forecasting System (IFS). *ECMWF Newsletter* 75, 2-7 (<http://www.ecmwf.int/publications/-newsletters/pdf/75.pdf>).
- Parrish, D. and Derber, J., 1992: The National Meteorological Center's spectral statistical interpolation analysis system. *Mon. Weather Rev.* 120, 1747-1763.

IDŐJÁRÁS

Quarterly Journal of the Hungarian Meteorological Service
Vol. 109, No. 4, October–December 2005, pp. 257–279

Development of regulatory transmission modeling in Hungary

Dezső Szepesi¹*, Katalin Fekete¹, Richárd Büki²,
László Koncsos³ and Endre Kovács⁴

¹*Consultants on Air Resources Management (CARM) Inc.,
Katona J. u. 41, V/25, H-1137 Budapest, Hungary; E-mail: szd12506@ella.hu*

²*Meteorological Service of the Hungarian Defence Forces,
P.O. Box 1885, Budapest, Hungary*

³*University of Technology and Economics, Műegyetem rkp. 11, H-1111 Budapest, Hungary*

⁴*Ministry of Environment and Water Management, P.O. Box 351, H-1394 Budapest, Hungary*

(Manuscript received in final form September 15, 2005)

Abstract—The paper describes the four-decade development of theoretical and practical steps (correct mathematical and atmospheric-physical simulation, temporal and spatial representativity of input data, scrutinised QA/QC, testing and validation, model comparison exercise) carried out to achieve a new regulatory model called HNS-TRANSMISSION for Hungary. Results of climatological assessments of meteorological input parameters (surface wind and atmospheric stability) and maps of base level urban and regional air pollution are also presented.

Key-words: base level air pollution, regional scale wind field, Szepesi-type stability categories, temporal and spatial representativity of meteorological data.

1. Introduction

Air quality modeling in Hungary have been developed in close co-operation among meteorologists, engineers, and project managers of national authorities. This work was helped by numerous able colleagues and technicians of the Department of Atmospheric Environment at the Hungarian Meteorological Service, later at CARM, Budapest, Hungary for many decades. Before 1960,

* Corresponding author

similarly as in other parts of the world, mostly public health people carried out air pollution surveys in Hungary, and some of them was even engaged in stack height calculations.

The ambient air in Hungarian cities before the 1980's was rather polluted, mostly due to solid fuel burning in individual stoves and to the exhaust gases of outdated car engines. *Fig. 1* shows the 50-year trend of air pollutant concentrations in ambient air of Budapest. Breaks in SO_2 curve are due to changes of sampling and evaluation methods (*Fehér and Szepesi, 1970*).

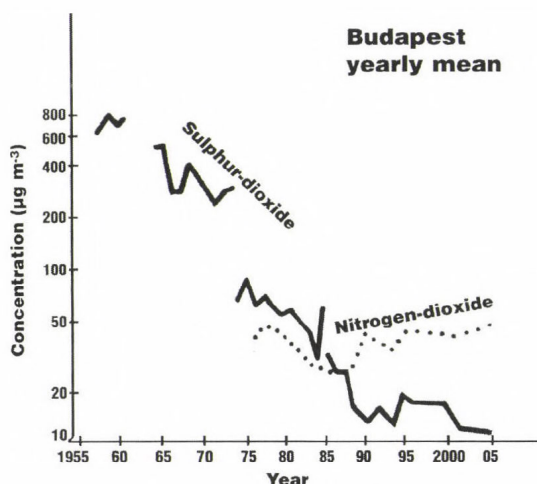


Fig. 1. 50-year trend of air pollutant concentrations in ambient air of Budapest.

At the beginning of the environmental conscious era (around 1970), project managers of national authorities worked out an effective air pollution abatement strategy for cities, including transition from solid fuel to natural gas, and from individual stoves to central and district heating. Heavy industry was placed out of the inner part of cities. This resulted in a considerable drop of SO_2 and soot concentrations soon. Parallel to this effort, intensity and duration of the London-type smog situations considerable dropped (see *Table I*).

Meteorologists were also active in these decades helping authorities in finding the necessary dimension of abatement strategy. Director of the Hungarian Meteorological Service established a research group for air pollution studies, and a scientist was sent to the US Weather Bureau as a UN fellow for one year to be familiarized with the whole spectrum of air pollution meteorology in 1964. The fellow visited 27 research establishments in the US, but the most profitable 3 months were spent at the US Weather Bureau

Research Station (R.A. Taft Center) in Cincinnati, Ohio. Here he took part in field measurements, theoretical and applied researches. In cooperation with American experts, the basis of the first generation transmission system was established (see *Table 2*).

Table 1. Most severe smog situations in Budapest, $\mu\text{g m}^{-3}$

Period with smog	SO ₂	Soot	NO ₂
1936–38, winter mean (Waldbauer, 1938)	–	1070	–
March 16, 1959	3500–4500	5400	–
January 21–23, 1970	1500–1800	1000	–
January–February, 1989; 55 days	200–670	8–350	20–200

During his stay in the USA, diffusion climatological investigations were carried out in Hungary for the period of 1959–63 by punch card technique for wind and atmospheric stability conditions. Mixing height conditions were evaluated, and the first generation model was programmed some years later.

In 1974, the second generation transmission model system named ISAQA was validated for a large power plant at Pécs, south Hungary. The project was ordered by the Ministry of Environment in cooperation with the public health authorities). SO₂ concentrations were measured for a year at 32 stations, surface wind was observed at 6 points, upper air was investigated by pilot balloons, lapse rate conditions were calculated using orographic temperature gradient measurements. Measured and calculated concentration values were in satisfactory correlation. Based on these results, the Ministry on Environment started to fine heavy polluting industrial sources, the first time in Hungarian history.

Description of this model (its acronym is ISAQA) is listed in the Compendium of Regulatory Air Quality Models, together with 182 other models collected worldwide in a program sponsored by the Climatological Commission of WMO, when the author served it as rapporteur of air pollution for 15 years (Szepesi, 1989). The model was applied for some hundreds of cases in three decades without any complains.

The third generation of this model, which was developed and programmed in an EOVS space-informatical system was named as HNS-TRANSMISSION. It is one of the standardized models in Hungary endorsed by the European Environmental Agency.

Table 2. Specifications and phases of the 3-generation model development

Generation	Model characteristics	
	Main goal	Considerations
First generation 1960's	Establishment of regulatory transmission modeling for Hungary (Szepesi, 1964, 1967)	Local scale model for point/area-sources, climatologically correct transmission input data system
Second generation 1970's and 1980's	Standardization of the transmission system for Hungary (Fekete <i>et al.</i> , 1983). Long-range and acid rain model (Fekete and Szepesi; 1987)	Orography, chemistry, initial dispersion, deposition, continental, regional, and urban scale polluting effects
Third generation 1990–2005	Regulatory model according to new domestic and EU regulations (HNS-TRANSMISSION) (<i>present paper</i>)	New definitions according to the demand of recent regulations (OGG, 2001). Simulation of the effects of 50 separate sources. Line sources, plaza parking lots, model estimation of base level air pollution, automatic estimation of area of significant impact, surface and most frequent wind maps, transmission input data system for the whole country (152 small areas). Regional and urban base level air pollution maps from recent measurements

In 1994, Hungary took part in a model intercalibration exercise of the European nations in Belgium (Cosemans *et al.*, 1994). The most important 1 hour maximum concentrations, calculated by the Hungarian standardized model HNS-TRANSMISSION, were in good agreement with values estimated by other national models. This model in its final form contains five years of meteorological data matrices, ready to apply to 150 localities covering all of Hungary. Results of a domestic model comparison of the two standardized models (AERMOD-HNS/HNS-TRANSMISSION) can be found at the web site: www.levegokornyezet.hu. Further model intercalibration was taken in the framework of COST Action 710 WG4. (Harmonization of the pre-processing of meteorological data for atmospheric dispersion models, E.C. Cost Action 710-Final Report, EUR 18195 EN.)

2. Mathematical considerations

Recently, new EU-conform regulations on air quality (OGG, 2001–2004) were promulgated and endorsed for Hungary. To meet the requirements of these regulations, development of a new, a third generation regulatory model system, named HNS-TRANSMISSION (domestic name TRANSZMISSZIÓ 1.1), was necessary. This article is to present major developments achieved.

We have introduced, among others, a new definition, called average concentration for the actual sector, which is similar to the most probable concentration, but refers to a narrower sector (Fig. 2). The difference is in the definition of the borders of the sector. In the new definition we use the concept of Meade and Pasquill (1958), that means that the borders of the sector are at the lines of the 10-percents value of the ground-level centerline concentration.

It will be shown, that this newly introduced definition can be simply estimated by multiplication of the ground-level centerline concentration by a constant. Finally, we introduce a factor which is vital of estimating the exceedences of 1-hour maximum concentration limit value.

Let us see the basic definition we should use, introducing the concept of the average concentration for the actual sector. The concentration is assumed to have Gaussian distribution. The well known and the new definitions of different types of concentrations and other related parameters are shown in Fig. 2.

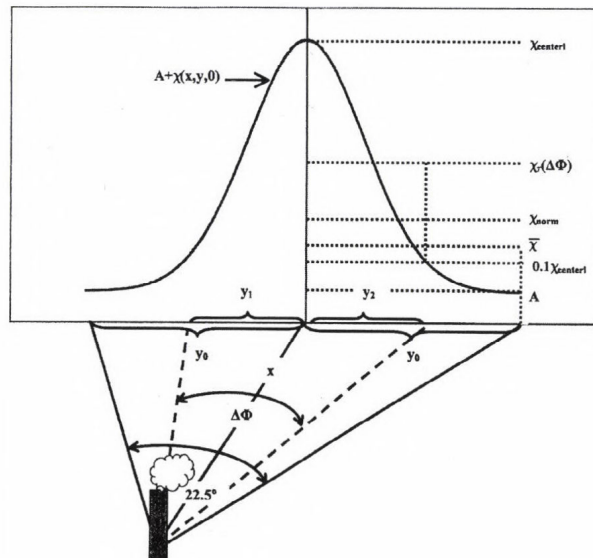


Fig. 2. The Gaussian distribution and the scheme of different types of estimated concentrations.

2.1 Ground-level concentration from an elevated point source

This well-known Gaussian formula specifies the concentration at the ground level along the downwind distance x from the source point:

$$\chi(x, y, 0) = \frac{E}{\pi \sigma_y \sigma_z u_h} e^{\left(-\frac{H^2}{2\sigma_z^2}\right)} e^{\left(-\frac{y^2}{2\sigma_y^2}\right)}, \quad (1)$$

where

- $\chi(x, y, 0)$: concentration, $\mu\text{g m}^{-3}$,
- (x, y, z) : receptor locations, m,
- x : downwind distance from source to receptor, m,
- y : crosswind distance, from source to receptor, m,
- z : height above the ground, m,
- E : pollutant emission rate, $\mu\text{g s}^{-1}$,
- σ_y : dispersion coefficient in the crosswind direction, m,
- σ_z : dispersion coefficient in the vertical direction, m,
- u_h : wind speed at the source-height, m s^{-1} ,
- H : effective height of the stack, m,
- A : base level air pollution.

2.2 Ground-level centerline concentration from an elevated point source

This is a special case of Eq. (1) when $y=0$.

$$\chi_{centerl} = \chi(x, 0, 0) = \frac{E}{\pi \sigma_y \sigma_z u_h} e^{\left(-\frac{H^2}{2\sigma_z^2}\right)}. \quad (2)$$

This type of maximum concentration occurs rarely, but according to the new air quality regulation (OGG, 2001–2004), this has to be taken into account for determining the area of significant impact (ASI) in environmental impact assessments (EIA) (see section 4).

2.3 The most probable concentration

This definition is also introduced by *Fekete et al.* (1983):

$$\begin{aligned}\overline{\chi_\tau} &= \frac{1}{2y_0} \int_{-\infty}^{+\infty} \chi_{centerl} e^{\left(-\frac{y^2}{2\sigma_y^2}\right)} dy = \frac{\chi_{centerl} \sqrt{2\pi}}{2y_0} \sigma_y = \\ &= \sqrt{2\pi} \left(\frac{1}{2y_0} \chi_{centerl} \sigma_y \right),\end{aligned}\quad (3)$$

where

$\overline{\chi_\tau}$: most probable concentration, $\mu\text{g m}^{-3}$,

y_0 : crosswind length belonging to the meteorological wind sector (22.5°), m,

$\chi_{centerl}$: the ground-level centerline concentration, as defined in Section 2.2, $\mu\text{g m}^{-3}$.

The other expressions used are the same as before.

This type of formula is used in the model for estimation of yearly mean ground level concentration.

2.4 Average concentration for the actual sector

Based on the suggestion of Meade and Pasquill (1958), we define this type of concentration distribution. The average concentration is the integral between the 10-percents limits of the ground-level centerline concentration. $\Delta\Phi$ is the angle between the two 10-percent isolines of the ground-level centerline concentrations.

In the first step we calculate the limits of the integral, which, in the previous case, was $\pm\infty$. Because of symmetry case, $y_1 = y_2$, the basic equations are

$$\begin{aligned}\chi(x, y, 0) &= 0.1 \chi(x, 0, 0), \\ y_{1,2} &= \pm \sigma_y \sqrt{2 \ln(10)} \approx \pm 2.15 \sigma_y, \\ 2y_1 &= 2y_0 \approx 4.30 \sigma_y,\end{aligned}\quad (4)$$

where y_1, y_2 is crosswind distances belonging to borders of sector $\Delta\Phi$, m.

Resulting from this transformation, we have got the average concentration for the actual sector ($\Delta\Phi$). With help of the Taylor-series and the definition of the exponential function the following equation can be derived from Eqs. (3) and (4):

$$\begin{aligned}
 (\overline{\chi_\tau})_{\Delta\Phi} &= \frac{1}{2y_0} \int_{-2.15\sigma_y}^{+2.15\sigma_y} \chi_{centerl} e^{\left(-\frac{y^2}{2\sigma_y^2}\right)} dy = \frac{1}{2y_0} \chi_{centerl} \int_{-2.15\sigma_y}^{+2.15\sigma_y} e^{\left(-\frac{y^2}{2\sigma_y^2}\right)} dy \approx \\
 &\approx 2.44 \left(\frac{1}{2y_0} \chi_{centerl} \sigma_y \right) = 1.22 \frac{\chi_{centerl} \sigma_y}{y_0}.
 \end{aligned} \tag{5}$$

This derivation is correct, because σ_y (and σ_z , respectively) is the function of x and not of y , so it can be considered as constant (Fekete *et al.*, 1983).

Comparing Eq. (3) to Eq. (5), we can see that the difference between the concentrations calculated between $\pm \infty$ and between the borders suggested by Meade and Pasquill (1958) is negligible, it is only about 2.7%.

Substituting y_0 from Eqs. (4) and (5) we got:

$$(\overline{\chi_\tau})_{\Delta\Phi} = 0.57 \chi_{centerl}. \tag{6}$$

The multiplication factor is constant, 0.57, because the crosswind dispersion parameter (σ_y) effects $\chi_{centerl}$ and y_0 similarly, so at the simplification of the equation it falls out. The reason for determining Eq. (6) and the average concentration for the actual sector is that the frequency of wind direction in the meteorological wind sectors (which are 22.5° wide) are available as climatologic data in Hungary, and not as the frequency of a certain direction by degrees. When the wind is not exactly in one of the usual wind sectors, and usually it is not, then we can estimate the climatologic frequency of the certain wind direction through weighting using the available information. This method can be adapted for planning purposes easily.

This is the critical formula used by Hungarian environmental inspectors to qualify whether a source complies with limit values and allowable limit value exceedences, or not.

Area sources were treated by an algorithm (Szepesi, 1972), its graphical scheme is shown in Fig. 3.

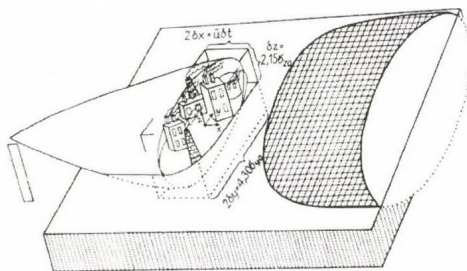


Fig. 3. Scheme of the initial dispersion (area or diffuse sources).

The correct estimation of exceedences of the limit values is vital for air resources management, air quality control, and air quality planning. If we calculate the 1-hour concentration and the base level air pollution, we should divide this sum by a factor denoted by e . So the yearly number of cases, ($Nt(w,x)$), when concentration is above the limit value, is the function of wind direction, w , downwind distance, x , wind speed, u , and atmospheric stability, S , beside of the source parameters:

$$Nt(w,x) = \left\{ \left[\sum_u \sum_S \left(\frac{f_{w,u,S}^{N1}}{e^{N1}} \right) \right] - a \right\} + \left[\sum_u \sum_S \left(\frac{f_{w,u,S}^{N2}}{e^{N2}} \right) \right], \quad (7)$$

where

$f_{w,u,S}^{N1}$: the number of cases, when the sum of the ground-level concentration and base level air pollution is over the 1-hour limit value with a tolerable degree,

$f_{w,u,S}^{N2}$: the number of cases, when the sum of the ground-level concentration and base level air pollution exceeds the 1-hour limit value more than tolerable,

a : number of cases with allowable exceedences,

e^{N1} , e^{N2} : factors of normalization to divide the number of cases to $f_{w,u,S}^{N1}$

and $f_{w,u,S}^{N2}$.

Practically the factor e is the ratio of the crosswind width of the 22.5° sector and that of the sector, where the concentration is greater than the limit value. Starting from this principle, the factor e cannot be less than 1. The value of e varies between 1 and 21 depending on the meteorological and physical conditions, such as emission rate, source parameters, temperature of the ambient air, etc.

An algorithm can be deduced for the factor e . Considering the geometry of Fig. 2 and the definition of the factor e :

$$e = \frac{2y_0}{|y_1| + |y_2|} = \frac{y_0}{|y_1|}, \quad (8)$$

$$y_0 = x \left(\frac{11.25^\circ \pi}{180^\circ} \right).$$

The inequality, which has to be solved, is:

$$\chi_{norm} \leq \chi(x, y, 0) + A, \quad (9)$$

where χ_{norm} : 1-hour mean limit value of concentration, $\mu\text{g m}^{-3}$,
 A : base level air pollution, $\mu\text{g m}^{-3}$.

After transformations and defining the χ_A as the difference below:

$$\chi_A = \chi_{norm} - A,$$

Eq. (9) has the form:

$$\chi_A \leq \chi(x, y, 0).$$

Let us define a source type factor Q , as:

$$Q = \frac{E}{\pi \sigma_y \sigma_z u_h} \quad (10)$$

We obtaine:

$$y_1 = \pm \sqrt{\left| 2\sigma_y^2 \ln\left(\frac{Q}{\chi_{norm} - A}\right) - H^2 \left(\frac{\sigma_y}{\sigma_z}\right)^2 \right|}. \quad (11)$$

Because only the positive resolution of Eq. (8) has physical meaning, we obtain the following algorithm for the e factor:

$$e = \frac{x\left(\frac{11.25^\circ \pi}{180^\circ}\right)}{\sqrt{\left| 2\sigma_y^2 \ln\left(\frac{Q}{\chi_{norm} - A}\right) - H^2 \left(\frac{\sigma_y}{\sigma_z}\right)^2 \right|}}. \quad (12)$$

3. Representative meteorological input data

3.1 Temporal representativity

For long-term planning purposes, it is important to apply meteorological parameters evaluated from data of 30 or 100 years long measurements, or by using shorter, but climatologically representative (normal) 3–5 years long data series.

To investigate this problem on a more objective way, a study of the Péczy-type macrosynoptic situations was carried out (see the web site www.levegokornyezet.hu/climatic aspects) for the period 1881–2001 for Hungary by using the following algorithm:

$$T = \left(\frac{(y_i - \bar{Y})^2}{D_i^2} \right), \quad i=1,2,3,\dots,13,$$

where

T : rate of closeness,

i : index of 13 macrosynoptic situation types,

y : frequency in a specific year,

\bar{Y} : mean frequency for a reference period,

D^2 : standard deviations for the whole reference period,

Upper bar denotes averaging for all i indices.

Table 3 presents the deviations of each year from the 1881–2001 mean, based on the frequency of occurrence of Péczy-type macrosynoptic situations.

By applying this algorithm, 1995, 1997, and 1998 can be considered as the most normal years in the latest decades, and the least normal years were 1981, 1983, and 1996. The mean climatological representativity index of the meteorological data of the 1959–1963 period (the transmission base of the HNS-TRANSMISSION model) was 1.07, which is in the range of 0.372–3.251, and can be considered representative.

In an earlier study (Szepesi *et al.*, 1993), it was also shown, that this base data period (1959–63) approximates the average macrosynoptic situation frequency satisfactorily (mean deviation=1.0, standard deviation=0.57), much better than other periods considered. As a conclusion we can say, that the view of some researchers, that data from the latest years are the most relevant, is not acceptable, it could be extremely misleading in certain cases. The method presented is able to take into account the quantitatively hypothetical changes of climatic regimes, too.

3.2 Regional representativity

The basic idea of meteorological data pre-processing is that for ground-level concentration estimations it is more representative to use regional scale meteorology – in other words, average meteorology for an area of 20–30 km in diameter – instead of measurements made at a single point. This is called

spatial representativity or regionalization of meteorological data. The method of data regionalization is described by *Fekete et al.* (1983), here we only summarize the main lines.

Table 3. Order of climatological representativity

Year	Representativity index for the most normal years	Year	Representativity index	Year	Representativity index	Year	Representativity index for the least normal years
1978	0.296	1987	0.699	1964	0.933	1961	1.154
1955	0.311	1985	0.706	2000	0.933	1975	1.155
1957	0.335	1896	0.708	1970	0.934	1929	1.164
1931	0.372	1908	0.723	1910	0.935	1907	1.165
1927	0.378	1934	0.729	1990	0.960	1923	1.175
1995	0.403	1912	0.745	1952	0.997	1958	1.177
1997	0.405	1913	0.746	1884	1.004	1963	1.203
1998	0.406	1926	0.747	1930	1.007	1991	1.216
1891	0.427	1894	0.749	1890	1.009	1966	1.219
1988	0.431	1992	0.752	1968	1.013	1984	1.225
1994	0.453	1909	0.759	1901	1.017	1976	1.238
1940	0.470	1893	0.760	1999	1.019	1932	1.240
1993	0.473	1954	0.761	1898	1.032	1945	1.245
1886	0.497	1917	0.766	1960	1.039	1887	1.252
1922	0.503	1950	0.780	1911	1.039	1967	1.259
1897	0.503	1979	0.781	1904	1.041	1969	1.286
1892	0.534	1986	0.809	1936	1.050	1972	1.327
1889	0.544	1883	0.822	1905	1.054	1933	1.336
1971	0.549	1925	0.831	1959	1.054	1921	1.443
1948	0.555	1956	0.832	1918	1.067	1982	1.496
1973	0.563	1947	0.834	1989	1.073	1938	1.539
1965	0.570	2001	0.835	1919	1.081	1916	1.585
1935	0.583	1943	0.856	1915	1.095	1944	1.597
1888	0.593	1962	0.860	1953	1.102	1996	1.615
1937	0.647	1942	0.865	1980	1.106	1983	1.625
1881	0.649	1974	0.880	1885	1.114	1946	1.968
1951	0.653	1924	0.883	1903	1.120	1939	2.012
1977	0.674	1928	0.893	1906	1.122	1900	2.050
1882	0.683	1949	0.916	1941	1.124	1920	2.252
1895	0.688	1914	0.922	1902	1.136	1981	2.466
						1899	3.251

3.3 Wind conditions

The aim of establishing wind maps is to furnish readily available regionally and temporally representative wind statistics for any location in the country, for environmental impact assessments. For the analysis of these, all available surface wind data series (more than 300 between 1881 and 1980) and upper air ascents (22 long series between 1929 and 1989) in Hungary were considered (Szepesi and Fekete, 1993).

This wind is representative for quasi-level terrain of average roughness without obstacles. The local effects of extreme roughness, sheltering by obstacles and mountainous terrain must be model-corrected.

Validation of the wind mapping concept gave satisfactory results. It also revealed many inconsistencies in the locating of instruments and former manual evaluation of wind record-charts. However, it also confirmed and quantified some previous findings, for example, that the frequencies of the westerlies and easterlies over the country are considerably increased by orographic channeling of the North Carpathian Mountains.

This is a non-computerized (graphical) data assimilation technique. After plotting all wind direction and speed data available (sixteen directions, and mean speed data for each direction, respectively), we can analyze these charts graphically, one by one (see *Figs. 4 and 5*). These maps make possible to pick up or interpolate yearly average wind direction frequencies and mean speed value data at any point of the country.

The last step is to apply the circular polar smoothing process presented by Tar (1991), then to use an interpolation technique built in the HNS-TRANSMISSION model to interpolate transmission data matrices to any point of interest over the country.

Transmission matrices, gained this way and built in the HNS-TRANSMISSION model, will be temporally and spatially representative and serve as readily applicable input database.

3.3.1 Most frequent winds

Evaluation of the most frequent meteorological situation was another important task. This was carried out in the following way. Since atmospheric stability category $S=6$ (Szepesi stability 1–7, see Fekete *et al.*, 1983) is the most frequent one, surface wind speed prevailing during this stability conditions were evaluated over Hungary. The numerical values ranged from 1.6 m s^{-1} to 3.1 m s^{-1} (see *Fig. 9h*). These parameters are essentials for the estimation of the area of significant impact (ASI) according to OGG (2001–2004).

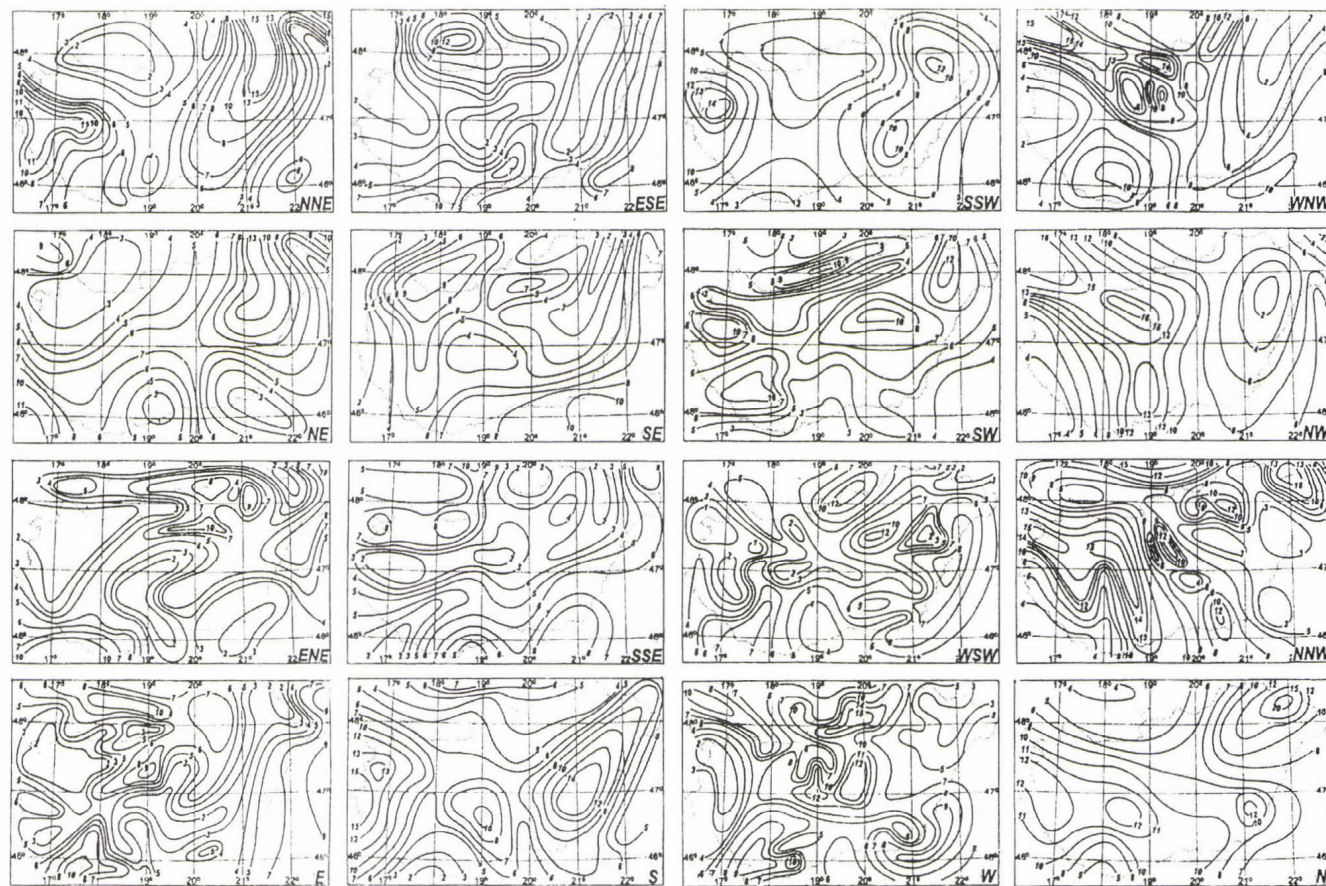


Fig. 4. Relative frequencies of surface wind direction in Hungary (1880–1990), %.

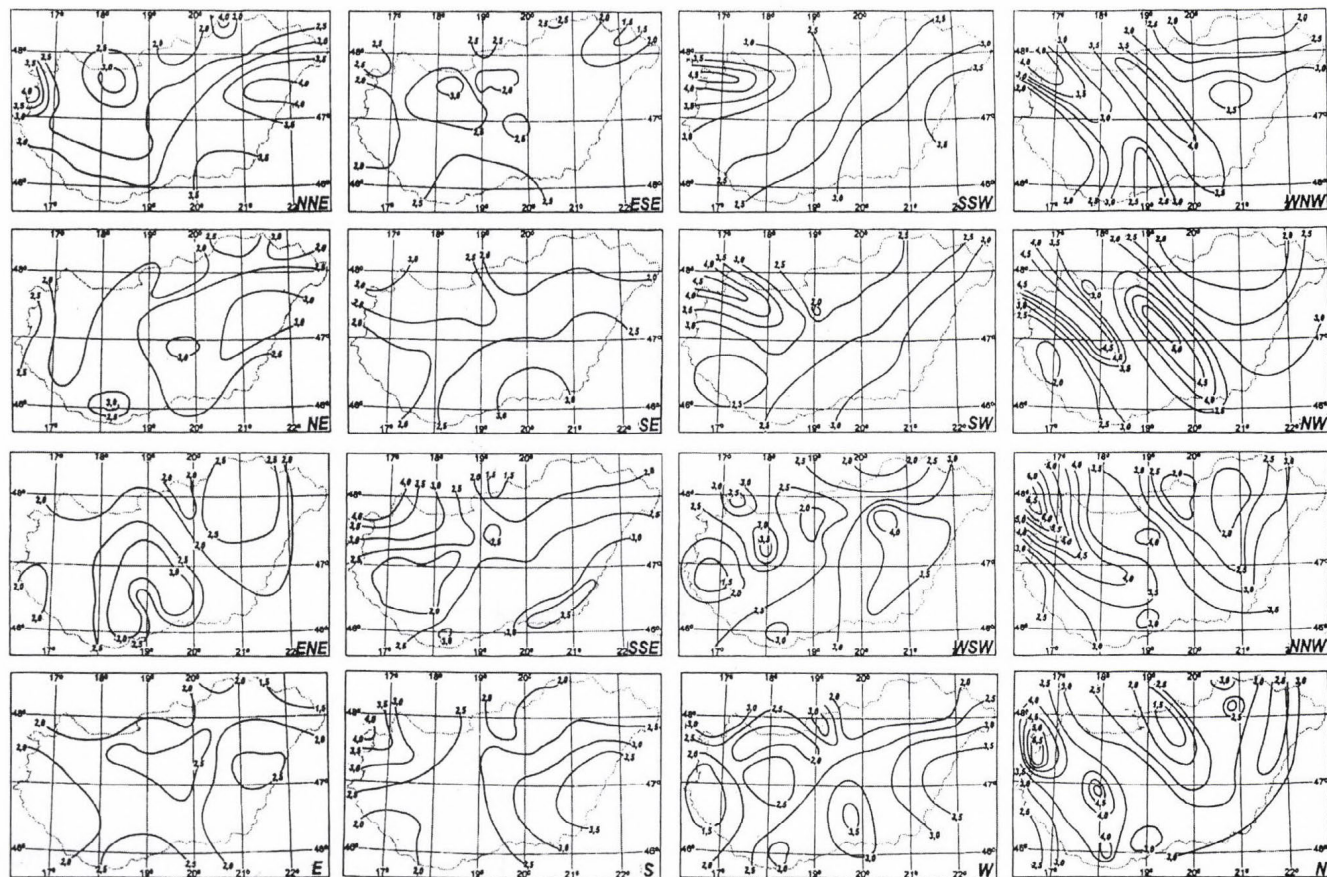


Fig. 5. Mean surface wind speed in Hungary (1880–1990), m/s.

3.4 Stability conditions

Atmospheric stability is estimated in Hungary for low sources by the Pasquill-Gifford-Turner (PGT) procedure, and for medium and high sources by the Szepesi method (Szepesi, 1967), based on classification of temperature lapse rates of the lowest 300 m layer. The climatology of the lapse rates is shown in Fig. 6. Frequency distributions were analyzed based on six daily radiosonde ascents between 1959 and 1963, resulting in a very characteristic and smooth pattern (Szepesi *et al.*, 1993).

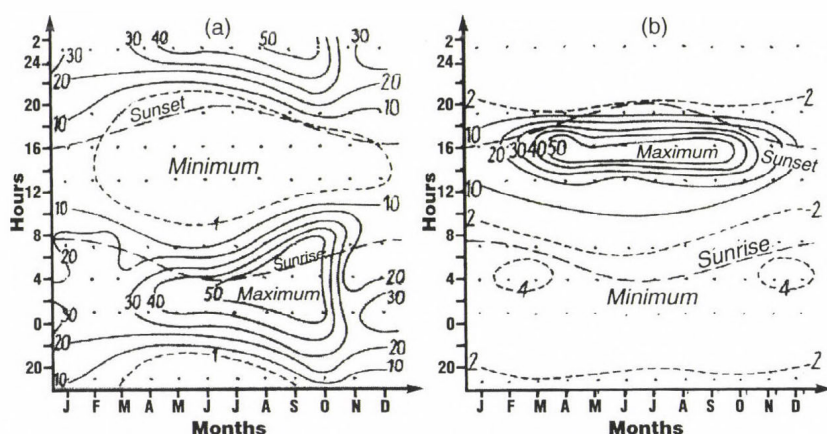


Fig. 6. (a) Relative frequency (%) of stable ($S=1, 2, 3$) and (b) superadiabatic ($S=7$) stratification of the lowest 300 m layer (1959–1963) over Budapest.

By using PGT or Szepesi-type stability classes, dispersion coefficients σ_y and σ_z were determined by the Nowicki (1976) formulas.

For deeper air layers, the exponent p and the stability indicators must be transformed using the diagram shown in Fig. 7. This diagram was constructed using a long series of temperature data measured on high meteorological towers and radiosondes.

3.5 Transmission matrices

Multidimensional transmission matrices are the input bases for long-term estimates of pollutant concentrations (Szepesi *et al.*, 1967, 1985). They were established first time for 40 synoptic stations for the period 1959–1963 in Hungary.

The next step is to pre-process the transmission matrices based on 5 years of measurements. This period (1959–1963) was selected because of having similar weather characteristics as those of the 100 years period (1880–1980). In other words, the frequency distribution of macrosynoptic (Pécze) weather types were nearly similar in both periods.

For low sources, they are based on surface wind direction (16 bins) and speed (7 bins) records, and PGT stability categories using 5 years of SYNOP data. For medium and high sources, 500 m level wind maps (pilot balloon and radiosound) were used, together with the stability conditions (7 bins) estimated on the basis of the lapse rate of the lowest 300 m layer. Between the 40 points for any location in Hungary, a transmission matrix can be interpolated by using statistics of wind maps (see *Figs. 4 and 5*).

For estimation of 24 h mean and maximum concentrations, time series of meteorological data for 7 regions were included.

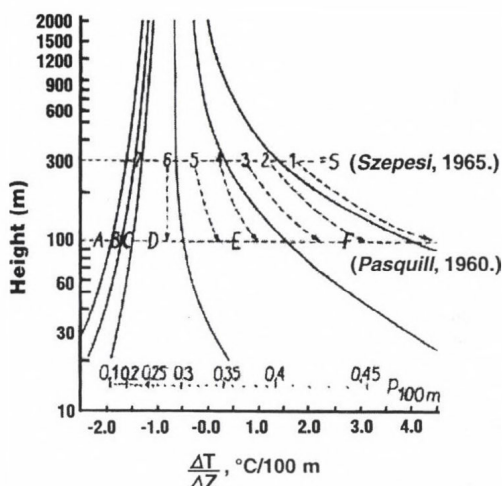


Fig. 7. Diagram for the transformation of wind profile equation exponent p and stability indicator S .

3.6 Background and base-level air pollution

3.6.1 Background pollution

Consistent estimation of background air pollution, originating from larger scale but less intense polluting sources, is of considerable importance for regulatory applications. Because of the very complex mechanisms involved, a practical simplifying approach was worked out (*Fig. 8*). By using this scheme,

contributions from global, continental, regional, and urban background pollution could be easily analyzed for any geographic locations. For local regulatory purposes, preparation of regional and urban background maps for the most important pollutants at 3-year intervals seems reasonable. The maps should be drawn based on all available measured data at urban and regional background stations and analyzed in the light of model estimated concentration patterns calculated using the relevant emission inventory and meteorological input.

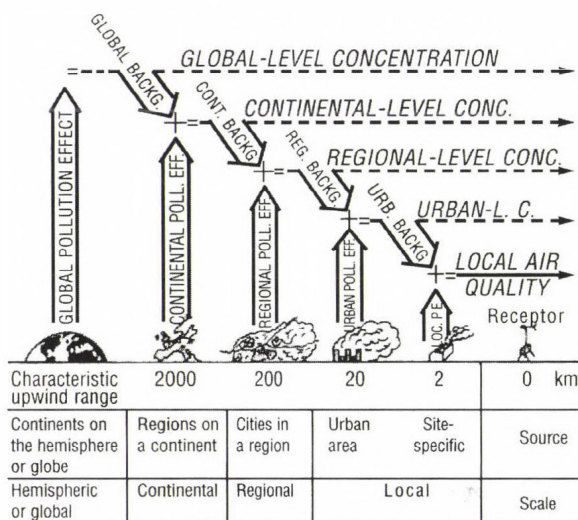


Fig. 8. Hierarchy of air pollution scales.

3.6.2 Base level air pollution

In conformity with Hungarian Clean Air Act Regulations (OGG, 2001–2004), it is necessary to introduce the concept of Base Level Air Pollution (BLAP), which is practically the long-term (yearly) average of background concentrations measured or estimated on a wider area around the planned source. It is an important parameter of any environmental impact assessments, and it is useful if it is available in advance.

Practical steps of its evaluation in the light of recent Clean Air Act regulations is described on the web-site www.levegokornyezet.hu. BLAP fields were estimated in a separate project, and maps presented here are possible examples of future official work.

There are two types: regional and urban BLAP maps.

- The regional BLAP maps were estimated for SO_2 and NO_2 by plotting all measured air pollution data available in Hungary for 1986–90. For the territorial analyses, emission inventories of SO_2 , NO_2 , and NH_3 were used (Figs. 9 a-b). For the total acid depositions maps, Acid Rain Model (Fekete and Szepesi, 1987) was run (see Fig. 9d).

The PM_{10} regional map was estimated by the latest version of EMEP Eulerian Unified Model System for 2003 (*MSC-W Data Note 1*, 2004). For model calculations updated, received emission data were used. As Fig. 9c shows, regional PM_{10} BLAP for Hungary is $10 \mu\text{g m}^{-3}$, and the number of days with limit value exceedencies in Budapest agglomeration is yearly 10. Preliminary model estimations show that over cities in Europe, where the share of diesel cars is over 70 percents (in Hungary it is 17%), exceedence days are close or above 35.

- Urban SO_2 , NO_2 , and CO BLAP maps for Budapest (see Figs. 9 e-g) were analyzed by Vámos *et al.* (2002). By the aid of the Budapest Public Health Institute, all measured high quality data were offered in processed form for 1998–2001. All urban measuring stations were visited and scrutinized. Parameters surrounding the stations, as building height, distance of nearby roads, street width, traffic intensity, and microclimatic characteristics were logged. These parameters are input data for model estimations. Direct impact polluting effect originating from nearby road traffic was subtracted from measured data. BLAP data gained this way were plotted and analyzed territorially by concentration isolines (see Figs. 9 a-c).

4. Model output

An example for the expected NO_x pollution around a new 2-source configuration, estimated by the model system HNS-TRANSMISSION, is shown in Fig. 10. The technical input data are emission rates ($80 \text{ kg NO}_x \text{ h}^{-1}$ and $200 \text{ kg NO}_x \text{ h}^{-1}$), stack heights 20 m and 40 m, respectively, base level air pollution of $20 \mu\text{g NO}_2 \text{ m}^{-3}$ (from Fig. 9), surface roughness of 0.5 m, most frequent wind speed of 2.5 m s^{-1} (from Fig. 5h) and NO_x limit values of $200 \mu\text{g m}^{-3}$ (1 h) and $100 \mu\text{g m}^{-3}$ (24 h).

To meet the requirements of present Hungarian air quality regulations (OGG, 2001–2004), the following concentration patterns are output: 1-hour maximum concentration (Fig. 10a), yearly number of estimated concentration exceedences (Fig. 10b), 24-hour maximum concentration (Fig. 10c), yearly mean concentration (Fig. 10d), and the area of significant impact (ASI) (Fig. 10e), which at condition (b) has the largest range of 11.5 km.

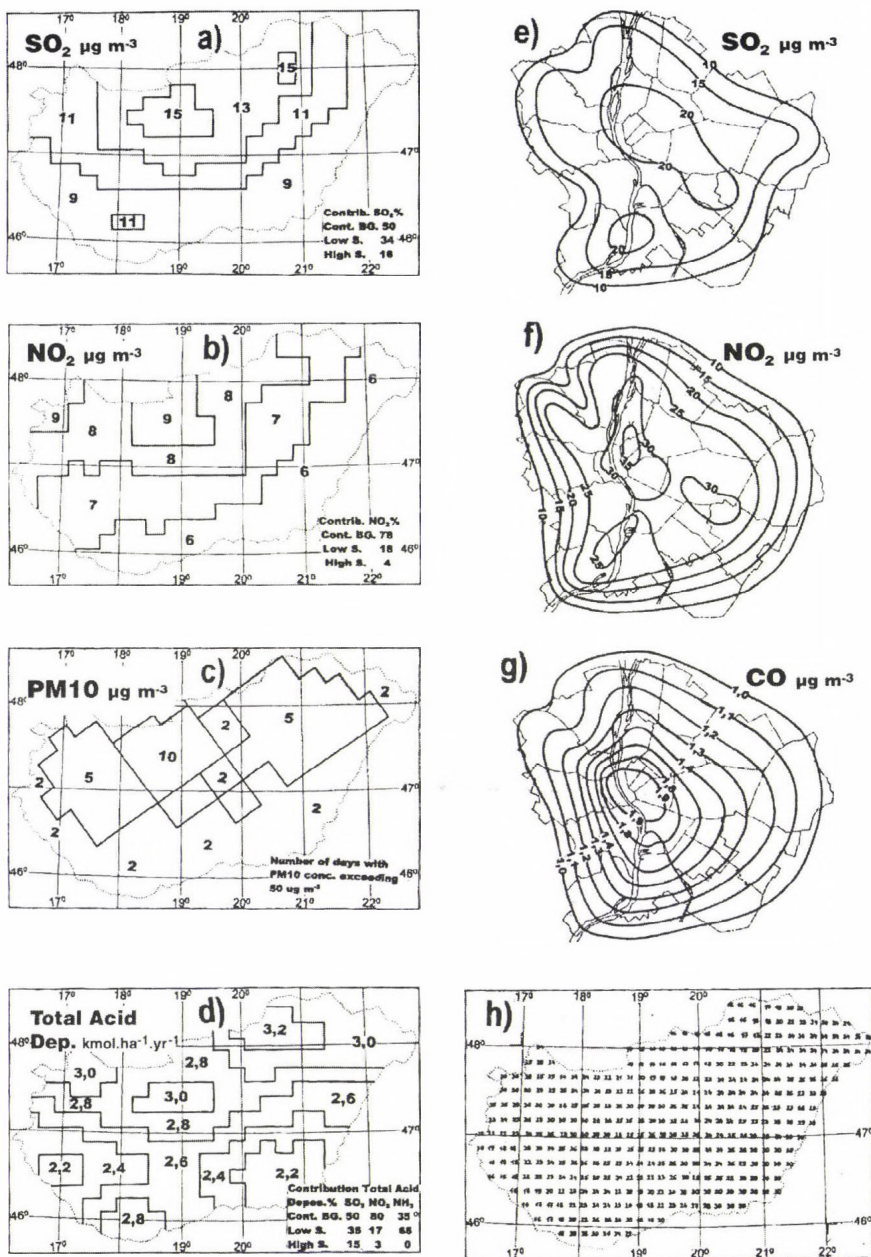


Fig. 9. Regional (a)–(d) and urban (e)–(g) base level air pollution and critical wind speed (h) over Hungary and Budapest.

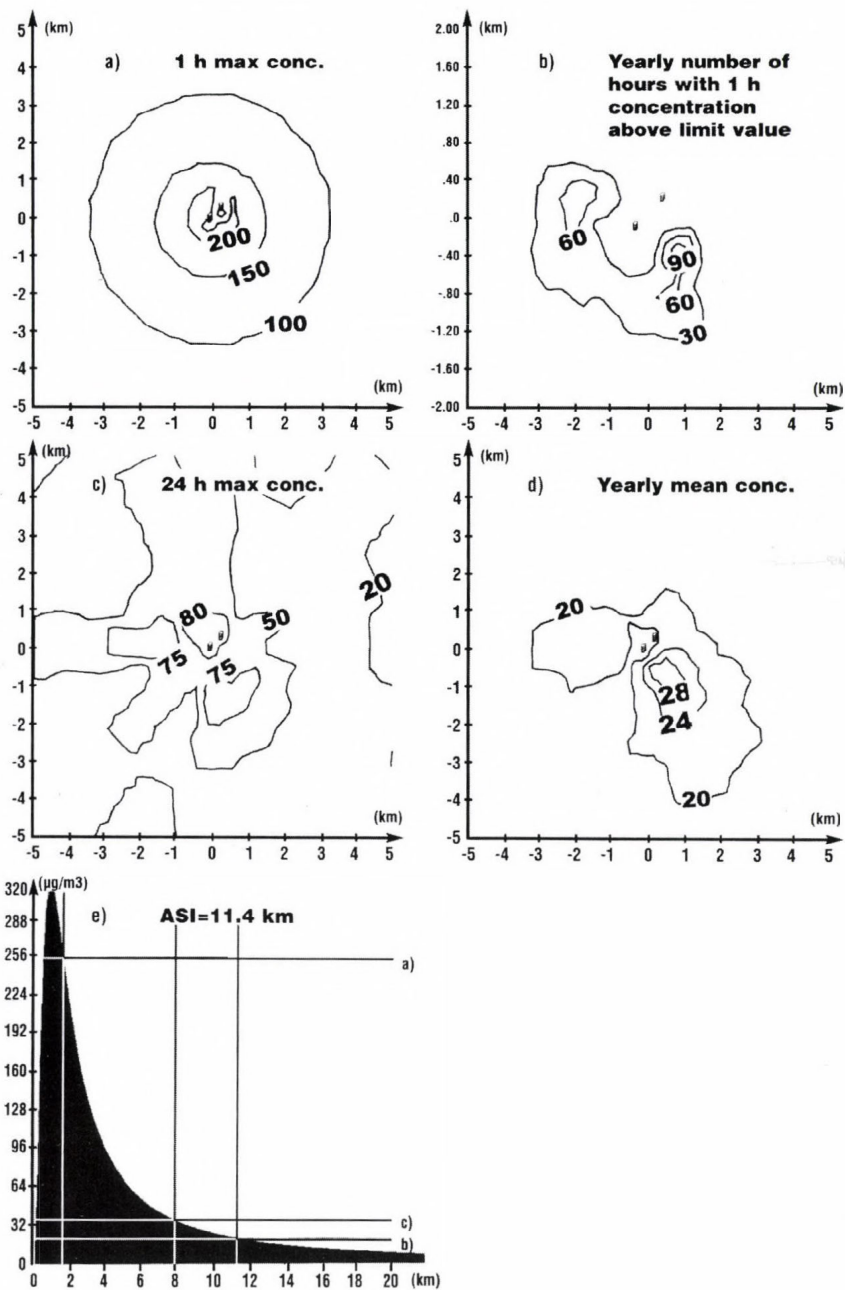


Fig. 10. Concentration distributions (a, b, c, d) and ASI (e) estimated by the HNS-TRANSMISSION model.

5. Characteristics of model HNS-TRANSMISSION

By using modules detailed in Section 2 and representative meteorological input data, regulatory model HNS-TRANSMISSION was prepared to satisfy the new regulations on air quality (OGG, 2001–2004). Major characteristics are the followings: the model estimates ground level concentration and deposition emitted by point and area sources – up to 50 sources –, located at different sites. It calculates 1 h, 24 h and yearly average, maximum values, and limit value exceedences. Their outputs are in tabled form or presented as territorial distributions on Unified Domestic Map System maps in selected colored forms. Dry deposition and chemical transformation modules are included as well.

Effects of inhomogeneous roughness, base level air pollution, and orographical effects in homogeneous or inhomogeneous distributions can also be easily simulated by the HNS-TRANSMISSION model.

Acknowledgements—Model development in Hungary was helped considerably by the successful programming work of Domokos Szász, Iván Mersich, Lajos Gyenes, István Elekes, and László Koncsos. Their contributions are highly appreciated.

References

- Cosemans, G., Janssen, L., and Maes, G., 1994: *The Third Workshop's Environmental Impact Assessment Model Intercomparison Exercise. Operational Short-Range Atmospheric Dispersion Models for Environmental Impact Assessment in Europe*. Mol, Belgium, 21-24 November 1994.
- Fehér, V. and Szepesi, D., 1970: Estimation of the allowable emissions for air pollution abatement program in Hungary. *Proc. of the Second International Clean Air Congress*. Washington D.C., December 10-14, 1970, 1081-1084.
- Fekete, K., Popovics, M., and Szepesi, D., 1983: *Guide to Estimate the Transmission of Air Pollutants* (in Hungarian). Orsz. Meteorológiai Szolgálat Hivatalos Kiadványai, LV, Budapest.
- Fekete, K. and Szepesi, D., 1987: Simulation of atmospheric acid deposition on a regional scale. *Environ. Manage.* 24, 17-28.
- Meade, P.J. and Pasquill, F., 1958: A study of the average distribution of pollution around Staythorpe. *Int. J. Air Pollut.* 1, 60.
- Nowicki, M., 1976: Ein Beitrag zur Bestimmung universeller Diffusions-Koeffizienten. *Arch. Meteor. Geophys. A.*, No. 25, 31-45.
- OGG, 2001-2004: *Official Government Gazettes* (Magyar Közlöny) (in Hungarian) 20/2001 (II.14), 21/2001 (II.14), 120/2001 (VI.30) and 4/2004 (IV.7), Budapest.
- MSC-W Data Note 1, 2004: EMEP, Oslo.
- Szepesi, D., 1964: A model for the long-term distribution of pollutants around a single source (in Hungarian). *Időjárás* 68, 257-269.
- Szepesi, D., 1967: *Meteorological Conditions of the Turbulent Diffusion of Atmospheric Pollutants in Hungary* (in Hungarian). Orsz. Meteorológiai Intézet Hivatalos Kiadványai, XXXII, Budapest.

- Szepesi D., 1972: Model for area sources (in Hungarian). *Időjárás* 76, 73-78.
- Szepesi, D.J. (ed.), 1981: *Planning of the Atmospheric Environment* (in Hungarian). Műszaki Könyvkiadó, Budapest.
- Szepesi, D.J., 1989: *Compendium of Regulatory Air Quality Simulation Models*. Akadémia Kiadó, Budapest.
- Szepesi, D.J. and Fekete, K.E., 1987: Background levels of air and precipitation quality for Europe. *Atmos. Environ.* 21, 1623-1630.
- Szepesi, D.J. and Fekete, K.E., 1993: Design wind maps for Hungary (in Hungarian). *Meteorológiai Tudományos Napok*, Magyar Tudományos Akadémia, Budapest.
- Szepesi, D.J. Fekete, K.E., and Gyenes, L., 1985: Regulatory models for environmental impact assessment in Hungary. *Int. J. Environ. Pollut.* 5, 497-507.
- Szepesi, D.J., Szalai, S., and Károssy, Cs., 1993: The climatological characteristics of the atmospheric environment (in Hungarian). *Magyar Meteorológiai Társaság, XXVII, Vándorgyűlés*, Debrecen.
- Tar, K., 1991: *A Complex Statistical Analysis of Wind Climatology* (in Hungarian). Orsz. Meteorológiai Szolgálat Kisebb Kiadványai 67 sz., Budapest.
- Vámos, A., Bobvos, J., Fekete, K., Szepesi, D., and Titkos, E., 2002: Base level air pollution of Budapest (in Hungarian). *CARM*, Budapest, 1-12.
- Waldbauer, O., 1938: The content of soot in the air of Budapest (in Hungarian). *Egészségügy* 52, 165-174.

BOOK REVIEW

J. R. Holton (editor-in-Chief), 2002: **Encyclopedia of Atmospheric Sciences**. Vol. 1-6. Elsevier Academic Press, 2780 pages, 1900 figures, maps, charts and photographs.

An encyclopedia (alternatively encyclopaedia) is a written compendium of knowledge. The term comes from the ancient Greek "enkuklios paideia" with the meaning "a circle of instructions" or "a well-rounded education", i.e., a repertory of wisdom young Greeks had to know on the seven liberal arts: grammar (science of language), rhetoric, dialectics (logic), arithmetic, astronomy, geometry, and music. Nowadays, an encyclopedia is either general or specializes in a particular field of studies.

A couple of years ago, Elsevier Academic Press started to publish a series of encyclopedias dealing with different fields of earth sciences. The *Encyclopedia of Volcanoes* and the four-volume set of the *Encyclopedia of Earth System Science* were published in 1999, the three-volume set of *Seas at the Millennium* and the five-volume set of the *Encyclopedia of Biodiversity* in 2000, the six-volume set of the *Encyclopedia of Ocean Sciences* in 2001, the six volumes of the *Encyclopedia of Atmospheric Sciences* in 2002, the ten-volume set of the *Treatise of Geochemistry* in 2003, the *Encyclopedia of Caves* and *Encyclopedia of Geology* in 2004. In the near future, two more encyclopedias will be published. The four volumes of the *Encyclopedia of Quaternary Science* are planned for 2006, the eleven volumes of the *Treatise on Geophysics* for 2007. The indicator of the series' success is not only the selling rates, but the title "Best Reference Source of the Year" from the Library Journal for the *Encyclopedia of Ocean Sciences* in 2001 and for the *Encyclopedia of Atmospheric Sciences* in 2002. James Holton editor-in-chief and his collaborators John Pyle and Judith A. Curry invited an enormous number of specialists from leading universities and research institutions from all over the world, for the formulation of the 350 entries. The entries of the encyclopedia cover all aspects of atmospheric sciences, including both theory and applications. It is an ideal resource for undergraduate and graduate students, active researchers, practicing meteorologists, climatologists, oceanographers, environmental scientists, ecologists, policy makers, and industrials to become acquainted with different atmospheric phenomena and to understand the relevance of the dynamical and physical processes of the atmosphere. An online version of the encyclopedia is also available for subscribers.

Gy. Gyuró

IDŐJÁRÁS

VOLUME 109 * 2005

EDITORIAL BOARD

AMBRÓZY, P. (Budapest, Hungary)
ANTAL, E. (Budapest, Hungary)
BARTHOLY, J. (Budapest, Hungary)
BATCHVAROVA, E. (Sofia, Bulgaria)
BRIMBLECOMBE, P. (Norwich, U.K.)
CZELNAI, R. (Dörgicse, Hungary)
DÉVÉNYI, D. (Boulder, CO, U.S.A.)
DUNKEL, Z. (Budapest, Hungary)
FISHER, B. (Reading, U.K.)
GELEYN, J.-Fr. (Toulouse, France)
GERESDI, I. (Pécs, Hungary)
GÖTZ, G. (Budapest, Hungary)
HANTEI, M. (Vienna, Austria)
HASZPRA, L. (Budapest, Hungary)
HORÁNYI, A. (Budapest, Hungary)
HORVÁTH, Á. (Siófok, Hungary)
KONDRATYEV, K.Ya. (St. Petersburg, Russia)
MAJOR, G. (Budapest, Hungary)

MÉSZÁROS, E. (Veszprém, Hungary)
MIKA, J. (Budapest, Hungary)
MERSICH, I. (Budapest, Hungary)
MÖLLER, D. (Berlin, Germany)
NEUWIRTH, F. (Vienna, Austria)
PAP, J. M. (Greenbelt, MD, U.S.A.)
PINTO, J. (R. Triangle Park, NC, U.S.A.)
PROBÁLD, F. (Budapest, Hungary)
RADNÓTI, G. (Budapest, Hungary)
ROCHARD, G. (Lannion, France)
S. BURÁNSZKY, M. (Budapest, Hungary)
SZALAI, S. (Budapest, Hungary)
TAR, K. (Debrecen, Hungary)
TÁNCZER, T. (Budapest, Hungary)
TOTH, Z. (Camp Springs, MD, U.S.A.)
VALI, G. (Laramie, WY, U.S.A.)
VARGA-HASZONITS, Z. (Moson-magyaróvár, Hungary)
WEIDINGER, T. (Budapest, Hungary)

Editor-in-Chief
LÁSZLÓ BOZÓ

Executive Editor
MARGIT ANTAL

BUDAPEST, HUNGARY

AUTHOR INDEX

Alexandru, S. (Bucharest, Romania)	233	Labancz, K. (Budapest, Hungary).....	157
Anda, A. (Keszthely, Hungary)	21	Ladics, T. (Budapest, Hungary)	173
Ács, F. (Budapest, Hungary)	71	Lóke, Zs. (Keszthely, Hungary)	21
Bartholy, J. (Budapest, Hungary).....	1, 217	Marinova, T. (Sofia, Bulgaria)	55
Bencze, P. (Sopron, Hungary)	189	Pongácz, R. (Budapest, Hungary).....	1, 217
Bocheva, L. (Sofia, Bulgaria)	55	Putsay, M. (Budapest, Hungary)	205
Büki, R. (Budapest, Hungary).....	257	Radriamampianina, R. (Budapest, Hungary)	143
Cseh, S. (Győr, Hungary)	189	Robaa, S. M. (Giza, Egypt)	123
Dezső, Zs. (Budapest, Hungary).....	217	Sharov, V. (Sofia, Bulgaria)	55
Drucza, M. (Budapest, Hungary)	71	Steib, R. (Budapest, Hungary).....	157
Fekete, K. (Budapest, Hungary)	257	Szász, G. (Debrecen, Hungary)	71
Horányi, A. (Budapest, Hungary)	233	Szepesi, D. (Budapest, Hungary).....	257
Hunkár, M. (Keszthely, Hungary).....	39	Szonda, S. (Budapest, Hungary).....	111
Kerényi, J. (Budapest, Hungary).....	205	Wantuch, F. (Budapest, Hungary)	111
Koncsos, L. (Budapest, Hungary)	257	Zsótér, E. (Budapest, Hungary)	89
Kovács, E. (Budapest, Hungary).....	257		

TABLE OF CONTENTS

I. Papers

<i>Alexandru, S. and Horányi, A.:</i> An evaluation of the performance of the three-dimensional variational data assimilation scheme for the ALADIN/HU spectral limited area model	233	<i>Kerényi, J. and Putsay, M.:</i> Extreme flood monitoring in Romania and Hungary using Earth Observation Data	205
<i>Anda, A. and Lóke, Zs.:</i> Microclimate simulation in maize with two watering levels	21	<i>Ladics, T.:</i> Analysis of the splitting error for advection-reaction problems in air pollution models.....	173
<i>Ács, F., Szász, G. and Drucza, M.:</i> Estimating soil moisture content of a grass-covered surface using an energy balance approach and agroclimatological observations	71	<i>Marinova, T., Bocheva, L. and Sharov, V.:</i> On some climatic changes in the circulation over the Mediterranean area	55
<i>Bartholy, J. and Pongrácz, R.:</i> Tendencies of extreme climate indices based on daily precipitation in the Carpathian Basin for the 20th century	1	<i>Radriamampianina, R.:</i> Radiance-bias correction for a limited area model.....	143
<i>Cseh, S. and Bencze, P.:</i> Long-term variations of temperature, wind, and precipitable water in the troposphere and lower stratosphere over Budapest, Hungary	189	<i>Robaa, S. M.:</i> A study of ultraviolet solar radiation at Cairo urban area, Egypt...	123
<i>Dezső, Zs., Bartholy, J. and Pongrácz, R.:</i> Satellite-based analysis of the urban heat island effect.....	217	<i>Steib, R. and Labancz, K.:</i> Regulatory modeling in Hungary – the AERMOD model. Part I. Description and application	157
<i>Hukár, M.:</i> On the use of standard meteorological data for microclimate simulation	39	<i>Szepesi, D., Fekete, K., Büki, R., Koncsos, L., and Kovács, E.:</i> Development of regulatory transmission modeling in Hungary	257
		<i>Wantuch, F. and Szonda, S.:</i> General characterization of the lightnings in the Carpathian Basin	111
		<i>Zsótér, E.:</i> Downscaling EPS probabilities using SYNOP precipitation data	89

II. Book review

- Gelencsér, A.*: Carbonaceous Aerosol (*E. Mészáros*) 139
Holton, J. R. (editor-in Chief): Encyclopedia of Atmospheric Sciences (*Gy. Gyuró*) 281
Hughton, J.: The Physics of Atmospheres (*Gy. Gyuró*) 203
Pap, J. M. and *Fox, P.* (eds.): Solar Variability and Its Effects on Climate (*G. Major*) 69
Zdunkowski, W. and *Bott, A.*: Dynamics of the Atmosphere. A Course in Theoretical Meteorology (*Gy. Gyuró*) 141
Zdunkowski, W. and *Bott, A.*: Thermodynamics of the Atmosphere. A Course in Theoretical Meteorology (*Gy. Gyuró*) .. 141

SUBJECT INDEX

A

- aerosol 139
 agglomeration 217
 agrometeorological station 71
 air pollution
 – modeling 157, 173, 257
 – limit values 257
 atmospheres, physics of 203
 atmospheric sciences 283

B

- Brier score 89
 boundary layer 157
 Budapest agglomeration 217
 Bulgaria 55

C

- canopy characteristics 39
 carbonaceous aerosol 139
 Carpathian Basin 1
 chemical reactions 173
 climate 69
 climate index 1
 complex terrain 157
 concentration
 – most probable 257
 – sector average 257
 condensation nuclei 139
 crop
 – microclimate 21
 – water stress index (CWSI) 21
 cyclone
 – activity 55
 – frequency 55

- paths 55

D

- data assimilation 143
 – variational 233
 dividing streamline height 157
 dispersion modeling 157
 distribution, bi-Gaussian 157
 dust 123

E

- Egypt 123
 electrical parameters 111
 elevated terrain 157
 encyclopedia, atmospheric sciences 283
 energy balance equation 71
 ensemble forecast 89
 error, splitting 173
 Europe 1
 extremes 1

F

- flood
 – management 205
 – detecting 205

G

- global solar radiation 123
 Goudriaan
 – crop microclimate simulation model 21
 grass-covered surface 71

H

- heat island, urban 217
- Hungarian large cities 217
- Hungary 21, 39, 71, 89, 111, 157, 189, 205, 217, 257

I

- industrialization 123
- interferometria 111
- irrigation 21

L

- land use map 205
- lightning
 - cloud-to-ground 111
 - detection system SAFIR 111
 - intra-cloud 111
- limit values, air pollution 257
- local-scale dispersion model 157
- long-term changes of meteorological parameters 189

M

- macrosynoptic situations 257
- maize 21, 39
- Mediterranean cyclones 55
- microclimate maize 21, 39
- model
 - limited area 143
 - mesoscale limited area 233
 - numerical solution 173
 - radiance-bias correction 143
 - regulatory dispersion model 157, 257
- Molenkamp-Crowley advection 173
- movement of cyclones 55

O

- operation splitting 173

P

- path of cyclones 55
- physics of atmospheres 203
- planetary boundary layer 157
- precipitable water 189
- precipitation
 - daily 1
 - extreme indices 1
 - probability forecast 89
 - SYNOP data 89

prediction

- ensemble system 89
- verification 89

probability

- distribution function 89
- downscaling 89

R

- radiance-bias correction 143
- regulatory dispersion modeling 157, 257
- relative operating characteristics 89
- remote sensing 143, 205, 217
- representativity
 - error 89
 - of meteorological data 257
- Romania 205
- roughness length 39
- rural areas 123

S

- SAFIR lightning detection system 111
- satellite
 - ATOVS/AMSU-A 143, 205
 - imagery 217
 - sensor MODIS 205, 217
- simulation model
 - of microclimate 21, 39
- soil moisture 71
- solar radiation
 - global 123
 - ultraviolet 123
- solar variability 69
- splitting error 173
- stability categories 257
- standard meteorological data 39
- surface
 - roughness length 39
 - soil moisture content 71

T

- tendency analysis 1
- temperature
 - long-term variation 189
 - surface 217
- terrain height scale 157
- transmission 257
- troposphere
 - temperature 189
 - precipitable water 189
 - warming 189

U

ultraviolet solar radiation 123
urban heat island effect 217
urbanization 123

V

3D-VAR 233
variational data assimilation 233

W

warming of the atmosphere 189
water-soluble organic species 139
weather prediction, numerical 233
wind, long-term variation 189

Z

zero-plane displacement 39

GUIDE FOR AUTHORS OF *IDŐJÁRÁS*

The purpose of the journal is to publish papers in any field of meteorology and atmosphere related scientific areas. These may be

- research papers on new results of scientific investigations,
- critical review articles summarizing the current state of art of a certain topic,
- short contributions dealing with a particular question.

Some issues contain "News" and "Book review", therefore, such contributions are also welcome. The papers must be in American English and should be checked by a native speaker if necessary.

Authors are requested to send their manuscripts to

Editor-in Chief of IDŐJÁRÁS

P.O. Box 39, H-1675 Budapest, Hungary

in three identical printed copies including all illustrations. Papers will then be reviewed normally by two independent referees, who remain unidentified for the author(s). The Editor-in-Chief will inform the author(s) whether or not the paper is acceptable for publication, and what modifications, if any, are necessary.

Please, follow the order given below when typing manuscripts.

Title part: should consist of the title, the name(s) of the author(s), their affiliation(s) including full postal and E-mail address(es). In case of more than one author, the corresponding author must be identified.

Abstract: should contain the purpose, the applied data and methods as well as the basic conclusion(s) of the paper.

Key-words: must be included (from 5 to 10) to help to classify the topic.

Text: has to be typed in double spacing with wide margins on one side of an A4 size white paper. Use of S.I. units are expected, and the use of negative exponent is preferred to fractional sign. Mathematical formulae are expected to be as simple as possible and numbered in parentheses at the right margin.

All publications cited in the text should be presented in a *list of references*,

arranged in alphabetical order. For an article: name(s) of author(s) in Italics, year, title of article, name of journal, volume, number (the latter two in Italics) and pages. E.g., *Nathan, K.K.*, 1986: A note on the relationship between photo-synthetically active radiation and cloud amount. *Időjárás* 90, 10-13. For a book: name(s) of author(s), year, title of the book (all in Italics except the year), publisher and place of publication. E.g., *Junge, C. E.*, 1963: *Air Chemistry and Radioactivity*. Academic Press, New York and London. Reference in the text should contain the name(s) of the author(s) in Italics and year of publication. E.g., in the case of one author: *Miller* (1989); in the case of two authors: *Gamov and Cleveland* (1973); and if there are more than two authors: *Smith et al.* (1990). If the name of the author cannot be fitted into the text: (*Miller*, 1989); etc. When referring papers published in the same year by the same author, letters a, b, c, etc. should follow the year of publication.

Tables should be marked by Arabic numbers and printed in separate sheets with their numbers and legends given below them. Avoid too lengthy or complicated tables, or tables duplicating results given in other form in the manuscript (e.g., graphs)

Figures should also be marked with Arabic numbers and printed in black and white in camera-ready form in separate sheets with their numbers and captions given below them. Good quality laser printings are preferred.

The text should be submitted both in manuscript and in electronic form, the latter on diskette or in E-mail. Use standard 3.5" MS-DOS formatted diskette or CD for this purpose. MS Word format is preferred.

Reprints: authors receive 30 reprints free of charge. Additional reprints may be ordered at the authors' expense when sending back the proofs to the Editorial Office.

More information for authors is available: antal.e@met.hu

Information on the last issues: http://omsz.met.hu/irodalom/firat_ido/ido_hu.html

Published by the Hungarian Meteorological Service

Budapest, Hungary

INDEX: 26 361

HU ISSN 0324-6329